UCLouvain

Faculté des bioingénieurs

Institute of Condensed Matter and Nanosciences

Preventing infections on medical implants: Integration of LL-37, an antimicrobial peptide, in multilayered coatings

Thèse soutenue en vue de l'obtention du grade de docteur
en sciences agronomiques et ingénierie biologique par

Cédric Vranckx

Composition du Jury

Pr. Christine Dupont-Gillain (UCLouvain/IMCN) – Promotrice
Pr. Olivier Cornu (UCLouvain/IREC) – Promoteur
Pr. Eric Gaigneaux (UCLouvain/IMCN) – Président
Pr. Sophie Demoustier-Champagne (UCLouvain/IMCN)
Pr. Françoise Van Bambeke (UCLouvain/LDRI)
Dr. Philippe Lavalle (Université de Strasbourg/UMR-S 1121)
Dr. Vincent Humblot (Université Franche-Comté/Institut FEMTO-ST)

Louvain-la-Neuve

Novembre 2024

IMCN

IREC
Institut de Recherche Expérimentale et Clinique

Acknowledgement

Sept ans… Il m'aura fallu sept ans pour écrire ce manuscrit. Bien qu'une thèse soit un accomplissement personnel, le fruit de ce dur labeur n'aurait jamais pu mûrir sans l'aide et le soutien de mes collègues, ami·e·s et famille. A travers ces remerciements, je tiens à leur faire savoir à quel point ils et elles ont été et sont important·e·s pour moi.

Tout d'abord, je tiens à remercier mes promoteur·rice·s. Ce projet de thèse est né des retrouvailles de Pr. Christine Dupont et Pr. Olivier Cornu, qui ont voulu unir leur expertise afin de développer un revêtement à la surface d'implants médicaux et qui aurait des propriétés antibactériennes dans le but de limiter les risques d'infection. Je me souviens comme si c'était hier de la réunion que nous avons eu avec Christine concernant ce projet qui m'a immédiatement emballé. Je remercie Christine pour son encadrement, malgré son emploi du temps chargé, jonglant entre son boulot de professeure, et ses mandats de vice-doyenne et de doyenne de la faculté des bioingénieurs. Cela n'a pas toujours été facile, mais vous avez toujours été présente quand j'en avais besoin. Bien que la créativité ne soit pas ma qualité première, vous m'avez permis de m'accomplir en tant que chercheur en me laissant la liberté d'innover, de tester, et parfois même d'échouer. Vous m'avez permis de devenir autonome dans mon métier de chercheur mais également d'assistant. Christine m'a également toujours soutenu dans ma passion de l'arbitrage. Vous m'avez toujours laissé la possibilité de partir en tournoi et m'avez encouragé en ce sens. Pour la confiance que vous m'avez accordée, la liberté que vous m'avez octroyée et la formation que vous m'avez apportée, je vous dis MERCI. Bien que moins impliqué au quotidien, Pr. Olivier Cornu m'a toujours soutenu dans la direction que je donnais à ma thèse. Sa porte était toujours grande ouverte malgré un emploi du temps chargé, voire surchargé, jonglant entre ses casquettes de chirurgien, responsable de service et professeur. Je me souviendrai toujours de l'opportunité que vous m'avez donné d'assister à une opération de la hanche, afin que la théorie rencontre la pratique et que je me rende compte de la réalité du terrain. Bien que j'ai passé les deux tiers du temps de l'opération dehors, à reprendre mes esprits et à essayer d'oublier l'odeur de chair brûlée, vous m'avez donné une opportunité unique. Merci pour votre confiance et les conseils que vous m'avez apportés.

Ce manuscrit ne serait pas ce qu'il est sans l'expertise des membres de mon jury de thèse. Merci à Pr. Eric Gaigneaux d'avoir présidé ce jury. Je tiens également à remercier Pr. Sophie Demoustier d'en avoir été la secrétaire. J'ai également eu la chance de pouvoir être impliqué, en tant qu'assistant, dans certains de vos cours et je tenais à vous remercier pour la liberté octroyée et votre confiance. Merci à Pr. Françoise Van Bambeke, pour ses précieux conseils en microbiologie. Grâce à une collaboration que nous avons entamée lors de ma troisième année de thèse, vous m'avez permis de me former aux techniques microbiologiques. Merci de m'avoir chaleureusement accueilli dans votre laboratoire comme un membre à part entière. Enfin, merci à Dr. Vincent Humblot et Dr. Philippe Lavalle d'avoir accepté de faire partie de mon jury de thèse et de vous êtes déplacés à deux reprises. J'ai eu l'occasion de rencontrer Dr. Vincent Humblot lors d'une école doctorale sur l'île de Porquerolles en 2019 et Dr. Philippe Lavalle lors d'une conférence en Guadeloupe en 2022. Ces endroits ont été propices à de très intéressantes discussions scientifiques et à des moments de partage. Je suis très heureux de vous avoir rencontrés. Merci à vous tou·te·s pour le temps passé et l'énergie donnée à la lecture de ce travail, ainsi que pour les améliorations que vous avez suggérées d'apporter à ce manuscrit. Cette thèse a hautement bénéficié de votre expertise et ce fut un réel plaisir de discuter de mes résultats avec vous pendant ma défense privée.

Cette thèse étant assez multidisciplinaire, il m'aurait été impossible de réaliser l'entièreté de ce qui a été accompli sans l'expertise et l'aide de certaines personnes. Merci à Dr. Clément Guibert de la Sorbonne université pour son aide précieuse, ses conseils avisés et le temps passé à réaliser les expériences de dichroïsme circulaire. Je tiens à remercier très chaleureusement Dr. Hervé Poilvache, avec qui j'ai eu l'occasion de collaborer pendant la première moitié de ma thèse et avec qui j'ai eu de très intéressantes discussions sur les biofilms. Un énorme merci à Dr. Steven De Soir avec qui j'ai eu l'immense plaisir de collaborer pendant la deuxième moitié de ma thèse. J'ai énormément apprécié travailler avec toi. Je te remercie pour toute l'expertise que tu m'as transmise et toute l'aide que tu m'as apportée. J'espère que notre collaboration n'est pas terminée et que nous pourrons mettre sur pied les nombreuses idées qu'ils nous restent à explorer. Merci à Alix Mangin et Romain Tricot, faisant partie de l'équipe de Pr. Françoise Van Bambeke, pour leur aide technique lors des expériences en

microbiologie. Je tiens enfin à remercier Pierre Eloy qui m'a formé aux mesures XPS et qui m'a grandement aidé lors de l'interprétation des résultats.

En sept ans, voire plus si l'on compte mes deux années passées au laboratoire avant d'entamer ma thèse, on en croise du monde dans les bureaux, les couloirs et surtout la cafétaria. Je vais essayer d'oublier personne, même si ce n'est pas gagné. Merci à Sara Mauquoy qui fut mon encadrante lors de mon mémoire. Tu m'as donné le goût de la recherche, ce qui m'a poussé à entamer une thèse. Je tiens à remercier Jean-François Art qui fut mon assistant avant d'être mon collègue, et Loïc Germain, mon premier collègue de bureau. Merci Loïc pour les discussions que nous avons pu avoir et pour ta gentillesse et ton altruisme. Ce fut un plaisir de partager une partie de ma thèse avec toi. Je tiens à remercier Aurélien vander Straeten. J'ai eu la chance de prendre la suite d'un projet que tu avais entamé pendant ta thèse. Vu la magnifique thèse que tu as réalisée, prendre ta suite n'a pas été chose facile. Merci pour ton aide et le partage de ton expertise. Je tiens également à remercier mon binôme de thèse, Vincent Delmez, pour la bonne ambiance au laboratoire et les discussions. Je ne te battrai jamais en course à pied, mais je m'y suis fait à l'idée depuis bien longtemps. Tout un symbole de présenter ma thèse publique deux ans, jour pour jour, après la tienne. Merci à Thibaut Huybrechts et Arnaud Detaille, mes deux collègues de bureau. Merci pour les nombreuses discussions que nous avons pu avoir et les parties de franche rigolade. Après votre départ, ce bureau m'a semblé bien vide ! Ma thèse aurait été beaucoup plus compliquée sans la magnifique ambiance que nous avons eue dans le laboratoire. Merci à Rose-Anne Jacob, pour son aide ô combien comptable, à Françoise Bouvy, Françoise Somers et enfin Anne Bouchat pour leur aide au niveau des tâches administratives. Je tiens à remercier très chaleureusement Yasmine Adriaensen, avec qui j'ai eu la chance de partager des heures et des heures de laboratoire lorsque je portais ma casquette d'assistant. Merci pour ton aide technique précieuse, ta gentillesse et ta ténacité envers VWR et Merck. Tu auras rendu ma tâche d'assistant beaucoup plus facile. Merci également pour les échanges et les nombreuses discussions que nous avons partagés. Comme je te l'ai déjà dit, tu auras passé près d'un quart de ta carrière en me connaissant. Je pense que tu m'auras vu grandir et évoluer depuis notre première rencontre en 2014. Une vie épanouie au travail va de pair avec des moments de détente,

de bonne ambiance et de rigolade. Et croyez-moi, il y en a eu des dizaines et des dizaines. Merci à Damien Debecker. Merci d'être comme tu es, le chercheur passionné, le professeur sympathique, et la personne bonne ambiance. J'ai eu la chance de pouvoir être ton assistant pour plusieurs de tes cours, et cela a été un réel plaisir. Merci pour ta confiance et la liberté que tu m'as donnée. Je ne compte plus le nombre de fous rires que j'ai eus grâce à tes blagues sur le temps de midi et les pauses-café. Ces moments me manqueront indéniablement. Je remercie mon binôme de train, François Devred. Ces deux dernières années, il me raccompagnait même jusque devant chez moi. Je garderai de ces nombreux voyages en train, pauses-midi et pauses-café, des moments de rigolade, des discussions sportives et des moments de partage. Ta bonne humeur et ta joie de vivre au quotidien me manqueront et font l'unanimité au laboratoire. Damien et François, j'espère que mon vomi de Grand-Duc vous manquera. Je tiens également à remercier Arnaud Delcorte, Nathalie Blangenois, Jean-Charles Godefroid, Giovanni Pampararo, Charlotte Lang, Isaac Meza Trujillo, Solène Le Bras, Anna Bratek-Skicki, Samuel Bertolini pour les moments que nous avons passés ensemble. En tant qu'assistant, j'en ai vu des étudiant·e·s. Et certain·e·s de ces étudiant·e·s sont devenu·e·s des collègues. Merci à Hippolyte Meersseman Arango et Fanny Hanon pour les trajets que nous avons partagés entre Bruxelles et Louvain-la-Neuve, pour votre bonne humeur et ambiance. Merci à Marty Kinnaer. Je pense que nous avons fait un bon binôme d'assistants. Je te laisse maintenant prendre ton envol avec Aurélien Doutry. Merci à Benjamin Tomasetti, Alexis Franco, Juliette de Meeûs, Mehdi Lakhdar, Ian Coupez, Noé Laloux, Margot Van Der Verren, Aurélien Doutry, Oscar Laurent et Alixandre Magerat. Merci à tout·e·s mes collègues de l'ACube. Je ne vais pas tout·e·s les citer afin de ne pas écrire dix pages de remerciements. Enfin je voudrais également remercier très chaleureusement tout·e·s les mémorant·e·s que j'ai eu la chance d'encadrer. Un tout grand merci à Romain Hardy, Alix Mertens, Antoine Matheys, Noémie de Suraÿ, Coralie Nerincx, Christophe Delcuve, Juliette Dewez et Bastien Croës. Vous avez tout·e·s grandement contribué à cette thèse.

Lorsque l'on réalise une thèse, un des challenges est de pouvoir dissocier vie professionnelle et vie privée afin de ne pas réfléchir non-stop à ses expériences, aux traitements de ses données et aux interprétations de ses résultats. Pour cela, il faut pouvoir s'octroyer des moments de qualité, de fun

et de partage avec sa famille et ses ami·e·s. Merci à ma deuxième famille, la famille de l'arbitrage, à mes petites « Lucioles ». Merci à Maxou, Soet, Flo, Gouigoui et Ced d'être là, et d'être comme vous êtes. Je ne compte plus les aventures et les moments de joie que j'ai partagés avec vous et grâce à vous. Vous êtes des ami·e·s en or. Sans vous ma vie ne serait pas la même. Un énorme merci à mes ami·e·s de très longue date du Sacré-Cœur de Jette, Sushi, Mickey, Damien, Pietro, Vincent, Noëlie, Marine, Jim, Sylvain et Diego. Votre amitié ainsi que les nombreux moments de partage que nous avons pu vivre et que nous vivrons encore me sont précieux. Merci à ma « belle-famille », Annick, Marc, Florine, Maëlle, Yoann, Max, Eloïse et Elliott. Merci de m'avoir si bien accueilli dans votre famille. Et merci pour tous les bons moments que nous avons passés ensemble depuis le début de ma thèse. Merci à Mamy, et j'ai une énorme pensée pour Mimi, Parrain et Papy, qui ne sont malheureusement plus avec nous, mais qui ont toujours été là pour moi et qui m'ont toujours soutenu. J'espère que vous êtes fier·e·s de la personne que je suis devenue. Merci à Maman et Papa de toujours avoir été présent·e·s. Merci pour votre aide, pour votre soutien, pour votre écoute, pour votre amour et pour l'éducation que vous m'avez inculquée. Je ne serais pas celui que je suis sans vous. Je vous aime. Enfin, merci à mon amour, mon cœur, Hortense, que j'ai rencontrée au début de ma thèse, et qui m'a donc vu grandir au travers de mon parcours doctoral. Merci d'être là au quotidien, de partager mes inquiétudes et mes joies. Merci de m'encourager, de me soutenir, merci pour l'amour que tu m'apportes, merci pour la joie et la paix que tu me procures. Tout paraît plus simple à tes côtés. Je t'aime.

Enfin, merci à toutes les personnes qui m'ont inspirées et merci à vous qui prendrez le temps de lire cette thèse.

Abstract

The use of antibacterial agents is essential in the treatment of patients with bacterial infections. However, the last decades have seen an increase in the number of antimicrobial-resistant bacteria, which could have catastrophic consequences. Antimicrobial resistance is highlighted as one of the most serious threats to global health. In addition to this concern, bacterial adhesion and colonization on the surface of medical implantable devices, leading to biofilm formation, are causing severe complications.

With a view to finding new effective strategies against these infections, this thesis aims at developing a coating displaying antibiofilm properties, that could be applied to the surface of medical devices. This was achieved through the assembly of multilayers integrating LL-37, an antimicrobial peptide (AMP), using the layer-by-layer (LbL) self-assembly method. It is well known that the charge heterogeneity of LL-37 can be a major setback for its LbL immobilization. Therefore, the surface charge of LL-37 was standardized via its complexation with heparin (Hep) to form protein-polyelectrolyte complexes ($PPCs_{LL\text{-}37\text{-}Hep}$). The resulting $PPCs_{LL\text{-}37\text{-}Hep}$ were then used as new building blocks for LbL assembly with chitosan (Chi). As a matter of comparison, bare LL-37 was directly assembled with Hep into multilayers. The results show that the nano-architecture and -organization are influenced by the assembly strategy. The films built with $PPCs_{LL\text{-}37\text{-}Hep}$ are more viscoelastic and more hydrated than the bare LL-37-based multilayers. However, multilayers based on bare LL-37 incorporate more LL-37 than the $PPCs_{LL\text{-}37\text{-}Hep}$-based multilayers because these latter would undergo a self-reorganization upon Chi adsorption. The LL-37 release profile from both LL-37- and $PPCs_{LL\text{-}37\text{-}Hep}$-based multilayers is particularly interesting as the initial burst release is relatively moderate, followed by a prolonged and gradual release of AMP over an extended duration, which is useful for targeting both bacteria in the early stages of infection and opportunistic pathogens beyond this period. The thorough study of assembly conditions and the characterization of the obtained multilayers increased our understanding of LbL assembly of proteins. The developed coating demonstrates promising antibiofilm properties. This study highlights nevertheless the requirement of a multifaceted approach that leverages all available antimicrobial weapons to overcome biofilm-associated infections.

Contributions and participations

The author contributed to the following papers:

- Vranckx, C., Lambricht, L., Préat, V., Cornu, O., Dupont-Gillain, C., vander Straeten, A. Layer-by-Layer Nanoarchitectonics Using Protein-Polyelectrolyte Complexes toward a Generalizable Tool for Protein Surface Immobilization. *Langmuir* **38**, 5579–5589 (2022).

The author participated to the following international scientific events:

- Presentation of a poster '*Antimicrobial Peptide-Polyelectrolyte Complexes to Prevent Bacterial Infections of Hip Prostheses*' at the Biosurf 2019, Porquerolles, France, June 2019
- Oral presentation '*Antimicrobial Peptide-Polyelectrolyte Complexes to Prevent Bacterial Infections of Titanium Medical Implants*' at the DelNAM workshop 2019, Ghent, Belgium, November 2019
- Presentation of a poster '*Protein/Peptide-Polyelectrolyte Complex: A Versatile Building Block for the Surface Immobilization of Proteins and Peptides using the Layer-by-Layer Assembly Method*' at the World Biomaterial Congress (WBC) 2020, Virtual, December 2020
- Oral presentation '*Protein-Polyelectrolyte Complexes: A Versatile Building Block for the Immobilization of Proteins using the Layer-by-Layer Assembly Method*' at the European Society for Biomaterials (ESB) 2021, Virtual, September 2021
- Oral presentation '*Architecture of LL-37-Heparin Layer-by-Layer Antimicrobial Coatings*' at NanoInBio 2022, Guadeloupe, France, June 2022
- Oral presentation '*Layer-by-Layer Assembled Antimicrobial Nanocoatings to Prevent Medical Implant-Related Infections*' at the 6th plenary days of GdR B2i, Louvain-la-Neuve, Belgium, June 2023
- Presentation of a poster '*Antibiotics or Antimicrobial Coatings? Evaluating Combined Treatment Approaches for the Removal of Staphylococcal Biofilm-Related Infections*' at the 9th Thesinge Biofilm meeting, Thesinge, The Netherlands, May 2024

List of abbreviations

A_{450}	Optical density at 450 nm wavelength
Acy	Acylase
Ag^{+}	Silver ion
AgNP	Silver nanoparticle
AL	Anchoring layer
Alg	Alginate
AMP	Antimicrobial peptide
AMR	Antimicrobial resistance
Amy	Amylase
BCA	Bicinchoninic acid
BMI	Body-mass index
CAMP	Cathelicidin antimicrobial peptide
CD	Circular dichroism
CFU	Colony forming unit
Chi	Chitosan
Col	Collagen
D	Dissipation
DD	Deacetylation degree
DAIR	Debridement surgery, antibiotic therapy, with implant retention
DKR	Danish knee arthroplasty register
DLS	Dynamic light scattering
Dox	Doxycycline
ECM	Extracellular matrix
eDNA	Extracellular DNA
EPS	Extracellular polymeric substance
EtOH	Ethanol
FDA	Food and drug administration
FITC	Fluorescein isothiocyanate
Fn	Fibronectin
FWHM	Full width at half the maximum intensity
Gox	Glucose oxidase
Hep	Heparin
I	Ionic strength
IEP	Isoelectric point

IM	Inner membrane
Ins	Insulin
k	Absorption coefficient
LB	Luria-Bertani
LbL	Layer-by-Layer
LCP	Left-circularly polarized
LEASA	Localized enzyme-assisted self-assembly
Lin	Linezolid
LOD	Limit of detection
LOQ	Limit of quantification
Lyz	Lysozyme
MBEC	Minimum biofilm eradication concentration
MHB	Mueller Hinton broth
MIC	Minimum inhibitory concentration
MNP	Metal-based nanoparticle
MRSA	Methicillin-resistant *Staphilococcus aureus*
MRSE	Methicillin-resistant *Staphilococcus epidermidis*
n	Refractive index
OM	Outer membrane
PAH	Poly(allylamine hydrochloride)
PBS	Phosphate-buffered saline
PE	Polyelectrolyte
PEI	Polyethyleneimine
PEC	Polyelectrolyte complexe
PEG	Poly(ethylene glycol)
PEM	Polyelectrolyte multilayer
PJI	Prosthetic joint infection
PMMA	Poly(methacrylic acid)
PPC	Protein-polyelectrolyte complexe
PSS	Poly(styrene sulfonate)
QCM-D	Quartz crystal microbalance with dissipation monitoring
RCP	Right-circularly polarized
R_h	Hydrodynamic radius
ROS	Reactive oxygen species
RPMI	Roswell Park Memorial Institute
SDS	Sodium dodecyl sulfate

THA	Total hip arthroplasty
TKA	Total knee arthroplasty
Tob	Tobramycin
TSA	Tryptic soy agar
TSB	Tryptic soy broth
UK	United Kingdom
USA	United States of America
Van	Vancomycin
WHO	World Health Organization
XPS	X-ray photoelectron spectroscopy
Δ	Phase difference
ΔD	Dissipation shift
Δf	Frequency shift
Δm	Mass shift
Θ	Degree of ellipticity
λ_D	Debye length
λ_B	Bjerrum length
Ψ	Amplitude ratio
Ψ_S	Surface potential

Table of contents

La devise Shadok de la semaine

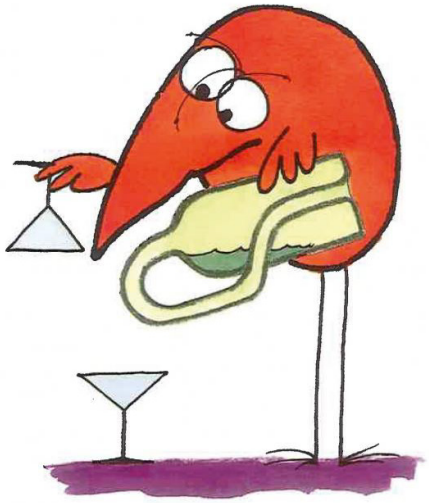

S'IL N'Y A PAS DE SOLUTION
C'EST QU'IL N'Y A PAS DE PROBLÈME.

Part I – Context of the research

1 'No Time to Wait'

Antimicrobial drugs – antibiotics, antivirals, antifungals and antiparasitics – are substances widely used to prevent and treat infections. Due to an increase in antimicrobial-resistant bacteria and a decline in the development of new antimicrobial strategies, the effectiveness of treatments that once worked is now in jeopardy.[1,2] The appearance of these 'superbugs', bacteria resistant to commonly used antimicrobials, is considered as one of the biggest threats to humanity by the World Health Organization (WHO). According to recent estimates, published in *The Lancet*, antimicrobial-resistant bacteria would have killed 1.27 million people in the world in 2019.[3] In 2016, *The Review on Antimicrobial Resistance* argued that the number of deaths attributable to antimicrobial resistance (AMR) could reach 10 million people per year by 2050, *i.e.*, one person dying every 3 seconds (Figure I. 1), and cost up to $100 trillion, if no action is taken.[4,5] Such AMR could result in severe consequences across different fields such as the agri-food, cosmetics and biomaterials (contact lenses, dressings, medical implants, etc.) sectors. Overuse of antibiotics in human and veterinary medicine, as well as in agricultural practices, misuse for treatment of viruses, inappropriate use in hospitals, and lack in the development of new antibacterial agents have resulted in selection of multidrug-resistant bacteria. With the increasing number of hospitalizations, and surgical operations and procedures, the risk of medical-related infections is sizable. The challenges of AMR are complex and multifaceted, but the potential future human and economic costs of AMR are too catastrophic to be ignored. The development of international collaborative actions to address this threat becomes urgent.[6] As said by a report of the *Interagency Coordination Group on Antimicrobial Resistance*, there is 'No Time to Wait'.[7]

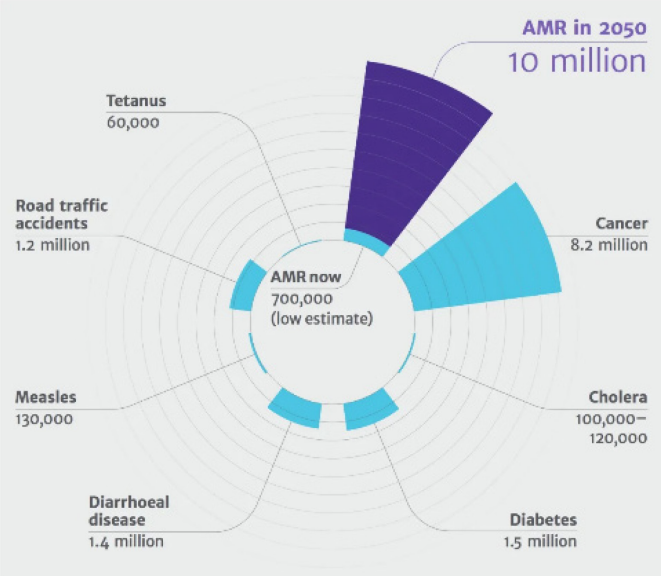

Figure I. 1 – Prediction of deaths attributable to AMR every year by 2050. Reproduced from O'Neill.[5]

2 Medical-related infections

As previously noted, while the issue extends across various domains, the present study specifically addresses the challenge of AMR in the context of medical-related infections. Medical-related infections, also known as healthcare-associated infections or nosocomial infections, are infections that patients acquire while receiving medical treatment in a healthcare facility. These infections can be caused by various pathogens, including bacteria, viruses, fungi, and parasites. Medical-related infections are a significant concern in healthcare settings because they can lead to prolonged hospital stays, increased medical costs, and even increased mortality in severe cases.

Over the past 50 years, the use of biomaterials and medical devices, such as catheters, contact lenses, medical implants, etc. is more and more common. This increase can be related to the advances in material technology and the ageing of the population. In 2020, the cost of medical implants' market was estimated at $89 billion, with a compound annual growth rate expected to witness 6.5% during the forecast period. It represents a cornerstone of our healthcare system. Among this, orthopedic implant sector is expected to hold a significant market share.[8] Due to the ageing population, demographic

development, increased access to healthcare and improved healthcare in developing countries, the demand for orthopedic implants has increased significantly.[9–11] Although joint replacement has a success rate around 95% after 10 years following the surgery, and a perioperative mortality rate that remains low, some complications may occur.[12–14] One of the most common and catastrophic complications of joint replacement surgeries is the development of an infection. The surface of orthopedic implants being conducive to bacterial adhesion, bacterial contamination can lead to the formation of a biofilm.[15] According to the *National Institute of Health*, up to 80% of human bacterial infections are caused by bacteria that form biofilms.[16] An in-depth understanding of these biofilms is thus crucial to prevent the risk of infection. As already mentioned, the problem of bacterial contamination affects a wide range of fields, including agri-food, cosmetics and biomaterials. However, this study remains primarily focused on infection-related issues within the medical field, and more particularly in orthopedy.

Prosthetic joint infection (PJI) is defined as an infection involving a joint replacement implant and its surrounding tissues. PJI is one of the main reasons of prosthetic joint failure and revision (22%).[17,18] While the risk of developing an infection over the lifetime of the prosthetic joint remains low (0.5-2%), PJI represents a tremendous burden because of the high number of joint replacements performed worldwide.[11,19,20] Moreover, in case of revision arthroplasty, this infection risk can reach 16%.[21]

PJI and its treatments cast significant ramifications upon patients, entailing a notable incidence of complications.[22,23] This includes not only physical distress such as pain, joint swelling or effusion, erythema, fever, and impaired joint function,[24,25] but also psychological strain,[26] and even increased mortality (~8% at one year).[27,28] Addressing PJI is an intricate and demanding endeavor, necessitating a fusion of medical and surgical approaches.[29] A key factor to the intricate nature of managing PJI lies in the development of biofilms on implantable medical devices.[30] Most PJIs are associated with biofilms. These biofilms consist of communities of microorganisms that attach to a surface and are embedded within their own produced extracellular matrix.[31] This biofilm formation not only hampers the capacity to detect the responsible pathogens (multi-species biofilms),[32,33] but also results in irreversible bacterial attachment to the affected surfaces,[34]

facilitates bacteria in evading immune responses,[34,35] and fosters the development of tolerance and resistance mechanisms to antimicrobial agents.[36,37] Therefore, biofilm-associated infections are particularly challenging to treat. An overview of biofilm biology, exploring how biofilms develop antibiotic tolerance and evade the host immune system, alongside discussions on therapeutic and prevention methods aimed at targeting biofilms will be presented later in this work.

2.1 Classification of PJIs

There are several useful classification schemes for PJIs.[29] One primary scheme categorizes infections by the time to onset: early, delayed, or late. Early-onset PJI occurs within 3 months post-surgery, typically caused by intraoperative contamination with relatively virulent microorganisms. Delayed-onset PJI arises between 3 and 12 or 24 months post-surgery, depending on the criteria used by different authors to differentiate between delayed- and late-onset PJIs. Despite varying time points, these infections are generally acquired during surgery and caused by less virulent microorganisms, with symptoms emerging after 3 months. Late-onset PJI, occurring more than 12 to 24 months after surgery, is often due to hematogenous infection but can also stem from a very indolent infection initiated during the surgical procedure.[29]

Another classification scheme was popularized by Tsukayama *et al*. in the 1990s.[38,39] It divides PJIs into four categories based on the time since surgery and the presumed mode of infection. The first category is positive intraoperative cultures, where a patient undergoing revision for presumed aseptic failure has a positive culture during surgery. The second category addresses early postoperative infections occurring within the first month after surgery, similar to early-onset PJI in the primary classification scheme. The third category, known as late chronic PJI, emerges more than 1 month after the initial operation and typically follows a slow-developing course. This category encompasses patients often categorized under delayed- and late-onset PJI in the other classification system. The last category is acute hematogenous infection. These classification schemes aid in guiding the approach to medical and surgical treatment.[29]

2.2 Global concerns of PJIs

In addition to the impact on patients' health, the economic and social costs of medical implant-related infections are significant.[40,41] Due to growing incidence of joint arthroplasties procedures, PJI is thus positioned to present substantial medical, social, and economic burdens in the years ahead. It thus becomes of paramount importance to explore innovative treatment options for PJIs or to devise strategies aimed at preventing the occurrence of such infections. To effectively pursue this goal, developing a comprehensive understanding of these medical-related infections is crucial.

3 Epidemiology

The epidemiology of PJI is closely linked to that of joint replacement procedures. Total hip and knee arthroplasty (THA and TKA) are some of the most frequently performed and effective surgeries worldwide. In 2019, in the OECD countries, the average numbers for hip and knee replacement were, respectively, 172 and 119 per 100,000 inhabitants.[11] The incidences were even higher in Belgium, reaching 271 THA/100,000 inhabitants and 164 TKA/100,000 inhabitants.[11] In the United States of America (USA), 2,244,587 hip and knee procedures were performed between 2012 and 2020.[42] Predictive rates show a worldwide significant rise in the use of THA and TKA in the future.[11] In 2040, in the USA, the annual number of THA and TKA is, respectively, estimated to 1,429,000 and 3,416,000.[43] These procedures yield a positive impact on patients' overall quality of life[44,45] and exhibit notably low rates of revision.[46,47] According to Karachalios *et al.*, the THA revision rate is 8.9% in Australia, and 6.8% in the United Kingdom (UK).[46] For TKA, Howell *et al.* determined an implant survival rate of 97.4%, regardless of the revision cause.[47] Among the factors driving the need for revision in THA and TKA, PJI stands out as the predominant concern, emerging as the first or second most frequent cause of failure in case of TKA,[48] and the third most common after THA.[18] The other common causes of failure are the wear, aseptic loosening, dislocation, instability, mechanical complications, reaction to metal debris, periprosthetic fracture, and unexplained pain.[18,46] Mathis & Hirschmann analyzed TKA failure modes in different parts of the world. Although regional discrepancies were identified, a detailed examination of these failure modes

clearly reveals the limitations of international comparisons.[49] Current literature shows infection as the main acute cause of TKA failure, while aseptic loosening and instability are the most common reasons for revisions overall. National registries indicate that aseptic loosening is the primary failure mode in Japan, the UK, New Zealand, and Switzerland. Early TKA failures due to infection are prevalent in Sweden, Australia, New Zealand, Japan, and the USA, with rates between 20-30%. Higher infection rates are reported in Asian clinical studies: Korea (38%), China (53%), Iran (44%), and India (87%).[49] In Belgium, in 2020, infection was the second most prevalent reason for TKA revision and the third for THA revision.[50] Consequently, the incidence of PJI varies globally, with a notably higher risk observed in Asian countries.

Patients afflicted with PJI confront considerable disability, increased morbidity, and heightened risk of mortality. The negative effects of PJI on joint function and patients' quality of life have been effectively described by numerous researchers. In 2021, a study conducted by Wildeman *et al.* on 442 patients with a PJI after THA concluded that 10-year mortality is higher for this group of patients compared with patients undergoing THA without PJI (45% vs. 29%). It also revealed a lower patient-reported outcome score (EQ-5D-5L index score of 0.83 vs. 0.94, higher scores are better), a greater proportion of assisted living (21% vs. 12%), a greater need of ambulatory aids (65% vs. 42%), and a lower Oxford hip score (OHS of 36 vs. 44, higher scores are better) for patients developing a PJI compared to the non-infected group.[51] The impact of PJI on joint function may be influenced by the therapeutic strategy used to treat the infection. Grammatopoulos *et al.* showed that less invasive debridement surgeries are associated with better functional outcome than two-stage revision procedures.[52] The different treatment strategies and thus the difference between debridement and two-stage revision procedure is explained in details in the section *Part I – 4.1 Surgical strategies*. In addition, the treatment of PJI frequently leads to a high prevalence of complications. In 2020, Hartzler *et al.* conducted a retrospective cohort study involving 134 patients undergoing two-stage revision for infected TKA. They found a 27% incidence of medical complications (*e.g.*, venous thromboembolism, kidney failure, cardiopulmonary issues) and a 41% incidence of surgical complications (*e.g.*, septic and aseptic reoperations, wound complications, recurrent infections),

highlighting the considerable morbidity associated with PJI.[22] Furthermore, several studies have established a significant rise in mortality rates among patients afflicted with PJI. In their study, conducted in 2013, Zmistowski *et al.* revealed a significant increase in one- and five-year mortality rates among patients with PJI compared to those necessitating arthroplasty revision for aseptic loosening.[53] The mortality estimates stood at 10.6% after one year and 25.9% after five years post-treatment, surpassing the mortality rates observed in prevalent cancers such as prostate cancer, breast cancer, or melanoma.[53] In a 2018 meta-analysis led by Lum *et al.*, results compiled from 14 studies, examining mortality rates among patients undergoing two-stage total revision for knee PJI, were pooled.[54] The analysis confirmed these estimates, indicating a total five-year mortality rate of 21.64%.[54] A more recent systematic review, based on 23 relevant studies, conducted by Natsuhara *et al.* in 2019, led to the same conclusions.[55] One- and five-year mortality rates were respectively estimated at 4.22% and 21.12% after total hip PJI with two-stage revision protocol.[55]

The intricate and resource-intensive treatments needed to manage patients with PJI, combined with the considerable morbidity and disability associated with this condition, present a substantial financial challenge for healthcare systems. Using the most recent data of hip and knee arthroplasty, the annual hospital costs due to PJI are estimated to $1.85 billion by 2030 in the USA.[56] An analysis of over 200,000 revision hip replacement procedures in the USA revealed an average cost of $87,000 per revision in 2014.[57] In Europe, in case of infections treated with a two-stage revision, significant differences in costs were found. In France, the mean cost of hip PJI treatment was evaluated at €21,324, in England, it was evaluated at £33,000 and in Portugal, the cost was respectively €11,415 and €13,793 for hip and knee PJIs.[58–60]

Despite an improved understanding of the risk factors associated with PJI and the implementation of stricter aseptic protocols, PJI is still one of the most common indications for revision surgery. However, the incidence of PJI over time varies throughout the literature and thus needs to be interpreted with caution. Kurtz *et al.* used the *2001-2009 US National Inpatient Sample* to study the PJI incidence rate, and indicated a moderate increase in PJI incidence among patients undergoing THA from 1.99% to 2.18% and from 2.05% to 2.18% among patients undergoing TKA.[61] Likewise, Dale *et al.* used the *Nordic Arthroplasty Registry* data, and showed a rise in adjusted

cumulative five-year revision rates for infected THA, increasing from 0.46% to 0.71% between 1999 and 2009.[62] A single-center study of 423 THAs between 2008 and 2021 conducted by Liukkonen *et al.* showed that the incidence of early infections increased from 0.11% to 1.09%.[63] It contrasts with findings from Wang *et al.* who reported a decrease in two-year PJI incidence of TKA from 1.93% to 0.76% between 2002 and 2014.[64] Similarly, Runner *et al.* reported a reduction in PJI occurrence from 1.43% to 0.61% spanning 2008 to 2016.[65] A 15-year population-based cohort study conducted by Bozzo *et al.*, using linked administrative databases from 2002 to 2016 in Ontario, Canada, revealed a decrease in the incidence of PJI following TKA over time.[66] However, it is important to point out that PJI revisions are underestimated in the national arthroplasty registries. In 2024, Anneberg *et al.* published a longitudinal observational cohort study on TKA, which highlights that revisions due to PJI in the *Danish Knee Arthroplasty Register* (DKR) were significantly underreported, with a rate of 42%, especially within the first 3 months after primary TKA. It is noteworthy that the majority of missed PJI cases in the DKR resulted from non-reporting rather than misclassification.[67]

What is clear from the existing literature is that the numbers of THAs and TKAs are increasing annually, since 2000 in OECD countries,[11,68] and are expected to increase significantly in high-income countries over the next decades.[43,69–72] These rises can be attributed to an expanding prevalence of osteoarthritis in these countries driven by ageing population, and a growing incidence of obesity and diabetes.[73] Kunutsor *et al.* conducted a meta-analysis in 2016, synthesizing data from 66 studies encompassing over 500,000 total joint replacements.[74] The findings revealed that patient-related factors including male gender, elevated body-mass index (BMI), steroid usage, diabetes, rheumatoid arthritis, congestive heart failure, depression, as well as smoking and alcohol consumption, were all correlated with a heightened risk of PJI.[74] While it is not the sole determinant, it seems obvious that the risk of infection can be limited by a healthy lifestyle.

In conclusion, nowadays, the rising number of arthroplasty procedures performed each year and the constant occurrence rate of PJI predict an upcoming escalation in total PJI (Figure I. 2a).[56] This rise is particularly concerning as it is expected to exert growing financial pressures on healthcare systems in the forthcoming decades (Figure I. 2b).[56]

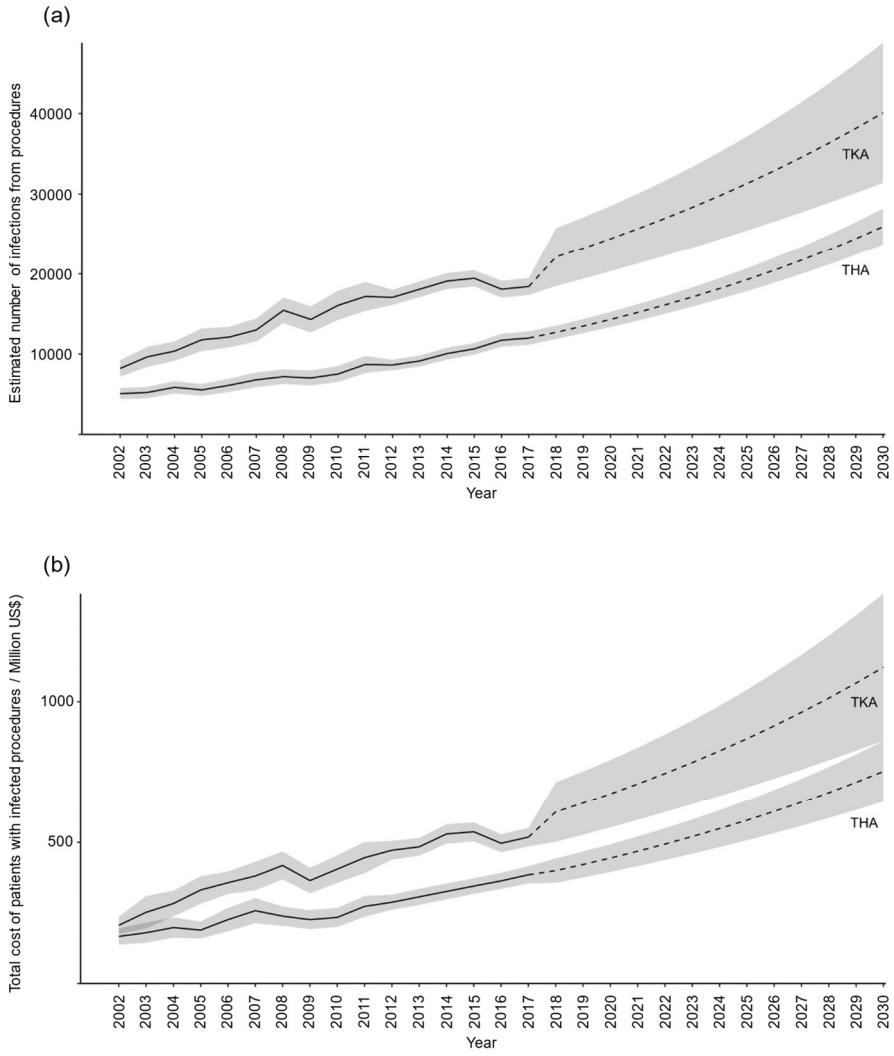

Figure I. 2 – Historical and projected (a) number of infected THA and TKA procedures and (b) cost of PJI-related THA and TKA revision procedures, in the USA (2002-2030). The solid and dashed lines represent, respectively, the historical and the projected values per surgery type. The shaded area represents a confidence interval of 95%. Reproduced from Premkumar *et al*.[56]

4 Treatment strategies

The management of PJIs requires a multidisciplinary approach, typically combining surgical and medical therapies. Following PJI, the formation of a biofilm on the implant surface can render antibiotic therapy alone ineffective to cure patients due to the inherent properties of biofilms. These characteristics will be detailed in the section *Part I – 5.2 Biofilm*. The antibiotic therapy should only be considered for patients unable to undergo surgery or requiring lifelong suppressive treatments.[75]

4.1 Surgical strategies

Usually, antibiotic therapy is preceded by a surgical procedure aiming at removing the infected and necrotic tissues. The choice of the surgical technique by which the tissue is eliminated is of paramount importance regarding the outcome of the infection and is guided by patient-, infection-, and implant-specific characteristics.

4.1.1 Debridement surgery, antibiotic therapy with implant retention

The debridement surgery, antibiotic therapy, with implant retention (DAIR) strategy is commonly attempted to treat patients suffering from early post-operative infections and acute hematogenous infections. This surgical strategy should be applied in the case of a PJI occurred on a well-fixed prosthesis without a sinus tract and within the 30 days of prosthesis implantation or usually less than 3 weeks of onset of infectious symptoms.[76] Van der Ende *et al.* refutes this last statement, showing that the timing of DAIR for early post-surgical hip and knee PJI does not influence 1-year re-revision rates.[77] In cases of delayed acute postoperative PJI, a DAIR procedure can be an effective treatment option to preserve the implant for at least up to 3 months.[77]

The procedure consists in an open approach and starts with a complete debridement, *i.e.*, the removal of the infected and necrotized tissues, and the exchange of mobile and modular components of the implant. The joint and implant are washed with a saline solution with or without an antiseptic.[78] It is then followed by a minimum of 12 weeks of antibiotic therapy.[79]

Compared to strategies involving implant revision, this approach offers notable benefits in terms of cost-effectiveness,[80] functional outcomes,[52] preservation of bone stock, and acceptable medium-term mortality.[81]

However, DAIR is characterized by a highly variable infection control rate. To do so, predictive tools of DAIR failure have been developed, such as KLIC score, CRIME80-score, and McPherson adapted score.[82–84] Based on a meta-analysis including 99 unique observational studies, Kunutsor *et al.* predicted an infection control rate for DAIR ranging from 25.5% to 91.8%.[85] This variation is related to multiple factors, including patient-related factors (age, sex, co-morbidities), duration of infection, type of infecting microorganisms, type and duration of antibiotic therapy, and implant characteristics.[86]

4.1.2 Implant revision

Another strategy used to treat PJIs is to remove the implant, and to clean it before replacing it. It is recommended in case of late chronic infections, in patients for whom the DAIR strategy is contra-indicated, or following DAIR failure.[87]

This procedure can be performed as a one- or two-stage revision. In the USA, the prevailing approach for treating infected THA and TKA is the two-stage revision method, recognized as the benchmark. With this two-stage strategy, the infected implant is explanted, the necrotic and infected tissues are removed, and an antibiotic-impregnated cement spacer is temporarily inserted.[88] Subsequently, antibiotics are administered to patients during several weeks. There is no optimal time between the two surgeries, and thus depending on the eradication of the infection, the new prosthesis can be implanted up to several months after the removal of the implant.[89] However, Winkler *et al.* suggest that short interval in two-stage exchange is preferable to reduce the period of immobilization.[90] Moreover, antibiotic-impregnated cement has an optimum surface for bacterial colonization and prolonged exposure to antibiotic allows mutational resistance to occur.[91]

Although a high success rate in eradication of infection, the two-stage revision strategy is associated with a long period of hospitalization, lengthy functional impairment, high health service cost, and more mortality than one-stage revision.[92] For these reasons, although less frequently used in

comparison to the two-stage revision approach, the one-stage strategy presents an appealing alternative.[93] It is recommended for non-immunocompromised patients, without systemic sepsis, presenting an adequate bone stock and a good soft tissue envelope, and with preoperatively identified pathogens that are susceptible to antimicrobial drugs. Interestingly, some studies partially contest this last idea. Indeed, Jenny *et al.* suggest that one-stage revision for *Candida albicans* PJI may be successful even without preoperative fungal identification.[94] Maale *et al.* showed that patients can be culture negative and thus the diagnosis of infection must be made through a combination of clinical observations, histology, radiological imaging, and laboratory markers.[95] Finally, Akkaya *et al.* reported poor microbiological concordance between preoperative and intraoperative cultures.[96] According to them, this overall discordance should advise surgeons against depending solely on preoperative synovial fluid culture data to guide treatment and antibiotic selection.[96]

Implant revision is generally considered to result in better infection control than DAIR strategy, with a mean infection eradication of 87-88% and 83-85% for, respectively, one- and two-stage revision in TKA.[93,95] However, this method also carries some limitations, explaining why DAIR strategy continues to be a recognized procedure in acute scenarios. Implant revision, and particularly two-stage revision, is associated with a high rate of complications,[22] inferior functional outcomes compared to DAIR or aseptic revisions,[25] significant five-year mortality,[22,55] and extremely high costs.[59] The difference between a DAIR strategy and a one-stage exchange procedure is the removal of the implant and the necessity for a revision implant, which typically imposes greater restrictions on the knee than on the hip due to mechanical considerations related to bone support and ligament stability.

4.1.3 Resection arthroplasty, arthrodesis, and amputation

As a last resort, if the other strategies failed, salvage procedures such as permanent resection arthroplasty (removal of the infected prosthesis without reimplantation), arthrodesis (fusion of the joint) or amputation may be performed.

Resection arthroplasty and arthrodesis are employed in patients who are nonambulatory, exhibit restricted bone stock, have inadequate soft tissue

coverage, or harbor infections caused by highly resistant organisms, for which effective medical therapies are either unavailable or limited. They are also considered for patients with medical comorbidities that contraindicate major surgical interventions, or for those who have experienced failure following a two-stage revision procedure, where the risk of recurrent infection following the staged exchange is deemed unacceptable (re-reinfection rates have been reported to be ranging from 22.2% to 51%).[76,97] These procedures are frequently performed with the aim to avoid amputation, and the eradication of infection occurs in 60-100% of cases.[72] However, amputation may be necessary in specific cases, including necrotizing fasciitis unresponsive to debridement, extensive bone loss, inadequate soft tissue coverage, or failed attempts at controlling infection through resection arthroplasty.[76] All these surgeries are performed in medically fragile patients and are associated with significant morbidity, high mortality, and high complication rate.[98,99]

An alternative procedure is the administration of antibiotics as a lifelong suppressive therapy. It can be considered only if the pathogens have been correctly identified. This therapy is performed with the aim to limit the bacterial proliferation rather than eradicating it and is considered palliative.[100]

4.2 Antibiotic therapy

Regardless of the surgical procedure adopted for treating the PJI, it is always accompanied by antibiotic therapy. In addition to their susceptibility to the causative pathogens, the selected antibiotics should ideally present a good activity against biofilms, a good penetration into bone, and be well tolerated. A synergistic action of two antibiotics can also be sought. For example, levofloxacin in combination with rifampin has demonstrated favorable outcomes for PJI treatment against staphylococci.[101] In contrast, certain antibiotic combinations may lead to an antagonistic effect. This occurs, for example, when clindamycin, gentamicin, or tetracycline are combined with rifampicin against staphylococci.[102,103]

Antibiotics should be given promptly following the diagnosis of an infection and be withheld for 2-4 weeks prior the intervention in case of revision surgery.[76,104–106] The duration of antibiotic therapy remains unclear and is

primarily based on expert recommendations rather than evidence.[79] Moreover, depending on the surgical strategy and the causative pathogen(s), the antibiotic therapy will be different, in terms of active molecule chosen and duration. *The Infectious Diseases Society of America* recommends guidelines based on the encountered surgical situation and the causative pathogen (Table I. 1).[76] It shows the importance of a well-targeted antibiotic therapy. A recent noninferiority randomized controlled trial compared 6 weeks and 12 weeks antibiotic therapy in patients treated for a PJI, irrespectively of the causative pathogen and the surgical procedure. The study highlighted that the shorter treatments resulted in higher percentage of unfavorable outcomes, while no difference in adverse events were observed between the two treatment durations.[79] While the authors suggest that additional randomized trials should explore the optimal treatment duration based on the surgical type, the findings of this study point towards prolonged treatment durations.[79]

It is evident that managing patients with PJI requires the administration of antibiotics, as recovery would be unattainable without them. However, this poses an increasing challenge as the effectiveness of some antibiotics has declined over time and thus more and more bacteria become non-susceptible.[107]

Table I. 1 – Recommended antibiotics for the treatment of PJI. Adapted from Poilvache.[108]

Causative Pathogen	Preferred Treatement	Alternative Treatment	Suppressive Treatment
Staphylococcus spp, Methicillin-susceptible[1]	Nafcillin, Cefazolin, Ceftriaxone	Vancomycin, Daptomycin, Linezolid	Cefalexin, Cefadroxil, Dicloxacillin, Clindamycin, Amoxicillin-clavulanate
Staphylococcus spp, Methicillin-resistant[1]	Vancomycin	Daptomycin, Linezolid	Cotrimoxazole, Minocycline, Doxycycline
Enterococcus spp, Penicillin-susceptible	Penicillin G, Ampicillin	Vancomycin, Daptomycin, Linezolid	Penicillin V, Amoxicillin
Enterococcus spp, Penicillin-resistant	Vancomycin	Linezolid, Daptomycin	
Pseudomonas aeruginosa	Cefepime, Meropenem	Ciprofloxacin, Ceftazidime	Ciprofloxacin
Enterobacter spp	Cefepime, Ertapenem	Ciprofloxacin	
Enterobacteriaceae	β-lactam, Ciprofloxacin		Co-trimoxazole, β-lactam
Streptococcus spp	Penicillin G, Ceftriaxone	Vancomycin	Penicillin V, Amoxicillin, Cefalexin
Cutibacterium acnes	Penicillin G, Ceftriaxone	Clindamycin, Vancomycin	

[1]In association with oral rifampicin in non-suppressive treatments

5 Multidrug-recalcitrant bacteria

The use of antibacterial agents is essential in the treatment of patients with bacterial infections. However, the last decades have seen the number of antimicrobial-recalcitrant bacteria rising, and a lack in the development of new therapeutic options to deal with it, which could have catastrophic consequences.[3] The WHO has declared antimicrobial non-susceptibility as one of the biggest threats to humanity.[109] Nowadays, antibiotics have become essential to bacterial infection treatment. They are widely prescribed due to their high effectiveness. However, bacteria have developed various resistance and tolerance mechanisms against these antibiotics.

5.1 Antibiotic resistance

Resistance is defined as the inherited ability of microorganisms to grow at high antibiotic concentrations, regardless of treatment duration, and is quantified by the minimum inhibitory concentration (MIC) of the particular antibiotic.[110] There are several genetic mechanisms by which resistance to antibiotics can develop in bacteria. Bacterial genetic modifications, either gene mutation or acquisition of new genetic material, lead to biochemical changes in bacterial cell properties which makes the cell less or no longer sensitive to an antibiotic. These mechanisms fall into four main categories: limitation of drug uptake; alteration of drug target; inactivation of drug; and activation of drug efflux. They are represented in Figure I. 3.[111]

Bacteria inherently vary in their ability to **limit the uptake of drugs**. For example, the structure and functions of the lipopolysaccharide layer of the outer membrane of Gram-negative bacteria provide a barrier to specific types of molecules, granting these bacteria an innate resistance to certain classes of antimicrobial agents.[111]

Resistance to antibiotics can also occur via **alteration of the drug target** in the cell envelope. Indeed, antibiotics, depending on their class and thus their mode of action, may target multiple components in the bacteria. However, all these targets can be modified by bacteria, preventing the receptor-binding to these agents and thereby conferring resistance.[111]

There are two main ways by which bacterial cells can **inactivate drugs**: by degradation, and by inactivation of the drug. Bacteria can secrete enzymes capable of degrading or introducing chemical changes to the antibiotics, thereby decreasing the affinity of the drug for its target.[111]

Efflux is the mechanism by which cells release toxic compounds into their surrounding environment and is mediated by transmembrane proteins known as efflux pumps. Therefore, in case where intact antibiotics enter bacteria and drug targets are freely accessible, active **drug efflux** systems can come into play for maintaining the cytoplasmic concentration of a specific antimicrobial drug below a critical threshold. This active transport is thus an essential mechanism of resistance in bacteria. The high-level expression of efflux pumps, commonly attributed to mutations, can confer high levels of resistance to antibiotics that were previously clinically effective.[111]

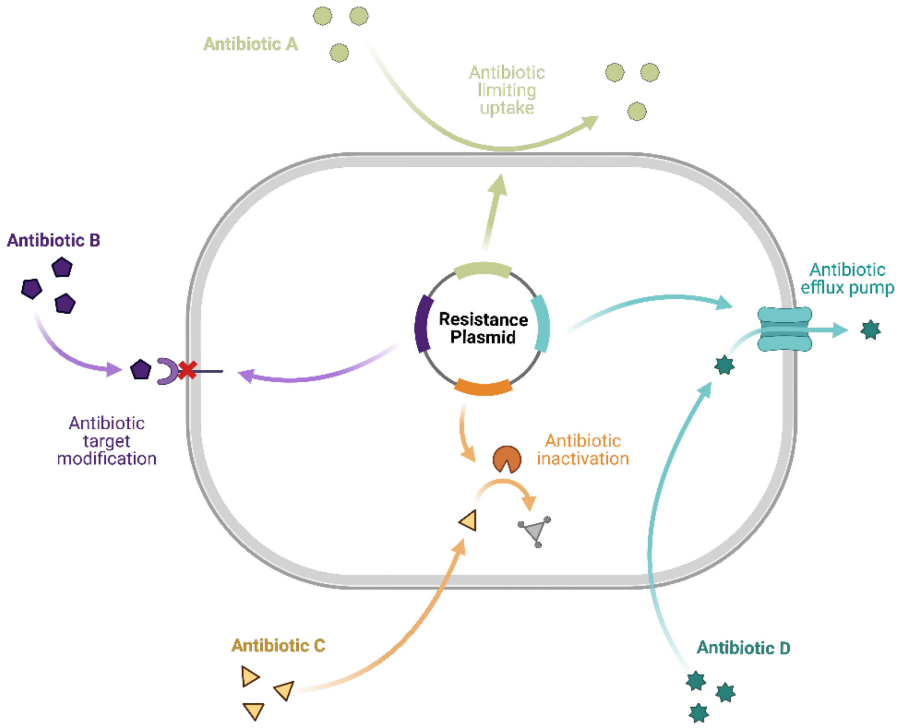

Figure I. 3 – Conventional antibiotic resistance mechanisms. Created with BioRender.

In addition to conventional mechanisms of antibiotic resistance, bacteria have also developed tolerance mechanisms towards antibacterial

compounds. Contrary to resistance, tolerance refers to the ability of microorganisms, whether inherent or not, to survive transiently under exposure to high concentrations of an antibiotic, which would otherwise be lethal, without a change in the MIC.[110] Bacterial tolerance is manifested by a special way of life that bacteria have developed – the biofilm – and that allows them to survive in hostile environmental conditions. Hence, the biofilm acts as a protective barrier for the bacteria embedded within it, reducing the effectiveness of antibacterial compounds commonly used in the treatment of infections. Understanding biofilms and the mechanisms by which they reduce antibacterial compounds efficacy is thus crucial for developing effective treatments.

5.2 Biofilm

Historically, scientists assumed that bacteria led solitary and asocial lives and thus existed only as independent free-floating, so-called planktonic, cells.[112] On the contrary, bacteria organize, communicate, interact, differentiate. At interfaces between a surface and a liquid phase, they live as a community embedded in their own extracellular matrix (ECM). They form microbial surface-attached sessile aggregates, which are known as biofilms.

Donlan & Costerton defined biofilms as "*a microbially derived sessile community characterized by cells that are irreversibly attached to a substratum or interface or to each other, are embedded in a matrix of extracellular polymeric substances that they have produced and exhibit an altered phenotype with respect to growth rate and gene transcription*".[15]

Biofilms were first described in 1693 by the Dutch scientist Antoni van Leeuwenhoek, who scrapped his own dental plaque. By microscopic observation, he noticed a vast accumulation of living objects that he called 'animalcules' because he thought that they were tiny living animals.[113] Despite other observations being in agreement with what he described (Henrici in 1933, Zobell in 1937, Heukelekian & Heller in 1940),[114–117] the study of this mode of bacterial life was overshadowed by that of planktonic bacteria. It was only from 1978 that Costerton *et al.* changed that view by explaining how bacteria stick to surfaces.[118] At this point, scientists began focusing on the study of biofilms and their role. In medicine, the study of

'biofilm-growing bacteria' has developed when surface-attached bacteria were first observed attached to a pacemaker lead, in 1982.[119]

Nowadays, the recognition of biofilm formation's significance in the emergence of infections, such as those associated with medical devices and chronic wounds, is widespread, prompting intensive research endeavors in this area. By the onset of the century, the recognition and implication of bacterial biofilms in the orthopedic field have become well-established, emerging as a major consideration in the diagnosis and management of patients afflicted with PJI.[87,120,121] Following that, research efforts intensified toward either treating well-formed biofilms or preventing their formation on medical implant surfaces. Importantly, non-surface-attached aggregated bacteria have also been recognized as biofilms.

5.2.1 The *in vitro* biofilm model: formation and regulation

The ECM plays a key role in the biofilm establishment, in its structural and functional integrity, while conferring many advantages to the bacteria embedded in it such as adhesion, intercellular aggregation, water retention, barrier protection, and nutritional support.[122] The ECM is composed of water and extracellular polymeric substances (EPS) such as polysaccharides, proteins and lipids, cellular debris, extracellular DNA (eDNA), signaling molecules and teichoic acid.[122] Biofilm is thus a heterogeneous and dynamic environment organized to optimize bacterial functions. Its formation and maturation are complex processes. They have been studied for decades using various *in vitro* models. The model mostly used by the scientific community to depict the *in vitro* surface-attached biofilm formation occurs in five main steps. This original model, first published in 2002, proposes that the biofilm formation is a cyclic process, and is based on a mushroom-shaped structure, characteristic of *Pseudomonas aeruginosa*, as described in Figure I. 4.[31,123,124] The distinct stages in the *P. aeruginosa* biofilm development are correlated with multiple phenotypes (structural and metabolic changes).[125] The five successive steps can be described as follows:

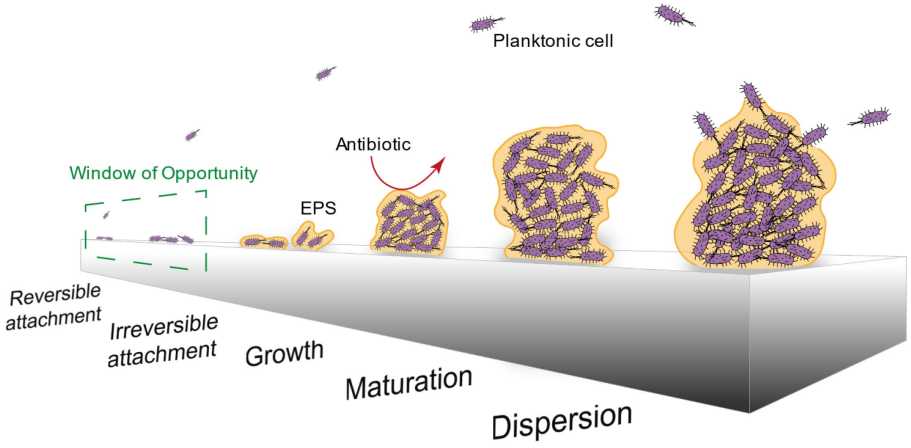

Figure I. 4 – The original five-step model of biofilm formation and development.

A prerequisite of biofilm formation is that bacteria get close enough to a surface. Upon reaching the surface via passive (Brownian motion and gravitational forces) or active (active motility of flagellated bacteria) motion, both attractive and repulsive forces come into play to initiate the **reversible attachment** of bacteria to the surface. The initial attachment of bacteria to abiotic surfaces arises from fundamental physicochemical mechanisms such as electrostatic interactions, van der Waals interactions, and hydrogen bonds, alongside mechanisms specific to certain species, like staphylococcal autolysin-mediated primary attachment to polystyrene surface.[126] Surface properties such as hydrophobicity, charge, and roughness,[127] as well as bacterial characteristics like cell surface composition and cell morphology,[128] contribute to the diverse affinities exhibited by certain bacterial species toward different materials.[129] In all cases, the **irreversible attachment** of bacteria is mediated by bacterial adhesins that can stick to the surface. Indeed, upon exposure to biological fluids, abiotic surfaces promptly adsorb host proteins, such as fibronectin (Fn), fibrinogen, or collagen (Col), which are the targets of bacterial surface-bound or secreted proteins (adhesins), facilitating bacterial adhesion to the surfaces.[130] This irreversible attachment initiate a physiological shift and the synthesis of EPS, in which the sessile bacteria are embedded.[131]

From this irreversible attachment, bacteria express genes associated with the production of their protective ECM made of EPS, and aggregate. From this aggregation, microcolonies emerge by clonal **growth**. After a period of

initial microcolonies formation by bacteria proliferation at fixed location, bacteria spread over the moist surface by means of twitching motility. Subsequently, a flat biofilm covering the entire surface forms.[132]

Once the first layer of the biofilm is established, same or other bacteria species are recruited to the biofilm from the bulk fluid. Bacteria "communicate" to each other, through signaling molecules (quorum sensing system), take specialized functions and thus differentiate. The **maturation** of the biofilm is almost unlimited as long as nutrients are available. More and more biofilm scaffolding molecules, such as polysaccharides, proteins, and eDNA are secreted into the biofilm by the entrapped bacteria. The maturation process of biofilm is intricately influenced by its environment and the various stresses to which it is confronted. Ranieri *et al.* highlighted that exposure of bacteria to subinhibitory concentrations of antimicrobials and disinfectants can provoke physiological changes that promote the biofilm production.[133] Similarly, mechanical stimuli, like shear stress at the biofilm interface and medium, or external pressure applied to the biofilm, are also recognized as factors that affect the production of EPS.[134]

Finally, due to outgrown population, intense competition, hypoxia or oxygen deprivation, lack of nutrients, and slow growth, the biofilm **dispersion** occurs.[135–137] The signaling molecules, regulating the density of the biofilm and thus its maturation, represent a key milestone in the dispersion phase. Indeed, once the bacterial density reaches a critical threshold, along with a corresponding increase in the concentration of these small signaling molecules, the biofilm undergoes rearrangement and dispersal.[138] It results in the release of planktonic bacteria or small aggregates, which colonize new sites of the surface and thus initiate the formation of new biofilms.

However, it has become evident that such mechanism does not correspond to the development process of all biofilms, such as for *S. aureus*,[139] and it remains debatable whether such *in vitro* biofilms actually resemble *in vivo* biofilms in chronic infections. Indeed, *in vivo* observation of biofilms in human infections shows distinct differences compared to *in vitro* biofilm growth.[140] Therefore, even if models are useful to predict or understand complex issues, they also can negatively affect the way we behave, reason and take decisions, with the risk to do not 'think outside the box'.[140] In consequence, the projection of the *in vitro* biofilm concept in real-world

settings can stuck the field of biofilm-related infections in an academic state with limited relevance to diagnostic, treatment and prevention of these infections.[140] To change this, the scientific community could broaden its mental model, incorporating the *in vivo* features.

5.2.2 Biofilm: a gap between models and reality?

While the simplified conceptual model depicting biofilm development based on *P. aeruginosa in vitro* biofilm formation is accessible and commonly applied to characterize various biofilms (Figure I. 4), it falls short in capturing the intricate nature of biofilms within real-world contexts such as industrial, natural, and clinical settings.[141] Importantly, this model does not reflect the relevant microenvironments that emerge within these biofilms. It is crucial to consider the significant differences between processes observed in a well-controlled laboratory flow cell and those leading to biofilm formation in real-world scenarios, such as pipelines, chronic wounds, air-water interface in the respiratory tract, prosthetic joints, and *ex vivo* organoids. In such varied systems, the dynamics of biofilms formation and dispersion may exhibit considerable variations and may not unfold in a sequential manner, as depicted in the simplified model.[141] To explain this gap between conceptual model and reality, Sauer *et al.* described at least four limitations.[141] First, it remains unclear whether biofilm formation can be described as a true developmental process when considering biofilms formed outside of the flow cell and by species other than the model biofilm species (*P. aeruginosa* and *S. aureus*). Second, the model does not consider the wide range of biofilm architectures, like microbial mats, encountered in real-life systems.[142] In fact, it has been shown that, even for *P. aeruginosa* biofilms, the architecture is highly related to growth condition and growth medium.[132] Third, the model does not encompass the wide range of aggregation and detachment mechanisms which involve both motile and non-motile organisms. It does not consider suspended bacterial aggregates that are not attached to surfaces, which are frequently encountered in clinical and environmental settings. Finally, the model is seen as a kind of closed system and does not consider the continual influx of new colonizers formed in open systems. Therefore, applying the five-step model to real-world biofilm systems is limited. For example, in the case of osteomyelitis involving implants, it is commonly assumed that bacteria adhere to the implant

surface, and so can be described by the conceptual biofilm model. Nonetheless, recent studies indicated that while bacteria may be present on the surface, implant colonization is not imperative to cause persistent infection.[143,144] Analysis of samples from implant-associated infections indicated the presence of bacteria in both peri-prosthetic tissue and on the implant, though not necessarily in both simultaneously.[145] Dastgheyb *et al.* demonstrated that *S. aureus* forms aggregates in synovial fluid.[146] The formation of these clumps beyond the implant surface could thus play a crucial role in the initiation of PJIs. Consequently, an adaptation of the five-step model has been recently proposed (Figure I. 5).[141] This model describes the three major steps in biofilm formation: aggregation, growth and disaggregation. It integrates the various possibilities and pathways governing the biofilm aggregate formation in an inclusive manner. Importantly, it considers an open system and thus a continuous influx of new biofilm members. This new proposed model is more inclusive in terms of types of biofilms (attached and suspended aggregates) and environments.

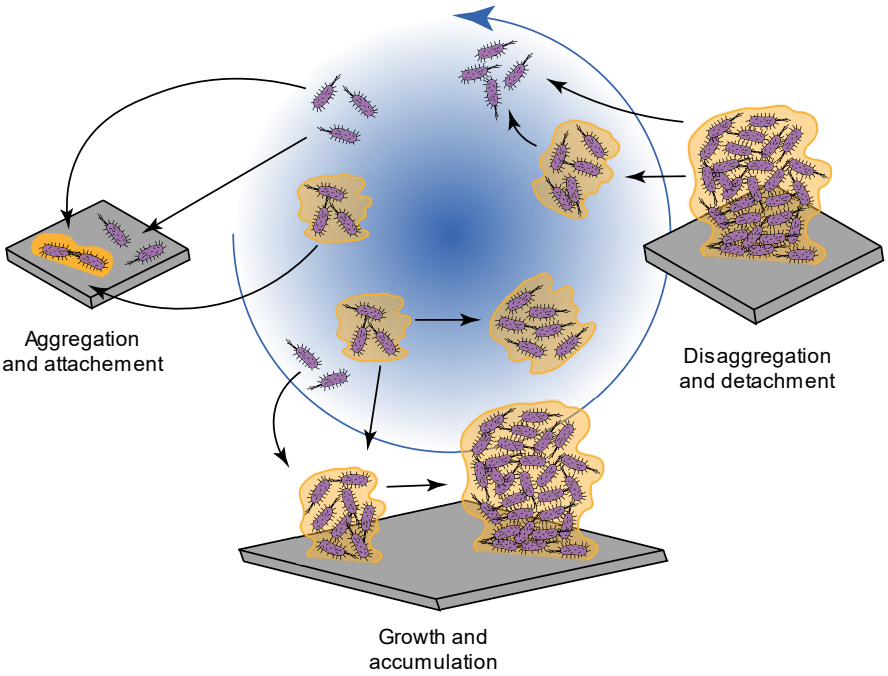

Figure I. 5 – The expanded conceptual model of biofilm formation. Adapted from Sauer *et al.*[141]

Beyond the concept, the experimental laboratory conditions do not capture the complexity of biofilms in industrial, clinical and environmental systems, where the scale, the chemical properties of the bulk fluid, the fluid dynamics, the surface topography, etc., highly impact the biofilm composition and structure, and thus its development. For example, for catheter-related infections, even if *in vitro* models help to understand mechanisms involved in biofilms development, they often fail to take into account interactions with blood components or blood flow.[147] In conclusion, it is essential to get things into perspective and not cling to the mental vision of a biofilm since there is no *in situ* sensors that can be incorporated into such complex systems to directly monitor biofilms on interfaces.

As already broached, depending on the bacterial growth media, the biofilm formation of a same bacterial strain can be completely different, questioning the *in vitro* conditions in which the studies should be performed.[148] It is important to keep in mind, when performing *in vitro* experiments, that biofilms from the researcher's perspective are not the ones from the clinician's one. Therefore, for studies aimed at treating biofilms, or reducing or preventing their formation, one might question the relevance of conducting *in vitro* studies compared to *in vivo* ones, given the significant impact that experimental conditions can exert on biofilms. The past decades have seen a myriad of *in vivo* models developed for several infectious diseases to address questions regarding initial adhesion, role of surface on biofilm formation, curative or preventive approaches. Hence, there is no 'gold-standard' as each model may provide appropriate information to answer a biological question.[147] However, there are numerous concerns surrounding the limited translation from *in vitro* and *in vivo* models to clinical studies.[149] This drawback highlights the limits of *in vivo* study, such as differences between humans and animals used for *in vivo* studies, the choice of animal for *in vivo* studies, or the choice of bacterial strains.[150]

Since the early 1980s, there has been a progressive expansion of our understanding of biofilms. However, many concerns are raised regarding the scarce translation from *in vitro* models, *in vivo* models, and clinical studies. This underscores the presence of substantial unresolved aspects, emphasizing the indispensable necessity for effective communication between researchers and clinicians to unravel the intricacies of these complex systems, ultimately aimed at combating biofilm-related infections.

5.3 Surviving as a community: biofilm-induced antimicrobial recalcitrance

Bacterial biofilm is a serious global health concern since it impacts the evolution and treatment of biomaterial-associated infections. Indeed, due to its ability to induce resistance mechanisms, and to tolerate antibiotics, host defense systems and other external stresses, it contributes to persistent chronic infections.[31,151] Acknowledging the complex interplay of resistance and tolerance mechanisms, many authors have adopted the term 'recalcitrance' to refer to the reduced susceptibility of biofilm cells to antibiotics.[152,153]

Bacteria embedded in a biofilm can withstand high levels of bactericidal antibiotics to some extent, even if these bacteria are fully susceptible to such antibiotics when tested *in vitro* under planktonic conditions. This phenomenon, referred to as 'recalcitrance of biofilm', is due to several tolerance and resistance mechanisms.[37] The tolerance of biofilms can be assessed by determining the minimum biofilm eradication concentration (MBEC), which represents the minimum antimicrobial concentration required to eliminate all bacteria within a biofilm. The MBEC may exhibit values 5000-fold higher than those observed for the MIC of planktonic cells.[154] Several mechanisms have been suggested to explain the recalcitrance of biofilms to antimicrobials (Figure I. 6).

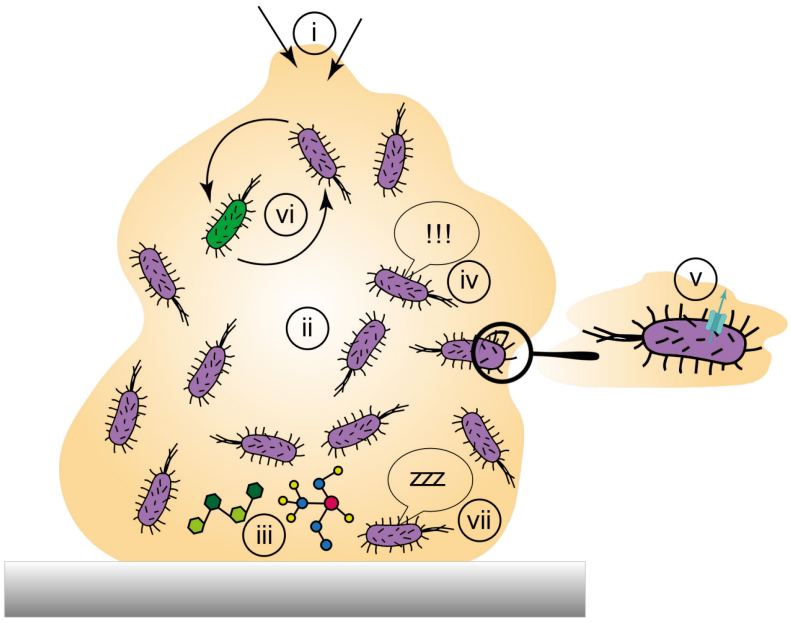

Figure I. 6 – Schematic overview of the major antimicrobial recalcitrance mechanisms developed by bacterial biofilms. Bacteria are embedded in the biofilm matrix (shown in orange). Pictorial representations of the recalcitrance mechanisms are numbered as follows: (i) decrease in antimicrobial penetration, (ii) establishment of gradients (demonstrated here as a color-intensity gradient), (iii) role of polysaccharides, enzymes and eDNA in the matrix, (iv) effect of stress responses, (v) role of multidrug efflux pumps, (vi) intercellular interactions, and (vii) presence of persister cells. Adapted from Hall & Mah.[153]

A **decrease in antimicrobial penetration** (i. in Figure I. 6) into biofilms was initially thought to be the main mechanism driving antimicrobial tolerance.[155] This hypothesis was supported by early observations indicating restricted penetration of antiseptics and antibiotics within biofilms. It is expected to depend on the biofilm thickness, the effective diffusivity and reactivity of the antimicrobial in the biofilm, the possible adsorption of the antimicrobial on the biofilm matrix, the dose concentration and dose duration, and the external mass transfer properties.[156] However, antibiotic penetration reduction through the biofilm matrix is not sufficient to fully explain the increased tolerance of biofilms to antimicrobial drugs.[157–164]

Biofilm formation leads to the establishment of **gradients** (ii. in Figure I. 6) of oxygen and nutrients concentration, pH level, signaling molecules and metabolic waste products. These foster the development of heterogeneous

bacterial populations within the biofilm, with bacteria at the center exhibiting lower metabolic activity and slower growth.[160,165] These results suggest that these gradients may play a role in the antibiotic tolerance exhibited by biofilms. Indeed, Borriello *et al.* shown that antibiotics such as tobramycin and ciprofloxacin, which target protein synthesis machinery and DNA synthesis, respectively, exert their activity on fast-growing bacteria, rendering slowly growing cells tolerant to their effects.[166]

Substances present in the biofilm matrix, such as **polysaccharides, enzymes** and **eDNA** can increase the level of recalcitrance of bacteria cells (iii. in Figure I. 6). Psl and Pel are exopolysaccharides synthesized by some *P. aeruginosa* strains. Even if the mechanisms by which they protect bacteria cells from antibacterial drugs is not yet clear, Billings *et al.* demonstrated that Psl affects sensitivity toward colistin, polymyxin B, tobramycin and ciprofloxacin in *P. aeruginosa* biofilms,[167] whereas Colvin *et al.* showed that Pel is capable of playing a structural and protective role in the biofilm matrix of *P. aeruginosa*.[168] Finally, eDNA, an important and universal component of the bacterial biofilm matrix can also induce recalcitrance to some antibiotics and antimicrobial peptides, such as tobramycin, gentamicin, vancomycin, polymyxin B, colistin, kanamycin and chloramphenicol. The mechanisms put forward to explain this recalcitrance are the alteration of the extracellular environment (chelation of cations such as Mg^{2+}, acidic microenvironments), the physical interaction with antimicrobials, and the horizontal transfer of antibiotic resistance genes (eDNA integrated in the genetic information).[153] This highlights that components of the biofilm ECM play a key role in the recalcitrance mechanisms.

Biofilms use **stress responses** to counteract antibiotics, such as oxidative stress response and stringent response (iv. in Figure I. 6). In addition to their classic mechanisms of action that contribute to bacteria death, some bactericidal agents kill bacterial cells by inducing the production of critical levels of reactive oxygen species (ROS).[169–171] However, below these lethal levels, several studies established that the generation of a moderate surge in ROS may potentiate the emergence of bacterial recalcitrance.[172–175] Therefore, whether ROS stimulate or mitigate stress-induced cell death depends on the severity of the encountered stress. The stringent response, one adaptive mechanism enabling bacteria to survive under stress conditions,[176] also plays a crucial role in the phenomenon of antibiotic

tolerance, as well as the acquisition, development, and expression of antibiotic resistance. Salzer & Wolz recently reviewed the mechanisms used by Firmicutes to evade antibiotic attacks under stringent response.[177] It has been demonstrated that high levels of alarmones ((p)ppGpp) are implicated in the mechanism of β-lactam resistance,[178,179] and induce lower metabolic activity and slower growth, rendering bacteria less sensitive to antibiotics, which induces tolerance.[177]

In addition to their role in the conventional mechanisms of antibiotic resistance, the **efflux pump** (v. in Figure I. 6) also play a key role in biofilm recalcitrance. Kvist *et al.* showed that in biofilm formed by two *Escherichia coli* strains, a significant fraction of genes that exhibited up-regulation, compared to planktonic cells, were found to be associated with efflux and transport mechanisms.[180] It was suggested that this up-regulation resulted directly from the challenges of "waste management" encountered in the confined environment of the biofilm. Exposure of cells from different *E. coli* strains and a *Klebsiella pneumoniae* strain to some efflux inhibitors notably repressed biofilm formation, suggesting the necessity of functional efflux systems for complete biofilm development. Moreover, these efflux pump inhibitors enhanced the efficacy of tetracycline against biofilms.[180] Baugh *et al.* also demonstrated that the use of efflux pump inhibitors decreased the formation of *E. coli*, *P. aeruginosa* and *S. aureus* biofilms. Therefore, efflux pump inhibitors could be used as antibiofilm agents.[181]

Intercellular interactions (vi. in Figure I. 6) are also known to be common in bacterial biofilms, facilitating their formation. First, **horizontal gene transfer** can occur through the transfer of plasmids between cells embedded in the biofilm via conjugation. Due to their sessile nature and spatial proximity, the conjugal plasmid transfer from one bacteria cell to another is more efficient in biofilms than in planktonic cultures. Therefore, the probability to transfer an antibiotic-resistant plasmid is higher.[153] For example, Savage *et al.* showed that the frequency transfer of a multidrug-resistant plasmid in *S. aureus* is more than 10,000 times greater in biofilms than in planktonic cultures.[182] An other example of how biofilms improve their ability to acquire resistance through horizontal gene transfer is the mobilization of antimicrobial resistance gene via integrons, which is more than 100-fold higher in biofilms than in planktonic cells.[183] The **quorum sensing** is the capacity of bacteria to regulate their gene expression in response to cell density fluctuations. It is

established that quorum sensing is involved in biofilm recalcitrance. For example, Brackman *et al.* demonstrated, by inhibiting the quorum sensing system of pre-established *S. aureus* biofilms, that the antimicrobial efficacy of cephalosporins, vancomycin, daptomycin, linezolid, tobramycin and fusidic acid is increased.[184] It seems clear that targeting the quorum sensing system provides an efficient strategy for decreasing biofilm recalcitrance. Finally, **multispecies' communication** is another intercellular interaction known to modulate the overall antimicrobial recalcitrance of the biofilm community.[153] For example, in an *in vivo* polymicrobial wound model, *P. aeruginosa* was 2-fold less susceptible to gentamicin when co-cultured with *S. aureus*, *Enterococcus faecalis* and *Finegoldia magna* than in a monospecies biofilm.[185] Other studies, analyzing the interactions between bacteria and *C. albicans* fungi, lead to the same conclusions. *S. aureus* is less susceptible to vancomycin and *E. coli* more tolerant to ofloxacin in a dual-species biofilm with *C. albicans*.[153] Moreover, multispecies biofilms can also promote antibiotic resistance by facilitating the transfer of antibiotic resistance genes between different species.

Persister cells (vii. in Figure I. 6) are a specific bacterial subpopulation that exhibits antibiotic tolerance while presenting no genetic difference from the rest of the population. These phenotypic variations cause these persisters to be in a non-dividing state in presence of antibiotics, but to resume growth once the antibiotics are removed, which may lead to infection relapse. While persisters are found in both biofilms and planktonic cultures, biofilms generally contain a higher proportion of persisters compared to planktonic cultures.[186] Peyrusson *et al.* recently presented *in vitro* evidence of *S. aureus* persisters residing within infected host cells, *i.e.*, intracellular persisters. Their results indicated that bacteria surviving antibiotic treatment within host cells exhibit characteristics of persisters.[187]

In addition to these recalcitrance mechanisms, bacteria embedded in biofilms also present the ability to evade the host immune system through various mechanisms. First, biofilm maturation appears to hamper the phagocytosis of staphylococci biofilms by polymorphonuclears and limits the phagocytosis by macrophages while inducing their death.[188] Second, staphylococcal biofilms are able to interfere with the inflammatory pathways of their hosts, reducing the synthesis of proinflammatory agents and

inducing a fibrotic response.[188] Finally, *S. aureus* can also produce toxins leading to the dysfunction or death of macrophages.[189]

Therefore, emergence of antimicrobial recalcitrance in nosocomial pathogens is one of the most important challenges in clinical epidemiology and biofilms become a major public healthcare issue. *The US National Institute of Health* estimated that microbial biofilms account for over 60% of microbial infections in humans and 80% of chronic infections.[190,191] Due to the myriad of strategies that bacteria have developed to resist to antibacterial agents, the eradication of biofilms on medical implants is very difficult.[192] In the subsequent sections, strategies aimed at either treating biofilms formed on the surface of medical implants or preventing their formation will be explored.

6 New therapeutic strategies against biofilms

Despite the increasing clinical focus, research advances, and growing literature relating to PJI, over the past few years, the rates of PJI treatment success have remained unchanged.[193] The literature on biofilms and biofilms' prevention has increased dramatically in terms of publications and there are also numerous books on the subject. However, at this moment, there is no drug approved by the *US Food and Drug Administration* (FDA) or other equivalent regulatory authorities that can effectively treat biofilm-related infections.[194] Novel techniques that could potentially enhance the treatment of these devastating complications would address an unmet need because current strategies are far from optimal.

As already detailed in the section *Part I – 4 Treatment strategies*, nowadays, treatment options include the use of suppressive antibiotics, debridement and retention of implants, excisional arthroplasty, and one-stage or two-stage revision.[21,40,75,195,196] However, all these treatment options are associated with substantial morbidity and a high risk of adverse outcomes. Depending on the surgical procedure, the current literature reports the rate of infection recurrence to range from 0-27% following treatment for PJI, with values up to 45% in case of DAIR.[29,197] Removing an infected implant is considered a heavy procedure and this surgery is associated with a 30-day readmissions rate of 11.1% and a 90-day mortality rate of 2.6%.[198]

Therefore, it becomes more and more urgent to deal with the development of new therapeutic strategies against biofilms.

6.1 Biofilm matrix-degrading enzymes

Biofilms are extremely difficult to eradicate due to their decreased antimicrobial susceptibility. Therefore, one strategy could be to release the bacteria from the biofilm to facilitate the elimination of planktonic cells by antimicrobial agents. Biofilm matrix-degrading enzymes mimic the natural process of biofilm dispersal with the aim of degrading EPS biofilm matrix.[199] However, even though the biofilm is disrupted, bacteria are not killed and little is known about how the host responds to the sudden dispersal of biofilm cells.[200] Chua *et al*. showed that dispersed *P. aeruginosa* cells are distinct from biofilm cells and from planktonic cells, being more virulent than planktonic cells, which can worsen the clinical outcome.[201] Fleming & Rumbaugh used glycoside hydrolases to target the exopolysaccharides and study the consequences of biofilm dispersal on the host.[200] They were the first to demonstrate that large-scaled dispersal of biofilm can induce fatal septicemia. However, this dispersal-mediated septicemia is dependent upon bacterial swimming-motility and wound size. Interestingly, they showed that antibiotics protect against the dispersal-induced septicemia and glycoside hydrolases increase the antibiotic effectiveness.[200] Therefore, it highlights that, used with caution and in combination with other drugs, biofilm matrix-degrading enzymes are of high interest in the effort to disrupt biofilms. Various classes of enzymes have been investigated for their potential on biofilm dispersal: proteases, deoxyribonucleases, and glycoside hydrolases.[202]

Loughran *et al*. demonstrated that proteases have the capacity to promote dispersal of various well-established *S. aureus* biofilms. Among the tested proteases (aureolysin, serine protease SspA, and cysteine proteases ScpA and SspB), aureolysin showed the greatest effect.[203] Another study highlighted that trypsin and pepsin alone are able to disperse preformed *P. aeruginosa* and *E. faecalis* biofilms up to 50% depending on the treatment time and the enzyme concentration. The combined treatment using both enzymes and carvacrol exhibited a synergistic effect of the enzymes'

dispersive activity and the carvacrol antimicrobial activity, leading to a greater reduction of the biofilm biomass and cell viability.[204]

DNase I is an endonuclease that specifically digests DNA and thus can affect the biofilm formation. Whitchurch *et al*. were the first, in 2002, to prove that DNase I strongly inhibits biofilm formation. They also demonstrated that less than 84h preformed *P. aeruginosa* biofilms were dissolved by DNase I.[205] More recently, Pirlar *et al*. noticed that the treatment of dual-species biofilms (*P. aeruginosa* and *S. aureus*) with a cocktail of enzymes (trypsin and DNase I) led to a significant increase in the number of bacterial cells dispersed in the medium, which show their biofilm-degrading effect.[206] No bactericidal effect was associated to these enzymes but the MBEC of meropenem and amikacin decreased by 2.5 to 5-fold compared to the treatment with the antibiotic alone. It highlights the combinatorial effects of enzymes and antibiotics as a strategy to disrupt and eliminate biofilms.[206] Other deoxyribonucleases have also showed good results in terms of biofilm dispersion.[202]

Similarly, Fleming *et al*. showed that glycoside hydrolases, α-amylase and cellulase, reduced the biomass of *S. aureus* and *P. aeruginosa* co-culture biofilms and led to their dispersion *in vitro* and *in vivo*.[207] The glycoside hydrolases cocktail increased the effectiveness of gentamicin sulfate therapy.[207] Ruiz-Sorribas *et al.* studied this synergy on a complex inter-kingdom biofilm model composed of *S. aureus*, *E. coli* and *C. albicans*.[208] They showed that subtilisin A as glycoside hydrolase and a cocktail of moxifloxacin/caspofungin or meropenem/caspofungin as antimicrobial disrupted the biofilm with a reduction of more than 50% of its biomass and a decrease ranging from 1 to 4 $\log_{10}$ of the colony forming units (CFUs), which depends on the tested bacterial strain. These results confirm the interest in using enzymes as biofilm dispersal agent in combination with bactericidal antimicrobials against hard-to-treat infections biofilms.[208]

Table I. 2 gives a summary of the biofilm matrix-degrading enzymes broached in this section with their mode of action. This list is not exhaustive as other biofilm matrix-degrading enzymes have also shown good results in terms of biofilm dispersion.[202] Combining the available data suggests that care should be taken to use biofilm dispersal as part of antibiofilm strategies. Even if enzymes can boost the efficiency of antibiotics thanks to their dispersal

action, before implementing this approach in clinical settings, information regarding the susceptibility of dispersed cells is imperative.[199]

Table I. 2 – Biofilm matrix-degrading enzymes showing good results in term of biofilm dispersion.

Class	Compound	Action	Reference
Protease	Aureolysin	Degradation of biofilm matrix proteins	203
	Serine protease SspA		203
	Cysteine protease ScpA		203
	Cysteine protease SspB		203
	Trypsin		204, 206
	Pepsin		204
Deoxyribonuclease	DNase I	Degradation of biofilm matrix DNA	205, 206
Glycoside hydrolase	α-amylase	Degradation of biofilm matrix exopolysaccharides	200, 207
	Cellulase		200, 207
	Subtilisin A		208

6.2 Quorum sensing inhibitors

As already discussed, many reports highlighted the involvement of quorum sensing in biofilm regulation mechanisms. In order to thwart the biofilm formation, quorum sensing inhibitors are molecules able to quench the quorum sensing regulatory pathway. Basically, quorum sensing inhibition can be achieved by inhibiting the signal molecule synthesis, inactivating or degrading the signal molecules, preventing the binding of the signal molecules to the receptors, and/or blocking the signal transduction cascades.[209,210] Many quorum sensing inhibitors have been developed by researchers over the years.[211] For instance, Zhang *et al.* demonstrated that 2 mM of coumarin, a plant-derived phenolic compound, significantly reduces the biofilm formation in several *P. aeruginosa* strains by affecting the quorum sensing system.[212] Furthermore, it has also been shown that antimicrobial efficiency of cephalosporins, vancomycin, daptomycin, linezolid, tobramycin and fusidic acid is increased if the quorum sensing system of preformed *S. aureus* biofilms is inhibited. It highlights the potential

synergetic effect of quorum sensing inhibition with other antimicrobial modes of action.[184]

However, it is essential to note that many known quorum sensing inhibitors are cytotoxic and the precise mechanisms by which they exert their regulatory functions are still poorly understood.[209] Therefore, more research is needed to understand their involvement in biofilm formation and their potential cytotoxicity before they can be used in clinical issues.

6.3 Metallic nanoparticles

Metal-based nanoparticles (MNPs), such as silver, gold, zinc oxide, copper, copper oxide, etc. nanoparticles, exhibit exceptional bactericidal properties against a variety of infectious and pathogenic microorganisms, including multidrug-resistant bacteria.[213,214] Several studies also reported the ability of other metals to exhibit antimicrobial activity, including Ni, Pb, Co, Mo, Zr, Sn, Ti, Al, Pd, W, and Fe.[215–217] The precise mechanism of action of MNPs is still not fully understood.[214] However, it is known that antibacterial activities of MNPs are based on their ability to inhibit the biological machinery, increase the formation of ROS, disrupt cell membranes, and prevent pathogens from receiving essential trace elements.[218] Basically, thanks to their extremely large surface area to volume ratio and positive charges, MNPs can interact electrostatically with negatively-charged bacteria cells, resulting in the final disruption of membranes. In addition, MNPs can release metal ions from the extracellular space, which can penetrate cells and interfere with biological functions. Inside the cell, either metal ions or MNPs themselves can trigger the generation of ROS, which leads, *in fine*, to cell death.[214] As the interaction between MNPs/metal ions and bacteria cells is non-specific, MNPs exhibit a broad spectrum of activity. Radzig *et al.* demonstrated that silver nanoparticles (AgNPs) and silver ions (Ag^+) exhibit antimicrobial and antibiofilm properties on *E. coli*, *P. aeruginosa* and *Serratia proteamaculans*.[219] The MIC values vary from 0.1 µg mL^{-1} to 8 µg mL^{-1} depending on the strain and the antibacterial agent. Concerning the biofilm formation, it is strongly inhibited by AgNPs in concentrations ranging from 5 µg mL^{-1} to 20 µg mL^{-1}. Interestingly, the AgNPs also showed an activity on pre-established biofilms. Concentrations of 150-200 µg mL^{-1} reduced the biomass

of the biofilm by half and resulted in the death of most cells in the biofilm. It highlights that AgNPs can also destroy preformed biofilms.[219]

However, MNPs present some drawbacks. MNPs may exhibit toxicity, leading to impaired viability of mammalian cells. This toxic effect can be the result of the MNPs themselves or the release of metal ions.[220] At low concentrations, MNPs are not harmful to human cells, but their intracellular accumulation can be toxic.[218]

6.4 Bacteriophages

Bacteriophages, also known as phages, are ubiquitous viruses that target, infect, and potentially kill bacteria with a high species specificity.[221] They were discovered for the first time in 1915.[222] However, the introduction of broad-spectrum antibiotics and the technical issues related to phage production overshadowed the development of phage therapeutics in many parts of the world.[223] With the upgrowing antimicrobial crisis, phage therapy is currently widely studied and has been shown to be very efficient in the treatment of antibiotic-resistant bacterial infections. Bacteriophages can undergo two different life cycles: the lytic and the lysogenic cycle (Figure I. 7).[224] First, the phage attaches to the bacterial host, specifically on a bacteria's surface receptor, and injects its genetic heritage into the cell. The genetic material can either be replicated into the host cell to produce progeny phages that will, *in fine*, destroy the host bacteria and infect neighboring bacterial cells (lytic cycle) or integrated in the host's genome at specific sites (lysogenic cycle). This phage DNA is thus replicated along with the bacterial host genome, establishing a stable relationship. Interestingly, environmental stressors on the bacterial host can induce a transition from the lysogenic cycle to the lytic cycle.[224] In phage therapy, the use of lysogenic phages must be avoided as they can render bacteria more virulent if the phage harbors deleterious genes, and thus only lytic phages must be used.[225]

Interestingly, phages can be used both for the prevention and the treatment of biofilms.[226] Moreover, phage therapy can be combined with other strategies. The combination of antibiotics and phages showed a synergistic effect. De Soir *et al.* demonstrated that the degree of synergy on 24h mature *P. aeruginosa* biofilms is highly dependent on phages and antibiotics (type and concentration).[221] They observed a reduction in viable cell counts of up

to 4.58 log_{10} CFU/well, a reduction in the biofilm biomass of up to 29.8%, and a decrease in the biofilm respiratory rate of up to 65%.

Gutiérrez *et al.* isolated and overexpressed the EPS depolymerase derived from bacteriophage vB_SepiS-phiIPLA7 (Dpo7). They showed that a maximum removal of more than 90% of biofilm-attached cells was obtained with 0.15 µM of Dpo7 in all strains that produce polysaccharides.[227] Moreover, the pre-treatment of surfaces with Dpo7 reduced the biofilm biomass by 53-85% in 67% of the tested strains.[227] It highlights that not only phages but also isolated enzymes expressed outside the phage can have antibiofilm properties.

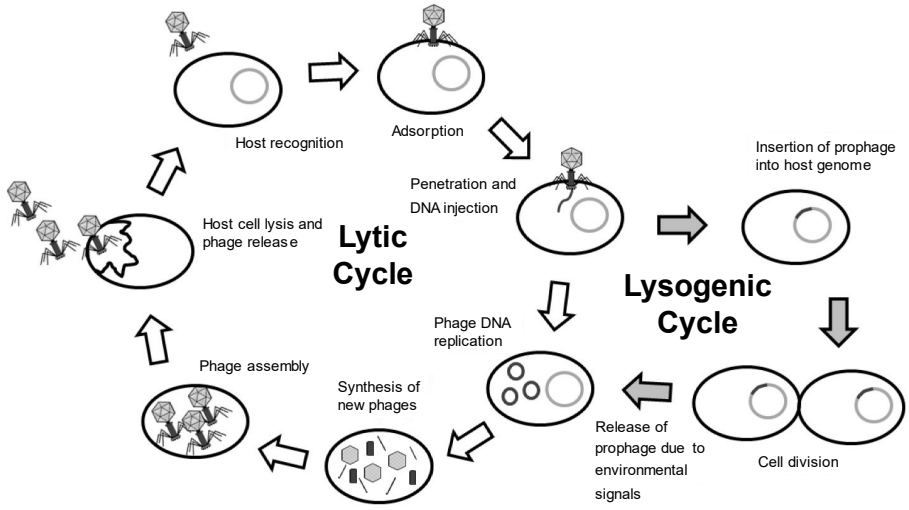

Figure I. 7 – The two different life cycles of phages. Reproduced from Doss *et al.*[224]

Phage therapy is suitable for use in humans, since phage do not infect eukaryotic cells and present few side-effects.[224] Since their first discovery in 1917, bacteriophages are widely studied. The countries of Eastern Europe, particularly Georgia, are pioneers in their study. Due to the emergence of antibiotics and geopolitical climate fostered by the Cold War reaction against Soviet science, research on phage therapy has been impeded in Western countries.[228] For instance, the first application of phage therapy in a patient suffering of a chronic PJI in Canada occurred in 2024.[229] Importantly, this approach opens the area of personalized medicine. Indeed, since phages target bacteria with a high species specificity, the phage selected for treatment is determined by the bacterial strain responsible for the infection.

Therefore, in case of polymicrobial infections, a cocktail of phages should be used to overcome them.

6.5 Antimicrobial peptides

Antimicrobial peptides (AMPs) are generally defined as being short peptides (10-50 amino acids) with a positive net charge (usually +2 to +9 at physiological pH) and a high ratio (≥30%) of hydrophobic residues. These properties allow the AMPs to fold in three dimensions into an amphiphilic structure, often upon contact with membranes, so they form separate domains rich in positively-charged and hydrophobic amino acids residues.[230] AMPs play a crucial role in the innate immunity system and are often referred to as natural antibiotics. However, they are less susceptible to pathogen resistance compared to conventional antibiotics and have a broad antimicrobial spectrum, targeting both Gram-negative and -positive bacteria. They are classified into four categories, according to their secondary structure: α-helix, β-sheets, αβ, and non-αβ.[231]

The cationic and amphiphilic nature of AMPs is associated with their direct killing antimicrobial activity (see Figure I. 8). Indeed, the positive net charge ensures their attraction and accumulation on the polyanionic surfaces of microbial cells that contain membrane-associated lipoteichoic acids in Gram-positive bacteria, and membrane-associated polymers, such as lipopolysaccharides, in Gram-negative bacteria (see Figure I. 9).[232] On the contrary, eukaryotic membranes are zwitterionic and are thus poorly negatively-charged, leading to very weak interactions with AMPs. Upon insertion into the membrane, AMPs can disrupt the bilayer's physical integrity, via membrane thinning, transient poration, and barrier function disruption.[230] They also can translocate across the membrane to target internal components, and kill bacteria through mechanisms involving the inhibition of DNA replication, RNA synthesis, protein synthesis, enzymatic activity, and the binding to DNA.[233] In addition to the direct killing mechanisms, it has been demonstrated that AMPs have a broad range of immunomodulatory properties (see in Figure I. 8), including the modulation in the expression of immune cells, epithelial cells and others, the chemoattraction of immune cells, and the induction of chemokines.[230]

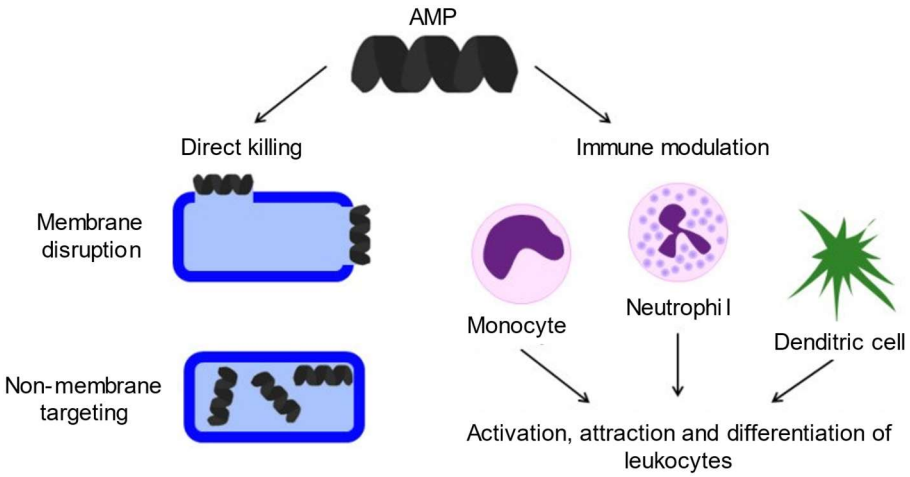

Figure I. 8 – Modes of action of AMPs. Adapted from Talapko *et al.*[233]

Three simple and controversial models are widely used to describe the mechanisms of action of AMPs involved in the bacterial membrane disruption (see Figure I. 9a). After the electrostatic interaction between the cationic AMP and the negatively-charged bacterial membrane, leading to the AMP lying parallel to the membrane, the AMP insertion into the bilayer can occur following three different models, which are depicted in Figure I. 9a. The barrel stave and toroidal pore models involve the formation of channels by reorientation of the AMP perpendicular to the membrane. In the barrel-stave pore model, AMPs interact laterally with one another to form a complex whose hydrophobic sides are bound to membrane compounds while the hydrophilic sides form the lumen of the channel. In the toroidal pore model, AMPs affect the local curvature of the membrane to create a pore that is partly formed by AMPs and partly by the phospholipid head groups. Finally, the carpet model suggests that AMPs aggregate parallel to the lipid bilayer, disturbing the membrane fluidity and energetics. At high concentration, AMPs cause the membrane collapse that leads to the formation of micelles.[234–236] In all cases, holes and deep craters are formed in the bacteria cell membranes leading to cell lysis (Figure I. 9b). However, due to their simplicity, those models are insufficient to explain the biological context of AMP-membrane interactions under *in vivo* conditions.[237]

(a)

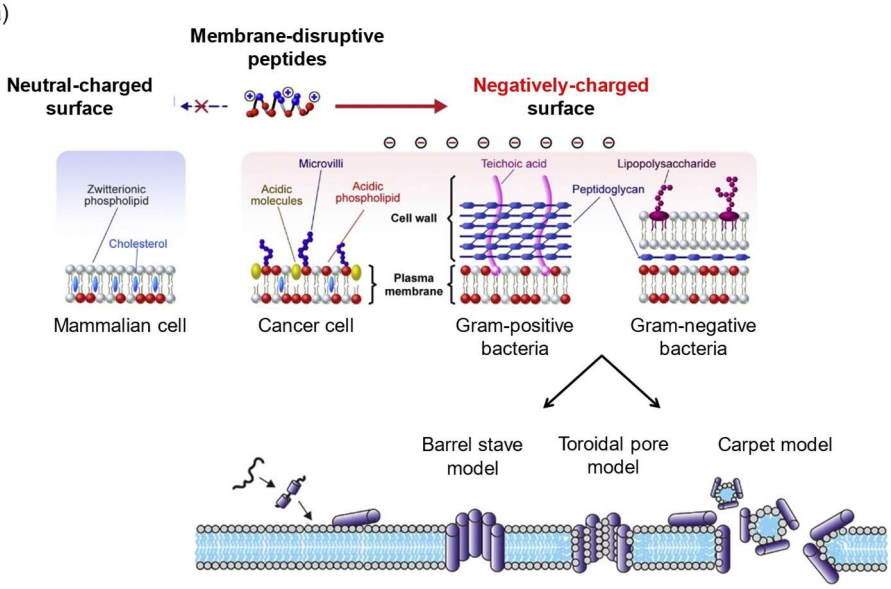

(b)

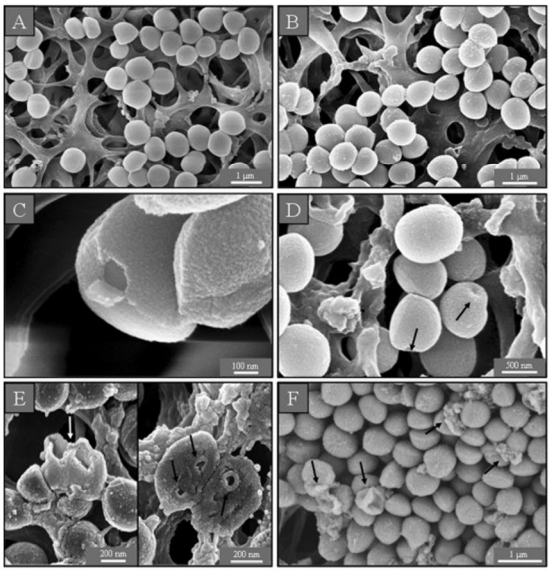

Figure I. 9 – (a) Understanding of membrane disrupting mechanisms of AMPs. The different compositions of mammalian, cancer and bacterial cells are represented. Finally, the different modes of action used by AMPs to disrupt the bacterial membrane are shown. Adapted from Lin *et al.*[232] (b) Scanning electron microscopy demonstration of (A-B) untreated and (C-F) treated *S. aureus*. After AMP treatment, bacteria show holes and deep craters which lead to burst and lysis of cells. Reproduced from Hartmann *et al*.[238]

AMPs are also known for their ability to promote the angiogenesis and the wound healing responses, and to exert an antitumor and antiviral activity.[234,239] In addition to their antibacterial activity, AMPs also show antibiofilm activity, which is very interesting for the goal of our study. Basically, the targeted stage of biofilm formation affected by AMPs can vary widely, going from the attachment stage to the eradication of pre-existing biofilms. AMPs can disrupt or degrade the membrane of biofilm-embedded cells, affect the quorum sensing system, degrade the EPS matrix, inhibit the alarmone system to avoid the bacterial stringent response, or down-regulate the genes responsible for biofilm formation and transportation of binding proteins.[240] Among all the existing AMPs, a particular focus will be given to LL-37, which was selected for the present thesis.

6.5.1 LL-37

In 1995, LL-37, the only human-cathelicidin AMP, was identified.[239] It owes its name to its 37 amino acid residues (4.5 kDa), with its N-terminus sequence starting with two leucine residues. LL-37 is an amphipathic, cationic, and linear α-helical peptide found throughout the body, such as in the epithelial cells of the testis, skin, gastrointestinal tract and respiratory tract, and in leukocytes such as monocytes, neutrophils, T cells, Natural Killer cells, and B cells.[241] LL-37 is thus present in the innate immune system of humans and involved as a first-line defense agent against a broad spectrum of pathogens, namely bacteria, fungi, and viruses.[241] This is the reason why it has been decided to focus the study on this AMP. Moreover, even it is initially recognized for its antimicrobial properties, LL-37 exhibits other interesting properties. Indeed, it shows a strong binding affinity for lipopolysaccharides, a chemotactic activity, an antibiofilm activity, an antitumor effect and it promotes the release of cytokines, wound healing, and angiogenesis.[239,241] Therefore, LL-37 appears to be a very attractive agent and deserves in-depth analysis.

The primary structure of LL-37, LLGDFFRKSKEKIGKEFKRIVQRIKDFLRNLV-PRTES, reveals its highly charged nature. Under physiological conditions, LL-37 shows an α-helical conformation (Figure I. 10a), and 16 residues are charged, 11 with a positive charge (6 Lys and 5 Arg) and 5 with a negative charge (3 Glu and 2 Asp), resulting in a +6 net charge (Figure I. 10b).

Interestingly, the LL-37 secondary structure reveals a lipophilic side (apolar) and a hydrophilic side (polar). This structure is very important and appears to correlate with either its antimicrobial action or its effect on host immunity.[241] Indeed, the cationic amphipathic α-helical structure allows LL-37 to interact electrostatically with anionic bacterial membranes, which leads to their disruption. Studies and experiments on LL-37 showed that the C-terminal α-helix is responsible for the antimicrobial effect.[239]

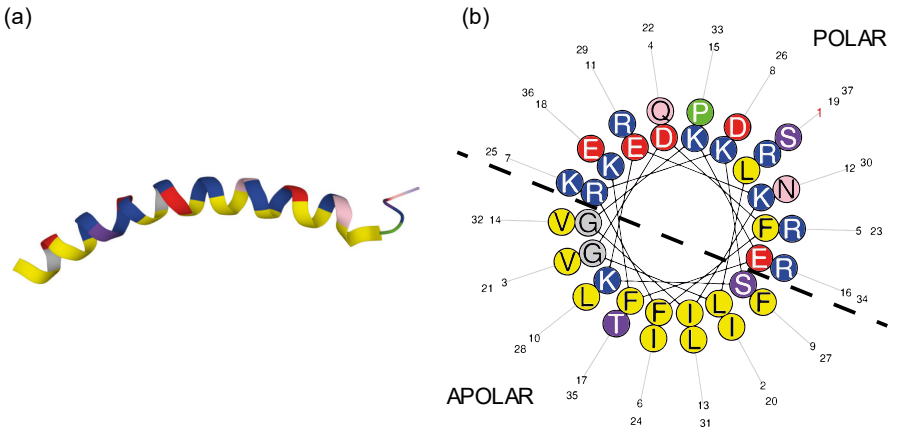

Figure I. 10 – Three-dimensional structure of LL-37, which (a) reveals an α-helical conformation, followed by a C-terminal tail. (b) Helical wheel representation of LL-37 illustrating its amphipathic and cationic nature. The negatively-charged residues are represented in red, the positively ones in blue, and the hydrophobic amino acids are represented in yellow. Created using the HeliQuest software.

6.5.2 Mode of action and activity of LL-37

As all AMPs, LL-37 plays a key role in the innate immune system and thus provides a first line of defense against pathogens. LL-37 has membrane-disrupting propensities. It interacts with bacterial cell membrane molecules and disrupts cytoplasmic membranes, ultimately causing bacterial cell death. The precise mechanism by which LL-37 interacts with the bacterial cell membrane has not been investigated in much detail. Sancho-Vaello *et al.* studied the interaction between LL-37 and the bacterial cell membrane *in vitro*, and in the presence of membrane-mimicking detergents and lipids (membrane-like environments), to propose a better mechanistic model for Gram-negative bacteria.[237] The suggested model is depicted in Figure I. 11.

As a first step, LL-37 interacts electrostatically with the outer membrane (OM) of Gram-negative bacteria via the formation of LL-37-lipopolysaccharide complexes. These interactions lead to the extraction of lipopolysaccharides to form holes in the outer membrane which may allow for the diffusion of LL-37 molecules into the periplasmic space (Figure I. 11a). As a second step, LL-37 interacts with the phosphatidyl-ethanolamine molecules of the inner membrane (IM, Figure I. 11b). In the case of Gram-positive bacteria, as there is no outer membrane, LL-37 directly interacts with the inner membrane. This interaction with the inner membrane leads to a structural reorganization of LL-37, to a higher oligomerization state and thus to the formation of LL-37 fibers. Fibril structures are formed exclusively from LL-37 interactions with detergent or lipid followed by structural reorganization of termini and polymerization.[242] LL-37 exhibits conformational flexibility and forms lower oligomeric states, which may transition into fibers in response to external stimuli.[237] The mechanisms of fiber formation and their supramolecular assemblies are formed via hydrophobic nesting structures and depend on the peptide structure and plasticity.[237,242] These fibers may be necessary to increase the local LL-37 concentration and to locally extract lipids from the cytoplasmic membrane after peptide interactions (Figure I. 11c). Consequently, LL-37 integrates into the membrane (Figure I. 11d) and forms a tetrameric channel structure with two antiparallel helices, suggesting a barrel stave pore model as another putatively final step of membrane targeting (Figure I. 11e). Finally, it leads to the breakdown of the transmembrane potential and thus to the cell lysis (Figure I. 11e).

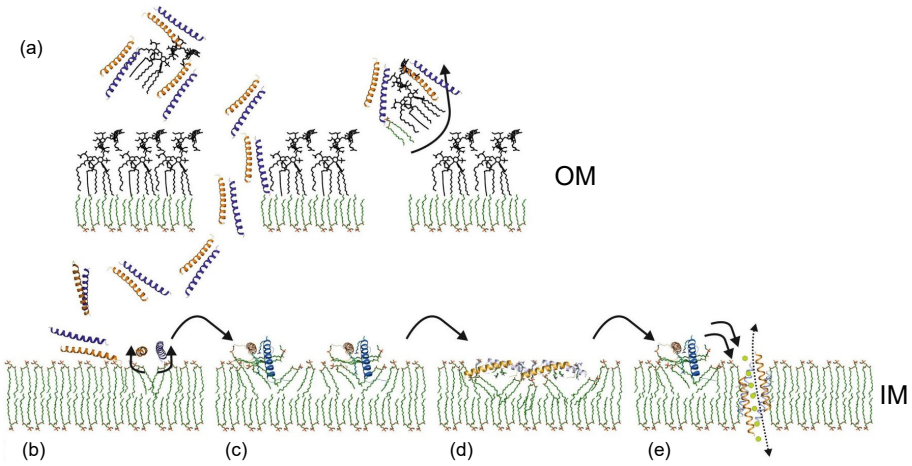

Figure I. 11 – Proposed model of LL-37 interactions with the bacterial cell membrane. Reproduced from Sancho-Vaello *et al.*[237]

This mechanism of action is relevant for free LL-37 molecules in solution. However, numerous studies are examining the antibacterial properties of LL-37 covalently immobilized on surfaces, where it is not released into the solution.[243,244] This raises questions regarding its mode of action in that case and the importance of LL-37 flexibility when it is covalently immobilized.

Interestingly, Sancho-Vaello *et al.* also demonstrated that the effect of LL-37 on the cell membrane was time- and concentration-dependent.[237] Usually, the effect of an antimicrobial drug is determined using the MIC measurement. Depending on the bacteria strain, and the culture medium, the MIC value of a specific antimicrobial agent can be completely different. Studies revealed MIC values for LL-37 ranging from <1 µg mL^{-1} (<0.2 µM) to >128 µg mL^{-1} (>28.5 µM).[234,241,245–248] Those differences highlight the importance of determining the MIC of a specific bacteria strain in a specific culture medium. However, several studies highlighted that the antimicrobial effect of LL-37 was significantly reduced in high salt concentration (up to 175 mM) and under serum conditions.[241,245] Moreover, proteinases of common pathogenic bacteria can degrade and thus inactivate LL-37.[241]

Regarding the LL-37 antibiofilm activity, Overhage *et al.* showed that LL-37 can prevent *P. aeruginosa* biofilm formation by decreasing the attachment of bacterial cells, stimulating twitching motility and down-regulating the quorum sensing system.[246] Indeed, at a concentration of 0.5 µg mL^{-1} (0.1 µM),

the researchers showed a decrease of around 50% in the formation of the biofilm on the surface.[246] This concentration is far below the one required to inhibit growth (MIC = 64 µg mL^{-1}, *i.e.* 14.2 µM), suggesting that antimicrobial and antibiofilm activity of AMPs may be due to different mechanisms. Antibiofilm activity could be mediated by alteration of bacterial gene expression.[246] Dean *et al.* also demonstrated a significant antibiofilm inhibition for *S. aureus* at 10 µg mL^{-1} (2.2 µM), reducing biofilm formation by about 40%.[249] Moreover, a decrease of 58% in the attachment of *S. aureus* biofilm was shown in the presence of LL-37, suggesting that the peptide may inhibit biofilm formation by interaction with bacterial adhesins.[249]

Finally, the *in vitro* cytotoxicity of LL-37 was also studied, and Johansson *et al.* referred to concentrations of 58.4-112.3 µg mL^{-1} (13-25 µM) to be sufficient to make human leukocytes and T-cells nonviable.[250] Physiological concentrations of 2-5 µg mL^{-1} (0.4-1.1 µM) of LL-37 have been found in most bodily fluids and is found at larger concentration at sites of chronic inflammation (30 µg mL^{-1}, *i.e.* 6.7 µM, in the cystic fibrosis lung).[246] It is known that overexpression of LL-37 has been associated with harmful inflammatory responses and apoptosis.[251] For example, extremely high concentrations of LL-37, exceeding several hundreds of µM, have been found in lesions of patients with autoimmune diseases, suggesting that LL-37 plays a critical role in these disease processes.[252] The effects of LL-37 on apoptosis appear to be cell type specific.[251] However, the signaling pathways and mechanisms underlying LL-37-mediated apoptosis are not yet fully understood. It seems to involve a pro-apoptotic effect and to be associated with plasma membrane permeabilization.[253]

It is important to note that LL-37 is highly susceptible to proteolysis, and thus can be degraded by proteases under *in vivo* conditions. vander Straeten demonstrated that LL-37 is prone to hydrolysis by α-chymotrypsin in TRIS-$CaCl_2$ buffer.[254] Therefore, striking a balance between achieving a concentration adequate to induce antibacterial and/or antibiofilm effects while preserving eukaryotic cell viability is a major challenge.

The different prevention strategies to fight biomaterial-associated infections and the immobilization methods of peptides will be discussed in details in sections *Part I – 7 Prevention of biomaterial-associated infections* and *Part I – 8 Immobilization of proteins at interfaces*, respectively.

6.5.3 Antibacterial activity of surface-immobilized LL-37

In this section, strategies developed to immobilize LL-37 on surfaces will be highlighted. Gabriel *et al*. used poly(ethylene glycol) (PEG) spacers to covalently immobilize Cys-LL-37 (*i.e.*, LL-37 with an additional N-terminal cysteine residue) to amino-silanized Ti surface, which expressed antimicrobial activity against *E. coli*.[243] Mishra & Wang covalently immobilized FK-16, which corresponds to the major antimicrobial region of LL-37, to amino-silanized Ti surface and showed a biofilm inhibition capability.[244] Another study demonstrated that LL-37 immobilized on poly-hydroxyethylmethacrylate surfaces using 1-ethyl-3-(3-dimethylaminopropyl) carbodiimide hydrochloride, which produced covalent attachment, resulted in up to 2.6 ± 1.0 log inhibition of CFUs against *P. aeruginosa*.[255] Interestingly, in addition to its antibacterial activity, it has been demonstrated that LL-37 coated on micro-structured Ti implants facilitates bone formation both *in vitro* and *in vivo* through mesenchymal stem cells recruitment.[256] These results highlight the interest of immobilizing LL-37 as an antibacterial agent on surfaces.

7 Prevention of biomaterial-associated infections

Instead of fighting the biofilm, other strategies involve preventing bacterial adhesion in its very early stage, and thus preventing its formation. Acting before the attachment of bacterial cells on the surface can thus be another way to act (see “Window of Opportunity” in Figure I. 4).

As already explained, when bacteria succeed in forming a biofilm within the human host, the infection often becomes very resistant to treatment and can develop into a chronic state. To deal with this issue, the adage '*prevention is better than cure*' could be a part of the solution. From this point of view, preventing the biofilm formation, and thus avoiding the risk of infection, could be a strategy. To do so, it is crucial to act before the growing stage of the biofilm and the EPS formation. The window of opportunity is thus limited (Figure I. 4). Indeed, although overt disease necessitates a substantial bacterial load, the presence of an implantable medical device can prompt infection even with a low bacterial inoculum, such as 10^2 CFU of *S. aureus*.[257] This highlights the importance of taking action before bacteria colonize

surfaces. To do so, several strategies, both bacteriostatic and bactericidal, have been developed. For bacteriostatic strategies, the challenge is to design coatings that specifically prevent the surface adhesion of bacteria without affecting the surface colonization by host's compounds such as proteins and eukaryotic cells (Figure I. 12a). Bactericidal strategies aim for the same objective, with coatings tailored to selectively target and kill bacteria by contact (Figure I. 12b) or by release of active compounds (Figure I. 12c).

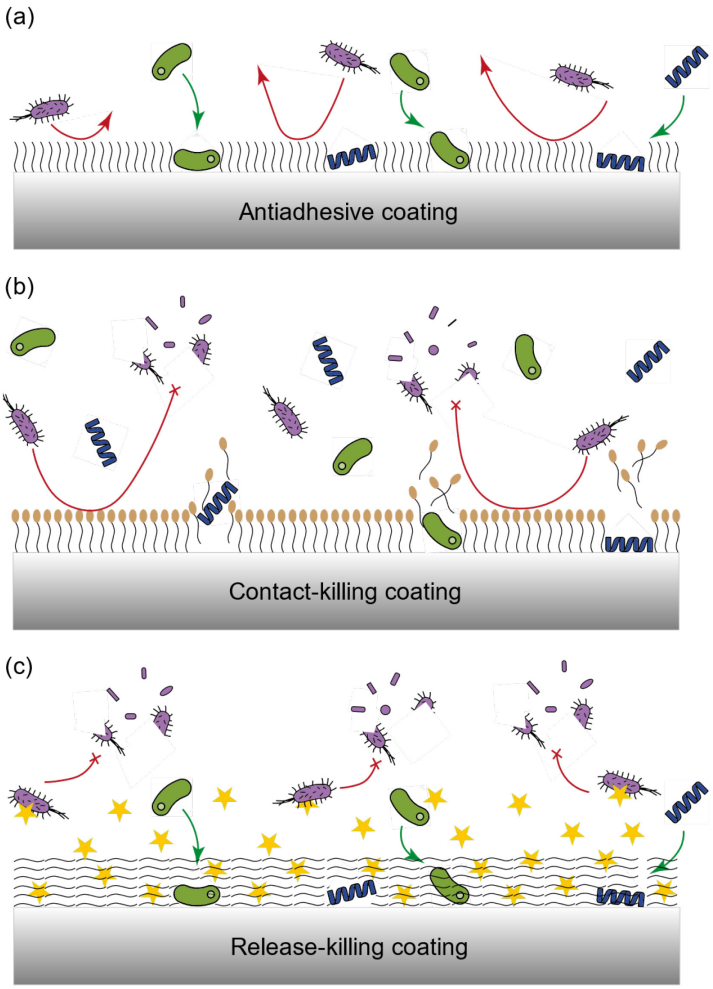

Figure I. 12 – Schematic representation of strategies that can be used to build (a) antiadhesive coatings or coatings that are bactericidal by (b) contact-killing or (c) release-killing.

7.1 Antimicrobial polymers

Polymers and polymer-based materials with antibacterial properties are widely studied. Synthetic polymers such as PEG or semi-synthetic polymers such as polylysine, polyarginine, and Chi have shown interesting results in the decrease of risk of infection of implant surface.[258–262] Because the initial step in bacterial infection on implant is the bacterial adhesion on the surface, the first strategy consists in the development of antiadhesive polymer coatings to prevent attachment and thus inhibit growth of pathogens on the surface (antiadhesive strategy, Figure I. 12a) without affecting the adhesion of host proteins and cells. Yet, since the pathogens are not killed, there is a risk of spread and colonization of surrounding area. Therefore, another strategy implies the design of bactericidal polymer coatings to damage bacteria when they come in contact with the surface of the material (contact-killing strategy, Figure I. 12b) without preventing the adsorption of host proteins and without killing the host cells. Hardy *et al*. demonstrated that chitosan (Chi)-heparin (Hep)-based multilayers are compatible with the proliferation of osteoblasts.[263] Finally, the release of bactericidal polymers from the film into the solution can also be a killing strategy (release-killing strategy, Figure I. 12c).

7.1.1 Antiadhesive polymers

It is well known that physicochemical properties of a surface can influence bacterial adhesion, thereby potentially restricting it, as represented in Figure I. 12a. Bruzaud *et al.* demonstrated that bacterial flagella, pivotal for irreversible adhesion, exhibit enhanced affinity towards hydrophobic surfaces.[264] Consequently, enhancing the hydrophilicity of a surface may represent a viable strategy for mitigating bacterial adhesion.[265] Immobilizing PEG is one of the most commonly used approach to impart antiadhesive properties. As explained in the section *Part I – 5.2.1 The in vitro biofilm model: formation and regulation*, the attachment of bacteria is mediated by bacterial adhesins that can stick to the surface. These adhesins recognize host proteins such as Fn, fibrinogen, and Col, which rapidly adsorb to abiotic surfaces, thereby promoting bacterial adhesion. Surface-immobilized PEG prevents protein adsorption, and *in fine* bacterial adhesion. On the other hand, the approach of bacteria towards the film induces compression of the

polymer chains, resulting in the generation of repulsive elastic forces. Additionally, it causes the removal of water molecules from the hydrated polymer chains during compression, leading to the development of unstable osmotic pressure. These unfavorable elastic and osmotic stresses subsequently generate a repulsive force, contingent upon surface density and polymer chain length.[266] Hydrophilic coatings made of Hep and Chi showed antiadhesive properties against *E. coli* bacteria when films were assembled at low pH and were rich in Hep.[260] The role of substrate elastic modulus in bacterial adhesion also appears to be noteworthy, although the results are still controversial. Lichter *et al.* were the first to study the influence of elastic moduli (from 1 to 100 MPa) on bacterial adhesion.[267] They have established that a decrease in elastic modulus results in reduced bacterial adhesion.[267] Another study, however, found that chemically cross-linking a multilayer film, thereby increasing its elastic modulus from 30 to 150 kPa, resulted in reduced bacterial adhesion.[268] This finding contradicts the conclusion drawn by Lichter *et al*. This contradiction could be explained by the difference in the studied elastic modulus range and the difference in the chemical composition of the substrate.[259]

Interestingly, the antiadhesive properties can thus be tuned by the hydrated structure and stiffness of the thin films.[259] However, the antiadhesive character raises two issues. First, the repulsive forces are not specific to bacteria and thus occur towards proteins and eukaryotic cells, also preventing their adsorption and adhesion, which can be problematic.[266] Indeed, in THA and TKA, successful osteointegration of the prosthesis is essential. This involves the adhesion and proliferation of osteoblasts on the implant surface to ensure successful integration with the surrounding bone. Second, since the bacteria are not killed by this approach, there is a heightened risk of them spreading and colonizing adjacent sites.

7.1.2 Contact-killing and release-killing polymers

As already described, bacterial cell membranes are negatively charged. Consequently, most antimicrobial polymers are positively-charged to enhance their interaction with bacterial membranes. Through the cationic charges available on their surface, polymers disrupt bacterial membranes, effectively inhibiting bacterial proliferation and inducing cell death. For

instance, Chi-rich surfaces present efficient antimicrobial properties.[260] Like Chi, ε-poly-L-lysine is a semi-synthetic cationic polymer presenting strong antifungal and antibacterial properties against Gram-positive and -negative bacteria.[258] Yang *et al.* covalently immobilized hyperbranched ε-poly-L-lysine to titanium surface and demonstrated antimicrobial activity against *E. coli* and *S. aureus* with an efficiency, respectively, of 92.2% and 89.4% *in vitro*.[269] Mutschler *et al.* were among the first to investigate the effect of the molar mass of polymer on the functionality of the film.[261] To do so, they studied the inhibition of bacterial growth of different polyarginine-based films. They selected polyarginine chains with either 10, 30, 100, or 200 residues and they demonstrated that only the coatings made of polyarginine chains with 30 residues displayed antibacterial activity. Indeed, an inhibition of at least 90% of *S. aureus*, *S. aureus* methicilin resistant, *Micrococcus luteus*, *E. coli*, and *P. aeruginosa* bacterial growth was observed after 24h, suggesting that polyarginine chains with 30 residues strongly impact the viability of both Gram-positive and -negative bacteria.[261] They investigated the mechanism of action to understand why the antibacterial properties are molar mass-dependent. It seems to be related to the mobility of the lower molar mass polyarginine chains, which diffuse out of the film and finally stick to the bacterial membrane.[261] In addition to the diffusion capacity, enough free polyarginine chains must be available to confer bactericidal effect to the films.[261] Although polyarginine was released in the supernatant, its concentration was significantly below the MIC. Consequently, it was hypothesized that the bactericidal effect is primarily attributed to direct contact with the bacteria (Figure I. 12b) than to the release of the active compound (Figure I. 12c).

7.2 Bioactive glasses

Bioactive glasses are synthetic silica-based bioactive materials that promote bone regeneration.[270] Some of them have been shown to have antibacterial and antibiofilm properties. In the event of hip, knee, etc. arthroplasty, the coating of these compounds on medical implants can thus be very helpful. When bioactive glass comes into contact with biological fluids, various biological responses are stimulated, and alkaline ions, particularly Ca^{2+}, are released from the surface (release-killing strategy, Figure I. 12c), causing an

increase in osmotic pressure and pH levels.[270] The local pH can increase up to 10. Consequently, the physiological conditions at the surrounding environment become inhospitable to microbial proliferation, without affecting the host tissues and while promoting osteointegration.[271] The modulation of the release rate of ions is thus at the center of the reported antimicrobial activity, which is directly influenced by surface area.[270,272] Munukka *et al.* were the first to examine the bactericidal effect of several different bioactive glasses on a large panel of clinically important aerobic bacteria strains.[273] They highlighted that even if the antibacterial efficacy varied among bacterial strains, glass compositions, and concentrations, all materials exhibited some level of inhibition against bacterial growth.[273] Cabal *et al.* studied the antimicrobial activity of a borosilicate glass on different bacterial strains (*S. aureus*, *S. epidermidis*, *P. aeruginosa*, *E. coli*, and *M. lutea*) and reported that this bioactive glass was able to minimize growth bacteria but also to inhibit bacterial adhesion and prevent biofilm formation by the perturbation of intracellular Ca^{2+} compartmentalization, while promoting cell proliferation.[274]

Studies investigating the use of bioactive glass in combination with other compounds, such as antibiotics and metallic nanoparticles have also been performed and demonstrated promising results.[275]

7.3 Nanostructured surfaces

The presence of nanostructured features on material surface has been shown to elicit antimicrobial properties. Indeed, bactericidal behavior through physical surface topography has been shown depending on the size, shape, density, rigidity/flexibility and surface chemistry of the surface nanotextures.[276] The development of nanostructured surfaces to kill bacteria by contact (Figure I. 12b), through the physico-mechanical deformation or rupture of the bacterial cell wall, as soon as they arrive on the surface, is widely studied to prevent biofilm formation.[276] Indeed, a myriad of plants and insects possess antimicrobial surfaces, which offer protection against pathogenic bacteria. Tripathy *et al.* listed some of these naturally-occurring (as well as artificial mimetic) nanostructured bactericidal surfaces.[276] In 2012, Ivanova *et al.* were the first to study the propensity of the cicada wings to resist *P. aeruginosa* bacterial contamination.[277] They showed that wings are

covered by superhydrophobic hexagonal arrays of spherically capped, conical, nanoscale pillars, which alter the cells' morphology by penetration, leading to cells' death within just a few minutes. Interestingly, they highlighted that the bactericidal properties are due to the physical surface structure of the wing, rather than the surface chemistry.[277] Indeed, they did not show any repelling of bacterial cells due to the superhydrophobic nature of the cicada wings.[277] However, Hasan *et al.* demonstrated that those cicada wings are only effective against Gram-negative bacteria and not on Gram-positive bacteria.[278] This selective killing was attributed to the difference in cell wall composition. Gram-positive cells have a thicker and more rigid wall, which may explain their ability to survive under the mechanical pressure.[278] Ivanova *et al.* studied the dragonfly wing and showed that their surface presents a random size, shape, and spatial distribution of nanoclusters, in contrary to the regular pattern of cicada wings.[279] This randomized surface was shown to be very effective against both Gram-negative and -positive bacteria.[279] Indeed, scanning electron microscopy images and confocal laser scanning micrographs reveal significant disruption in *P. aeruginosa*, *S. aureus*, vegetative *B. subtilis* cells, and *B. subtilis* spores following interaction with dragonfly wings (Figure I. 13a-h). Similar results were obtained by mimicking dragonfly wings with black silicone nanopillars (Figure I. 13i-p). Therefore, the development of such nanopillar surfaces, biomimicking the nanoscale patterns, has enormous potential for application in the production of bactericidal coatings and is thus widely studied.[279–284]

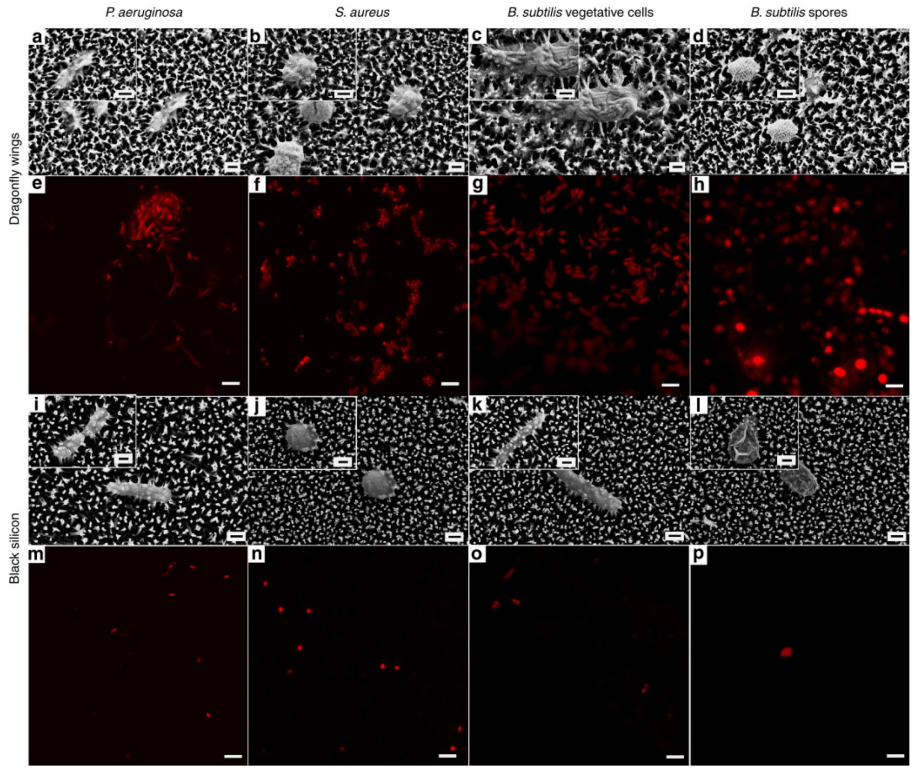

Figure I. 13 – Cell morphology on dragonfly wings and black silicon. Scanning electron microscopy images reveal significant disruption in *P. aeruginosa*, *S. aureus*, vegetative *B. subtilis* cells, and *B. subtilis* spores following interaction with both dragonfly wings (a-d) and black silicon (i-l). Scale bars: 200 nm. Confocal laser scanning micrographs further confirm that the damage caused by dragonfly wings (e-h) and black silicon (m-p) was lethal, as non-viable bacterial cells and spores, stained with propidium iodide (red), were predominant, while viable cells stained with SYTO 9 (green) were absent. All cells appeared red, indicating the high efficiency of surfaces in inactivating the bacteria. Scale bars, 5 mm. Reproduced from Ivanova *et al*.[279]

The advantages and limitations of therapeutic and preventive strategies broached in this *Part I – Context of the research* are summarized in Table I.3.

Table I. 3 – Advantages and limitations of therapeutic and preventive strategies against medical-related infections.

Strategy	Advantages	Limitations
Biofilm matrix-degrading enzymes	Degrade the biofilm matrix leading to bacterial release	May lead to septicemia
Quorum sensing inhibitors	Inhibit the bacterial communication pathways	May be cytotoxic. There is a lack of understanding regarding the precise mechanism
Metallic nanoparticles	Inhibit the biological machinery, increase the formation of ROS, disrupt the cell membranes, and prevent bacteria from receiving essential trace elements	May be cytotoxic due to intracellular accumulation
Bacteriophages	Kill bacteria with a high species specificity and thus open the area of personalized medicine	Only lytic phages must be used, and lysogenic phages must be avoided as they can render bacteria more virulent
Antimicrobial peptides	Possess a broad range of immunomodulatory properties and promote the angiogenesis and the wound healing responses	Long AMP sequences are economically and synthetically challenging for pharmaceutical scale synthesis. AMPs are susceptible to proteases
Antimicrobial polymers	Present a long-term activity, a limited residual toxicity and a chemical stability	May prevent the adhesion of host's proteins and cells
Bioactive glasses	May promote osteointegration	Challenging to produce in large quantities at a low cost and high purity
Nanostructured surfaces	Kill bacteria through physico-mechanical deformations	Strain-specific bacterial responses to external physico-mechanical stimuli

8 Immobilization of proteins at interfaces

Surface biofunctionalization is the key to many biomedical applications. There are many studies aiming at immobilizing active biomacromolecules on surfaces in different fields of research such as biosensing,[285,286] heterogeneous biocatalysis,[287,288] drug delivery,[289,290] and tissue engineering.[291,292] In this respect, a myriad of methods was developed to functionalize material surfaces with proteins (Figure I. 14). Since this work focusses on the development of antimicrobial coatings based on LL-37; in the following, an overview of the existing methods that could be used to immobilize LL-37 on surfaces is presented.

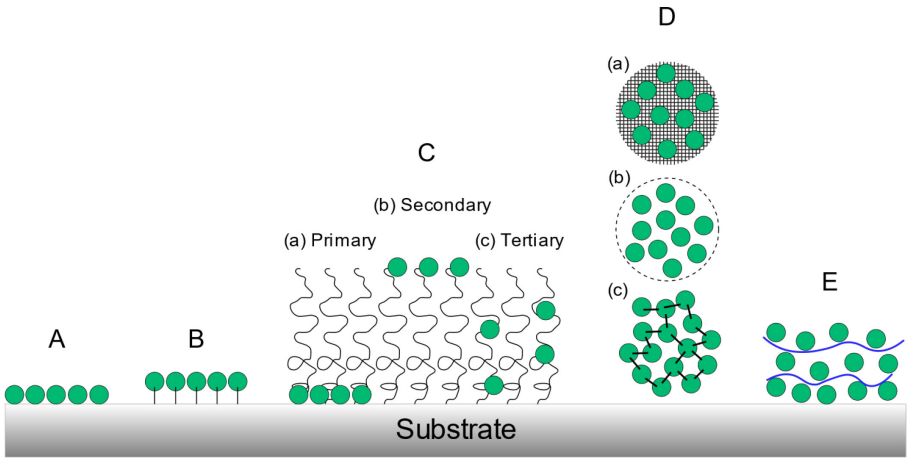

Figure I. 14 – Protein immobilization strategies. Proteins are represented by green circles. A – Proteins are spontaneously adsorbed on the surface (physisorption). B – Proteins are covalently linked to the surface. C – Schematic of polymer brushes on a surface and modes of protein adsorption: (a) primary adsorption at the brush-substrate interface, (b) secondary adsorption at the brush-liquid interface, and (c) tertiary adsorption along the polymer chains. Adapted from Taylor *et al.*[293] D – Protein immobilization strategies under the form of particles: (a) entrapment, (b) encapsulation, (c) self-immobilization. Adapted from Braddy & Jordaan.[294] E – Self-assembly of proteins at interface using a polyelectrolyte (in blue).

8.1 Physisorption

Proteins are highly surface active and usually exhibit spontaneous adsorption on a wide range of surfaces (Figure I. 14A). This observation implies that the

process of protein adsorption results in a decrease in the Gibbs free energy of the system. This propensity stems from their amphiphilic nature, allowing them to readily optimize interactions with surfaces.[295] Because of their complex nature, protein adsorption is a multifaceted process involving diverse interaction types such as electrostatic interactions, van der Walls and hydrophobic forces, and conformational changes. It is thus challenging to predict the outcome of their interaction with a surface. To do so, Norde introduced the difference between structurally stable ('hard') and labile ('soft') proteins, which indicates the strength of their internal structure.[296] A 'soft' protein is more prone to undergo conformational changes upon adsorption, unlike a 'hard' protein. Since conformational change is one of the major driving forces, 'soft' proteins tend to adsorb more easily on surfaces compared to 'hard' proteins.[296] Even if spontaneous adsorption is a very straightforward method to immobilize proteins on a surface, several drawbacks may be highlighted. Protein bioactivity is conformation-dependent. Structural changes, *i.e.,* unfolding, upon adsorption can lead to a loss of protein bioactivity. Furthermore, the amount of immobilized protein is constrained by the surface area of the supporting material and molecular crowding usually limits the surface loading.[295] The deposited quantity is usually restricted to one monolayer. Another concern is that protein adsorption occurs under dynamic equilibrium and thus protein removal from the surface is very likely, especially upon condition change.[295] Therefore, spontaneous adsorption may not be the most suitable method for functionalizing surfaces with active proteins. However, Cassin *et al*. used spontaneous adsorption to immobilize LL-37 on Col/hyaluronic acid polyelectrolyte multilayers and studied the release profile and the antimicrobial effect of such system.[297]

8.2 Covalent linking

To limit protein desorption, grafting (or chemisorption), involving covalent linking of the protein to the surface, thanks to the functional groups present on the protein, has been routinely used (Figure I. 14B). This method is not straightforward to implement since the surface must bear functional groups reacting with the protein. Moreover, such chemisorption might result in a loss of bioactivity caused by protein denaturation or reaction with the

functional group. It is widely known that even if the covalent bond is positioned far from the active site, it may cause a loss of protein function.[298] Lastly, the immobilized amount is also limited to the surface area and to a monolayer. Like spontaneous adsorption, covalent binding thus presents major drawbacks when it comes to the immobilization of large amounts of bioactive proteins.

8.3 Polymer brushes

Polymer brushes have found extensive application in the immobilization of proteins.[299] This is achieved by either grafting a polymer to a surface or polymerizing it directly and thus grafting it from the interface.[300,301] Upon exposure to proteins, polymer brushes exhibit either repulsion or adsorption depending on the conditions, the used polymer, and the protein. When the protein-brush interaction is favorable, three distinct adsorption positions are observed: primary adsorption, occurring at the interface between the brush and the substrate (Figure I. 14Ca), secondary adsorption, taking place at the interface between the brush and the liquid (Figure I. 14Cb), and tertiary adsorption, characterized by protein adsorption throughout the brush due to attractive interactions between the proteins and the polymeric chains (Figure I. 14Cc).

8.4 Immobilization in particles

Strategies targeting the immobilization of proteins in particles through entrapment within molecular networks or into core-shell particles have been widely investigated. Three distinct approaches for protein immobilization within particles are depicted in Figure I. 14D. First, protein can be entrapped in polymer matrices (Figure I. 14Da). For example, Chereddy *et al*. entrapped LL-37 in poly (lactic-co-glycolic acid) nanoparticles to promote wound healing.[302] Second, protein can be encapsulated in lipid-based vesicles (Figure I. 14Db), such as for LL-37 in the Garcia-Orue *et al*. study.[303] Finally, another method consists in protein self-immobilization which is achieved by the formation of cross-linked aggregates (Figure I. 14Dc).[294] In the latter case, freestanding aggregates of potentially active proteins are obtained. Compared to the spontaneous adsorption and the covalent linking, these

strategies offer significant advantages. The immobilization is not limited to the surface of the material and the whole nanoparticle volume can be filled with proteins. As a result, highly active materials can be generated. Except for cross-linked aggregates, there are no chemical reactions, which prevent protein deactivation. However, a limitation of these methods is that they are usually limited to particles. Therefore, they are often used as drug delivery systems.[304]

8.5 Self-assembly

Self-assembly is the process through which a disordered set of constituents interact with one another to form organized structures.[305] Through the self-assembly process, a myriad of structures can emerge depending on the conditions of assembly. These structures can be thermodynamically stable but also out of equilibrium.[306] Out of equilibrium means that various metastable (or transient) states can be achieved depending on the path that is followed to generate the system. Indeed, not all systems inherently progress towards the lower energy state spontaneously; some may be trapped in non-equilibrium states.[306,307] In these cases, energy and matter need to be supplied to the system to overcome the energy barrier necessary for the system to reach its state of lower energy. Currently, there is a great deal of interest for these out of equilibrium system since, depending on the self-assembly pathway, different functionalities can be obtained. Actually, this idea is very intuitive. In cells, self-assembled structures are organized in hierarchical levels in which different kinds of structures interact and affect the formation and maintenance of other structures. If all these structures were mixed together, they would not spontaneously self-assemble into a functional cell. In other words, the pathway followed for the assembly matters.

With the goal to immobilize protein at surfaces, careful selection of self-assembling molecules and mixing method can lead to the spontaneous formation of structures capable of immobilizing proteins, either at interfaces or in solution (Figure I. 14E). In this way, self-assembled multilayered structures can be obtained by the alternated adsorption of layers of compounds on top of each other, using the layer-by-layer (LbL) self-assembly technique. This approach is widely used to functionalize surfaces with

proteins. In solution, proteins can be self-assembled with polyelectrolytes (PEs) to form protein-polyelectrolyte complexes (PPCs). These two techniques are at the heart of the present research and will be thus discussed in the following.

9 Layer-by-layer self-assembly

Each surface modification technique offers advantages and drawbacks. The perfect antimicrobial coatings should, on top of offering the desired functionalities, be developed easily and in soft conditions, be versatile in terms of chemistry and surface geometry, and exhibit adequate durability. In this view, self-assembled multilayered films are popular functional nanocoatings.[308]

9.1 Principle of layer-by-layer assembly

Nanostructured films are obtained by the successive buildup of layers of materials through LbL assembly. This LbL nomenclature appeared, for the first time in the scientific community, in the late 1960's. It usually stands for the alternated adsorption of oppositely-charged materials. The electrostatic interactions, and thus the charge surface overcompensation by the new layer of material that is adsorbed, are the driving forces of the multilayer growth. It results in a surface charge inversion, which allows adsorbing a next layer of oppositely-charged material. Charged soluble polymers, *i.e.*, PEs, are the most widely used materials. Their LbL buildup was first demonstrated by Decher *et al.* in 1992, by alternately dipping a surface into a solution of a positively- and negatively-charged PEs (Figure I. 15).[309] The assembly is achieved according to the following sequence of steps. First, the surface is immersed in a solution of positively-charged PE, *i.e.*, a polycation. Second, the surface is rinsed in ultrapure water to remove excess and non-adsorbed polycation chains. Third, the surface is immersed in a solution of negatively-charged PE, *i.e.*, a polyanion, which adsorbs on the now positively-charged surface. Finally, the surface is rinsed again in ultrapure water. By repeating this sequence, a polyelectrolyte multilayer (PEM), whose thickness can be precisely controlled by the number of adsorption steps, can be obtained.[310] Therefore, the immobilization is not limited to one monolayer as it is the case

if proteins are immobilized by spontaneous adsorption or covalent binding. This self-assembled multilayered structure can only be obtained because of the alternated adsorption pathway. If the same compounds were mixed and simultaneous adsorbed on the surface, the film obtained would be different in terms of composition and morphology. Mauquoy & Dupont-Gillain highlighted this structural difference depending on the pathway used.[311] In this context, out of equilibrium self-assemblies take on its full meaning. The ability to create these multilayered architectures at surfaces is directly related to the assembly technique.

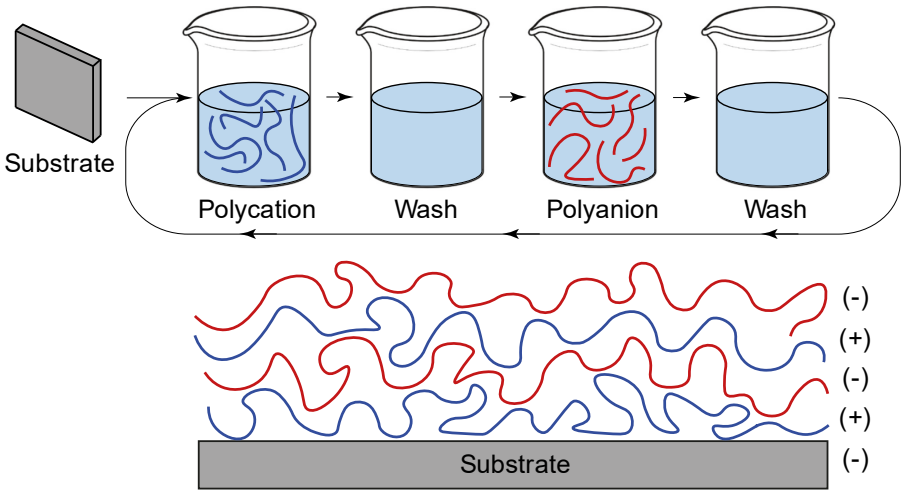

Figure I. 15 – Schematic representation of the different steps of the fabrication of LbL-assembled PEMs. Adapted from Decher *et al.*[310]

9.2 Layer-by-layer films: linear *vs.* exponential growth

Both strong and weak PEs can be used for the construction of PEMs by LbL assembly. The PEMs growth can be linear or exponential. Linear growth is noticed when a constant amount of PE molecules is immobilized at each adsorption step whatever the number of adsorption cycles. The adsorbed PEs interact exclusively with the outermost surface layer of the film.[312] In contrary, exponential growth is observed when a higher amount of PE is adsorbed at each new adsorption step. This exponential growth was first observed by Elbert *et al.*,[313] and may be explained by the diffusion of at least one of the PE within the growing film during each deposition step, which acts as a reservoir. Let us assume that a polycation is mobile into the film: it can

diffuse throughout the multilayer after each new polycation adsorption step. Then, when the surface is in contact with the polyanion solution, the polycation diffuses towards the surface of the film. Since the polycation reaches the outer layer of the multilayer, it interacts with the incoming polyanion, forming a new layer of polycation-polyanion complexes. Hence, the amount of this new layer is proportional to the amount of polycation that diffuses out of the film during the buildup step. Thus, this regime not only involves a superposition of the two species, but also an 'in and out' diffusion process.[314,315] Following several deposition steps, films that initially exhibited exponential growth may shift to a linear growth phase.[316,317] This shift may result from a reorganization within the film, which progressively restricts PEs diffusion throughout the entire film, limiting the film thickness and leading to linear growth. The growth regime of LbL films is related to the interaction strength between the two PEs. In linearly growing films, the assembly process is driven by both enthalpic and entropic contributions to PEs complexation. In contrast, for exponentially growing films, the complexation is entirely entropically driven.[318]

9.3 Layer-by-layer assembly: a widespread technique

The electrostatic interactions, and thus charge reversal, are often believed to drive the LbL assembly. However, the driving force is more a gain of entropy than the enthalpy of such interactions, which is due to the release of counterions during the assembly, involving also other forces such as hydrophobic interactions and hydrogen bonding.[314,315,319] This is highligted by the fact that charge reversal is not observed for each kind of LbL assembly,[314] and that molecules with a low charge density can be assembled by LbL strategy.[315]

One of the major advantages of the LbL technique is its ability to be achieved under soft conditions, *i.e.*, in aqueous solutions and at room temperature, and its versatility toward surface geometry and chemical nature.[315] LbL is also versatile in terms of deposition method as it can be performed by dipping, spin coating or spraying.[320] However, in terms of functionality, it is directly related to the selected adsorbed compounds, and thus to their chemical functions and properties. Therefore, over the past decades, the LbL method has been extended to a wide range of charged materials[310] such as clay

minerals,[321,322] viruses,[323] dendrimers,[324,325] gold colloids,[326] silica particles,[327] DNA,[328] and proteins.[311,329]

9.4 Layer-by-layer assembly of proteins

Proteins were among the first building blocks to be assembled using the LbL method. Within the three years of Decher *et al*.'s pioneering paper on the LbL assembly of PEs, seven distinct globular proteins were successfully immobilized through alternate adsorption with PEs on surfaces.[330,331] Since proteins are charged molecules and soluble in water, the basic principles of the LbL assembly of PEs can be applied, and thus proteins can be immobilized with PEs based on the charge overcompensation concept. However, this immobilization is not straightforward since proteins are polyampholyte molecules with various degrees of charge anisotropy and a low conformational entropy. Moreover, they are "weak PE" since their net charge is related to the pH of the solution. Finally, the isoelectric point (IEP) of some proteins is difficult to predict. Indeed, IEP is determined by factors such as the protein's structure, the nature of surrounding ions, and the experimental conditions. Therefore, depending on the protein, PE, pH, and ionic strength (I) used for assembly, the multilayer may fail to grow. This difficulty to assemble proteins using the LbL method is consistent with the loss of impetus in the number of new proteins immobilized using the LbL approach between 1990 and 2017.[332] Nevertheless, despite the acknowledged challenges, there has been relatively little emphasis on these issues in research studies. The polyampholyte nature of proteins and their complex three-dimensional structure could lead to a lack of charge overcompensation upon the LbL assembly. Even if they successfully assembled type-I Col with hyaluronic acid (HA), Zhang *et al*. showed that the surface charge of the film, and thus the charge overcompensation, decreased upon the multilayer growth, until an equilibrium was reached (Figure I. 16a).[333] Mauquoy & Dupont-Gillain tried to assemble two ECM proteins, namely type-I Col and Fn, using the LbL approach. Three different conditions were tested, and the hydrated mass (expressed as a frequency shift) was measured as a function of the adsorption step. The three systems led to the failure of growing a LbL assembly (Figure I. 16b).[311] Interestingly, the lack of charge overcompensation by the protein layer, *i.e.*, the repulsion between

the PE that is further adsorbed and the protein patches of the same charge, is believed to be the major cause for this failure.[334]

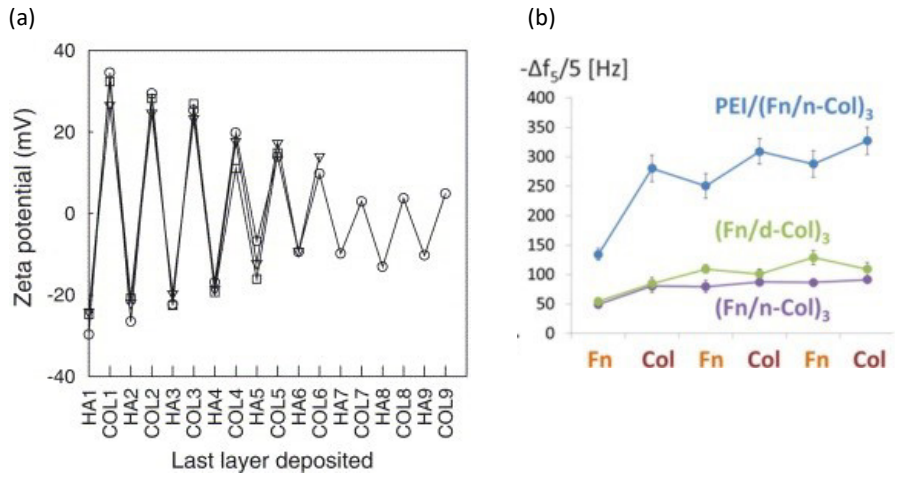

Figure I. 16 – (a) Evolution of the zeta potential for three independent PEI/(HA/COL)$_n$ multilayer films during their construction. Reproduced from Zhang *et al.*[333] (b) Evolution of the hydrated mass (expressed as a frequency shift) of a LbL assembly made of native type-I collagen (n-Col) with Fn (purple), denaturated type-I collagen (d-Col) with Fn (green), and n-Col with Fn on a polyethyleneimine (PEI) anchoring layer (blue). Reproduced from Mauquoy & Dupont-Gillain.[311]

Despite these difficulties, the LbL assembly of proteins has already been reported. vander Straeten *et al*. reviewed the literature related to the LbL assembly of proteins.[254,332]. The successful LbL assembly of 25 different proteins from 91 different systems was highlighted.[254,332] Interestingly, most of the time, proteins were assembled with strong and/or synthetic PEs.[332] The assembly of these multilayers containing a polypeptide usually followed an exponential growth.[314] Importantly, the parameters governing the LbL assembly are both intrinsic, such as the nature of the PE, the protein, and the substrate, and extrinsic, including the pH of the solution, the I and thus the presence of salts in the solution, the temperature, the concentration, and the adsorption time. By tuning these parameters, films with desired properties can be obtained. In their review, vander Straeten *et al.* explained in detail the importance and the impact of all these parameters on the LbL assemblies.[332]

Basically, a wide variety of proteins exists in terms of structure, size, charge density, charge anisotropy. Therefore, the conditions required for the LbL assembly of one protein may vary significantly from those of another. To point out this wide variety of proteins, vander Straeten *et al.* illustrated, at scale, some of the proteins mostly used in LbL assemblies (Figure I. 17).[332] Given the important role of charges in LbL assembly, protein surface was colored in red (negative residues) and in blue (positive residues). This electrostatic coloring highlights the polyampholyte nature of all proteins. Figure I. 17 also depicts the diversity of proteins' size. For comparison, a PE with an aliphatic carbon chain and a polymerization degree of 340 is represented at scale. These molecular illustrations distinctly illustrate the remarkable heterogeneity and ordered structure of proteins in contrast to PEs, which exacerbate the complexity of their surface immobilization.

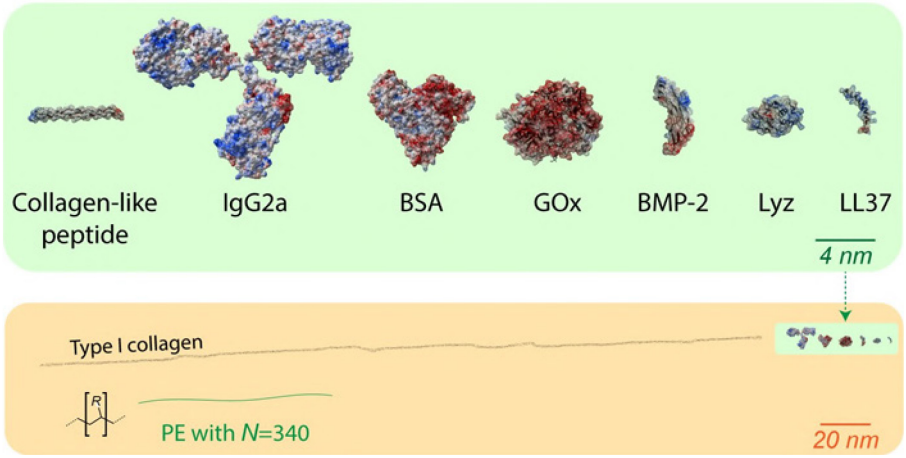

Figure I. 17 – Molecular structure of type I collagen (PDB: 3HQV), collagen-like peptide (PDB: 1CGD), IgG2a (PDB: 1IGT), BSA (PDB: 4F5S), GOx (PDB: 1GAL), BMP-2 (PDB: 3BMP), Lyz (PDB:1HEL) and LL-37 (PDB: 2K6O). The electrostatic surface was calculated using the UCSF Chimera software.[335] The protein surface is colored in red for the negative residues and in blue for the positive residues. Reproduced from vander Straeten *et al*.[332]

Protein-based LbL multilayers are used in various biomedical applications such as antibacterial films, hemocompatible films, drug delivery, bone regeneration and neural interfaces.[336] Since this work focuses on antibacterial applications, our investigation lies in the antibacterial

properties that can be achieved through the construction of multilayered systems using the LbL assembly method, using proteins as key components.

Yuan *et al*. assembled Lyz with Col on silk fibroin and nylon-6 electrospun nanofibrous mats using the LbL approach.[337] They showed that especially surfaces functionalized with multilayers of 10 and 10.5 bilayers of [Lyz-Col] displayed excellent antibacterial activity against *S. aureus* and *E. coli* (over 98% and 87% reduction in viable count, respectively) independently of the ending layer.[337] Ivanova *et al*. coated silicone urinary catheters using a LbL deposition method with acylase (acy) and α-amylase (amy) enzymes, which target and degrade bacterial quorum-sensing molecules and polysaccharides, respectively.[338] These two negatively-charged enzymes were assembled using positively-charged branched polyethyleneimine. Multilayer coatings containing either acylase or amylase alone effectively reduced biofilm formation by Gram-negative *P. aeruginosa* and Gram-positive *S. aureus*. Figure I. 18A shows that multilayers integrating amylase inhibit biofilm formation of single species *S. aureus* and *P. aeruginosa* by 57% and 30%, respectively, and of mixed species by 40%. The multilayers immobilizing acylase inhibit biofilm formation of single species *P. aeruginosa* by 30% without affecting *S. aureus*, and of mixed species by 46%. These results are confirmed by fluorescence analysis that are depicted in Figure I. 18B, C and D. The incorporation of both enzymes into hybrid nanocoatings led to enhanced mixed species biofilm inhibition as a function of acylase or amylase position in the layers. Hybrid coatings with acylase as the outermost layer, which degrades quorum-sensing signals, showed at least a 20% greater antibiofilm effectiveness compared to other configurations. This is evident in Figure I. 18D, which illustrates a reduction in biofilm formation (less green fluorescence) when amylase is adsorbed in the outermost layer. These nanocoatings also significantly decreased the formation of both single-species (*P. aeruginosa*) and mixed-species (*P. aeruginosa* and *E. coli*) biofilms on silicone catheters, under dynamic conditions. Additionally, in an *in vivo* animal model, the combination of quorum-quenching and matrix-degrading enzyme assemblies delayed biofilm growth by up to 7 days. [338]

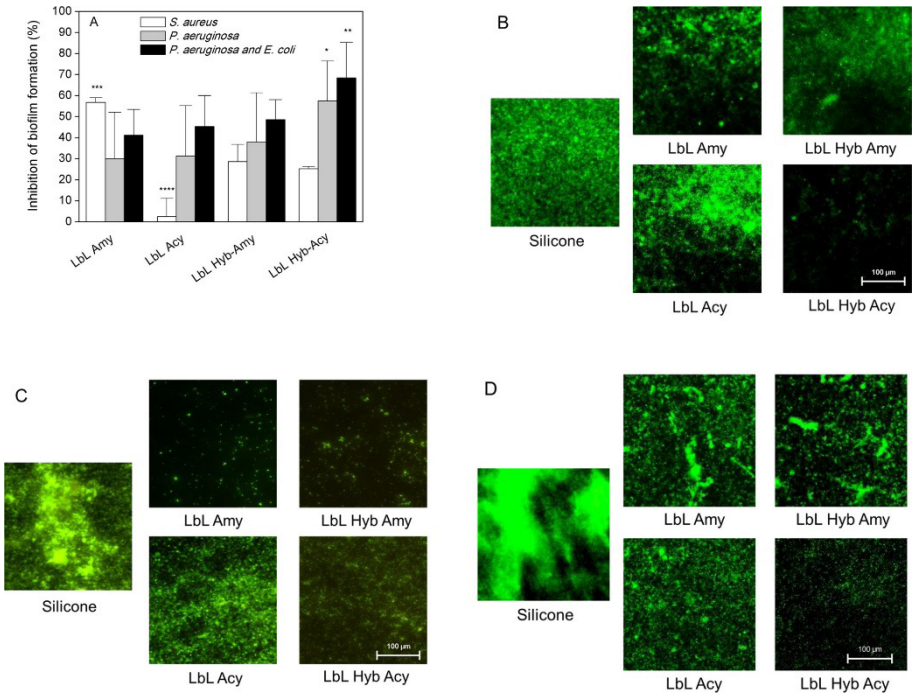

Figure I. 18 – (A) Inhibition (%) of single-species (*P. aeruginosa* and *S. aureus*) and dual-species (*P. aeruginosa* and *E. coli*) biofilm formation on enzyme-coated silicone catheters. Stars represent the statistical differences between the different groups of samples; $p < 0.05$. (B) Fluorescence microscopy images of *P. aeruginosa* biofilms grown for 24h on pristine and enzyme-coated silicone materials analyzed after Live/Dead staining. (C) Fluorescence microscopy images of *S. aureus* biofilms grown for 24h. (D) Fluorescence microscopy images of mixed *P. aeruginosa* and *E. coli* biofilms. The green and red fluorescence images are overlaid in one picture for better comparison of live and dead cells, respectively. Reproduced from Ivanova *et al*.[338]

With the goal to sustain and control the release of drugs, the LbL approach provides enormous potential and serves as a significantly improved alternative to traditional drug encapsulation methods.[339] LbL films can be used as drug reservoir for their sustained release at a specific location and at a controlled concentration.[336] This approach is relevant for preventing bacterial adhesion and growth during the critical post-implantation period, ranging from 6-12 hours to several days. Studies have shown that this timeframe is essential for the bio(integration) of the biomaterial.[340] LbL films for antimicrobial agent release were commonly designed through either (i)

degradation or dissolution of the LbL film or (ii) diffusion of agents from the film layers. To address solubility limitations, Col-based LbL films were generally assembled at an acidic pH, leading to their partial or complete dissolution at physiological pH due to changes in the overall charge. This property was used by Shi *et al*. who grafted chemically the Tet213 AMP on type-IV Col and assembled into LbL film with hyaluronic acid.[341] The antibacterial effect of the LbL films was associated to the controlled release of the peptide in a physiological medium as the LbL structure degraded. Following 24h of contact with 10 layers of Col-peptide/hyaluronic acid, inhibition rates of *Porphyromonas gingivalis* (58.5%) and *S. aureus* (56.4%) proliferation were achieved, along with a significant reduction in early biofilm formation.[341] Vaterrodt *et al*. incorporated cellobiose dehydrogenase into a zwitterionic polycation/poly(styrene sulfonate) (PSS) LbL system.[342] In the presence of cellobiose, this enzyme produced H_2O_2, achieving an antibiofilm effect by reducing *S. aureus* biofilm formation by 53% compared to an uncoated poly(dimethylsiloxane) catheter.[342]

9.4.1 Mechanism of layer-by-layer assembly of proteins with polyelectrolytes

The assembly process of proteins with PEs is governed by both extrinsic parameters, *i.e.* that are not specific to the desired multilayer (pH, nature and concentration of salts, temperature, concentration of protein and PE), and intrinsic parameters, *i.e.* that defines the multilayer (nature and characteristics of PE, nature and concentration of protein, effect of solid substrate). The impact of the pH, presence of salts in solution, and the nature of the PE and the protein will be discussed hereunder and were explained in detail by vander Straeten *et al*.[332]

9.4.1.1 pH of the solution

The pH was identified as a key parameter in the very first study reporting the LbL assembly of proteins with PEs. It was shown that the protein solution's pH must be set away from the IEP to ensure adequate protein charging, thereby promoting favorable interactions with PE. [331] The protein surface charge depicted in Figure I. 17 represents the situation at physiological pH. Yet, it is well known that depending on the pH, the protein net surface charge

varies. This is determined by the charge of the amino acid residues that constitute the protein. By definition, at IEP, the net charge of the protein is equal to zero. Therefore, if the pH of the solution is adjusted lower than protein IEP, the protein will take a net positive charge. In this condition, the protein must be LbL assembled with a polyanion. If the pH of the solution is set above the protein IEP, the opposite stands and the protein must be LbL assembled with a polycation. This fundamental principle is illustrated in Figure I. 19 for LL-37 that displays a theoretical IEP of 11.[343] The LL-37 surface charge was computed as a function of pH using its three-dimensional structure (PDB structure of LL-37: 2K6O) and the PDB2PQR software.[343] It shows that as the pH of the protein solution moves away from its IEP, the net charge of the protein increases. This is also depicted in Figure I. 19 through molecular graphics of LL-37 at different pH values. The electrostatic surface potential was calculated using the APBS-PDB2PQR software and the molecular graphics were viewed in 3Dmol. The negative potential, *i.e.*, negative charge on the LL-37 backbone, is colored in red, and the positive potential, *i.e.*, positive charge on the LL-37 backbone, in blue. Importantly, around the IEP of LL-37, it is noteworthy that there is a small net charge, even though both positive and negative charges are present. Since the electrostatic interactions matter in the LbL assembly, vander Straeten *et al.* put the emphasis on the pH of the protein solution that is used for the construction, which must be chosen a few units above or below the IEP.[332]

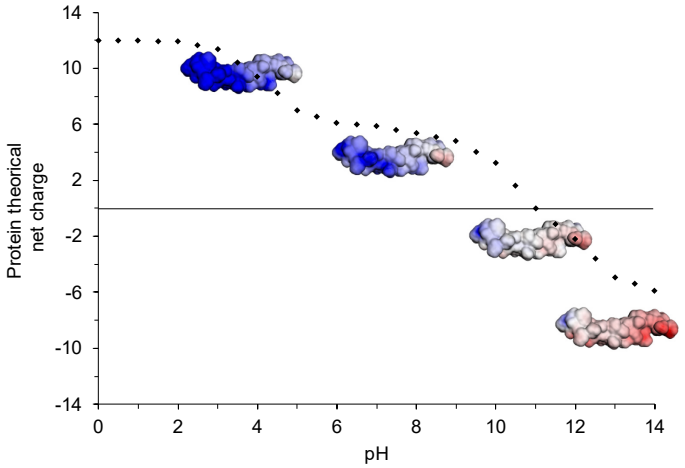

Figure I. 19 – The LL-37 charge, as a function of the pH, was computed from the PDB2PQR online tool, using the 2K6O PDB structure.[343] The electrostatic surface potential of LL-37 was calculated using the APBS-PDB2PQR software and the molecular graphics were viewed in 3Dmol. LL-37 is colored in red for the negative potential and in blue for the positive potential. It only represents the LL-37 surface charge variation with pH and does not take into account the change in the LL-37 structure.

Due to the significant variation in protein charge with pH (Figure I. 19), it has been demonstrated that the higher the protein net charge, the better the LbL assembly. This improvement is attributed to more favorable electrostatic interactions during the assembly process.[332,344] Similarly, it has been demonstrated that |pH − IEP| correlates with the amount of protein adsorbed onto an oppositely-charged multilayer.[345] When a weak PE is used, the ionization balance between the protein and the PE dictates the LbL assembly process. For instance, it has been shown that the amount of lysozyme (Lyz) immobilized in assemblies with poly(methacrylic acid) (PMAA), a weak polyacid, is strongly influenced by the degree of PMAA ionization.[346] When PMAA is highly ionized, bearing more negative charges, soluble Lyz/PMAA complexes form, leading to the removal of Lyz from the multilayer. As a result, LbL film growth fails.

The pH for multilayer construction must also be carefully chosen based on the specific requirements of the intended application. Indeed, any change in condition can destabilize the formed film, especially if the charge of the protein or PE decreases. Most proteins have an IEP that is close to

physiological pH.[332] This suggests that higher or lower pH values should be selected for LbL assembly to maximize |pH − IEP| and increase protein adsorption. However, the pH for most applications typically falls between 5 and 8.[332] This means that after multilayer assembly at a pH far from the IEP, placing the multilayer into application-specific conditions leads to a decrease in the net charge of the protein. This may result in the disruption of the multilayer. In the case of a drug release application, this destabilization can be sought. However, if film stability is necessary, two potential approaches can be considered. First, it could be interesting to construct the multilayer at the pH of the application. While this may lead to a lower amount of protein being immobilized, it could enhance stability, as the pH would remain unchanged when exposed to the medium. Second, several studies have investigated crosslinking strategies to stabilize LbL multilayers in response to changes in pH. Brynda *et al*. demonstrated that IgG could be assembled with dextran sulfate at pH 4; however, an ELISA assay conducted at pH 7.4 led to the disruption of the multilayer.[347] To address this, the LbL film was crosslinked with glutaraldehyde after multilayer construction.[347] It is important to highlight that while crosslinking enhances stability, it may negatively impact protein functionality by reacting with the amine groups of the protein.

9.4.1.2 Presence of salts in solution

Similar to the influence of pH, the presence of salts in solution plays a crucial role in multilayer growth. Ions in solution with proteins and PEs affect interactions at two distinct length scales: at short distances through ion pairing and at longer distances through Debye screening. At short distances, it has been observed that ions accumulate around the charged sites of proteins and PE. These condensed ions, known as counterions, are released when the protein and PE form a complex. This release leads to an entropy gain, which promotes the cooperative formation of ionic pairs between the protein and the PE. At longer distances (on the molecular scale), the electrostatic screening of charges is crucial for LbL assembly.[348,349] This screening can be assessed by computing the Debye length (λ_D) and the Bjerrum length (λ_B). λ_D represents the distance over which electrostatic interactions are significant. λ_B represents the distance at which the electrostatic interaction between two charges is equal in magnitude to the

thermal energy scale. When λ_D reaches values below λ_B, the electrostatic contribution to LbL growth is regarded as negligible.[332]

Salt concentration also affects the conformation of PEs, which is a critical factor in LbL assembly. As depicted by vander Straeten *et al*., as the salt concentration increases (*i.e.*, λ_D decreases) the electrostatic repulsion between charged monomers diminishes, resulting in greater flexibility of the PEs and leading it to adopt a less extended, more coiled conformation in solution.[332] As a result, polymer loops are formed upon adsorption onto the surface at intermediate salt concentrations. Caruso *et al*. demonstrated that higher amounts of both PSS and anti-IgG were deposited as the concentration of $MnCl_2$ increased.[350] This observation was attributed to the more coiled conformation of PSS that becomes more pronounced at higher salt concentrations. It was suggested that this coiled conformation increases the surface area available for anti-IgG adsorption.[350]

The increase in protein quantity with the increase in salt concentration has also been attributed to the reduced lateral repulsion between adsorbed proteins. As the salt concentration decreases, λ_D increases, leading to greater repulsion between charged proteins. This results in a lower protein density in each layer of a LbL film at low salt concentration.[351]

In contrast to the behavior observed when increasing the salt concentration from low to medium levels, excessive charge screening at high salt concentrations prevents the formation of a film through alternating adsorption. For example, the alternating adsorption of type 1-Col with hyaluronic acid did not result in any LbL growth at high salt concentrations.[333] Additionally, recent findings suggest that the failure to achieve LbL assembly in concentrated salt solutions is related to a decreased strength of the entropic contribution to ion pairing.[352]

Therefore, when the salt concentration increases from low to medium levels, the PEs exhibit greater flexibility and lateral repulsion between proteins is screened. This leads to an increased incorporation of protein into the LbL film as the salt concentration rises. However, when the salt concentration increases from medium to high values, the electrostatic attraction weakens, making LbL growth no longer possible.[332]

As it is the case for the pH, it is customary to design multilayers under salt concentration conditions that vary from those of their application. Typically,

when the salt concentration exceeds a certain threshold, the electrostatic screening of charges disrupts the LbL multilayer, which is interesting in case of drug release applications. However, the stability of multilayers in salt solutions can be enhanced by the formation of hydrogen bonds within the multilayer. This can be achieved by adjusting the pH and protonating the PEs. For example, a multilayer made of poly(acrylic acid) and Lyz was found to be unstable when the salt concentration was increased to physiological levels at neutral pH. In contrast, the multilayer exhibited stability when the salt concentration was increased at pH 5. This observation was attributed to the lower ionization degree of poly(acrylic acid) at lower pH which enables hydrogen bond formation that stabilizes the multilayer.[346]

9.4.1.3 Nature of PE and protein

When PEs are assembled with proteins using the LbL technique, PEs can adopt an extended or a 'loop and tail' conformation, depending on salt concentration, pH and nature of the PE (strong or weak PE). For both strong and weak PEs, by increasing the salt concentration, *i.e.* by decreasing λ_D, the electrostatic repulsions between monomers are decreased and thereby the PE flexibility is increased. For weak PEs, their ionization degree can be tuned by varying the pH of the solution. When the PE is fully ionized, the repulsion between its monomers leads to increased stiffness of the PE.

Therefore, the nature of the charged group of the PEs plays a crucial role in the LbL assembly. At the molecular scale, the interaction between oppositely-charged PEs is driven by the cooperative formation of ionic pairs.[353] The free energy of this association, *i.e.* of complexation, is generally attributed to an entropic gain from the release of counterions with a lesser contribution from the enthalpy change due to water perturbation.[348] The interaction between the polyanion and polycation can thus vary depending on the nature of the charged groups and the counterions involved.[332] It has been demonstrated that in solution, the PE-PE free energy of complexation follows the Hofmeister series.[332]

The capacity of PEs to establish hydrogen bonds with proteins is also essential for successful LbL assembly. Lee *et al*. demonstrated that thicker multilayers are obtained when the PE forms hydrogen bonds with the protein.[354] Finally, the hydrophobicity of the PEs is also a crucial factor in the

LbL assembly. Hydrophobic interactions seem to be involved in the build-up process. Therefore, the protein-PE interactions arise from an interplay of interactions involving van der Waals forces, dipolar or hydrogen bonds, electrostatic forces and hydrophobic effects.[332,355]

Finally, the effect of the protein nature on LbL assembly is highly case-specific, given the vast diversity of protein structures. While certain factors, such as geometric features, unfolding tendency upon adsorption (soft vs. hard proteins), and charge distribution, can aid in predicting their behavior in LbL assembly, the lack of consistent reporting on unsuccessful LbL assembly makes it difficult to establish general principles.[332] In their review paper, vander Straeten *et al*. tentatively reported all proteins that have been successfully assembled using the LbL approach.[332]

9.5 Layer-by-layer assembly of antimicrobial peptides

With the goal to prevent medical implant-related infections, many researchers studied strategies to immobilize AMPs on surface. Nicolas *et al.* recently reviewed the commonly used strategies.[356] Although several techniques exist, as explained in section *Part I – 8. Immobilization of proteins at interfaces*, we will focus on studies that aimed at immobilizing AMPs using the LbL approach.[357]

Shukla *et al.* LbL-incorporated ponericin G1 into a hydrolytically-degradable PEM film.[358] This LbL structure was assembled by alternate adsorption of a tetralayer repeat architecture denoted as [poly(β-amino ester)/polyanion/ ponericin G1/polyanion]$_n$. Several film architectures have been studied to obtain various drug loadings that ranged from 20 to 150 µg cm^{-2} and released ponericin G1 for up to ten days. They highlighted that the AMP released from the film retained its full activity against *S. aureus* and effectively prevented bacterial attachment.[358] Cado *et al.* covalently coupled cateslytin to hyaluronic acid, which was subsequently LbL-assembled with Chi.[359] For each pathogen tested, they noticed that an increase in the number of [hyaluronic acid-cateslytin/Chi] bilayers led to a decrease in microbial growth. After 24h of incubation, the growth of *M. luteus*, *C. albicans* and *S. aureus* was fully inhibited with 5, 15 and 30 [hyaluronic acid-cateslytin/Chi] bilayers, respectively.[359] Other AMPs immobilized using the LbL method, such as

defensin,[360] β-peptide,[361] parasin I,[362] or nisin Z[363] were also shown to inhibit the growth of pathogens.

AMPs have been immobilized not only in release-based antibacterial LbL films but also for stable immobilization in LbL assemblies for contact killing purpose. Faure *et al.* covalently bound nisin in a LbL system made of a synthetic oxidized poly(3,4-dihydroxyphenylalanine) and poly(allylamine hydrochloride) (PAH).[364] This LbL coating exhibited durable and encouraging antibacterial efficacy against *Bacillus subtilis* through contact killing.[364]

To the best of our knowledge, we are the first to use the LbL technique for the surface immobilization of LL-37, with the goal to develop antimicrobial coating.[365] Cassin *et al*. physisorbed and chemically immobilized LL-37 on cross-linked Col/hyaluronic acid PEMs and studied the contact-killing properties toward *E. coli* and the LL-37 release profile, but they did not directly self-assemble LL-37 into the multilayers.[297] Using these methods, they showed that concentration of the immobilized peptide played an important role in increasing the contact-killing efficiency, reaching 85-90% against *E. coli* after 24 h of contact with the highest concentrations. The action of contact-killing LbL films is efficient with time but limited to the vicinity of the functionalized surface.

9.6 Protein-polyelectrolyte complexes

As already discussed, due to their polyampholyte nature, the LbL assembly of proteins can be challenging.29 To overcome this issue, alternative LbL assemblies were developed. In 1997, Ariga *et al.* established that LbL assembly of proteins is enhanced when they are pre-mixed with linear polyions.[366] In 2001, Jin *et al.* found that the LbL formation of catalase microcrystals coated with PSS and assembled with PAH resulted in films with a better preserved enzymatic activity and a mass that was at least one order of magnitude higher than the ones obtained with uncoated catalase crystals and solubilized catalase (Figure I. 20).[367] They suggested that the complexation of the enzyme crystals by the PSS brings a higher negative charge density, which enables a better LbL assembly. In other words, when the LbL assembly relies on PE-PE interactions rather than on protein-PE interactions, the multilayer growth is improved.[367] However, this method requires protein crystals which limits its wide use.

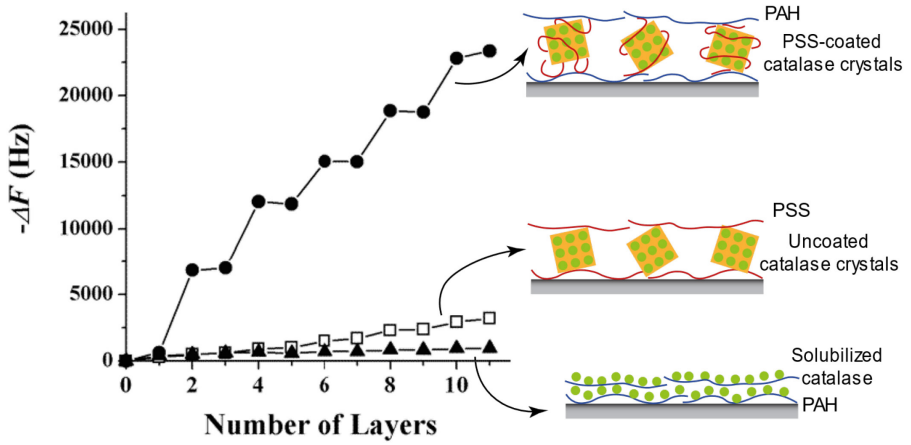

Figure I. 20 – Quartz crystal microbalance frequency shifts as a function of number of layers for the assembly of solubilized catalase with PAH (triangles), uncoated catalase crystals with PSS (squares) and PSS-coated catalase crystals with PAH (circles). Adapted from Jin e*t al*.[367] and vander Straeten *et al*.[332]

With a view to further facilitate the use of the LbL approach for protein immobilization, PPCs were introduced.[368,369] Their formation relies on the principle that when two oppositely-charged species are mixed together, they spontaneously self-assemble. The formation of polyelectrolyte complexes (PECs) based on the self-assembly of two oppositely-charged PEs is a well-known process, which is largely studied in different fields of research. Since proteins are also charged biomolecules, they can also form complexes upon mixing with an oppositely-charged PE, leading to the formation of a so-called PPC. The principle by which the PPC is formed is depicted in Figure I. 21. Protein complexation is very interesting since it has been demonstrated that the PE corona of the PPC standardizes the charge of the protein molecules. It results in a LbL growth that is independent of the protein surface charge.[344]

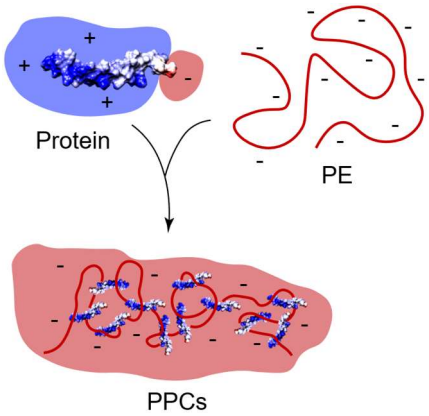

Figure I. 21 – Schematic representation of PPCs formation. The polyampholyte protein is colored in red for the negative potential and in blue for the positive potential. The PE is homogeneously negatively charged. The molecular structure and the surface potential were produced using the UCSF Chimera package.[335]

The earliest documented research papers on PPCs date from the years 1952 to 1955.[370,371] Interestingly, at that time, the most important parameters governing PPCs formation were already identified, namely the PE nature, pH, I, PE-to-protein ratio and PE molar mass. Remarkably, afterwards, interest for PPCs exhibited a decline. It was during the 1990's,[372] and particularly in the 2000's, that PPCs came back into the spotlight, notably with the publication of two review papers by Dubin *et al*.[373,374]

The forces that drive the complexation of two oppositely-charged macromolecules, such as protein-PE, in solution are similar to the ones driving LbL assembly.[375] The details of PE-protein interactions are difficult to ascribe to a particular mechanism, even if the formation of PPCs has been demonstrated to primarily arise from electrostatic interactions.[374] However, these coulombic interactions by themselves fail to fully explain the formation process of PPCs. De Luca *et al*. studied the complexation between the polymer poly(ethylene glycol) methyl ether acrylate-*b*-poly(carboxyethyl acrylate (PEGMEA-*b*-PCEA) and Lyz and found that, at physiological pH, the binding process is driven by electrostatic interactions between oppositely-charged groups of the PE and Lyz.[376] However, they demonstrated that when the pH decreased, the coulombic interactions alone become insufficient to fully explain the observed experimental data.[376] To explain the PPCs stability at low pH, they pointed out the importance of other interactions beyond

electrostatics, such as hydrogen bonding, van der Waals interactions, and water-water interactions.[376] This is also explained in a recent study, conducted by Xu *et al.*, wherein it is demonstrated that the predominant driving force behind the complexation of Lyz with dendritic polyglycerol sulfate is the release of counter-ions, excepted below a salt concentration of 25 mM where long range electrostatic interactions are at play.[377] Importantly, these recent studies enabled to elucidate that the PPCs formation is governed by electrostatics, but also by enthalpic and entropic contributions.[348]

As already mentioned, PPCs formation is influenced by several parameters. Among them, both PE and protein concentration, or more specifically the PE-to-protein molar ratio, plays a crucial role in the PPCs structure. Cousin *et al.* showed that a wide range of PPCs architectures can be obtained depending on the amount of PSS added to Lyz, expressed as [-]/[+] charge ratio, where [-] represents the charges from PSS and [+] those from Lyz (Figure I. 22).[378] Therefore, depending on this [-]/[+] charge ratio, PPCs can exist either as particles/solid-like precipitate or as a mixture without any specific structure. Particles with a well-defined surface are obtained when PSS is not in excess, *i.e.*, [-]/[+] < 1, and PPCs formed in these conditions are neutral since the PSS charges compensate those of Lyz.[378] However, when PSS is in excess, *i.e.*, [-]/[+] > 1, the external surface is more fuzzy (Figure I. 22), and thus some parts of chains are dangling out at the surface, similar to a core-corona structure. At those [-]/[+] charge ratios, the core is neutral, whereas the PSS chains provide a negatively-charged corona.[378] Figure I. 22 also shows that with increasing concentrations of Lyz and PSS while maintaining a constant [-]/[+] charge ratio, larger PPCs are obtained. Typically, precipitates are formed at [-]/[+]=1 in low I solution. Interestingly, Karayianni *et al.* showed that above a specific [-]/[+] charge ratio, PPCs, initially in the form of precipitates, can undergo solubilization.[379] Therefore, the protein charge, PE molar mass, PE charge density, pH, I, and PE-to-protein ratio hugely influence the PPCs architecture.

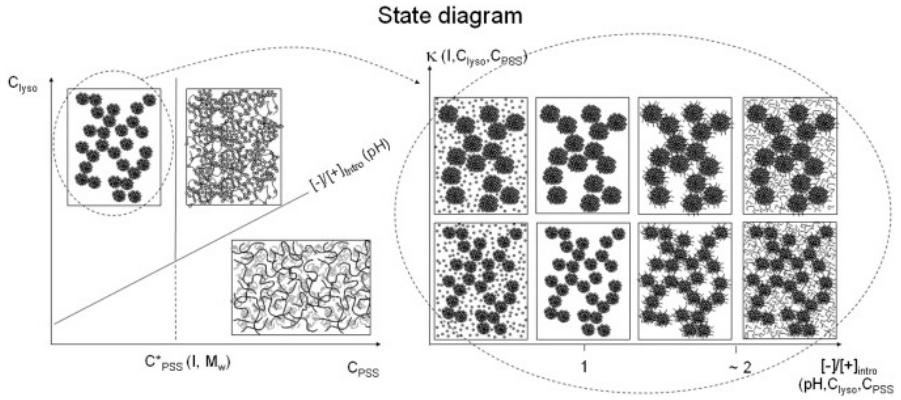

Figure I. 22 – Different structures of PPCs obtained by mixing Lyz with PSS as a function of concentration and other parameters (pH and I) able to tune PPCs formation. Reproduced from Cousin *et al.*[378]

10 References

1. World Health Organization. *Antimicrobial Resistance: Global Report on Surveillance*. (2014).
2. World Health Organization. *Antimicrobial Resistance Surveillance in Europe 2023 - 2021 Data*. (2023).
3. Murray, C. J. *et al.* Global burden of bacterial antimicrobial resistance in 2019: a systematic analysis. *The Lancet* **6736**. (2022).
4. O'Neill, J. Securing new drugs for future generations: The pipeline of antibiotics. *The Review on Antimicrobial Resistance*, London, (2015).
5. O'Neill, J. Tackling drug-resistant infections infections globally: Final report and recommendations. *The Review on Antimicrobial Resistance*, London, (2016).
6. Goff, D. A. *et al.* A global call from five countries to collaborate in antibiotic stewardship: united we succeed, divided we might fail. *Lancet Infect Dis* **17**, e56–e63 (2017).
7. Interagency Coordination Group on Antimicrobial Resistance. *No Time to Wait: Securing the Future from Drug-Resistant Infections*. (2019).
8. Market Research Report. *Medical Implants Market - Growth, Trends, COVID-19 Impact, and Forecasts (2022 - 2027)*. (Mordor Intelligence Pvt Ltd, 2022).
9. Leitner, L. *et al.* Trends and Economic Impact of Hip and Knee Arthroplasty in Central Europe: Findings from the Austrian National Database. *Sci Rep* **8**, 4707 (2018).
10. Ben-Shlomo, Y. *et al.* The National Joint Registry 18th Annual Report 2021. National Joint Registry, London, (2021).
11. OECD. 'Hip and Knee Replacement'*, in Health at a Glance 2023: OECD Indicators*, Paris, (2023).
12. Dale, H. *et al.* Perioperative, short-, and long-term mortality related to fixation in primary total hip arthroplasty: a study on 79,557 patients in the Norwegian Arthroplasty Register. *Acta Orthop* **91**, 152–158 (2020).
13. Best, M. J. *et al.* Incidence and risk factors for perioperative death after revision total hip arthroplasty: a 20-year analysis. *HIP International* **32**, 94–98 (2022).

14. Evans, J. T. *et al.* How long does a hip replacement last? A systematic review and meta-analysis of case series and national registry reports with more than 15 years of follow-up. *Lancet* **393**, 647–654 (2019).
15. Donlan, R. M. & Costerton, J. W. Biofilms: Survival Mechanisms of Clinically Relevant Microorganisms. *Clin Microbiol Rev* **15**, 167–193 (2002).
16. National Institute of Health. Research on Microbial Biofilms. (2002).
17. Hsieh, P. H. *et al.* Gram-negative prosthetic joint infections: risk factors and outcome of treatment. *Clinical Infectious Diseases* **49**, 1036–1043 (2009).
18. Kenney, C., Dick, S., Lea, J., Liu, J. & Ebraheim, N. A. A systematic review of the causes of failure of Revision Total Hip Arthroplasty. *J Orthop* **16**, 393–395 (2019).
19. Edwards, J. R. *et al.* National Healthcare Safety Network (NHSN) report: Data summary for 2006 through 2008, issued December 2009. *Am J Infect Control* **37**, 783–805 (2009).
20. Namba, R. S., Inacio, M. C. S. & Paxton, E. W. Risk factors associated with deep surgical site infections after primary total knee arthroplasty: An analysis of 56,216 knees. *Journal of Bone and Joint Surgery* **95**, 775–782 (2013).
21. Goud, A. L. *et al.* Reinfection rates after one- and two-stage revision surgery for hip and knee arthroplasty: a systematic review and meta-analysis. *Arch Orthop Trauma Surg* **143**, 829–838 (2021).
22. Hartzler, M. A., Li, K., Geary, M. B., Odum, S. M. & Springer, B. D. Complications in the treatment of prosthetic joint infection. *Bone Joint J* **102-B**, 145–150 (2020).
23. Li, K. *et al.* Complications in the treatment of periprosthetic joint infection of the hip: when do they occur? *J Bone Jt Infect* **6**, 295–303 (2021).
24. Tsaras, G. *et al.* Incidence, Secular Trends, and Outcomes of Prosthetic Joint Infection: A Population-Based Study, Olmsted County, Minnesota, 1969–2007. *Infect Control Hosp Epidemiol* **33**, 1207–1212 (2012).
25. Mur, I. *et al.* Do prosthetic joint infections worsen the functional ambulatory outcome of patients with joint replacements? A retrospective matched cohort study. *Antibiotics* **9**, 872 (2020).

26. Lueck, E. *et al.* The psychological burden of a two-stage exchange of infected total hip and knee arthroplasties. *J Health Psychol* **27**, 470–480 (2022).
27. Fischbacher, A. & Borens, O. Prosthetic-joint infections: Mortality over the last 10 years. *J Bone Jt Infect* **4**, 198–202 (2019).
28. Thompson, O., W-Dahl, A. & Stefánsdóttir, A. Increased short- and long-term mortality amongst patients with early periprosthetic knee joint infection. *BMC Musculoskelet Disord* **23**, 1069 (2022).
29. Tande, A. J. & Patel, R. Prosthetic joint infection. *Clin Microbiol Rev* **27**, 302–345 (2014).
30. Khatoon, Z., McTiernan, C. D., Suuronen, E. J., Mah, T. F. & Alarcon, E. I. Bacterial biofilm formation on implantable devices and approaches to its treatment and prevention. *Heliyon* **4**, e01067 (2018).
31. Costerton, J. W., Stewart, P. S. & Greenberg, E. P. Bacterial Biofilms: A Common Cause of Persistent Infections. *Science* **284**, 1318–1322 (1999).
32. Burmølle, M., Ren, D., Bjarnsholt, T. & Sørensen, S. J. Interactions in multispecies biofilms: Do they actually matter? *Trends Microbiol* **22**, 84–91 (2014).
33. Rao, Y., Shang, W., Yang, Y., Zhou, R. & Rao, X. Fighting Mixed-Species Microbial Biofilms With Cold Atmospheric Plasma. *Front Microbiol* **11**, (2020).
34. Arciola, C. R., Campoccia, D. & Montanaro, L. Implant infections: adhesion, biofilm formation and immune evasion. *Nat Rev Microbiol* **16**, 397–409 (2018).
35. de Vor, L., Rooijakkers, S. H. M. & van Strijp, J. A. G. Staphylococci evade the innate immune response by disarming neutrophils and forming biofilms. *FEBS Lett* **594**, 2556–2569 (2020).
36. Ciofu, O. & Tolker-Nielsen, T. Tolerance and Resistance of *Pseudomonas aeruginosa* Biofilms to Antimicrobial Agents-How *P. aeruginosa* Can Escape Antibiotics. *Front Microbiol* **10**, 913 (2019).
37. Ciofu, O., Moser, C., Jensen, P. Ø. & Høiby, N. Tolerance and resistance of microbial biofilms. *Nat Rev Microbiol* **20**, 621–635 (2022).
38. Tsukayama, D. T., Estrada, R. & Gustilo, R. B. Infection after Total Hip Arthroplasty. A Study of the Treatment of One Hundred and Six Infections. *J Bone Joint Surg Am* **78**, 512–523 (1996).

39. Tsukayama, D. T., Goldberg, V. M. & Kyle, R. Diagnosis and management of infection after total knee arthroplasty. *J Bone Joint Surg Am* **85-A (Suppl 1)**, S75–S80 (2003).
40. Parisi, T. J., Konopka, J. F. & Bedair, H. S. What is the Long-term Economic Societal Effect of Periprosthetic Infections After THA? A Markov Analysis. *Clin Orthop Relat Res* **475**, 1891–1900 (2017).
41. Puhto, T., Puhto, A. P., Vielma, M. & Syrjälä, H. Infection triples the cost of a primary joint arthroplasty. *Infect Dis* **51**, 348–355 (2019).
42. *American Joint Replacement Registry (AJRR): 2021 Annual Report. Rosemont, IL: American Academy of Orthopaedic Surgeons (AAOS)*. (2021).
43. Singh, J. A., Yu, S., Chen, L. & Cleveland, J. D. Rates of total joint replacement in the United States: Future projections to 2020-2040 using the national inpatient sample. *Journal of Rheumatology* **46**, 1134–1140 (2019).
44. Shan, L., Shan, B., Suzuki, A., Nouh, F. & Saxena, A. Intermediate and long-term quality of life after total knee replacement: A systematic review and meta-analysis. *Journal of Bone and Joint Surgery - American Volume* **97**, 156–168 (2015).
45. Neuprez, A. *et al.* Total joint replacement improves pain, functional quality of life, and health utilities in patients with late-stage knee and hip osteoarthritis for up to 5 years. *Clin Rheumatol* **39**, 861–871 (2020).
46. Karachalios, T., Komnos, G. & Koutalos, A. Total hip arthroplasty: Survival and modes of failure. *EFORT Open Rev* **3**, 232–239 (2018).
47. Howell, S. M., Shelton, T. J. & Hull, M. L. Implant Survival and Function Ten Years After Kinematically Aligned Total Knee Arthroplasty. *Journal of Arthroplasty* **33**, 3678–3684 (2018).
48. Inui, H., Yamagami, R., Kono, K. & Kawaguchi, K. What are the causes of failure after total knee arthroplasty? *Journal of Joint Surgery and Research* **1**, 32–40 (2023).
49. Mathis, D. T. & Hirschmann, M. T. Why do knees after total knee arthroplasty fail in different parts of the world? *J Orthop* **23**, 52–59 (2021).
50. Orthopride. Belgian Hip and Knee Arthroplasty Registry - Annual Report 2020. *Inami* (2022).

51. Wildeman, P., Rolfson, O., Söderquist, B., Wretenberg, P. & Lindgren, V. What Are the Long-term Outcomes of Mortality, Quality of Life, and Hip Function after Prosthetic Joint Infection of the Hip? A 10-year Follow-up from Sweden. *Clin Orthop Relat Res* **479**, 2203–2213 (2021).
52. Grammatopoulos, G. *et al.* Functional outcome of debridement, antibiotics and implant retention in periprosthetic joint infection involving the hip. *Bone Joint J* **99B**, 614–622 (2017).
53. Zmistowski, B., Karam, J. A., Durinka, J. B., Casper, D. S. & Parvizi, J. Periprosthetic Joint Infection Increases the Risk of One-Year Mortality. *J Bone Joint Surg* **95**, 2177–2184 (2013).
54. Lum, Z. C. *et al.* Mortality During Total Knee Periprosthetic Joint Infection. *J Arthroplasty* **33**, 3783–3788 (2018).
55. Natsuhara, K. M., Shelton, T. J., Meehan, J. P. & Lum, Z. C. Mortality During Total Hip Periprosthetic Joint Infection. *J Arthroplasty* **34**, S337–S342 (2019).
56. Premkumar, A. *et al.* Projected Economic Burden of Periprosthetic Joint Infection of the Hip and Knee in the United States. *J Arthroplasty* **36**, 1484–1489 (2021).
57. DeGouveia, W. *et al.* An Economic Evaluation of Over 200,000 Revision Total Hip Arthroplasties: Is the Current Model Sustainable? *Surg Technol Int* **28**, 367–370 (2020).
58. Serrier, H. *et al.* Economic Study of 2-Stage Exchange in Patients With Knee or Hip Prosthetic Joint Infection Managed in a Referral Center in France: Time to Use Innovative(s) Intervention(s) at the Time of Reimplantation to Reduce the Risk of Superinfection. *Front Med (Lausanne)* **8**, 552669 (2021).
59. Garfield, K. *et al.* What are the inpatient and day case costs following primary total hip replacement of patients treated for prosthetic joint infection: a matched cohort study using linked data from the National Joint Registry and Hospital Episode Statistics. *BMC Med* **18**, (2020).
60. Sousa, A. *et al.* Economic Impact of Prosthetic Joint Infection - An Evaluation Within the Portuguese National Health System. *J Bone Jt Infect* **3**, 197–202 (2018).
61. Kurtz, S. M., Lau, E., Watson, H., Schmier, J. K. & Parvizi, J. Economic Burden of Periprosthetic Joint Infection in the United States. *J Arthroplasty* **27**, 61-65.e1 (2012).

62. Dale, H. *et al.* Increasing risk of prosthetic joint infection after total hip arthroplasty. *Acta Orthop* **83**, 449–458 (2012).
63. Liukkonen, R. J. *et al.* Trends in Revision Hip Arthroplasty for Prosthetic Joint Infection: A Single-Center Study of 423 Hips at a High-Volume Center Between 2008 and 2021. *J Arthroplasty* **38**, 1151–1159 (2023).
64. Wang, F. Der, Wang, Y. P., Chen, C. F. & Chen, H. P. The incidence rate, trend and microbiological aetiology of prosthetic joint infection after total knee arthroplasty: A 13 years' experience from a tertiary medical center in Taiwan. *Journal of Microbiology, Immunology and Infection* **51**, 717–722 (2018).
65. Runner, R. P. *et al.* Prosthetic Joint Infection Trends at a Dedicated Orthopaedics Specialty Hospital. *Adv Orthop* **2019**, 4629503 (2019).
66. Bozzo, A. *et al.* Incidence and Predictors of Prosthetic Joint Infection Following Primary Total Knee Arthroplasty: A 15-Year Population-Based Cohort Study. *J Arthroplasty* **37**, 367-372.e1 (2022).
67. Anneberg, M. *et al.* Enhancing the data capture of periprosthetic joint infections in the Danish Knee Arthroplasty Registry: validity assessment and incidence estimation. *Acta Orthop* **95**, 166–173 (2024).
68. OECD. 'Hip and Knee Replacement'*, in Health at a Glance 2017: OECD Indicators*, Paris, (2017).
69. Patel, A., Pavlou, G., Mújica-Mota, R. E. & Toms, A. D. The epidemiology of revision total knee and hip arthroplasty in England and Wales. *Bone Joint J* **97-B**, 1076–1081 (2015).
70. Ackerman, I. N. *et al.* The projected burden of primary total knee and hip replacement for osteoarthritis in Australia to the year 2030. *BMC Musculoskelet Disord* **20**, 90 (2019).
71. Erivan, R. *et al.* Progression and projection for hip surgery in France, 2008-2070: Epidemiologic study with trend and projection analysis. *Orthopaedics and Traumatology: Surgery and Research* **105**, 1227–1235 (2019).
72. Rupp, M., Lau, E., Kurtz, S. M. & Alt, V. Projections of Primary TKA and THA in Germany From 2016 Through 2040. *Clin Orthop Relat Res* **478**, 1622–1633 (2020).
73. World Health Organization. Osteoarthritis, Fact Sheet. (2023).

74. Kunutsor, S. K., Whitehouse, M. R., Blom, A. W. & Beswick, A. D. Patient-Related Risk Factors for Periprosthetic Joint Infection after Total Joint Arthroplasty: A Systematic Review and Meta-Analysis. *PLoS One* **11**, e0150866 (2016).
75. Cobo, J. & Escudero-Sanchez, R. Suppressive antibiotic treatment in prosthetic joint infections: A perspective. *Antibiotics* **10**, 743 (2021).
76. Osmon, D. R. *et al.* Diagnosis and Management of Prosthetic Joint Infection: Clinical Practice Guidelines by the Infectious Diseases Society of America. *Clinical Infectious Diseases* **56**, e1–e25 (2013).
77. Van der Ende, B. *et al.* Timing of debridement, antibiotics, and implant retention (DAIR) for early post-surgical hip and knee prosthetic joint infection (PJI) does not affect 1-year re-revision rates: data from the Dutch Arthroplasty Register. *J Bone Jt Infect* **6**, 329–336 (2021).
78. Haasper, C. *et al.* Irrigation and Debridement. *Journal of Arthroplasty* **29**, 100–103 (2014).
79. Bernard, L. *et al.* Antibiotic Therapy for 6 or 12 Weeks for Prosthetic Joint Infection. *New England Journal of Medicine* **384**, 1991–2001 (2021).
80. Szymski, D., Walter, N., Hierl, K., Rupp, M. & Alt, V. Direct Hospital Costs per Case of Periprosthetic Hip and Knee Joint Infections in Europe — A Systematic Review. *Journal of Arthroplasty* **39**, 1876–1881 (2024).
81. Urish, K. L. *et al.* A Multicenter Study of Irrigation and Debridement in Total Knee Arthroplasty Periprosthetic Joint Infection: Treatment Failure Is High. *Journal of Arthroplasty* **33**, 1154–1159 (2018).
82. Tornero, E. *et al.* KLIC-score for predicting early failure in prosthetic joint infections treated with debridement, implant retention and antibiotics. *Clinical Microbiology and Infection* **21**, 786.e9-786.e17 (2015).
83. Wouthuyzen-Bakker, M. *et al.* Timing of implant-removal in late acute periprosthetic joint infection: A multicenter observational study. *Journal of Infection* **79**, 199–205 (2019).
84. Morcillo, D. *et al.* Debridement, antibiotics, irrigation and retention in prosthetic joint infection : predictive tools of failure. *Acta Orthop Belg* **86**, 636–643 (2020).
85. Kunutsor, S. K., Beswick, A. D., Whitehouse, M. R., Wylde, V. & Blom, A. W. Debridement, antibiotics and implant retention for

periprosthetic joint infections: A systematic review and meta-analysis of treatment outcomes. *Journal of Infection* **77**, 479–488 (2018).

86. Argenson, J. N. *et al.* Hip and Knee Section, Treatment, Debridement and Retention of Implant: Proceedings of International Consensus on Orthopedic Infections. *Journal of Arthroplasty* **34**, S399–S419 (2019).
87. Zimmerli, W., Trampuz, A. & Ochsner, P. E. Prosthetic-Joint Infections. *N Engl J Med* **351**, 1645–1654 (2004).
88. Shahpari, O. *et al.* The use of antibiotic impregnated cement spacers in the treatment of infected total joint replacement: Challenges and achievements. *Archives of Bone and Joint Surgery* **8**, 11–20 (2020).
89. Sousa, R., Carvalho, A., Soares, D. & Abreu, M. A. Interval between two-stage exchanges: what is optimal and how do you know? *Arthroplasty* **5**, 33 (2023).
90. Winkler, T. *et al.* Outcome of short versus long interval in two-stage exchange for periprosthetic joint infection: a prospective cohort study. *Arch Orthop Trauma Surg* **139**, 295–303 (2019).
91. Thornes, B., Murray, P. & Bouchier-Hayes, D. Development of resistant strains of *Staphylococcus epidermidis* on gentamicin-loaded bone cement *in vivo*. *J Bone Joint Surg Br* **84**, 758–760 (2002).
92. Gomez, M. M., Tan, T. L., Manrique, J., Deirmengian, G. K. & Parvizi, J. The Fate of Spacers in the Treatment of Periprosthetic Joint Infection. *J Bone Joint Surg Am* **97**, 1495–1502 (2015).
93. Lazic, I., Scheele, C., Pohlig, F., von Eisenhart-Rothe, R. & Suren, C. Treatment options in PJI – is two-stage still gold standard? *J Orthop* **23**, 180–184 (2021).
94. Jenny, J. Y., Goukodadja, O., Boeri, C. & Gaudias, J. May one-stage exchange for *Candida albicans* peri-prosthetic infection be successful? *Orthopaedics & Traumatology: Surgery & Research* **102**, 127–129 (2016).
95. Maale, G. E., Eager, J. J., Srinivasaraghavan, A., Kazemi Mohammadi, D. & Kennard, N. The evolution from the two stage to the one stage procedure for biofilm based periprosthetic joint infections (PJI). *Biofilm* **2**, (2020).
96. Akkaya, M. *et al.* What Is the Most Reliable Concordance Rate of Preoperative Synovial Fluid Aspiration and Intraoperative Biopsy to Detect Periprosthetic Joint Infection in Knee, Hip and Shoulder Arthroplasty? *Antibiotics* **12**, 1482 (2023).

97. Steinicke, A. C. *et al.* Repeat two-stage exchange arthroplasty for recurrent periprosthetic hip or knee infection: what are the chances for success? *Arch Orthop Trauma Surg* **143**, 1731–1740 (2023).
98. Vincenten, C. M., Den Oudsten, B. L., Bos, P. K., Bolder, S. B. T. & Gosens, T. Quality of life and health status after Girdlestone resection arthroplasty in patients with an infected total hip prosthesis. *J Bone Jt Infect* **4**, 10–15 (2019).
99. Orfanos, A. V., Michael, R. J., Keeney, B. J. & Moschetti, W. E. Patient-reported outcomes after above-knee amputation for prosthetic joint infection. *Knee* **27**, 1101–1105 (2020).
100. Pradier, M. *et al.* Suppressive antibiotic therapy with oral tetracyclines for prosthetic joint infections: a retrospective study of 78 patients. *Infection* **46**, 39–47 (2018).
101. Miller, R. *et al.* Periprosthetic Joint Infection: A Review of Antibiotic Treatment. *JBJS Rev* **8**, e1900224 (2020).
102. Obst, G., Gagnon, R. F., Prentis, J. & Richards, G. K. Rifampin Activity Against *Staphylococcus epidermidis* Biofilms. *ASAIO Trans* **34**, 782–784 (1988).
103. Goulenok, T. *et al.* Pharmacokinetic interaction between rifampicin and clindamycin in staphylococcal osteoarticular infections. *Int J Antimicrob Agents* **62**, 106885 (2023).
104. Brügger, J., Saner, S. & Nötzli, H. P. A Treatment Pathway Variation for Chronic Prosthesis-Associated Infections. *JBJS Open Access* **5**, e20.00042 (2020).
105. Burnett, R. S. J. *et al.* Prophylactic Antibiotics Do Not Affect Cultures in the Treatment of an Infected TKA: A Prospective Trial. *Clin Orthop Relat Res* **468**, 127–134 (2010).
106. American Academy of Orthopaedic Surgeons. *Evidence-Based Clinical Practice Guideline for Diagnosis and Prevention of Periprosthetic Joint Infections*. (2019).
107. Ventola, C. L. The Antibiotic Resistance Crisis - Part 1: Causes and Threats. *Pharmacy and Therapeutics* **40**, 277–283 (2015).
108. Poilvache, H. *In-vitro* and *in-vivo* study of biofilm disruption strategies for the treatment of prosthetic joint infections. (PhD Thesis, UCLouvain, 2021).
109. World Health Organization. Antimicrobial Resistance, Fact Sheet. (2023).

110. Brauner, A., Fridman, O., Gefen, O. & Balaban, N. Q. Distinguishing between resistance, tolerance and persistence to antibiotic treatment. *Nat Rev Microbiol* **14**, 320–330 (2016).
111. Reygaert, W. C. An overview of the antimicrobial resistance mechanisms of bacteria. *AIMS Microbiol* **4**, 482–501 (2018).
112. Dufour, D., Leung, V. & Lévesque, C. M. Bacterial biofilm: structure, function, and antimicrobial resistance. *Endod Topics* **22**, 2–16 (2012).
113. van Leeuwenhoek, A. IV. An extract of a letter from Mr. Anth. Van Leuwenhoek, concerning animalcules found on the teeth; of the scaleyness of the skin, &c. *Philos Trans R Soc Lond* **17**, 646–649 (1693).
114. Henrici, A. T. Studies of freshwater bacteria: I. A direct microscopic technique. *J Bacteriol* **25**, 277–287 (1933).
115. Zobell, C. E. The influence of solid surface upon the physiological activities of bacteria in seawater. *J Bacteriol* **33**, 86 (1937).
116. Zobell, C. E. The Effect of Solid Surfaces upon Bacterial Activity. *J Bacteriol* **46**, 39–56 (1943).
117. Heukelekian, H. & Heller, A. Relation between food concentration and surface for bacterial growth. *Journal of Bacterio* **40**, 547–558 (1940).
118. Costerton, J. W., Geesey, G. G. & Cheng, K. J. How bacteria stick. *Sci Am* **238**, 86–95 (1978).
119. Marrie, T. J., Nelligan, J. & Costerton, J. W. A scanning and transmission electron microscopic study of an infected endocardial pacemaker lead. *Circulation* **66**, 1339–1341 (1982).
120. Tunney, M. M. *et al.* Improved detection of infection in hip replacements. A currently underestimated problem. *J Bone Joint Surg Br* **80**, 568–572 (1998).
121. Zimmerli, W. & Sendi, P. Orthopaedic biofilm infections. *APMIS* **125**, 353–364 (2017).
122. Karygianni, L., Ren, Z., Koo, H. & Thurnheer, T. Biofilm Matrixome: Extracellular Components in Structured Microbial Communities. *Trends Microbiol* **28**, 668–681 (2020).
123. Bjarnsholt, T. *et al.* The *in vivo* biofilm. *Trends Microbiol* **21**, 466–474 (2013).
124. Rabin, N. *et al.* Biofilm formation mechanisms and targets for developing antibiofilm agents. *Future Med Chem* **7**, 493–512 (2015).

125. Sauer, K., Camper, A. K., Ehrlich, G. D., Costerton, J. W. & Davies, D. G. *Pseudomonas aeruginosa* Displays Multiple Phenotypes during Development as a Biofilm. *J Bacteriol* **184**, 1140–1154 (2002).
126. Heilmann, C., Hussain, M., Peters, G. & Götz, F. Evidence for autolysin-mediated primary attachment of *Staphylococcus epidermidis* to a polystyrene surface. *Mol Microbiol* **24**, 1013–1024 (1997).
127. Alam, F. & Balani, K. Adhesion force of *Staphylococcus aureus* on various biomaterial surfaces. *J Mech Behav Biomed Mater* **65**, 872–880 (2017).
128. Ivanova, E. P. *et al.* Differential attraction and repulsion of *Staphylococcus aureus* and *Pseudomonas aeruginosa* on molecularly smooth titanium films. *Sci Rep* **1**, 165 (2011).
129. Koseki, H. *et al.* Early Staphylococcal Biofilm Formation on Solid Orthopaedic Implant Materials: *In Vitro* Study. *PLoS One* **9**, e107588 (2014).
130. Berne, C., Ducret, A., Hardy, G. G. & Brun, Y. V. Adhesins involved in attachment to abiotic surfaces by Gram- negative bacteria. *Microbiol Spectr* **3**, (2015).
131. Davies, D. G. & Geesey, G. G. Regulation of the alginate biosynthesis gene algC in *Pseudomonas aeruginosa* during biofilm development in continuous culture. *Appl Environ Microbiol* **61**, 860–867 (1995).
132. Klausen, M. *et al.* Biofilm formation by *Pseudomonas aeruginosa* wild type, flagella and type IV pili mutants. *Mol Microbiol* **48**, 1511–1524 (2003).
133. Ranieri, M. R., Whitchurch, C. B. & Burrows, L. L. Mechanisms of biofilm stimulation by subinhibitory concentrations of antimicrobials. *Curr Opin Microbiol* **45**, 164–169 (2018).
134. Hou, J., Veeregowda, D. H., van de Belt-Gritter, B., Busscher, H. J. & van der Mei, H. C. Extracellular Polymeric Matrix Production and Relaxation under Fluid Shear and Mechanical Pressure in *Staphylococcus aureus* Biofilms. *Appl Environ Microbiol* **84**, e01516-17 (2018).
135. Liao, J., Schurr, M. J. & Sauera, K. The merR-like regulator brlR confers biofilm tolerance by activating multidrug efflux pumps in *Pseudomonas aeruginosa* biofilms. *J Bacteriol* **195**, 3352–3363 (2013).

136. Heacock-Kang, Y. *et al.* Spatial transcriptomes within the *Pseudomonas aeruginosa* biofilm architecture. *Mol Microbiol* **106**, 976–985 (2017).
137. Kowalski, C. H., Morelli, K. A., Stajich, J. E., Nadell, C. D. & Cramer, R. A. A heterogeneously expressed gene family modulates the biofilm architecture and hypoxic growth of *Aspergillus fumigatus*. *mBio* **12**, 03579-20 (2021).
138. Thoendel, M., Kavanaugh, J. S., Flack, C. E. & Horswill, A. R. Peptide signaling in the Staphylococci. *Chem Rev* **111**, 117–151 (2011).
139. Moormeier, D. E. & Bayles, K. W. *Staphylococcus aureus* biofilm: a complex developmental organism. *Mol Microbiol* **104**, 365–376 (2017).
140. Bjarnsholt, T. *et al.* The impact of mental models on the treatment and research of chronic infections due to biofilms. *APMIS* **129**, 598–606 (2021).
141. Sauer, K. *et al.* The biofilm life cycle: expanding the conceptual model of biofilm formation. *Nat Rev Microbiol* **20**, 608–620 (2022).
142. Prieto-Barajas, C. M., Valencia-Cantero, E. & Santoyo, G. Microbial mat ecosystems: Structure types, functional diversity, and biotechnological application. *Electronic Journal of Biotechnology* **31**, 48–56 (2018).
143. Jensen, L. K. *et al.* Novel Porcine Model of Implant-Associated Osteomyelitis: A Comprehensive Analysis of Local, Regional, and Systemic Response. *Journal of Orthopaedic Research* **35**, 2211–2221 (2017).
144. Li, C., Renz, N. & Trampuz, A. Management of Periprosthetic Joint Infection. *Hip Pelvis* **30**, 138–146 (2018).
145. Dudareva, M. *et al.* Sonication versus Tissue Sampling for Diagnosis of Prosthetic Joint and Other Orthopedic Device-Related Infections. *J Clin Microbiol* **56**, (2018).
146. Dastgheyb, S. S. *et al.* Staphylococcal Persistence Due to Biofilm Formation in Synovial Fluid Containing Prophylactic Cefazolin. *Antimicrob Agents Chemother* **59**, 2122–2128 (2015).
147. Lebeaux, D., Chauhan, A., Rendueles, O. & Beloin, C. From *in vitro* to *in vivo* Models of Bacterial Biofilm-Related Infections. *Pathogens* **2**, 288–356 (2013).

148. Hancock, V., Witsø, I. L. & Klemm, P. Biofilm formation as a function of adhesin, growth medium, substratum and strain type. *International Journal of Medical Microbiology* **301**, 570–576 (2011).
149. Romero, D. & Kolter, R. Will biofilm disassembly agents make it to market? *Trends Microbiol* **19**, 304–306 (2011).
150. Von Herrath, M. G. & Nepom, G. T. Lost in translation: Barriers to implementing clinical immunotherapeutics for autoimmunity. *Journal of Experimental Medicine* **202**, 1159–1162 (2005).
151. de la Fuente-Núñez, C., Reffuveille, F., Fernández, L. & Hancock, R. E. W. Bacterial biofilm development as a multicellular adaptation: Antibiotic resistance and new therapeutic strategies. *Curr Opin Microbiol* **16**, 580–589 (2013).
152. Lebeaux, D., Ghigo, J.-M. & Beloin, C. Biofilm-Related Infections: Bridging the Gap between Clinical Management and Fundamental Aspects of Recalcitrance toward Antibiotics. *Microbiology and Molecular Biology Reviews* **78**, 510–543 (2014).
153. Hall, C. W. & Mah, T. F. Molecular mechanisms of biofilm-based antibiotic resistance and tolerance in pathogenic bacteria. *FEMS Microbiol Rev* **41**, 276–301 (2017).
154. Khatoon, Z., McTiernan, C. D., Suuronen, E. J., Mah, T. F. & Alarcon, E. I. Bacterial biofilm formation on implantable devices and approaches to its treatment and prevention. *Heliyon* **4**, e01067 (2018).
155. Davies, D. Understanding biofilm resistance to antibacterial agents. *Nat Rev Drug Discov* **2**, 114–122 (2003).
156. Stewart, P. S. Theoretical aspects of antibiotic diffusion into microbial biofilms. *Antimicrob Agents Chemother* **40**, 2517–2522 (1996).
157. Dunne, W. M., Mason, E. O. & Kaplan, S. L. Diffusion of rifampin and vancomycin through a *Staphylococcus epidermidis* biofilm. *Antimicrob Agents Chemother* **37**, 2522–2526 (1993).
158. Anderl, J. N., Franklin, M. J. & Stewart, P. S. Role of Antibiotic Penetration Limitation in Klebsiella pneumoniae Biofilm Resistance to Ampicillin and Ciprofloxacin. *Antimicrob Agents Chemother* **44**, 1818–1824 (2000).
159. Zheng, Z. & Stewart, P. S. Penetration of rifampin through *Staphylococcus epidermidis* biofilms. *Antimicrob Agents Chemother* **46**, 900–903 (2002).

160. Walters III, M. C., Roe, F., Bugnicourt, A., Franklin, M. J. & Stewart, P. S. Contributions of Antibiotic Penetration, Oxygen Limitation, and Low Metabolic Activity to Tolerance of *Pseudomonas aeruginosa* Biofilms to Ciprofloxacin and Tobramycin. *Antimicrob Agents Chemother* **47**, 317–323 (2003).
161. Stewart, P. S., Davison, W. M. & Steenbergen, J. N. Daptomycin rapidly penetrates a *Staphylococcus epidermidis* biofilm. *Antimicrob Agents Chemother* **53**, 3505–3507 (2009).
162. Singh, R., Ray, P., Das, A. & Sharma, M. Penetration of antibiotics through *Staphylococcus aureus* and *Staphylococcus epidermidis* biofilms. *Journal of Antimicrobial Chemotherapy* **65**, 1955–1958 (2010).
163. Singh, R., Sahore, S., Kaur, P., Rani, A. & Ray, P. Penetration barrier contributes to bacterial biofilm-associated resistance against only select antibiotics, and exhibits genus-, strain- and antibiotic-specific differences. *Pathog Dis* **74**, ftw056 (2016).
164. Boudjemaa, R. *et al.* New Insight into Daptomycin Bioavailability and Localization in *Staphylococcus aureus* Biofilms by Dynamic Fluorescence Imaging. *Antimicrob Agents Chemother* **60**, 4983–4990 (2016).
165. Flemming, H. C. *et al.* Biofilms: An emergent form of bacterial life. *Nat Rev Microbiol* **14**, 563–575 (2016).
166. Borriello, G., Richards, L., Ehrlich, G. D. & Stewart, P. S. Arginine or Nitrate Enhances Antibiotic Susceptibility of *Pseudomonas aeruginosa* in Biofilms. *Antimicrob Agents Chemother* **50**, 382–384 (2006).
167. Billings, N. *et al.* The Extracellular Matrix Component Psl Provides Fast-Acting Antibiotic Defense in *Pseudomonas aeruginosa* Biofilms. *PLoS Pathog* **9**, e1003526 (2013).
168. Colvin, K. M. *et al.* The Pel Polysaccharide Can Serve a Structural and Protective Role in the Biofilm Matrix of *Pseudomonas aeruginosa*. *PLoS Pathog* **7**, e1001264 (2011).
169. Kohanski, M. A., Dwyer, D. J., Hayete, B., Lawrence, C. A. & Collins, J. J. A Common Mechanism of Cellular Death Induced by Bactericidal Antibiotics. *Cell* **130**, 797–810 (2007).

170. Foti, J. J., Devadoss, B., Winkler, J., Collins, J. & Walker, G. Oxidation of the Guanine Nucleotide Pool Underlies Cell Death by Bactericidal Antibiotics. *Science* **336**, 315–319 (2012).
171. Dwyer, D. J., Collins, J. J. & Walker, G. C. Unraveling the Physiological Complexities of Antibiotic Lethality. *Annu Rev Pharmacol Toxicol* **55**, 313–332 (2015).
172. Wu, Y., Vulić, M., Keren, I. & Lewis, K. Role of Oxidative Stress in Persister Tolerance. *Antimicrob Agents Chemother* **56**, 4922–4926 (2012).
173. Mosel, M., Li, L., Drlica, K. & Zhao, X. Superoxide-Mediated Protection of *Escherichia coli* from Antimicrobials. *Antimicrob Agents Chemother* **57**, 5755–5759 (2013).
174. Hoeksema, M., Brul, S. & ter Kuilea, B. H. Influence of Reactive Oxygen Species on De Novo Acquisition of Resistance to Bactericidal Antibiotics. *Antimicrob Agents Chemother* **62**, e02354-17 (2018).
175. Rowe, S. E. *et al.* Reactive oxygen species induce antibiotic tolerance during systemic *Staphylococcus aureus* infection. *Nat Microbiol* **5**, 282–290 (2020).
176. Irving, S. E., Choudhury, N. R. & Corrigan, R. M. The stringent response and physiological roles of (pp)pGpp in bacteria. *Nat Rev Microbiol* **19**, 256–271 (2021).
177. Salzer, A. & Wolz, C. Role of (p)ppGpp in antibiotic resistance, tolerance, persistence and survival in Firmicutes. *microLife* **4**, uqad009 (2023).
178. Mwangi, M. M. *et al.* Whole-Genome Sequencing Reveals a Link Between β-Lactam Resistance and Synthetases of the Alarmone (p)ppGpp in *Staphylococcus aureus*. *Microbial Drug Resistance* **19**, 153–159 (2013).
179. Aedo, S. & Tomasz, A. Role of the Stringent Stress Response in the Antibiotic Resistance Phenotype of Methicillin-Resistant *Staphylococcus aureus*. *Antimicrob Agents Chemother* **60**, 2311–2317 (2016).
180. Kvist, M., Hancock, V. & Klemm, P. Inactivation of Efflux Pumps Abolishes Bacterial Biofilm Formation. *Appl Environ Microbiol* **74**, 7376–7382 (2008).
181. Baugh, S., Phillips, C. R., Ekanayaka, A. S., Piddock, L. J. V. & Webber, M. A. Inhibition of multidrug efflux as a strategy to prevent biofilm

formation. *Journal of Antimicrobial Chemotherapy* **69**, 673–681 (2014).

182. Savage, V. J., Chopra, I. & O'Neill, A. J. *Staphylococcus aureus* biofilms promote horizontal transfer of antibiotic resistance. *Antimicrob Agents Chemother* **57**, 1968–1970 (2013).
183. Strugeon, E., Tilloy, V., Ploy, M.-C. & Da Re, S. The Stringent Response Promotes Antibiotic Resistance Dissemination by Regulating Integron Integrase Expression in Biofilms. *mBio* **7**, e00868-16 (2016).
184. Brackman, G. *et al.* The Quorum Sensing Inhibitor Hamamelitannin Increases Antibiotic Susceptibility of *Staphylococcus aureus* Biofilms by Affecting Peptidoglycan Biosynthesis and eDNA Release. *Sci Rep* **6**, 20321 (2016).
185. Dalton, T. *et al.* An *In Vivo* Polymicrobial Biofilm Wound Infection Model to Study Interspecies Interactions. *PLoS One* **6**, e27317 (2011).
186. Wilmaerts, D., Windels, E. M., Verstraeten, N. & Michiels, J. General Mechanisms Leading to Persister Formation and Awakening. *Trends in Genetics* **35**, 401–411 (2019).
187. Peyrusson, F. *et al.* Intracellular *Staphylococcus aureus* persisters upon antibiotic exposure. *Nat Commun* **11**, 2200 (2020).
188. Roilides, E., Simitsopoulou, M., Katragkou, A. & Walsh, T. J. How Biofilms Evade Host Defenses. *Microbiol Spectr* **3**, 287–300 (2015).
189. Scherr, T. D. *et al. Staphylococcus aureus* Biofilms Induce Macrophage Dysfunction Through Leukocidin AB and Alpha-Toxin. *mBio* **6**, (2015).
190. Bjarnsholt, T. The role of bacterial biofilms in chronic infections. *APMIS Suppl* **136**, (2013).
191. Vishwakarma, A., Dang, F., Ferrell, A., Barton, H. A. & Joy, A. Peptidomimetic Polyurethanes Inhibit Bacterial Biofilm Formation and Disrupt Surface Established Biofilms. *J Am Chem Soc* **143**, 9440–9449 (2021).
192. McConoughey, S. J. *et al.* Biofilms in periprosthetic orthopedic infections. *Future Microbiol* **9**, 987–1007 (2014).
193. Xu, C. *et al.* Is Treatment of Periprosthetic Joint Infection Improving Over Time? *J Arthroplasty* **35**, 1696-1702.e1 (2020).
194. Goh, G. S., Tornetta, P. & Parvizi, J. Facilitating the Approval Process of Anti-Infective Technologies and Advancing Them to the Market - Insights from an FDA Workshop on Orthopaedic Device-Related Infections. *J Bone Joint Surg* **103**, e57 (2021).

195. Löwik, C. A. M. *et al.* Debridement, antibiotics, and implant retention is a viable treatment option for early periprosthetic joint infection presenting more than 4 weeks after index arthroplasty. *Clinical Infectious Diseases* **71**, 630–636 (2020).
196. Goldman, A. H. *et al.* Definitive Resection Arthroplasty of the Knee: A Surprisingly Viable Treatment to Manage Intractable Infection in Selected Patients. *Journal of Arthroplasty* **35**, 855–858 (2020).
197. Longo, U. G. *et al.* Debridement, antibiotics, and implant retention (DAIR) for the early prosthetic joint infection of total knee and hip arthroplasties: a systematic review. *Journal of ISAKOS* **9**, 62–70 (2024).
198. Browne, J. A., Cancienne, J. M., Novicoff, W. M. & Werner, B. C. Removal of an Infected Hip Arthroplasty Is a High-Risk Surgery: Putting Morbidity Into Context With Other Major Nonorthopedic Operations. *Journal of Arthroplasty* **32**, 2834–2841 (2017).
199. Wille, J. & Coenye, T. Biofilm dispersion: The key to biofilm eradication or opening Pandora's box? *Biofilm* **2**, 100027 (2020).
200. Fleming, D. & Rumbaugh, K. The Consequences of Biofilm Dispersal on the Host. *Sci Rep* **8**, 10738 (2018).
201. Chua, S. L. *et al.* Dispersed cells represent a distinct stage in the transition from bacterial biofilm to planktonic lifestyles. *Nat Commun* **5**, 4462 (2014).
202. Wang, S. *et al.* Strategy to combat biofilms: a focus on biofilm dispersal enzymes. *NPJ Biofilms Microbiomes* **9**, 63 (2023).
203. Loughran, A. J. *et al.* Impact of individual extracellular proteases on *Staphylococcus aureus* biofilm formation in diverse clinical isolates and their isogenic sarA mutants. *Microbiologyopen* **3**, 897–909 (2014).
204. Mechmechani, S. *et al.* Pepsin and Trypsin Treatment Combined with Carvacrol: An Efficient Strategy to Fight *Pseudomonas aeruginosa* and *Enterococcus faecalis* Biofilms. *Microorganisms* **11**, 143 (2023).
205. Whitchurch, C. B., Tolker-Nielsen, T., Ragas, P. C. & Mattick, J. S. Extracellular DNA Required for Bacterial Biofilm Formation. *Science* **295**, 1487 (2002).
206. Pirlar, R. F. *et al.* Combinatorial effects of antibiotics and enzymes against dual-species *Staphylococcus aureus* and *Pseudomonas*

aeruginosa biofilms in the wound-like medium. *PLoS One* **15**, e0235093 (2020).

207. Fleming, D., Chahin, L. & Rumbaugh, K. Glycoside Hydrolases Degrade Polymicrobial Bacterial Biofilms in Wounds. *Antimicrob Agents Chemother* **61**, e01998 (2017).
208. Ruiz-Sorribas, A., Poilvache, H., Kamarudin, N. H. N., Braem, A. & Van Bambeke, F. Hydrolytic Enzymes as Potentiators of Antimicrobials against an Inter-Kingdom Biofilm Model. *Microbiol Spectr* **10**, e02589-21 (2022).
209. Brackman, G. & Coenye, T. Quorum sensing inhibitors as anti-biofilm agents. *Curr Pharm Des* **21**, 5–11 (2015).
210. Paluch, E., Rewak-Soroczyńska, J., Jędrusik, I., Mazurkiewicz, E. & Jermakow, K. Prevention of biofilm formation by quorum quenching. *Appl Microbiol Biotechnol* **104**, 1871–1881 (2020).
211. Vashistha, A. *et al.* Quorum sensing inhibitors as Therapeutics: Bacterial biofilm inhibition. *Bioorg Chem* **136**, 106551 (2023).
212. Zhang, Y. *et al.* Coumarin Reduces Virulence and Biofilm Formation in *Pseudomonas aeruginosa* by Affecting Quorum Sensing, Type III Secretion and C-di-GMP Levels. *Front Microbiol* **9**, 1952 (2018).
213. Bruna, T., Maldonado-Bravo, F., Jara, P. & Caro, N. Silver Nanoparticles and Their Antibacterial Applications. *Int J Mol Sci* **22**, 7202 (2021).
214. Sánchez-López, E. *et al.* Metal-Based Nanoparticles as Antimicrobial Agents: An Overview. *Nanomaterials* **10**, 292 (2020).
215. Zhang, E. *et al.* Antibacterial metals and alloys for potential biomedical implants. *Bioact Mater* **6**, 2569–2612 (2021).
216. Gudkov, S. V. *et al.* Do Iron Oxide Nanoparticles Have Significant Antibacterial Properties? *Antibiotics* **10**, 884 (2021).
217. Haque, S., Tripathy, S. & Patra, C. R. Manganese-based advanced nanoparticles for biomedical applications: future opportunity and challenges. *Nanoscale* **13**, 16405–16426 (2021).
218. Luo, L., Huang, W., Zhang, J., Yu, Y. & Sun, T. Metal-Based Nanoparticles as Antimicrobial Agents: A Review. *ACS Appl Nano Mater* **7**, 2529–2545 (2024).
219. Radzig, M. A. *et al.* Antibacterial effects of silver nanoparticles on Gram-negative bacteria: Influence on the growth and biofilms

formation, mechanisms of action. *Colloids Surf B Biointerfaces* **102**, 300–306 (2013).

220. Milić, M. *et al.* Cellular uptake and toxicity effects of silver nanoparticles in mammalian kidney cells. *Journal of Applied Toxicology* **35**, 581–592 (2015).
221. De Soir, S. *et al.* Exploiting phage-antibiotic synergies to disrupt *Pseudomonas aeruginosa* PAO1 biofilms in the context of orthopedic infections. *Microbiol Spectr* **12**, e03219 (2024).
222. Ball, P. Phage stories. *The Lancet* **402**, 1824–1825 (2023).
223. Nikolich, M. P. & Filippov, A. A. Bacteriophage Therapy: Developments and Directions. *Antibiotics* **9**, 135 (2020).
224. Doss, J., Culbertson, K., Hahn, D., Camacho, J. & Barekzi, N. A Review of Phage Therapy against Bacterial Pathogens of Aquatic and Terrestrial Organisms. *Viruses* **9**, 50 (2017).
225. Suh, G. A. *et al.* Considerations for the Use of Phage Therapy in Clinical Practice. *Antimicrob Agents Chemother* **66**, e02071 (2022).
226. Donlan, R. M. Preventing biofilms of clinically relevant organisms using bacteriophage. *Trends Microbiol* **17**, 66–72 (2009).
227. Gutiérrez, D. *et al.* Role of the Pre-neck Appendage Protein (Dpo7) from Phage vB_SepiS-phiIPLA7 as an Anti-biofilm Agent in Staphylococcal Species. *Front Microbiol* **6**, 1315 (2015).
228. Summers, W. C. The Cold War and Phage Therapy: How Geopolitics Stalled Development of Viruses as Antibacterials. *Annu Rev Virol* **11**, 381–393 (2024).
229. University of Ottawa. First patient in Canada treated with phage therapy for artificial joint infection. https://www.uottawa.ca/en/news-all/first-patient-canada-treated-phage-therapy-artificial-joint-infection.
230. Hancock, R. E. W. & Sahl, H.-G. Antimicrobial and host-defense peptides as new anti-infective therapeutic strategies. *Nat Biotechnol* **24**, 1551–1557 (2006).
231. Wang, G. Improved Methods for Classification, Prediction and Design of Antimicrobial Peptides. *Methods in Molecular Biology* **1268**, 43–66 (2015).
232. Lin, L. *et al.* Membrane-disruptive peptides/peptidomimetics-based therapeutics: Promising systems to combat bacteria and cancer in the drug-resistant era. *Acta Pharm Sin B* **11**, 2609–2644 (2021).

233. Talapko, J. *et al.* Antimicrobial Peptides—Mechanisms of Action, Antimicrobial Effects and Clinical Applications. *Antibiotics* **11**, 1417 (2022).
234. Duplantier, A. J. & van Hoek, M. L. The Human Cathelicidin Antimicrobial Peptide LL-37 as a Potential Treatment for Polymicrobial Infected Wounds. *Front Immunol* **4**, 143 (2013).
235. Wimley, W. C. Describing the Mechanism of Antimicrobial Peptide Action with the Interfacial Activity Model. *ACS Chem Biol* **5**, 905–917 (2010).
236. Kumar, P., Kizhakkedathu, J. N. & Straus, S. K. Antimicrobial Peptides: Diversity, Mechanism of Action and Strategies to Improve the Activity and Biocompatibility *In Vivo*. *Biomolecules* **8**, 4 (2018).
237. Sancho-Vaello, E. *et al.* The structure of the antimicrobial human cathelicidin LL-37 shows oligomerization and channel formation in the presence of membrane mimics. *Sci Rep* **10**, 17356 (2020).
238. Hartmann, M. *et al.* Damage of the Bacterial Cell Envelope by Antimicrobial Peptides Gramicidin S and PGLa as Revealed by Transmission and Scanning Electron Microscopy. *Antimicrob Agents Chemother* **54**, 3132–3142 (2010).
239. Vandamme, D., Landuyt, B., Luyten, W. & Schoofs, L. A comprehensive summary of LL-37, the factotum human cathelicidin peptide. *Cell Immunol* **280**, 22–35 (2012).
240. Yasir, M., Willcox, M. D. P. & Dutta, D. Action of Antimicrobial Peptides against Bacterial Biofilms. *Materials* **11**, 2468 (2018).
241. Dürr, U. H. N., Sudheendra, U. S. & Ramamoorthy, A. LL-37, the only human member of the cathelicidin family of antimicrobial peptides. *Biochimica et Biophysica Acta (BBA) - Biomembranes* **1758**, 1408–1425 (2006).
242. Sancho-Vaello, E. *et al.* Structural remodeling and oligomerization of human cathelicidin on membranes suggest fibril-like structures as active species. *Sci Rep* **7**, (2017).
243. Gabriel, M., Nazmi, K., Veerman, E. C., NieuwAmerongen, A. V & Zentner, A. Preparation of LL-37-Grafted Titanium Surfaces with Bactericidal Activity. *Bioconjug Chem* **17**, 548–550 (2006).
244. Mishra, B. & Wang, G. Titanium surfaces immobilized with the major antimicrobial fragment FK-16 of human cathelicidin LL-37 are potent

against multiple antibiotic-resistant bacteria. *Biofouling* **33**, 544–555 (2017).

245. Turner, J., Cho, Y., Dinh, N. N., Waring, A. J. & Lehrer, R. I. Activities of LL-37, a cathelin-associated antimicrobial peptide of human neutrophils. *Antimicrob Agents Chemother* **42**, 2206–2214 (1998).
246. Overhage, J. *et al.* Human host defense peptide LL-37 prevents bacterial biofilm formation. *Infect Immun* **76**, 4176–4182 (2008).
247. Nelson, A. *et al. Staphylococcus epidermidis* Isolated From Newborn Infants Express Pilus-Like Structures and Are Inhibited by the Cathelicidin-Derived Antimicrobial Peptide LL37. *Pediatr Res* **66**, 174–178 (2009).
248. Friberg, C. *et al.* Human antimicrobial peptide, LL-37, induces non-inheritable reduced susceptibility to vancomycin in *Staphylococcus aureus*. *Sci Rep* **10**, 8 (2020).
249. Dean, S. N., Bishop, B. M. & van Hoek, M. L. Natural and synthetic cathelicidin peptides with anti-microbial and anti-biofilm activity against *Staphylococcus aureus*. *BMC Microbiol* **11**, 114 (2011).
250. Johansson, J., Gudmundsson, G. H., Rottenberg, M. E., Berndt, K. D. & Agerberth, B. Conformation-dependent Antibacterial Activity of the Naturally Occurring Human Peptide LL-37. *Journal of Biological Chemistry* **273**, 3718–3724 (1998).
251. Säll, J. *et al.* The Antimicrobial Peptide LL-37 Alters Human Osteoblast Ca2+ Handling and Induces Ca2+-Independent Apoptosis. *J Innate Immun* **5**, 290–300 (2013).
252. Svensson, D., Wilk, L., Mörgelin, M., Herwald, H. & Nilsson, B. O. LL-37-induced host cell cytotoxicity depends on cellular expression of the globular C1q receptor (p33). *Biochemical Journal* **473**, 87–98 (2016).
253. Aidoukovitch, A., Bankell, E., Svensson, D. & Nilsson, B. O. Vitamin D triggers hCAP18/LL-37 production: Implications for LL-37-induced human osteoblast cytotoxicity. *Biochem Biophys Res Commun* **712–713**, 149962 (2024).
254. vander Straeten, A. Protein-polyelectrolyte complexes for the surface immobilization of bioactive proteins. (PhD Thesis, UCLouvain, 2019).
255. Dutta, D., Kumar, N. & Willcox, M. D. P. Antimicrobial activity of four cationic peptides immobilised to poly-hydroxyethylmethacrylate. *Biofouling* **32**, 429–438 (2016).

256. He, Y. *et al.* Peptide LL-37 coating on micro-structured titanium implants to facilitate bone formation *in vivo* via mesenchymal stem cell recruitment. *Acta Biomater* **80**, 412–424 (2018).
257. Zimmerli, W., Waldvogel, F. A., Vaudaux, P. & Nydegger, U. E. Pathogenesis of foreign body infection: description and characteristics of an animal model. *J Infect Dis* **146**, 487–497 (1982).
258. Lebaudy, E., Guilbaud-Chéreau, C., Frisch, B., Vrana, N. E. & Lavalle, P. The High Potential of ε-Poly-l-Lysine for the Development of Antimicrobial Biomaterials. *Adv Nanobiomed Res* **3**, 2300080 (2023).
259. Séon, L., Lavalle, P., Schaaf, P. & Boulmedais, F. Polyelectrolyte Multilayers: A Versatile Tool for Preparing Antimicrobial Coatings. *Langmuir* **31**, 12856–12872 (2015).
260. Fu, J., Ji, J., Yuan, W. & Shen, J. Construction of anti-adhesive and antibacterial multilayer films via layer-by-layer assembly of heparin and chitosan. *Biomaterials* **26**, 6684–6692 (2005).
261. Mutschler, A. *et al.* Unexpected Bactericidal Activity of Poly(arginine)/Hyaluronan Nanolayered Coatings. *Chemistry of Materials* **28**, 8700–8709 (2016).
262. Knopf-Marques, H. *et al.* Multifunctional polymeric implant coatings based on gelatin, hyaluronic acid derivative and chain length-controlled poly(arginine). *Materials Science and Engineering: C* **104**, 109898 (2019).
263. Hardy, R., Vranckx, C. & Dupont-Gillain, C. Titanium Implant Coatings Composed of Chitosan and Heparin to Promote Osseointegration. (UCLouvain, Louvain-la-Neuve, 2019).
264. Bruzaud, J. *et al.* Flagella but not type IV pili are involved in the initial adhesion of *Pseudomonas aeruginosa* PAO1 to hydrophobic or superhydrophobic surfaces. *Colloids Surf B Biointerfaces* **131**, 59–66 (2015).
265. Faille, C. *et al.* Adhesion of Bacillus spores and *Escherichia coli* cells to inert surfaces: role of surface hydrophobicity. *Can J Microbiol* **48**, 728–738 (2002).
266. Banerjee, I., Pangule, R. C. & Kane, R. S. Antifouling Coatings: Recent Developments in the Design of Surfaces That Prevent Fouling by Proteins, Bacteria, and Marine Organisms. *Advanced Materials* **23**, 690–718 (2011).

267. Lichter, J. A. *et al.* Substrata Mechanical Stiffness Can Regulate Adhesion of Viable Bacteria. *Biomacromolecules* **9**, 1571–1578 (2008).
268. Saha, N., Monge, C., Dulong, V., Picart, C. & Glinel, K. Influence of Polyelectrolyte Film Stiffness on Bacterial Growth. *Biomacromolecules* **14**, 520–528 (2013).
269. Yang, Z. *et al.* Covalent grafting of hyperbranched poly-L-lysine on Ti-based implants achieves dual functions of antibacteria and promoted osteointegration *in vivo*. *Biomaterials* **269**, 120534 (2021).
270. Drago, L., Toscano, M. & Bottagisio, M. Recent Evidence on Bioactive Glass Antimicrobial and Antibiofilm Activity: A Mini-Review. *Materials* **11**, 326 (2018).
271. Drago, L. *et al.* Antimicrobial activity and resistance selection of different bioglass S53P4 formulations against multidrug resistant strains. *Future Microbiol* **10**, 1293–1299 (2015).
272. Fernandes, J. S., Gentile, P., Pires, R. A., Reis, R. L. & Hatton, P. V. Multifunctional bioactive glass and glass-ceramic biomaterials with antibacterial properties for repair and regeneration of bone tissue. *Acta Biomater* **59**, 2–11 (2017).
273. Munukka, E. *et al.* Bactericidal effects of bioactive glasses on clinically important aerobic bacteria. *J Mater Sci Mater Med* **19**, 27–32 (2008).
274. Cabal, B. *et al.* A New Biocompatible and Antibacterial Phosphate Free Glass-Ceramic for Medical Applications. *Sci Rep* **4**, 5440 (2014).
275. Rivadeneira, J. & Gorustovich, A. Bioactive glasses as delivery systems for antimicrobial agents. *J Appl Microbiol* **122**, 1424–1437 (2016).
276. Tripathy, A., Sen, P., Su, B. & Briscoe, W. H. Natural and bioinspired nanostructured bactericidal surfaces. *Adv Colloid Interface Sci* **248**, 85–104 (2017).
277. Ivanova, E. P. *et al.* Natural Bactericidal Surfaces: Mechanical Rupture of *Pseudomonas aeruginosa* Cells by Cicada Wings. *Small* **8**, 2489–2494 (2012).
278. Hasan, J. *et al.* Selective bactericidal activity of nanopatterned superhydrophobic cicada *Psaltoda claripennis* wing surfaces. *Appl Microbiol Biotechnol* **97**, 9257–9262 (2013).
279. Ivanova, E. P. *et al.* Bactericidal activity of black silicon. *Nat Commun* **4**, 2838 (2013).

280. Jenkins, J. *et al.* Antibacterial effects of nanopillar surfaces are mediated by cell impedance, penetration and induction of oxidative stress. *Nat Commun* **11**, 1626 (2020).
281. Kelleher, S. M. *et al.* Cicada Wing Surface Topography: An Investigation into the Bactericidal Properties of Nanostructural Features. *ACS Appl Mater Interfaces* **8**, 14966–14974 (2016).
282. Pogodin, S. *et al.* Biophysical Model of Bacterial Cell Interactions with Nanopatterned Cicada Wing Surfaces. *Biophys J* **104**, 835–840 (2013).
283. Huang, L. Z. Y. *et al.* Cell Adhesion, Elasticity, and Rupture Forces Guide Microbial Cell Death on Nanostructured Antimicrobial Titanium Surfaces. *ACS Appl Bio Mater* **7**, 344–361 (2024).
284. Le, P. H. *et al.* Impact of multiscale surface topography characteristics on *Candida albicans* biofilm formation: From cell repellence to fungicidal activity. *Acta Biomater* **177**, 20–36 (2024).
285. Han, C. & Guo, W. Fluorescent Noble Metal Nanoclusters Loaded Protein Hydrogel Exhibiting Anti-Biofouling and Self-Healing Properties for Electrochemiluminescence Biosensing Applications. *Small* **16**, 2002621 (2020).
286. Teanphonkrang, S. & Schulte, A. Automated Quantitative Enzyme Biosensing in 24-Well Microplates. *Anal Chem* **89**, 5261–5269 (2017).
287. Büscher, N. *et al.* Biocatalyst Immobilization by Anchor Peptides on an Additively Manufacturable Material. *Org Process Res Dev* **23**, 1852–1859 (2019).
288. Zhang, G., Johnston, T., Quin, M. B. & Schmidt-Dannert, C. Developing a Protein Scaffolding System for Rapid Enzyme Immobilization and Optimization of Enzyme Functions for Biocatalysis. *ACS Synth Biol* **8**, 1867–1876 (2019).
289. Schoeller, J. *et al.* pH-responsive chitosan/alginate polyelectrolyte complexes on electrospun PLGA nanofibers for controlled drug release. *Nanomaterials* **11**, 1850 (2021).
290. Lu, Y., Aimetti, A. A., Langer, R. & Gu, Z. Bioresponsive materials. *Nat Rev Mater* **2**, 16075 (2017).
291. Kitsara, M. *et al.* Polysaccharide–Protein Multilayers Based on Chitosan–Fibrinogen Assemblies for Cardiac Cell Engineering. *Macromol Biosci* **22**, e2100346 (2021).
292. Zander, N. E., Orlicki, J. A., Rawlett, A. M. & Beebe, T. P. Quantification of protein incorporated into electrospun polycaprolactone tissue

engineering scaffolds. *ACS Appl Mater Interfaces* **4**, 2074–2081 (2012).

293. Taylor, W., Ebbens, S., Skoda, M. W. A., Webster, J. R. P. & Jones, R. A. L. Mode of lysozyme protein adsorption at end-tethered polyethylene oxide brushes on gold surfaces determined by neutron reflectivity. *European Physical Journal E* **38**, 14 (2015).
294. Brady, D. & Jordaan, J. Advances in enzyme immobilisation. *Biotechnol Lett* **31**, 1639–1650 (2009).
295. Norde, W., Horbett, T. A. & Brash, J. L. Proteins at Interfaces III: Introductory Overview. *ACS Symposium Series* **1120**, 1–34 (2012).
296. Norde, W. My voyage of discovery to proteins in flatland ...and beyond. *Colloids Surf B Biointerfaces* **61**, 1–9 (2008).
297. Cassin, M. E., Ford, A. J., Orbach, S. M., Saverot, S. E. & Rajagopalan, P. The design of antimicrobial LL37-modified collagen-hyaluronic acid detachable multilayers. *Acta Biomater* **40**, 119–129 (2016).
298. Agarwal, P. K. A Biophysical Perspective on Enzyme Catalysis. *Biochemistry* **58**, 438–449 (2019).
299. Delcroix, M. F., Laurent, S., Huet, G. L. & Dupont-Gillain, C. C. Protein adsorption can be reversibly switched on and off on mixed PEO/PAA brushes. *Acta Biomater* **11**, 68–79 (2015).
300. Delcroix, M. Ionic strength and pH-dependent conformation of mixed polymer brushes for cycles of protein adsorption and desorption. (PhD Thesis, UCLouvain, 2013).
301. Das, S., Banik, M., Chen, G., Sinha, S. & Mukherjee, R. Polyelectrolyte brushes: Theory, modelling, synthesis and applications. *Soft Matter* **11**, 8550–8583 (2015).
302. Chereddy, K. K. *et al.* PLGA nanoparticles loaded with host defense peptide LL37 promote wound healing. *Journal of Controlled Release* **194**, 138–147 (2014).
303. Garcia-Orue, I. *et al.* LL37 loaded nanostructured lipid carriers (NLC): A new strategy for the topical treatment of chronic wounds. *European Journal of Pharmaceutics and Biopharmaceutics* **108**, 310–316 (2016).
304. Lin, X., Wang, R. & Mai, S. Advances in delivery systems for the therapeutic application of LL37. *J Drug Deliv Sci Technol* **60**, 102016 (2020).
305. Arango-Restrepo, A., Barragán, D. & Rubi, J. M. Self-assembling outside equilibrium: Emergence of structures mediated by

dissipation. *Physical Chemistry Chemical Physics* **21**, 17475–17493 (2019).

306. Mattia, E. & Otto, S. Supramolecular systems chemistry. *Nat Nanotechnol* **10**, 111–119 (2015).
307. Whitelam, S. & Jack, R. L. The Statistical Mechanics of Dynamic Pathways to Self-Assembly. *Annu Rev Phys Chem* **66**, 143–163 (2015).
308. Richardson, J. J., Björnmalm, M. & Caruso, F. Technology-driven layer-by-layer assembly of nanofilms. *Science* **348**, 411–422 (2015).
309. Decher, G., Hong, J. D. & Schmitt, J. Buildup of ultrathin multilayer films by a self-assembly process: III. Consecutively alternating adsorption of anionic and cationic polyelectrolytes on charged surfaces. *Thin Solid Films* **210–211**, 831–835 (1992).
310. Decher, G. Fuzzy Nanoassemblies: Toward Layered Polymeric Multicomposites. *Science* **277**, 1232–1237 (1997).
311. Mauquoy, S. & Dupont-Gillain, C. Combination of collagen and fibronectin to design biomimetic interfaces: Do these proteins form layer-by-layer assemblies? *Colloids Surf B Biointerfaces* **147**, 54–64 (2016).
312. Félix, O., Zheng, Z., Cousin, F. & Decher, G. Are sprayed LbL-films stratified? A first assessment of the nanostructure of spray-assembled multilayers by neutron reflectometry. *Comptes Rendus Chimie* **12**, 225–234 (2009).
313. Elbert, D. L., Herbert, C. B. & Hubbell, J. A. Thin Polymer Layers Formed by Polyelectrolyte Multilayer Techniques on Biological Surfaces. *Langmuir* **15**, 5355–5362 (1999).
314. V. Klitzing, R. Internal structure of polyelectrolyte multilayer assemblies. *Physical Chemistry Chemical Physics* **8**, 5012–5033 (2006).
315. Borges, J. & Mano, J. F. Molecular interactions driving the layer-by-layer assembly of multilayers. *Chem Rev* **114**, 8883–8942 (2014).
316. Hübsch, E. *et al.* Controlling the Growth Regime of Polyelectrolyte Multilayer Films: Changing from Exponential to Linear Growth by Adjusting the Composition of Polyelectrolyte Mixtures. *Langmuir* **20**, 1980–1985 (2004).
317. Porcel, C. *et al.* From Exponential to Linear Growth in Polyelectrolyte Multilayers. *Langmuir* **22**, 4376–4383 (2006).
318. Laugel, N. *et al.* Relationship between the Growth Regime of Polyelectrolyte Multilayers and the Polyanion/Polycation

Complexation Enthalpy. *Journal of Physical Chemistry B* **110**, 19443–19449 (2006).

319. Hammond, P. T. Recent explorations in electrostatic multilayer thin film assembly. *Curr Opin Colloid Interface Sci* **4**, 430–442 (1999).
320. Guzmán, E., Rubio, R. G. & Ortega, F. A closer physico-chemical look to the Layer-by-Layer electrostatic self-assembly of polyelectrolyte multilayers. *Adv Colloid Interface Sci* **282**, 102197 (2020).
321. Kleinfeld, E. R. & Ferguson, G. S. Stepwise Formation of Multilayered Nanostructural Films from Macromolecular Precursors. *Science* **265**, 370–373 (1994).
322. de Lucena, N. C., Miyazaki, C. M., Shimizu, F. M., Constantino, C. J. L. & Ferreira, M. Layer-by-layer composite film of nickel phthalocyanine and montmorillonite clay for synergistic effect on electrochemical detection of dopamine. *Appl Surf Sci* **436**, 957–966 (2018).
323. Lvov, Y., Hass, H., Decher, G. & Möhwald, H. Successive Deposition of Alternate Layers of Polyelectrolytes and a Charged Virus. *Langmuir* **10**, 4232–4236 (1994).
324. Watanabe, S. & Regen, S. L. Dendrimers as Building Blocks for Multilayer Construction. *J Am Chem Soc* **116**, 8855–8856 (1994).
325. Yoshida, K. *et al.* Adsorption and release of rose bengal on layer-by-layer films of poly(vinyl alcohol) and poly(amidoamine) dendrimers bearing 4-carboxyphenylboronic acid. *Polymers (Basel)* **12**, 1854 (2020).
326. Jiang, Y., Shen, Y. & Wu, P. Self-assembly of multilayer films containing gold nanoparticles via hydrogen bonding. *J Colloid Interface Sci* **319**, 398–405 (2008).
327. Yuehui, W. & Xing, Y. High-reflection optical thin films based on SiO2/TiO2 nanoparticles multilayers by dip coating. *Micro Nano Lett* **13**, 1349–1351 (2018).
328. Lvov, Y., Decher, G. & Sukhorukov, G. Assembly of thin films by means of successive deposition of alternate layers of DNA and poly(allylamine). *Macromolecules* **26**, 5396–5399 (1993).
329. Delechiave, G. *et al.* Tuning protein delivery from different architectures of layer-by-layer assemblies on polymer films. *Mater Adv* **1**, 2043–2056 (2020).
330. Lvov, Y., Ariga, K. & Kunitake, T. Layer-by-Layer Assembly of Alternate Protein/Polyion Ultrathin Films. *Chem Lett* **23**, 2323–2326 (1994).

331. Lvov, Y., Ariga, K., Ichinose, I. & Kunitake, T. Assembly of Multicomponent Protein Films by Means of Electrostatic Layer-by-Layer Adsorption. *J Am Chem Soc* **117**, 6117–6123 (1995).
332. vander Straeten, A., Lefèvre, D., Demoustier-Champagne, S. & Dupont-Gillain, C. Protein-based polyelectrolyte multilayers. *Adv Colloid Interface Sci* **280**, 102161 (2020).
333. Zhang, J. *et al.* Natural polyelectrolyte films based on layer-by-layer deposition of collagen and hyaluronic acid. *Biomaterials* **26**, 3353–3361 (2005).
334. Becker, A. L., Henzler, K., Welsch, N., Ballauff, M. & Borisov, O. Proteins and polyelectrolytes: A charged relationship. *Curr Opin Colloid Interface Sci* **17**, 90–96 (2012).
335. Pettersen, E. F. *et al.* UCSF Chimera - A visualization system for exploratory research and analysis. *J Comput Chem* **25**, 1605–1612 (2004).
336. Iqbal, M. H., Kerdjoudj, H. & Boulmedais, F. Protein-based layer-by-layer films for biomedical applications. *Chem Sci* **15**, 9408–9437 (2024).
337. Yuan, M. *et al.* Lysozyme/collagen multilayers layer-by-layer deposited nanofibers with enhanced biocompatibility and antibacterial activity. *Materials Science and Engineering: C* **112**, 110868 (2020).
338. Ivanova, K. *et al.* Quorum-Quenching and Matrix-Degrading Enzymes in Multilayer Coatings Synergistically Prevent Bacterial Biofilm Formation on Urinary Catheters. *ACS Appl Mater Interfaces* **7**, 27066–27077 (2015).
339. Uhrich, K. E., Cannizzaro, S. M., Langer, R. S. & Shakesheff, K. M. Polymeric Systems for Controlled Drug Release. *Chem Rev* **99**, 3181–3198 (1999).
340. Hetrick, E. M. & Schoenfisch, M. H. Reducing implant-related infections: active release strategies. *Chem Soc Rev* **35**, 780–789 (2006).
341. Shi, J. *et al.* Biological and immunotoxicity evaluation of antimicrobial peptide-loaded coatings using a layer-by-layer process on titanium. *Sci Rep* **5**, 16336 (2015).
342. Vaterrodt, A. *et al.* Antifouling and Antibacterial Multifunctional Polyzwitterion/Enzyme Coating on Silicone Catheter Material

Prepared by Electrostatic Layer-by-Layer Assembly. *Langmuir* **32**, 1347–1359 (2016).

343. Dolinsky, T. J., Nielsen, J. E., McCammon, J. A. & Baker, N. A. PDB2PQR: An automated pipeline for the setup of Poisson-Boltzmann electrostatics calculations. *Nucleic Acids Res* **32**, 665–667 (2004).
344. vander Straeten, A., Bratek-Skicki, A., Jonas, A. M., Fustin, C.-A. & Dupont-Gillain, C. Integrating Proteins in Layer-by-Layer Assemblies Independently of their Electrical Charge. *ACS Nano* **12**, 8372–8381 (2018).
345. Müller, M., Rieser, T., Dubin, P. L. & Lunkwitz, K. Selective Interaction Between Proteins and the Outermost Surface of Polyelectrolyte Multilayers: Influence of the Polyanion Type, pH and Salt. *Molecular Rapid Communications* **22**, 390–395 (2001).
346. Izumrudov, V. A., Kharlampieva, E. & Sukhishvili, S. A. Multilayers of a Globular Protein and a Weak Polyacid: Role of Polyacid Ionization in Growth and Decomposition in Salt Solutions. *Biomacromolecules* **6**, 1782–1788 (2005).
347. Brynda, E., Homola, J., Houska, M., Pfeifer, P. & Škvor, J. Antibody networks for surface plasmon resonance immunosensors. *Sens Actuators B Chem* **54**, 132–136 (1999).
348. Fu, J. & B. Schlenoff, J. Driving Forces for Oppositely Charged Polyion Association in Aqueous Solutions: Enthalpic, Entropic, but Not Electrostatic. *J Am Chem Soc* **138**, 980–990 (2016).
349. Glinel, K., Moussa, A., Jonas, A. M. & Laschewsky, A. Influence of Polyelectrolyte Charge Density on the Formation of Multilayers of Strong Polyelectrolytes at Low Ionic Strength. *Langmuir* **18**, 1408–1412 (2002).
350. Caruso, F., Niikura, K., Furlong, D. N. & Okahata, Y. 2. Assembly of Alternating Polyelectrolyte and Protein Multilayer Films for Immunosensing. *Langmuir* **13**, 3427–3433 (1997).
351. He, P. & Hu, N. Interactions between Heme Proteins and Dextran Sulfate in Layer-by-Layer Assembly Films. *Journal of Physical Chemistry B* **108**, 13144–13152 (2004).
352. Lounis, F. M. *et al.* Interactions between Oppositely Charged Polyelectrolytes by Isothermal Titration Calorimetry: Effect of Ionic Strength and Charge Density. *Journal of Physical Chemistry B* **121**, 2684–2694 (2017).

353. Lowack, K. & Helm, C. A. Molecular Mechanisms Controlling the Self-Assembly Process of Polyelectrolyte Multilayers. *Macromolecules* **31**, 823–833 (1998).
354. Lee, J. H. *et al.* In Situ Fibril Formation of κ-Casein by External Stimuli within Multilayer Thin Films. *ACS Macro Lett* **2**, 688–693 (2013).
355. Salloum, D. S. & Schlenoff, J. B. Protein adsorption modalities of polyelectrolyte multilayers. *Biomacromolecules* **5**, 1089–1096 (2004).
356. Nicolas, M. *et al.* Strategies for Antimicrobial Peptides Immobilization on Surfaces to Prevent Biofilm Growth on Biomedical Devices. *Antibiotics* **11**, 13 (2022).
357. Zhu, X. & Jun Loh, X. Layer-by-layer assemblies for antibacterial applications. *Biomater Sci* **3**, 1505–1518 (2015).
358. Shukla, A. *et al.* Controlling the release of peptide antimicrobial agents from surfaces. *Biomaterials* **31**, 2348–2357 (2010).
359. Cado, G. *et al.* Self-Defensive Biomaterial Coating Against Bacteria and Yeasts: Polysaccharide Multilayer Film with Embedded Antimicrobial Peptide. *Adv Funct Mater* **23**, 4801–4809 (2013).
360. Etienne, O. *et al.* Multilayer Polyelectrolyte Films Functionalized by Insertion of Defensin: a New Approach to Protection of Implants from Bacterial Colonization. *Antimicrob Agents Chemother* **48**, 3662–3669 (2004).
361. Rodríguez López, A. de L. *et al.* Preventing *S. aureus* biofilm formation on titanium surfaces by the release of antimicrobial β-peptides from polyelectrolyte multilayers. *Acta Biomater* **93**, 50–62 (2019).
362. Xu, G. *et al.* Tannic acid anchored layer-by-layer covalent deposition of parasin I peptide for antifouling and antimicrobial coatings. *RSC Adv* **6**, 14809–14818 (2016).
363. Roupie, C., Labat, B., Morin-Grognet, S., Thébault, P. & Ladam, G. Nisin-based antibacterial and antiadhesive layer-by-layer coatings. *Colloids Surf B Biointerfaces* **208**, 112121 (2021).
364. Faure, E. *et al.* Sustainable and bio-inspired chemistry for robust antibacterial activity of stainless steel. *J Mater Chem* **21**, 7901–7904 (2011).
365. Vranckx, C. *et al.* Layer-by-Layer Nanoarchitectonics Using Protein-Polyelectrolyte Complexes toward a Generalizable Tool for Protein Surface Immobilization. *Langmuir* **38**, 5579–5589 (2022).

366. Ariga, K., Onda, M., Lvov, Y. & Kunitake, T. Alternate Layer-by-Layer Assembly of Organic Dyes and Proteins is Facilitated by Pre-mixing with Linear Polyions. *Chem Lett* **26**, 25–26 (1997).
367. Jin, W., Shi, X. & Caruso, F. High Activity Enzyme Microcrystal Multilayer Films. *J Am Chem Soc* **123**, 8121–8122 (2001).
368. Xia, J. & Dubin, P. L. Protein-Polyelectrolyte Complexes. In: Dubin P., Bock J., Davis R., Schulz D.N., Thies C. *Macromolecular Complexes in Chemistry and Biology* (ed. Springer) 247–271 (Berlin, Heidelberg, 1994).
369. Cooper, C. L., Dubin, P. L., Kayitmazer, A. B. & Turksen, S. Polyelectrolyte–protein complexes. *Curr Opin Colloid Interface Sci* **10**, 52–78 (2005).
370. Morawetz, H. & Hughes, W. L. Jr. The Interaction of Proteins with Synthetic Polyelectrolytes. I. Complexing of Bovine Serum Albumin. *J Phys Chem* **56**, 64–69 (1952).
371. Morawetz, H. & Sage, H. The effect of poly(acrylic acid) on the tryptic digestion of hemoglobin. *Arch Biochem Biophys* **56**, 103–109 (1955).
372. Park, J. M., Muhoberac, B. B., Dubin, P. L. & Xia, J. Effects of protein charge heterogeneity in protein-polyelectrolyte complexation. *Macromolecules* **25**, 290–295 (1992).
373. Cooper, C. L., Dubin, P. L., Kayitmazer, A. B. & Turksen, S. Polyelectrolyte–protein complexes. *Curr Opin Colloid Interface Sci* **10**, 52–78 (2005).
374. Kayitmazer, A. B., Seeman, D., Minsky, B. B., Dubin, P. L. & Xu, Y. Protein–polyelectrolyte interactions. *Soft Matter* **9**, 2553–2583 (2013).
375. Salehi, A., Desai, P. S., Li, J., Steele, C. A. & Larson, R. G. Relationship between Polyelectrolyte Bulk Complexation and Kinetics of Their Layer-by-Layer Assembly. *Macromolecules* **48**, 400–409 (2015).
376. De Luca, S., Chen, F., Seal, P., H. Stenzel, M. & C. Smith, S. Binding and Release between Polymeric Carrier and Protein Drug: pH-Mediated Interplay of Coulomb Forces, Hydrogen Bonding, van der Waals Interactions, and Entropy. *Biomacromolecules* **18**, 3665–3677 (2017).
377. Xu, X. *et al.* Counterion-Release Entropy Governs the Inhibition of Serum Proteins by Polyelectrolyte Drugs. *Biomacromolecules* **19**, 409–416 (2018).

378. Cousin, F., Gummel, J., Combet, S. & Boué, F. The model Lysozyme–PSSNa system for electrostatic complexation: Similarities and differences with complex coacervation. *Adv Colloid Interface Sci* **167**, 71–84 (2011).
379. Karayianni, M. *et al.* Complexation of Lysozyme with Poly(sodium(sulfamate-carboxylate)isoprene). *Biomacromolecules* **12**, 1697–1706 (2011).

Part II – Aim and Strategy of the thesis

1 Aim of the thesis

A century after the discovery of the first antibiotic, which marked a milestone in modern medicine, we are now at a turning point in the fight against medical implant-related infections. Antibacterial resistance and the growing number of orthopedic implant procedures are causing great concern. In this fight, the prevention of biofilm formation is paramount.

This work is focused, firstly, on the development of a method allowing the surface immobilization of proteins and peptides of biological interest, and secondly, on the development, physicochemical characterization, and study of antibacterial properties of LL-37-based coatings. LL-37 must be immobilized on flat surfaces while maintaining its activity. To reach such target, LbL assembly, a versatile technique performed in soft conditions, was preferred. Due to the polyampholyte character of proteins and peptides, their integration in multilayers by LbL assembly is very challenging. Therefore, the multilayers' properties must be well understood before evaluating the antibiofilm activity of LL-37-based coatings on staphylococci biofilms as sole preventive strategy or in combination with bacteriophages and commonly used antibiotics.

To summarize, this thesis aims at developing antimicrobial surfaces, in a way that facilitates the immobilization of active LL-37, with the final goal of reducing or even preventing medical-related infections. The adopted strategy should allow designing antibacterial self-assembled coatings with a controlled architecture. This would open perspectives for preventive applications of medical implant-related infections, which also could be applied in close collaboration with therapeutic strategies.

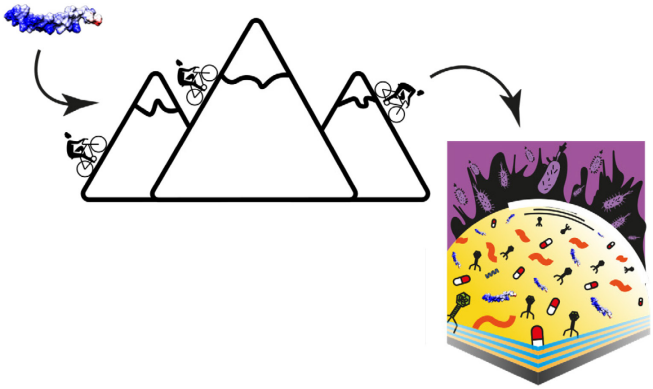

2 Strategy of the thesis

Due to their polyampholyte nature and their heterogeneous distribution of chemical functions as they are made out of different sequences of amino acids, the LbL assembly of proteins and peptides is very challenging. Establishing a method for standardizing their surface properties could offer a pathway to assemble any protein or peptide with a PE using the LbL approach. From this perspective, PPCs stand out as promising candidates. In theory, any PE can interact with a protein or a peptide to form a complex, as long as they possess opposite global charge. The resulting PPCs get a surface charge depending on the PE-to-protein ratio. Therefore, through the formation of PPCs in solution and the control of their charge, we foresee the ability to use the LbL method to assemble them with another PE bearing a charge opposite to that of the PPCs. Interestingly, the reported neutral charge of the PPCs core suggests that the subsequent LbL assembly would not be influenced by the protein or peptide charge. This statement is based on the thesis work of Aurélien vander Straeten who developed PPCs for the surface immobilization of bioactive proteins.[1]

Aurélien vander Straeten investigated the formation of complexes made of Lyz and PSS and their subsequent surface immobilization using PAH through the LbL method. The majority of his research focused on systems involving these three compounds. The first step of my thesis is to demonstrate the feasibility and the versatility of PPCs as a generalizable tool for the protein and peptide surface immobilization by using different proteins/peptides and PEs. To do so, proteins and peptides of interest, *i.e.*, LL-37, insulin (Ins), Lyz, and glucose oxidase (Gox) were complexed with alginate (Alg), PSS, Hep, or PAH at different pH conditions (3.5, 5 and 7.5). These PEs were chosen for their various characteristics. Alg is a weak natural polyanion, PSS is a strong synthetic polyanion, Hep is a strong naturally-occuring polyanion and PAH is a weak synthetic polycation. PPCs formation was monitored by turbidimetry measurements and the resulting PPCs were then LbL assembled with Chi, PAH, or Hep using the LbL method. Chi is a weak semi-synthetic polycation. The LbL assembly of bare proteins or peptides with PEs*, i.e.*, the classical LbL assembly, was carried out as a matter of comparison. These two strategies are represented in Figure II. 1. The multilayer growth was monitored by

quartz crystal microbalance with dissipation monitoring (QCM-D). This study is presented in *Part IV – Results and discussion – Chapter 1*.

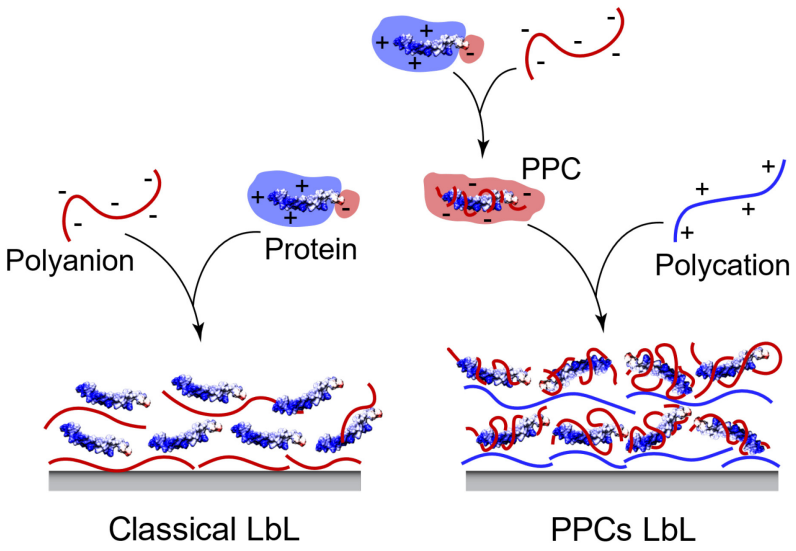

Figure II. 1 – Schematic representation of the two immobilization strategies performed along the thesis.

Prior to protein/peptide immobilization, an anchoring layer is adsorbed, consisting of two bilayers, obtained by repeating twice the deposition of one layer of the PE used to complex the protein/peptide followed by the PE used to immobilize the PPCs within the multilayer structure. This anchoring layer allows to screen the effect of the material surface.[2] Consequently, multilayers can be constructed on various substrates, with the substrate's characteristics exerting minimal influence on the multilayer formation process. The nature of the substrate on multilayer assembly was investigated using QCM-D on different modified quartz crystal surfaces (coated with Au, Ti, and SiO_2). The results demonstrated similar adsorption behavior and adsorbed quantities whatever the substrate (data not shown).

The following steps of the work focus on the LL-37 multilayers study. The decision to focus this study on LL-37 was based on its endogenous production in humans, the extensive research to which it is submitted in the scientific community, and its wide range of properties, including antibacterial, antifungal, antiviral, anticancer, and pro-angiogenic activities. LL-37 was complexed with Hep, used for its strong anionic character, independently of

the pH of the solution, and because it harbors binding sites for different groups of polypeptide growth factors, and many growth factors involved in bone regeneration provide Hep binding domains.[3] Therefore, in terms of osteointegration of an orthopedic implant, it could play an important role. PPCs were formed from solutions with an ionic strength (I) as low as possible (close to zero) and a pH value of 3.5 or 5. vander Straeten *et al*. showed that, when PPCs were used to immobilize Lyz molecules, higher protein content was obtained in the multilayers at low I.[2] It has been decided to form the PPCs at the same I and pH values as the ones used in the LbL assembly to avoid destabilizing the PPCs due to changes in solution conditions (I and pH). PPCs were formed by mixing Hep with LL-37 in such a way that the resulting $PPCs_{LL\text{-}37\text{-}Hep}$ are negatively charged (see Figure II. 2). As turbid solutions were obtained, turbidimetry was used to monitor the formation of $PPCs_{LL\text{-}37\text{-}Hep}$. Another significant parameter is their size, which was assessed through dynamic light scattering (DLS). In order to confirm the negative charge of the $PPCs_{LL\text{-}37\text{-}Hep}$, ζ-potential measurements were performed.

The negatively-charged $PPCs_{LL\text{-}37\text{-}Hep}$ were then assembled with Chi using the LbL approach. Chi was used since it is a weak polybase and thus it is positively charged under its pK_a value, which ranges between 6.46 and 7.32 depending on the degree of acetylation.[4] Moreover, it possesses antimicrobial properties, making it an ideal compound for our final goal. As a matter of comparison, bare LL-37 molecules were LbL-assembled with Hep. The multilayers were assembled using solutions with I as low as possible (close to zero) and a pH value of pH 3.5 or 5. These pH conditions were chosen in relation to the pKa of Chi. The total hydrated mass adsorbed on the surface was monitored by QCM-D. Since, on the one hand, three species were used to build the $PPCs_{LL\text{-}37\text{-}Hep}$-based multilayer, and on the other hand only two for the classical assembly, completely different film organization and architecture are expected to be observed. This may affect the water content of the multilayers. Therefore, the dry thickness of the multilayers was investigated and measured by ellipsometry. In addition, an in-depth analysis of the multilayer composition was conducted by X-ray photoelectron spectroscopy (XPS), which is presented in *Part IV – Results and discussion – Chapter 2*. The results related to $PPCs_{LL\text{-}37\text{-}Hep}$ size and surface electrical properties, as well as the properties of the multilayers, are presented in *Part IV – Results and discussion – Chapter 3*. Importantly, the effect of pH will be

extensively discussed throughout this work, while the effect of I will not be considered, as it was maintained close to 0 mM during all stages of PPCs formation and multilayer construction. However, it is important to note that the absence of discussion on I does not imply that this parameter lacks significance regarding multilayer formation, structure and function, as highlighted in *Part I – Context of the research*.

With the goal to design antibacterial coatings, the ability to maintain the antibacterial activity of LL-37 is critical. It has been demonstrated that this activity is conformation-dependent and function of the concentration. Therefore, the conformation of LL-37 in different media, *i.e.*, ethanol, ultrapure water and phosphate-buffered saline (PBS) was investigated. To do so, circular dichroism (CD) measurements were performed on bare LL-37 and $PPCs_{LL\text{-}37\text{-}Hep}$ solutions. This enables the assessment of the secondary structure of free or complexed LL-37. As far as concentration is concerned, the aim is to immobilize as much active LL-37 as possible on the surface. The design of the coatings has a direct impact on the quantity of LL-37 incorporated into these multilayers. Therefore, we varied the pH, adjusted the number of bilayers, and changed the building block (either bare LL-37 or $PPCs_{LL\text{-}37\text{-}Hep}$) to understand their respective influence on the growth of LbL films. LL-37 in the multilayers was quantified using bicinchoninic acid (BCA) assays. Once the multilayers have been built, their stability was monitored by studying the release profiles. Given that LL-37 must bind to bacterial membranes to fulfill its antibacterial function, it is compelling to assess the proportion of LL-37 released from the multilayers into the medium and the one retained on the surface. This study was performed in a simple buffer, mimicking the physiological pH conditions, *i.e.*, the PBS, and with a fluorescein isothiocyanate labelled LL-37 (FITC-LL-37). The amount of released LL-37 was thus monitored by fluorescence measurements. The results related to LL-37 conformation, and to the amount of LL-37 in and released from the multilayers are presented in *Part IV – Results and discussion – Chapter 4*. Contrary to enzymes such as Lyz, LL-37 activity cannot be evaluated using enzymatic activity tests, but must be directly investigated on bacteria, which renders the task rather intricate. Indeed, it is well established that antibacterial properties of a drug are highly dependent of the experimental conditions, such as the medium and the bacterial species and strains. Therefore, before studying the implication of LL-37 on biofilm formation, the conditions in which

experiments should be performed needed to be fixed. To do so, the solubility of LL-37 was assessed in different commonly used bacterial growth media, *i.e.*, Mueller Hinton broth (MHB), Luria-Bertoni (LB) medium, tryptic soy broth (TSB), and Roswell Park Memorial Institute (RPMI) medium. As discussed in *Part IV – Results and discussion – Chapter 5*, RPMI is the medium chosen to study the antibacterial effect of LL-37 on a reference *S. aureus* strain (*ATCC 33591*), a reference *S. epidermidis* strain (*ATCC 35984*) and a clinical *S. epidermidis* strain (*10168*). Finally, the effect of the coating on the biofilm formation of the two *S. epidermidis* strains was further investigated by studying the biomass, the metabolism, and the bacterial viability of biofilms. In an effort to combine preventive and therapeutic strategies, we have explored the synergistic effects of coating with antibiotics, *i.e.*, vancomycin, tobramycin, doxycycline and linezolid, and bacteriophages. This study of antibacterial activity is presented in *Part IV – Results and discussion – Chapter 5*.

The global strategy that was followed in this work with a view to better understand the LbL immobilization of LL-37 and to evaluate its antibacterial properties on staphylococci biofilms is depicted in Figure II. 2.

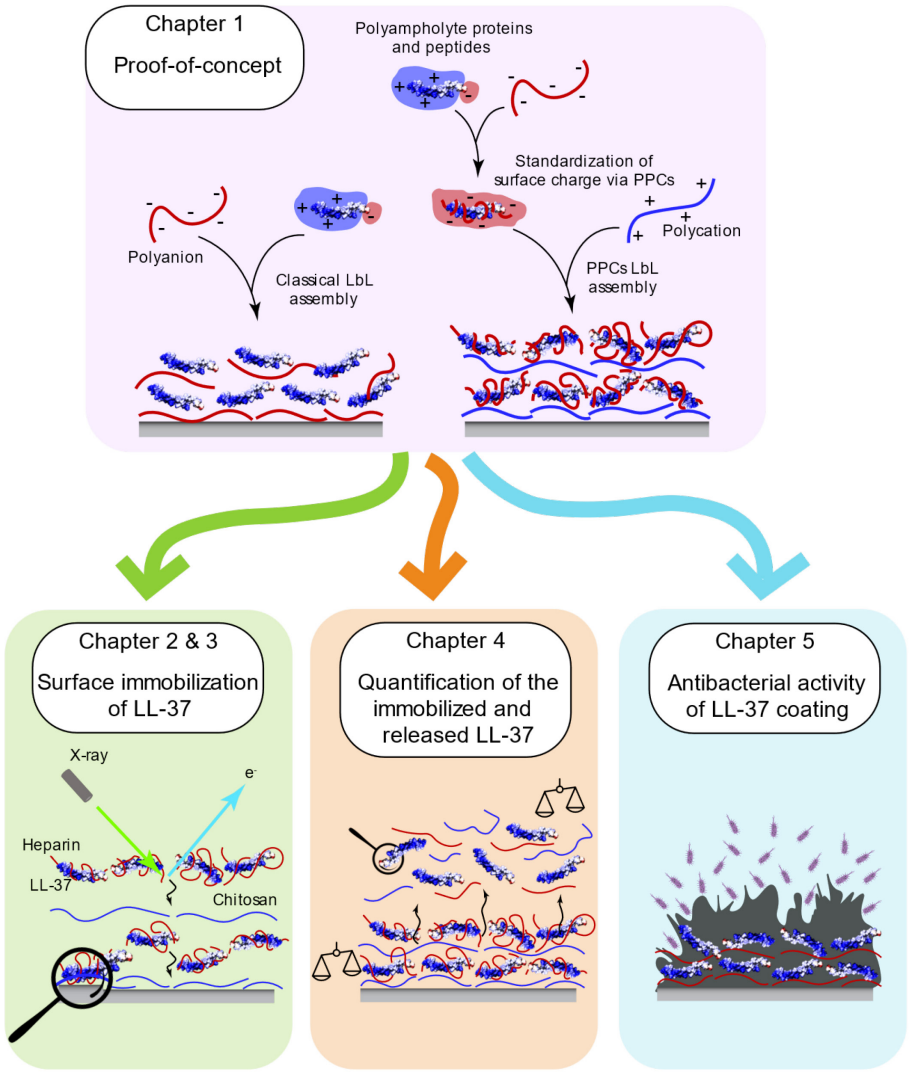

Figure II. 2 – Strategy of the thesis. LL-37 is first complexed with Hep. The Hep-to-LL-37 ratio is adjusted in such a way that the resulting $PPCs_{LL\text{-}37\text{-}Hep}$ are negatively charged. The immobilization of $PPCs_{LL\text{-}37\text{-}Hep}$ with Chi, as well as the immobilization of bare LL-37 molecules with Hep (not represented on this schematic) is performed and their properties are investigated. Then, the LL-37 immobilized in the multilayers and released from the multilayers is quantified. Finally, the antibacterial properties of LL-37-based coatings are studied.

3 References

1. vander Straeten, A. Protein-polyelectrolyte complexes for the surface immobilization of bioactive proteins. (PhD Thesis, UCLouvain, 2019).
2. vander Straeten, A., Bratek-Skicki, A., Jonas, A. M., Fustin, C.-A. & Dupont-Gillain, C. Integrating Proteins in Layer-by-Layer Assemblies Independently of their Electrical Charge. *ACS Nano* **12**, 8372–8381 (2018).
3. Behrens, C. *et al.* Development of a system of heparin multilayers on titanium surfaces for dual growth factor release. *J Biomed Mater Res A* **110**, 1599–1615 (2022).
4. Domard, A. pH and c.d. measurements on a fully deacetylated chitosan: application to CuII—polymer interactions. *Int J Biol Macromol* **9**, 98–104 (1987).

Part III – General methods

1 General methods

In this part, the main methods that were used throughout this thesis are presented. Emphasis is put on the working principle and the information it brings. The operating details are presented in the experimental section of each chapter in *Part IV – Results and discussion*.

1.1 PPCs formation

PPCs formation was monitored using turbidimetry, DLS, electrophoretic mobility, and CD measurements. In the following, the technical principle of these methods is briefly presented.

1.1.1 Turbidimetry

Turbidimetry is based on the measurement of the degree of turbidity of a suspension. It is determined by the loss of intensity, due to light scattering, of a light beam passing through the suspension (Figure III. 1). This light scattering, unlike absorption, does not occur at a specific wavelength. It results in a general elevation of the signal caused by the decreased intensity of the detected light. Buchhammer *et al*. have shown that turbidity can be related to the concentration, size and polydispersity of the PPCs suspension.[1] Importantly, our group has also demonstrated that the turbidimetry can be used to estimate the charge ratio at which the protein charge is overcompensated by the added PE.[2] This informs on the charge ratio (or molar ratio) necessary to obtain a PPCs. In the following, turbidimetry measurements were thus used to monitor PPCs formation as a PE is added to the protein solution.[3]

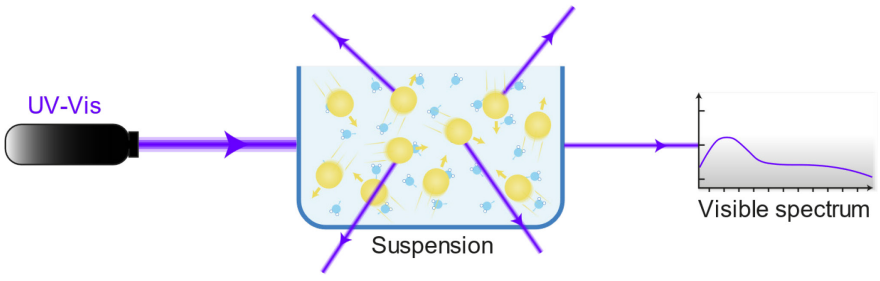

Figure III. 1 – Schematic representation of the turbidimetry principle.

1.1.2 Dynamic light scattering

DLS is a well-established technique for particle size analysis in the nanometer range. It provides information on the hydrodynamic radius (R_h) as well as on particle size distribution. In DLS, the Brownian motion of dispersed particles is measured by recording the scattered light signal. In practice, a single frequency laser beam is directed to the sample. The particles scatter the light and thereby imprint information about their motion as a function of time. This scattered light density is measured at 90° in our case (Figure III. 2). Then, the correlation function is computed. It is a mathematical description of the fluctuations of the scattered light. In fact, larger particles are moving at slower speeds than smaller particles. The consequence is that the correlation is slowly lost for large particles and rapidly lost for small particles. This feature is shown in Figure III. 2. Once the correlation function has been found, the translational diffusion coefficient, *i.e.*, the speed of the particles, is determined from different mathematical analyses. Finally, the relation between the speed of the particles and R_h is given by the Stokes-Einstein equation. The choice between the mathematical algorithms used to extract the DLS data is motivated by the polydispersity of the suspension (monodisperse vs. polydisperse). In this work, polydisperse suspensions were always assumed and a CONTIN algorithm (Laplace Transform inversion) was used.

It is important to keep in mind that the particle size of the sample is not measured directly but its determination is based on the particle motion, fitting the correlation functions. Therefore, R_h refers to the particle size of spherical and smooth particles which diffuse at the same speed as the particles of the sample. If one or several size distributions are obtained, it means that the mathematical model fits the correlation functions with respectively one or several spherical particles that have the given size. Interestingly, for rod-like particles, the fitting could give two populations that correspond to the diameter and the length of the particle. This shows the limits of this technique.

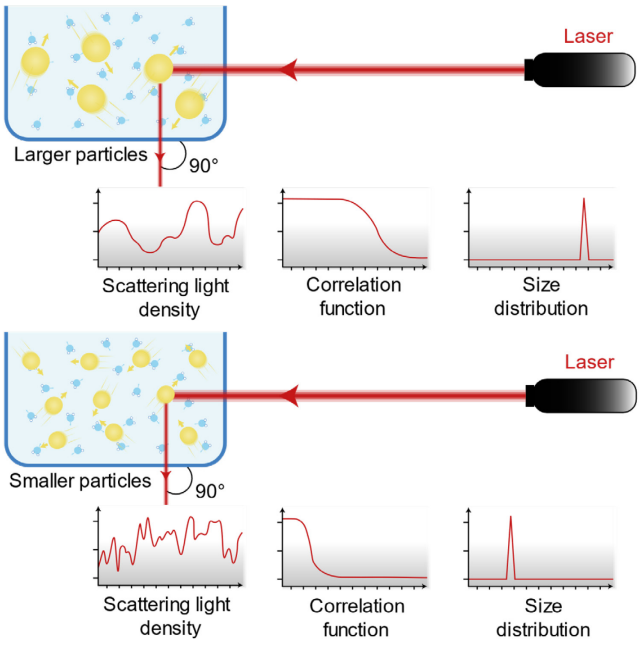

Figure III. 2 – Schematic representation of the DLS principle applied to a suspension of small and large particles.

1.1.3 Electrophoretic mobility

The ζ-potential, *i.e.*, the electrokinetic potential, is caused by the presence of electrical charges at interfaces. As presented in the *Part II – Aim and Strategy of the thesis*, analyzing the charge of the surface of PPCs is important. Since PPCs exhibit solid-like characteristics, *i.e.*, similar to precipitates in a solution, the ζ-potential measurement, via the electrophoretic mobility, will thus be described in the context of solid-liquid interfaces. This description also applies to tiny charged entities such as proteins. The charging behavior at the solid-liquid interface and the definition of the ζ-potential are explained using the model of the electrical or electrochemical double layer shown in Figure III. 3.[4] Upon contact with an aqueous solution, a solid surface becomes charged, resulting in an interfacial charge distribution that differs from that of the bulk of the solution. As depicted in Figure III. 3, positively-charged species accumulate at the interface of a negatively-charged particle. In the frame of the electrical double layer model, two layers can be distinguished: a stationary immobile layer and a diffuse mobile layer. The stationary layer comprises charged species that are strongly adsorbed onto the surface

through short-distance interactions. The diffuse layer consists of mobile charged species that compensate the surface charge through thermal motion and coulombic attraction. By applying a voltage across a pair of electrodes in the solution, charged species are put in motion and their electrophoretic mobility is measured using a Doppler anemometer, which analyzes speed and direction. The surface charge density that is obtained originates from the boundary between the stationary layer and the diffuse layer of counterions. This boundary is known as the shear plane (see Figure III. 3). Electrophoretic mobility measurement thus allows to assess the charge density at the shear plane, *i.e.*, the ζ-potential. The surface potential (Ψ_S) of the solid is not experimentally accessible.[4]

This method has been widely used to investigate the electrical characteristics of PPCs. Notably, Štajner *et al.* conducted extensive research on the complexation of Lyz with PSS.[5] They used this technique to evaluate the charge of PPCs in relation to the PSS-to-Lyz ratio. Their findings indicate that upon initial addition of PSS to Lyz, $PPCs_{Lyz\text{-}PSS}$ exhibit a positive charge attributed to the excess of Lyz charge. Subsequently, with further addition of PSS, the charge of $PPCs_{Lyz\text{-}PSS}$ is inversed, resulting in negative values due to the PSS excess. These findings are consistent with previous studies, indicating the suitability of this method for assessing the charge properties of PPCs.[3,5]

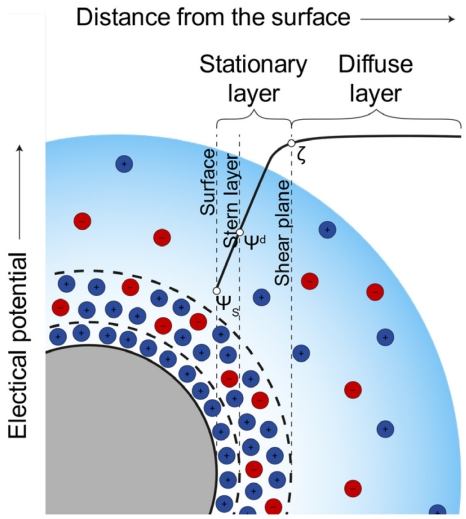

Figure III. 3 – Model of the electrochemical double layer at the solid-liquid interface. Ψ_S is the surface potential, Ψ^d the stern potential, and ζ the zeta potential. Adapted from Luxbacher.[4]

1.1.4 Circular dichroism

CD is a very sensitive spectroscopy technique commonly used to analyze chirality in molecules through their optical activity. It is widely used to elucidate the structure of biomolecules such as proteins and nucleic acids. In this work, the technique was used to determine the conformation of LL-37 in solution. As illustrated in Figure III. 4, the principle is based on the difference in the absorption of right- and left-circularly polarized (RCP and LCP) light by optically-active substances. Therefore, to be detected by CD, molecules must be asymmetrical, and thus must have one or more chiral chromophores. As with linear polarized light, circularly polarized light can be absorbed by a sample. When LCP and RCP lights of the same amplitude are superimposed, they produce a linearly polarized light. However, based on the Beer-Lambert law, the LCP and RCP molar absorption coefficients, for a given sample, are different. The difference in molar absorption coefficient is known as the molar circular dichroism. Basically, since the two circularly polarized lights are absorbed in different amounts, the change in amplitude of LCP and RCP lights means that superimposed light is no longer linearly polarized but becomes elliptically polarized. The difference in absorption of the RCP and LCP light can be measured and quantified, and CD spectrum is often represented by degrees of ellipticity (Θ). Importantly, the change in polarization is a function of wavelength, as well as the absorbing molecules' structure, which depends on the concentration, the temperature, and the environment conditions of the sample.[6]

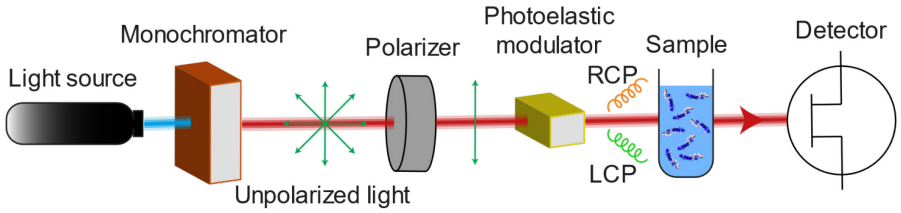

Figure III. 4 – Schematic representation of CD spectroscopy.

1.2 Multilayer formation

QCM-D, ellipsometry, XPS and BCA assay were used in order to assess the multilayer construction and to quantify the mass of immobilized LL-37.

1.2.1 Quartz crystal microbalance with dissipation monitoring

QCM-D is a powerful acoustic method that allows to monitor the real-time surface adsorption and desorption phenomena. A piezoelectric quartz crystal is embedded between two gold electrodes and the application of a voltage results in mechanical deformation. Therefore, by alternating voltage, an oscillatory motion can be obtained. In QCM-D, the resonant frequency (f_0, in Hz) of the quartz crystal is measured. Upon adsorption of any material on the gold surface, the resonant frequency changes, and a frequency shift (Δf) is recorded (Figure III. 5).

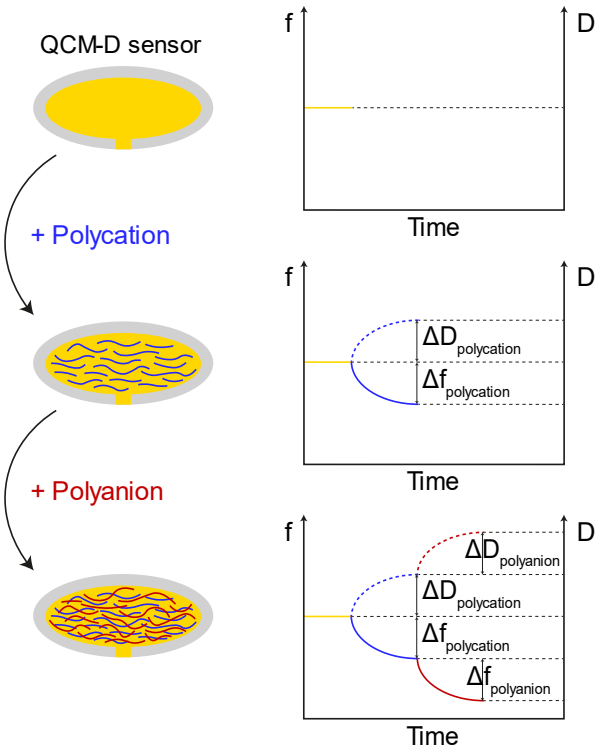

Figure III. 5 – Schematic representation of the QCM-D principle. The Δf and the ΔD, observed after each adsorption step, can be related to the adsorbed mass/thickness of the film and to the viscoelasticity of the adsorbed layer.

If the deposited layer is thin (<250 nm), homogeneous, and rigid, Δf can be directly related to the adsorbed mass (Δm) according to the Sauerbrey equation (Equation III. 1):[7]

$$\Delta m = \frac{-c}{n}\Delta f \quad with\ c = \frac{t_q \rho_q}{f_0}$$ Equation III. 1

where n is the harmonic number, c the mass sensitivity constant (property intrinsic to the crystal), t_q the thickness of the crystal, and ρ_q the volumetric mass density. Typically, the Sauerbrey equation can be used if the different overtones are superimposed after normalization by the overtone number.[7] However, this equation is not always applicable because the deposited material layers can be soft, heterogeneous, or thick. They can also be swollen with water and thus highly viscoelastic. This is especially the case with biological molecules. To assess the film viscoelastic properties, and, *in fine*, the Sauerbrey applicability, the dissipation (D) is also measured by QCM-D. It corresponds to the vibration energy dissipated in the adsorbed layer after turning off the alternate voltage. The viscoelastic properties of the layer are given by the vibration decay. The longer the decay, the more rigid the adsorbed layer. A rigid deposited material follows the crystal oscillation without deformation and consequently gives low D. In that case, the Sauerbrey equation can be used. Therefore, by measuring the shift of D (ΔD) between two adsorption steps of matter, the viscoelastic changes can be probed. Simultaneous measurement of Δf and ΔD can thus give relevant information about the properties of the adsorbed layer. Viscoelastic models, such as the Voigt-Voinova and Johannsmann models, can be used to estimate the thickness of viscoelastic films.[8–10] However, the use of such models is not trivial, especially with complex systems made of several layers with different properties. In such case, fitting procedures and necessity of approximations sometimes do not lead to converging results. It is also important to mention that water coupled to the adsorbed layers is included in the deduced mass/thickness, which is thus a hydrated mass/thickness.

Concretely, Figure III. 6a presents the Δf resulting from adsorption via the LbL assembly of a polycation, poly(L-arginine hydrochloride) (PAR), with various polyanions: alginate (ALG), chondroitin sulfate A (CSA), hyaluronic acid (HA), heparin (HEP), poly(l-glutamic acid) (PGA), and poly(styrene sodium sulfonate) (PSS).[11] Depending on the nature of the film, the growth pattern

is different. Between all combinations, PAR/HA has the strongest exponential behavior. These results highlight that QCM-D is a powerful technique for studying the growth of films immobilized on material surfaces. The thickness of these films was determined from the Δf using the model developed by Voinova *et al*. (Figure III. 6b).[8,11]

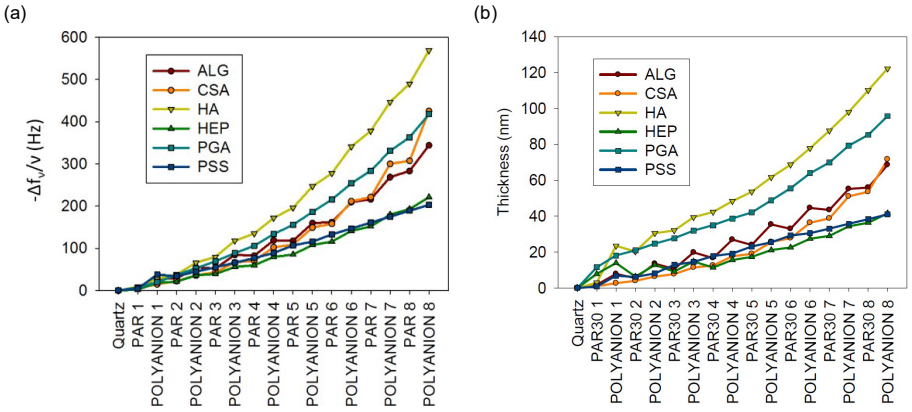

Figure III. 6 – Buildup of (PAR/polyanion)$_8$ multilayer film on a SiO_2-coated crystal followed by QCM-D with ALG (dark red), CSA (orange), HA (light green), HEP (dark green), PGA (light blue), and PSS (dark blue) as polyanions. (a) Evolution of the normalized frequency $-\Delta f_v/v$ (for v = 3) as a function of the number of adsorbed layers. (b) Evolution of the estimated thickness as a function of the number of adsorbed layers. Reproduced from Mutschler *et al*.[11]

The main advantage of QCM-D monitoring is that *in situ* and real time measurements are feasible. The sensor frequency is continuously recorded, which allows to have real-time information on adsorption, desorption, kinetics, and influence of rinsing steps. The main disadvantages of this technique are that it records mass gains or losses without identifying the nature of the compounds being adsorbed or desorbed, and, as explained before, data treatment is not trivial. The calculated adsorbed mass or thickness of the deposited film may highly depend on the chosen model. As already said, the Sauerbrey equation can be used if the different normalized overtones are superimposed. It can also be applied even if the model assumptions are not met, *e.g.*, for the adsorption of soft matter, such as proteins, forming hydrated heterogeneous layers. In these conditions, it is worth mentioning that the application of the Sauerbrey equation will give the lower limit of the adsorbed mass value. According to Reviakine *et al.*, the

Sauerbrey equation can be used as long as $\left|\Delta D_n/(\frac{\Delta f}{n})\right|$ << 4 × 10^{-4} Hz^{-1} for a 5 MHz crystal.[7] This criterion needs to be monitored for each studied system and even for each adsorption experiment, to take the appropriate decision on data treatment.

In the following, QCM-D sensors will be first covered with two bilayers of polycations and polyanions, as anchoring layer, before monitoring adsorption and desorption of proteins, peptides and PEs in several conditions. For the sake of clarity, not all overtones, but only the 7^{th}, will be presented in this work. Nevertheless, they were systematically measured to guarantee the appropriate use of the Sauerbrey equation when required. Therefore, when applicable, this equation will be used to quantify the adsorbed mass, or more exactly the hydrated adsorbed mass. In our work, this technique is combined with ellipsometry, the latter being used to determine the dry thickness, and *in fine*, the water content of the multilayer films.

1.2.2 Ellipsometry

Ellipsometry is a non-destructive optical technique widely used to analyze surfaces with the goal to obtain information about composition, refractive index, roughness, and thickness of thin films. This latter application will be exploited in this thesis as it allows the measurement of film thickness ranging from sub-nanometers to a few microns. As illustrated in Figure III. 7, the principle relies on the change of polarization state of light upon reflection from the thin film, which depends on the properties of the sample. The polarization goes from linear to elliptical. Without detailing the underlying complex mathematical theory, this change is represented and measured as an amplitude ratio (Ψ) and a phase difference (Δ).

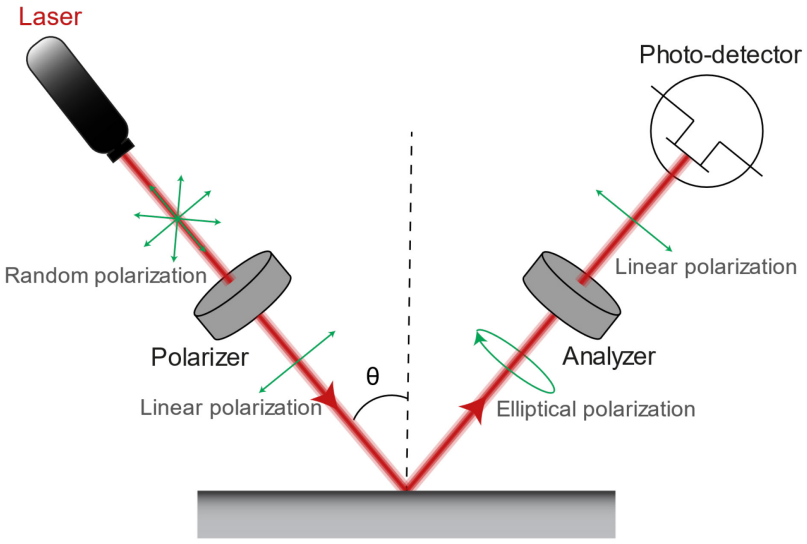

Figure III. 7 – Schematic representation of an ellipsometry experimental set-up.

The main advantage of ellipsometry lies in its rapid measurement of a key parameter for monitoring LbL assembly, *i.e.*, the dry thickness. However, ellipsometry is an indirect technique, as it relies on the use of known models and regression-based data fitting procedures. Therefore, the main drawback is that assumptions need to be made to use these models. It is indeed assumed that the analyzed layer is homogeneous and smooth. In this work, all the samples were similar, namely multilayers composed of LL-37, Hep and Chi adsorbed on a Si wafer. The Si wafer was described as two distinct layers, *i.e.*, an elemental Si bulk covered by an oxidized layer of SiO_2. The samples were then modelled as follows: Si/SiO_2/ [LL-37-Hep-Chi], and the multilayers built in different conditions were considered as continuous films having the same properties, which is a simplification of the reality. However, the same assumptions of homogeneous and continuous film were done for all the measurements, so that the obtain values can be compared. Therefore, to measure the dry thickness of thin films, a refractive index (n) of 1.46 and an absorption coefficient (k) of 0 have been considered. The refractive index was set at 1.46 based on the work of Lundin *et al.*, who studied multilayers composed of Hep and Chi.[12]

1.2.3 X-ray photoelectron spectroscopy

XPS is a surface-sensitive technique used to analyze the outermost 1-10 nm of material surface. Based on the photoelectric effect, it allows to characterize the chemical composition of interfaces. In practice, the sample is irradiated with X-ray photons and core-level electrons are ejected from atoms. Expelled photoelectrons are recovered in the hemispherical analyzer and their kinetic energy is measured at the detector (Figure III. 8).

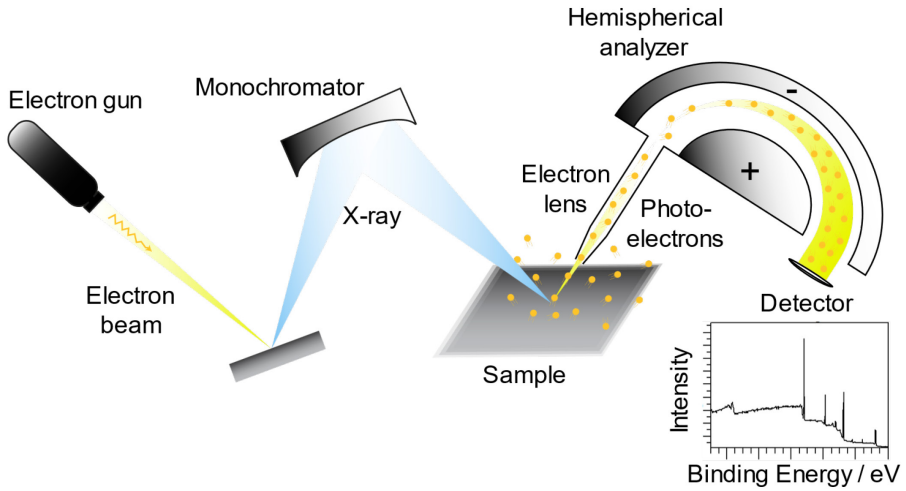

Figure III. 8 – Schematic representation of the XPS principle.

Knowing the kinetic energy of electrons and the energy of X-rays, the binding energy of each electron can be obtained through the energy conservation principle. This binding energy is highly specific to each element and core level, and also depends on the neighboring atoms and the oxidation state of the atoms. For example, carbon electrons from a C=O bond appear at a higher binding energy than carbon electrons from a C-H bond. Oxygen being more electronegative than hydrogen, the electrons are more difficult to extract due to the reduced electron density around carbon atoms, and the binding energy is higher. Therefore, XPS gives information about the elemental composition of the sample and the chemical functions in which atoms are involved.[13] Each peak attributed to a core level of a given element can be decomposed into contributions representing the chemical environment of this element, which can be translated in the chemical functions in which this element is involved. For example, Figure III. 9

represents the decomposition of C 1s spectrum into four components at 289.0 eV ($C^{289.0}$), 287.9 eV ($C^{287.9}$), 286.3 eV ($C^{286.3}$) and 284.8 eV ($C^{284.8}$), corresponding, respectively, to carboxyl groups O=**C**-O, amide groups N-**C**=O, O-**C**-O or **C**=O links, amine or alcohol groups **C**-(N,O) and aliphatic carbon chains **C**-(C,H). In our study, the information from XPS spectra was obtained after Shirley-type background correction. Peak decomposition was performed after deconvolution, which aims at correcting for instrumental peak broadening. A mixed Gaussian/Lorentzian line shape with a ratio of 85:15 was used for peak components, as recommended by the manufacturer of the used XPS instrument.

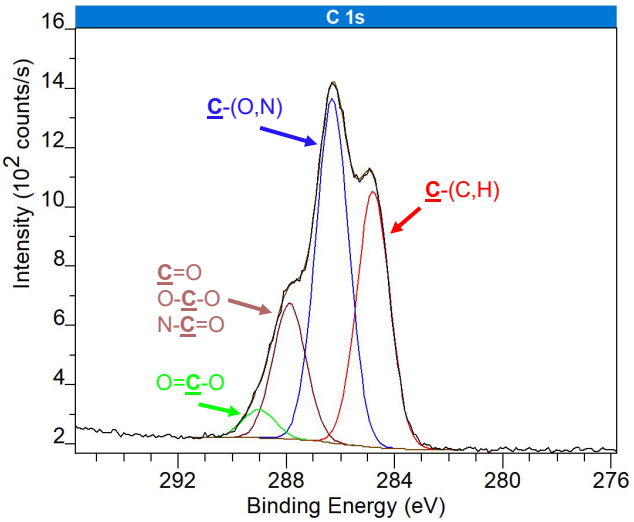

Figure III. 9 – C 1s peak recorded by XPS and decomposed into its four contributions.

Each component is characterized by a minimum of three parameters: height or area, full width at half maximum intensity (FWHM), and position (binding energy).[13] The FWHM is the convolution of three main contributions: the intrinsic line width (ΔE_n; the line profile is of Lorentzian character), the width of the excitation source (ΔE_x; the X-ray line is assumed to be Lorentzian) and the width of the kinetic energy analyzer (ΔE_p; the energy analyzer function is of Gaussian character).[13] In our study, the Gaussian/Lorentzian ratio (85:15) is maintained consistently across all peak components. We also introduced constraints in the iteration process, such as peak intensity ratios, equality of FWHM, and imposed binding energy (the aliphatic carbon component is fixed at 284.8 eV). Peak decomposition requires careful consideration due to the

large number of involved variables. The best fit provided by a computer does not always represent a unique solution or one with meaningful physical interpretation. Therefore, common sense and knowledge of the analyzed systems are required when appreciating the variation of the best-fitting parameters from one spectrum to another one.[13]

Only the photoelectrons extracted from the extreme surface layers are detected and participate to the signal. The electrons from atoms located deeper in the sample undergo collisions preventing them to be excerpted from the sample or making them appear in the background of the XPS spectrum. Quantification of each element present at the interface is done using sensitivity factors, which convert the area underneath each peak into atomic percentage. Except for hydrogen and helium, all elements can be detected and quantified, even if their molar fraction is low (limit of detection of the order of 0.1%).

Since it gives a very precise quantification of the elements present at the extreme surface of a material, XPS will be used in this work to obtain the surface chemical composition of LbL multilayers.

1.2.4 Bicinchoninic acid assay

BCA assay is a sensitive method for determining the total concentration of protein in a solution. The principle is based on the Biuret reaction. The amide bonds of proteins reduce Cu^{2+} to Cu^{+}. The resulting Cu^{+} form an intense purple-colored complex with the BCA salt in alkaline condition (Figure III. 10). The absorbance of this complex is then measured at 562 nm. The color produced by this reaction is stable and increases proportionally over a wide working range of protein concentrations (5-250 µg mL^{-1}). The advantage of this assay is that a detergent can be added to dissolve the multilayers and subsequently quantify the amount of protein released. In this work, BCA will be useful to quantify LL-37 in multilayers and 1% of sodium dodecyl sulfate (SDS) was used to dissolve the multilayers.[14]

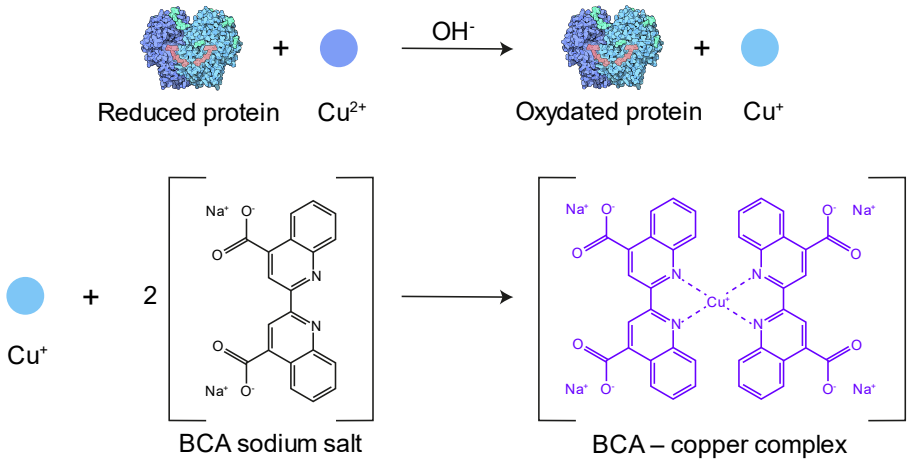

Figure III. 10 – Reaction of BCA assay. The amide bond of the protein reduces Cu^{2+} to Cu^{+}, which then reacts with the bicinchoninic acid to form a colored complex.[14]

1.3 Evaluation of antibacterial properties

Finally, the influence of LL-37-based multilayers on biofilm formation has been assessed. Studying the antimicrobial effect of multilayers is an important part of the research strategy. The evaluation of the MIC of LL-37 in solution was first performed to better understand its antibacterial behavior. Resazurin assay, crystal violet staining and counting of CFUs were performed to study the antibacterial effect of active compounds brought in solution (LL-37, antibiotics, phages) and of multilayers on biofilm formation.

1.3.1 Minimum inhibitory concentration

MIC is defined as the lowest concentration of an antimicrobial agent that inhibits the visible growth of bacteria under defined test conditions.[15] MIC is often used as a research tool to determine the *in vitro* activity of antimicrobial substances. In practice, the effect of an antimicrobial agent is studied in a microtiter plate by doubling dilutions of the highest tested antimicrobial concentration. After the incubation of bacteria in presence of the antimicrobial drug, the presence of turbidity or a sediment indicates growth of the organism. MIC is the lowest antimicrobial concentration that prevents the presence of this turbidity or sediments (Figure III. 11).

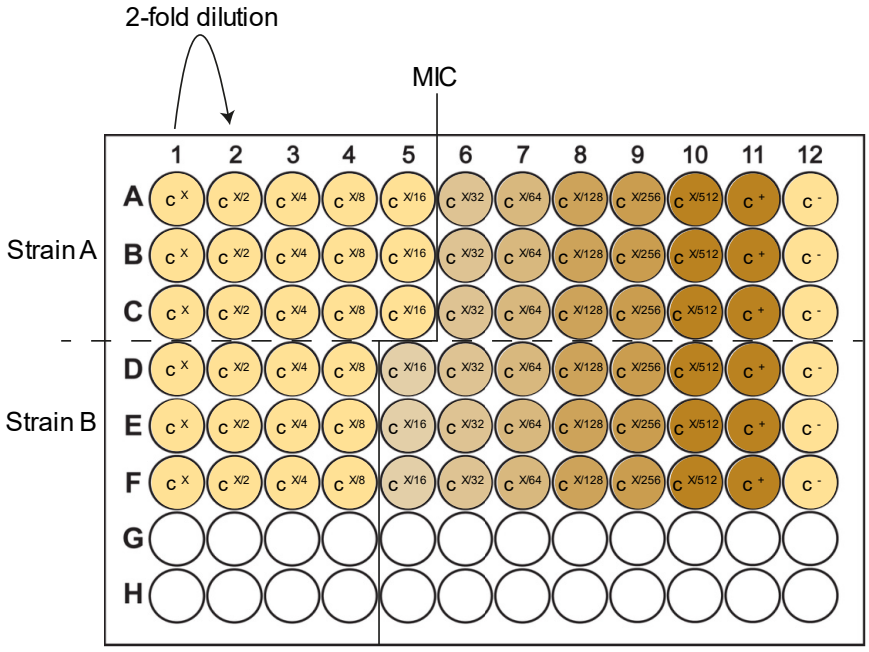

Figure III. 11 – Outline of the setup of a microtiter plate for antimicrobial susceptibility testing with doubling dilutions of one antimicrobial agent on two different bacterial strains. C, the antimicrobial drug concentration; X, the highest concentration tested (µg mL^{-1}); C^+, growth control (broth with bacterial inoculum and no antimicrobial drug); C^-, sterility control (broth only).

1.3.2 Bacterial viability assay

This assay aims at estimating the number of living bacterial cells present in biofilms. A conventional approach to quantifying viable bacterial cells in a sample involves culturing on solid media, a method initially developed by Robert Koch in 1881.[16] In the setting of biofilm study, bacteria are typically detached from their substrate and dispersed in a buffer solution using mechanical techniques such as scraping and sonication in an ultrasound bath. Following this resuspension step, bacteria are diluted serially, plated on solid agar medium, and incubated for a variable duration depending on the selected bacterial strains and culture conditions (Figure III. 12). After growth, CFUs are counted. Standard round Petri dishes containing 25 to 250 CFUs are usually considered for quantitative analysis, while the lower limit of detection is 1 CFU.[17] One drawback of this method is the risk

of underestimating the bacterial count in the sample as a subpopulation of viable but non-culturable bacteria may be present or still attached to the substrate.

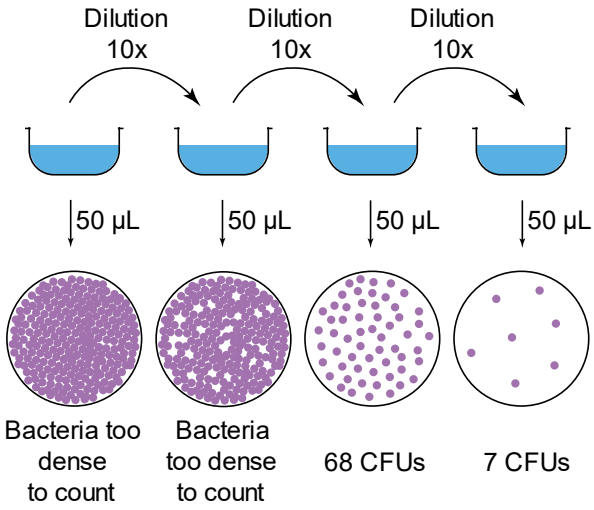

Figure III. 12 – Procedure for CFUs counting. After a serial 10x dilution, bacteria are plated on solid agar medium. The plates are incubated to allow bacterial growth, and the CFUs are finally counted.

1.3.3 Bacterial metabolic assay

Metabolic assays are frequently used to investigate bacterial development and biofilm formation as well as their response to antimicrobial treatments. Among these, resazurin staining assay is a sensitive metabolic activity test that allows to depict the viability of mammalian cells and bacteria. The principle is that living cells are metabolically active and are able to reduce resazurin, a blue, non-fluorescent and non-toxic dye, to resorufin, a pink-fluorescent dye (Figure III. 13). The recorded fluorescence is proportional to the number of viable cells, or more precisely to the metabolic activity, over a wide concentration range. It is measured at 590 nm with an excitation wavelength of 550 nm. The advantage of the assay is its reproducibility and rapidity. Indeed, it is less time consuming than CFUs counts. However, it is limited by narrow linear ranges (from 5 to 8 $\log_{10}$ CFU/well for resazurin assays), which reduces its interest in case of a large treatment effect.[18]

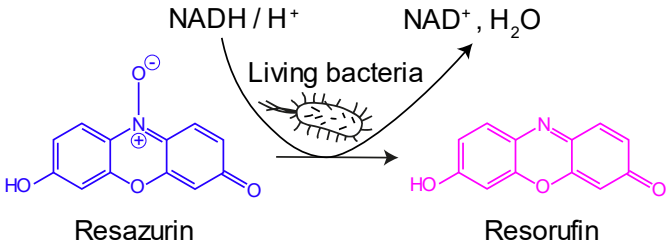

Figure III. 13 – Reaction of resazurin assay. The living cells metabolize resazurin to resofurin, a strongly-pink fluorescent dye.

1.3.4 Bacterial biomass assay

The determination of the total amount of biological materials of biofilms, which includes the EPSs, and live and dead bacteria cells, is crucial to estimate the formation and the development of biofilms.[19] The most common technique used for this purpose involves staining heat-fixed biofilms with crystal violet, a cationic dye that binds to anionic molecules, and subsequently dissolving them in acetic acid. The concentration of crystal violet in the supernatant, which is directly correlated to the quantity of biological compounds of biofilms, is then determined by absorbance at 570 nm (Figure III. 14).[19] This method presents the advantage of staining any microorganism cell and avoiding the need to detach the biofilm from the surface. Nevertheless, the results exhibit considerable variability due to potential detachment of pieces of biofilm during the repeated washing steps, and moreover, part of the measured biomass could originate from planktonic cells settling onto the biofilm. Finally, this method lacks specificity and does not differentiate between live and dead bacteria.[20]

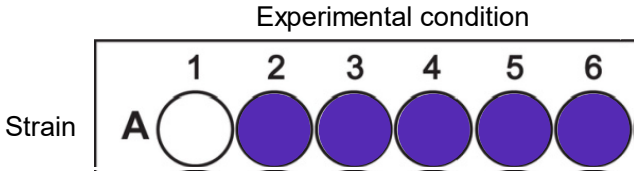

Figure III. 14 – Crystal violet staining of wells was performed. The absorbance of light was measured at 570 nm using a spectrophotometer.

2 References

1. Buchhammer, H. M., Mende, M. & Oelmann, M. Preparation of monodisperse polyelectrolyte complex nanoparticles in dilute aqueous solution. *Prog Colloid Polym Sci* **124**, 98–102 (2004).
2. vander Straeten, A. *et al.* Protein–polyelectrolyte complexes to improve the biological activity of proteins in layer-by-layer assemblies. *Nanoscale* **9**, 17186–17192 (2017).
3. Kayitmazer, A. B., Seeman, D., Minsky, B. B., Dubin, P. L. & Xu, Y. Protein-polyelectrolyte interactions. *Soft Matter* **9**, 2553–2583 (2013).
4. Luxbacher, T. The ZETA Guide: Principles of the Streaming Potential Technique. (Anton Paar GmbH, Austria, 2014).
5. Štajner, L., Požar, J. & Kovačević, D. Complexation between lysozyme and sodium poly(styrenesulfonate): The effect of pH, reactant concentration and titration direction. *Colloids Surf A Physicochem Eng Asp* **483**, 171–180 (2015).
6. Subadini, S., Hota, P. R., Behera, D. P. & Sahoo, H. Circular Dichroism Spectroscopy: Principle and Application. in *Optical Spectroscopic and Microscopic Techniques: Analysis of Biological Molecules* (ed. Sahoo, H.) 19–33 (Rourkela, 2022).
7. Reviakine, I., Johannsmann, D. & Richter, R. P. Hearing What You Cannot See and Visualizing What You Hear. *Anal Chem* **83**, 8838–8848 (2011).
8. Voinova, M. V, Rodahl, M., Jonson, M. & Kasemo, B. Viscoelastic Acoustic Response of Layered Polymer Films at Fluid-Solid Interfaces: Continuum Mechanics Approach. *Phys Scr* **59**, 391–396 (1999).
9. Johannsmann, D. Viscoelastic Analysis of Organic Thin Films on Quartz Resonators. *Macromol. Chem. Phys* **200**, 501–516 (1999).
10. Johannsmann, D. Viscoelastic, mechanical, and dielectric measurements on complex samples with the quartz crystal microbalance. *Physical Chemistry Chemical Physics* **10**, 4516–4534 (2008).
11. Mutschler, A. *et al.* Nature of the Polyanion Governs the Antimicrobial Properties of Poly(arginine)/Polyanion Multilayer Films. *Chemistry of Materials* **29**, 3195–3201 (2017).

12. Lundin, M., Solaqa, F., Thormann, E., Macakova, L. & Blomberg, E. Layer-by-Layer Assemblies of Chitosan and Heparin: Effect of Solution Ionic Strength and pH. *Langmuir* **27**, 7537–7548 (2011).
13. Genet, M. J., Dupont-Gillain, C. C. & Rouxhet, P. G. XPS analysis of biosystems and biomaterials. in *Medical Applications of Colloids* (ed. Matijevic, E.) 177–307 (New York, 2008).
14. Smith, P. K. *et al.* Measurement of protein using bicinchoninic acid. *Anal Biochem* **150**, 76–85 (1985).
15. Wiegand, I., Hilpert, K. & Hancock, R. E. W. Agar and broth dilution methods to determine the minimal inhibitory concentration (MIC) of antimicrobial substances. *Nat Protoc* **3**, 163–175 (2008).
16. Gradmann, C. Zur Untersuchung von Pathogenen Organismen (1881) in *Robert Koch: Zentrale Texte*. (Springer Berlin Heidelberg, Berlin, 2018).
17. Sutton, S. Accuracy of Plate Counts. *Journal of Validation Technology* **17**, 42–46 (2011).
18. Peeters, E., Nelis, H. J. & Coenye, T. Comparison of multiple methods for quantification of microbial biofilms grown in microtiter plates. *J Microbiol Methods* **72**, 157–165 (2008).
19. Stepanović, S. *et al.* Quantification of biofilm in microtiter plates: overview of testing conditions and practical recommendations for assessment of biofilm production by staphylococci. *APMIS* **115**, 891–899 (2007).
20. Azeredo, J. *et al.* Critical review on biofilm methods. *Crit Rev Microbiol* **43**, 313–351 (2017).

Part IV – Results and discussion

1 Layer-by-layer nanoarchitectonics using protein-polyelectrolyte complexes toward a generalizable tool for protein surface immobilization

Cédric Vranckx[1*], Laure Lambricht[2], Véronique Préat[2], Olivier Cornu[3,4], Christine Dupont-Gillain[1*], and Aurélien vander Straeten[1]

[1]Institute of Condensed Matter and Nanosciences, Bio-and Soft Matter, Université catholique de Louvain, Place Louis Pasteur, 1 bte L4.01.10, B-1348 Louvain-la-Neuve, Belgium
[2]Louvain Drug Research Institute, Advanced Drug Delivery and Biomaterials, Université catholique de Louvain, 1200 Brussels, Belgium
[3]Neuro-Musculo-Skeletal Pole, Experimental and Clinical Research Institute, Université catholique de Louvain, 1200 Brussels, Belgium
[4]Orthopaedic and Trauma Department, Cliniques Universitaires Saint-Luc, Université catholique de Louvain, 1200 Brussels, Belgium

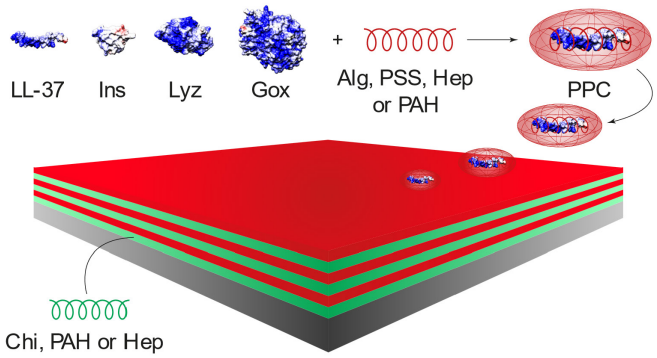

Vranckx, C., Lambricht, L., Préat, V., Cornu, O., Dupont-Gillain, C., vander Straeten, A. Layer-by-Layer Nanoarchitectonics Using Protein-Polyelectrolyte Complexes toward a Generalizable Tool for Protein Surface Immobilization. *Langmuir* **38**, 5579–5589 (2022).

Abstract

Layer-by-layer (LbL) self-assembly is an attractive method for the immobilization of macromolecules at interfaces. Integrating proteins in LbL thin films is however challenging due to their polyampholyte nature. Recently, we developed a method to integrate lysozyme into multilayers using protein-polyelectrolytes complexes (PPCs). In this work, we extended this method to a wide range of protein-polyelectrolyte combinations. We demonstrated the robustness and versatility of PPCs as building blocks. LL-37, insulin, lysozyme, and glucose oxidase were complexed with alginate, poly(styrenesulfonate), heparin (Hep), and poly(allylamine hydrochloride) (PAH). The resulting PPCs were then LbL self-assembled with chitosan, PAH, and Hep. We demonstrated that multilayers built with PPCs are thicker compared to the LbL self-assembly of bare protein molecules. This is attributed to the higher mass of protein and/or polyelectrolyte (PE) in the multilayers and/or the more hydrated state of the assemblies. PPCs enabled the self-assembly of proteins that could otherwise not be LbL-assembled with a PE or with another protein. Furthermore, the results also showed that LbL with PPCs enabled the construction of multilayers combining different proteins, highlighting the formation of multifunctional films. Importantly, we showed that the adsorption behavior and thus the multilayer growth strongly depends on the nature of the protein and PE used. In this work, we elaborated a rationale to help and guide the use of PPCs for protein LbL assembly. It will therefore be beneficial to the many scientific communities willing to modify interfaces with hard-to-immobilize proteins and peptides.

1.1 Introduction

The immobilization of active biomacromolecules is topical in biosensing,[1,2] heterogeneous biocatalysis,[3,4] drug delivery,[5,6] and tissue engineering.[7,8] In this respect, a myriad of methods was developed to functionalize material surfaces with proteins and peptides.[9] However, protein immobilization is far from straightforward because for most applications proteins should retain their bioactivity. Hence, their immobilization should protect them from denaturation and degradation.

The simplest approach to immobilize proteins is to use their tendency to spontaneously adsorb on surfaces.[10] However, in addition to affecting the protein functionality through conformation[11,12] and orientation changes,[13,14] spontaneous protein adsorption can be reversible, and the amount is often limited to a monolayer.[15–17] To limit protein desorption, chemical grafting has been used routinely. This method is not straightforward to implement since the surface must bear functional groups reacting with the protein. Moreover, chemical grafting might result in a loss of bioactivity caused by protein denaturation or reaction with the functional groups.[10,18,19] Finally, the adsorbed amount is also limited to a monolayer. Spontaneous adsorption and covalent grafting thus present major drawbacks when it comes to the immobilization of large amounts of bioactive proteins. Therefore, developing a versatile immobilization method without loss of protein activity is topical.

In 1992, Decher *et al.* demonstrated that polyelectrolyte multilayers (PEMs) can be constructed via a so-called layer-by-layer (LbL) self-assembly, *i.e.*, by alternating the deposition of oppositely-charged polyelectrolyte (PE) layers.[20,21] At each PE adsorption step, the surface charge is overcompensated, which allows the adsorption of the next layer of material. This results in the formation of a multilayer whose thickness can be precisely controlled by the number of adsorption steps.[22] Though the latter mechanism is believed to drive PEM growth, other forces, such as hydrophobic interactions and hydrogen bonding, also participate in the assembly.[23,24] One of the major advantages of LbL assembly is that it is achievable under soft conditions, *i.e.*, in aqueous solutions at room temperature, and it is versatile toward surface geometry and chemistry.[24] Therefore, the LbL assembly method has considerable potential for

developing biofunctionalized materials with a great variety of architectures.[25]

Since Decher *et al.*'s first report, the LbL method has been extended to a wide range of deposited materials[22] such as clay minerals,[26,27] viruses,[28] dendrimers,[29,30] gold colloids,[31] silica particles,[32] and proteins.[33–35] Interestingly, this versatile method enables the assembly of multicomponent protein films, which open a way to construct multifunctional systems.[36] This is topical for various fields of research such as biomaterials, drug release, tissue engineering, and regenerative medicine. Importantly, proteins, peptides, and enzymes embedded in PEMs can also find applications in continuous flow chemistry and biocatalysis, as illustrated by the use of localized enzyme-assisted self-assembly (LEASA).[37–40] While the surface protein immobilization is crucial, their alternate adsorption with a PE in LbL fashion is not straightforward. Indeed, while PEs have a homogeneous charge distribution and are flexible macromolecules, proteins are polyampholytes with various degrees of charge anisotropy and a low conformational entropy. Hence, depending on the protein, PE, pH and ionic strength (I) used for assembly, the multilayer may fail to grow.[41] The lack of charge overcompensation by the protein layer, *i.e.*, the repulsion between the PE that is further adsorbed and the protein patches of the same charge, is believed to be the major cause of this failure.[42] The ineffective LbL assembly of the highly positively-charged lysozyme (Lyz) with poly(methacrylic acid) at pH 8.4 was, for example, reported.[43] In this context, finding ways to circumvent the current limitations of protein LbL assembly with PEs is paramount.[34]

In 1996, Ariga *et al.* established that the LbL assembly of non-flexible molecules, such as proteins and organic dyes, is enhanced when they are premixed with linear polyions.[44] In 2001, Jin *et al*. found that the LbL formation of catalase microcrystals coated with poly(styrenesulfonate) (PSS) and assembled with poly(allylamine hydrochloride) (PAH) resulted in films with a better preserved enzymatic activity and a mass that was 1 order of magnitude higher than the ones obtained with uncoated catalase crystals.[45] However, this method requires protein crystals which limits its wide use. With a view to further facilitate the use of the LbL method for protein immobilization, protein-polyelectrolyte complexes (PPCs)[46,47] were recently introduced by our group as building blocks for the LbL assembly.[48,49] It was

demonstrated that the PE corona of the PPCs standardizes the charge of the protein. The result is a LbL growth that is independent of the protein surface charge. This was shown for Lyz complexation with PSS and its subsequent LbL assembly with PAH.[49] Compared to the classical LbL assembly of bare Lyz, the PPCs-based self-assembly was shown to immobilize protein that has 75% more enzymatic activity.[48,49]

However, while PPCs have shown great potential to facilitate protein LbL assembly and maintain a high level of bioactivity, only one protein has been used to date, and the suggested versatility of PPCs remains theoretical. The objective of this chapter is to investigate whether PPCs can be used to immobilize a wide range of proteins and peptides, in combination with various PEs, using the LbL method. LL-37, insulin (Ins), Lyz, and glucose oxidase (Gox) were chosen because they are involved in different biomedical and biotechnological applications. These proteins were first complexed with an oppositely-charged PE, *i.e.*, alginate (Alg), PSS, heparin (Hep), and PAH. The resulting PPCs were then assembled with a second PE, *i.e.*, chitosan (Chi), PAH and Hep to form [PE-PPCs] multilayers. LL-37 is a human antimicrobial peptide of 37 amino acids, of 4.5 kDa, with an isoelectric point (IEP) of 11. It stimulates wound healing and angiogenesis and fights infections.[50,51] Ins is a peptide hormone of 5.8 kDa, with an IEP of 5.6, that regulates glycemia and that is used as a treatment for Type I diabetes. Lyz is an antimicrobial globular enzyme of 14.3 kDa, with an IEP of 11.1. It acts against some Gram-positive bacteria, through hydrolyzation of glycosidic bonds of peptidoglycans.[52,53] Gox is an enzyme of 66 kDa, with an IEP of 5.2, that catalyzes the oxidation of glucose. It is commonly used for the detection of blood glucose concentration.[54] The use of natural PEs is attractive for biomedical applications because they are usually biocompatible, biodegradable, and/or non-toxic. Alg is a polysaccharide naturally present in brown seaweed cell walls, with residues featuring a pK_a of 3.38 and 3.65.[55] It has become one of the most important biomaterials for regenerative medicine applications.[56,57] It is a weak polyacid due to its carboxyl groups. Hep is a glycosaminoglycan, used as an antithrombotic drug, which has the highest negative charge density of any known biological polyanion due to the presence of one carboxyl and three sulfonate groups per dimer.[58] Chi is a polysaccharide derived from the chitin. This weak polycation, with an intrinsic pK_a varying from 6.46 to 7.32, depending on the degree of acetylation,[59] can be used for

its antibacterial activity.[60] More generally, the use of biodegradable PEs can also be advantageous to promote the release of proteins from the multilayers and achieve controlled delivery of active ingredients.[61] In addition to natural PEs, synthetic PEs, *i.e.*, PSS, and PAH, are also used to study the formation of PPCs and further LbL assembly. [PAH-PSS] multilayers are indeed one of the most documented PEMs.[22] PSS is a strong polyanion, due to its sulfonate groups, whereas PAH is a weak polycation with a pK_a estimated to be between 8 and 9.[62]

PPCs were first fabricated, and their formation was evaluated by measuring the turbidity of the solution. Then, the PPCs were LbL-assembled with PEs and the multilayer growth was evaluated using quartz-crystal microbalance with dissipation monitoring (QCM-D). The resulting multilayered films were compared to the ones obtained by the alternate assembly of bare proteins with PEs, *i.e.*, the classical LbL method.

1.2 Experimental section

1.2.1 Materials

LL-37 (Proteogenix, Schiltigheim, France), human Ins (Sigma-Aldrich, Steinheim, Germany), Lyz (Sigma-Aldrich, Steinheim, Germany), and Gox from *Aspergillus niger* (Sigma-Aldrich, Steinheim, Germany) were the selected proteins. Sodium Alg, M_W <75,000 g mol^{-1}, (Pronova UP VLVM, NovaMatrix, Norway), low molar mass PSS_l, M_W = 7,540 g mol^{-1}, (Scientific Polymer, Ontario, USA), and Hep sodium salt, 5,000 I.E. mL^{-1}, (B. Braun, Melsungen, Germany), were used as polyanions. Chi, M_W = 10,000-50,000 g mol^{-1} and deacetylation degree (DD) of 95% (Heppe Medical Chitosan Gmbh, Halle, Germany), and PAH, M_W = 17,500 g mol^{-1} (Sigma-Aldrich, Steinheim, Germany), were used as polycations. Solutions were prepared at I ≈ 0 mM, in ultrapure water (Elga Purelab Chorus 1, 18.2 MΩ.cm, Veolia, United Kingdom), with only the ions necessary for the pH adjustment. Chi is not soluble in ultrapure water and must be dissolved in acidic conditions. Therefore, Chi solution was obtained by first dissolving 50 mg of Chi in approximately 25 mL of ultrapure water and 60 µL of HCl 37% at 60 °C for 1 h. Then, pH was adjusted with NaOH 10 M and the volume was brought to exactly 100 mL. Finally, the Chi solution was filtered with a 5 and 0.2 µm

filters to remove small impurities and non-dissolved particles. I was kept as low as possible, with only the ions necessary for Chi dissolution and pH adjustment, and is around 10 mM. The pH value was measured using a pH-indicator strip (MQuant, Merck, Darmstadt, Germany).

1.2.2 Formation of PPCs

Since electrostatic interactions drive PPCs formation, the PE-to-protein molar ratio in the complexes is usually expressed as the PE-to-protein charge ratio. The charge ratio was calculated as the ratio of PE net charge to the protein net structural charge at a given pH. The PE charge was calculated using the Henderson-Hasselbalch equation (the ionization degree, as a function of pH, was taken into account). For Alg, a pK_a of 3.5 was considered for the carboxylate groups.[55] The pK_a of PAH is approximately 8.5 due to the amine groups.[62] Finally, for Hep and PSS, the sulfonate groups were considered as fully negatively charged. The protein charge was determined using the PDB2PQR server.[63] It was computed as a function of pH, based on the amino acid sequence and on the structure (PDB files of, respectively, 2K6O for LL-37, 3I40 for Ins, 1HEL for Lyz, and 1GAL for Gox). PPCs were prepared from solutions at I ≈ 0 mM obtained by adding to ultrapure water only NaOH or HCl necessary to obtain the desired pH (3.5, 5 or 7.5). Proteins were used below their IEP and associated with a polyanion, or conversely, they were used above their IEP and complexed with a polycation. For example, PPCs at a (-)/(+net) charge ratio of 2 were prepared by mixing 2 volumes of a negatively-charged PE solution (0.5 mM negative charge) with 5 volumes of a protein solution (0.1 mM net positive charge) and PPCs at a (+)/(-net) charge ratio of 2 were prepared by mixing 2 volumes of a positively-charged PE solution (0.5 mM positive charge) with 5 volumes of a protein solution (0.1 mM net negative charge). PPCs were formed by mixing the volumes in a single step, without gradual addition or stirring. In such conditions, PPCs formation was immediate.

Therefore, the protein and PE concentrations, in the PPCs with a charge ratio of 2, are, respectively, 0.07 and 0.14 mM positive or negative net charge. For turbidity measurements, the negative or positive PE solution was always added to the protein solution in such a way that (-)/(+net) or (+)/(-net) charge ratio varied between 0 and 2, *e.g.*, 0.4 mL of negative or positive PE solution

was added to 1 mL of protein solution to reach a (-)/(+net) or (+)/(-net) charge ratio of 2.

1.2.3 Turbidimetry

Buchhammer *et al*. have shown that the turbidimetry can be related to the concentration, size and polydispersity of the PPCs.[64] Importantly, our group has also demonstrated that the turbidity measurement can be used to estimate the charge ratio at which the protein charge is overcompensated by the added PE. This informs on the charge ratio (or molar ratio) necessary to obtain a PPCs that can be assembled using the LbL method. In the following, turbidity measurements were thus used to monitor PPCs formation as a PE is added to the protein solution.[65] The turbidity at λ = 450 nm (A_{450}) of the suspension was measured at pH 3.5, 5 or 7.5, depending on the PPCs system, using a UV-vis spectrophotometer (DU800, Beckman Coulter, USA). The A_{450} values were normalized by the dilution factor according to the Beer-Lambert law. Measurements were all performed at 25°C and were made in triplicate.

1.2.4 Multilayer construction

Multilayers were constructed by successive adsorption steps. For all experiments, an anchoring layer of two bilayers of a positively- or negatively-charged PE (Chi, PAH, or Hep) alternately adsorbed with a negatively- or positively-charged PE (Alg, Hep, high molar mass PSS_h, M_W = 70,000 g mol^{-1}, Sigma Aldrich, Steinheim, Germany or PAH) was constructed from PE solutions (0.5 g L^{-1}). Then, two different multilayers were built on this anchoring layer: bare proteins or PPCs, assembled with oppositely-charged PEs. Each of these multilayers is formed of five successive bilayers. The following solutions were used: Chi or PAH (0.5 g L^{-1}), Hep, Alg or PSS_l (0.5 g L^{-1}) and LL-37, Ins, Lyz or Gox bare molecules (0.07 mM positive or negative net charge), as well as PPCs suspensions, prepared as described in the section *Part IV – 1.2.2 Formation of PPCs*. Depending on the experimental conditions, the pH of solutions was adjusted to 3.5, 5 or 7.5 with NaOH or HCl. After each adsorption step, a rinsing step with ultrapure water at same pH than the solution used to build the multilayers was performed.

1.2.5 Quartz crystal microbalance with dissipation monitoring

The successive adsorption steps described in the section *Part IV – 1.2.4 Multilayer construction* were monitored using QCM-D. 4.95 MHz AT-cut gold-coated quartz sensors (Q-sense, Stockholm, Sweden) were used. The sensors were washed in H_2O_2/H_2SO_4 1:3 (v:v), successively rinsed with water and ethanol, and finally exposed to UV-ozone (UVO Cleaner 42-220, Jelight Company, Irvine, USA). Layer growth on gold-coated quartz sensors was monitored using a QCM-D monitoring system (Q-sense E4 system, Q-Sense, Stockholm, Sweden). The solution flow rate and the temperature were, respectively, set at 20 µL min^{-1} and 20°C. The adsorption time for each compound is not fixed. The solutions were passed through the QCM-D cells until stabilization of the frequency and dissipation shifts. Each adsorption step was followed by a rinsing step of 10 min with ultrapure water adjusted to the same pH value. The frequency and dissipation shifts were recorded for the third to eleventh overtones and the results for the seventh are presented here. The total mass adsorbed on QCM-D crystals (µg cm^{-2}) was computed using the Sauerbrey equation: $\Delta m = -\Delta f_7$ C 7^{-1}, where Δm is the shift of adsorbed mass (ng cm^{-2}), Δf_7 is the frequency shift measured for the seventh overtone (Hz), C is the mass sensitivity constant (ng cm^{-2} Hz^{-1}) and 7 is the overtone number.

1.3 Results and discussion

1.3.1 Formation of PPCs

PEs are water-soluble polymers containing ionizable groups that provide them with a positive or negative charge, depending on pH. Thanks to their charged nature, these polymers can interact with proteins to form soluble or insoluble complexes. Protein and PE concentration, ionization degree, charge distribution, hydrophobicity, ionizable group nature, and molecular weight all influence the PPCs formation.[66,67] The first part of this chapter aims at investigating the complexation of LL-37, Ins, Lyz and Gox with Alg, PPS_I, Hep, and PAH in ultrapure water adjusted to a given pH (3.5, 5 or 7.5). In particular, we aim at determining the PE-to-protein charge ratio that will allow the subsequent successful LbL assembly of the PPCs with PEs.

At pH 3.5 and 5, all proteins used have a positive net charge. When the pH increases to 7.5, Ins and Gox switch to a negative net charge while LL-37 and Lyz are still positively charged (Figure IV-1. 1). Therefore, all proteins were complexed with a polyanion at pH 3.5 and 5 while Ins and Gox were complexed with a polycation at pH 7.5.

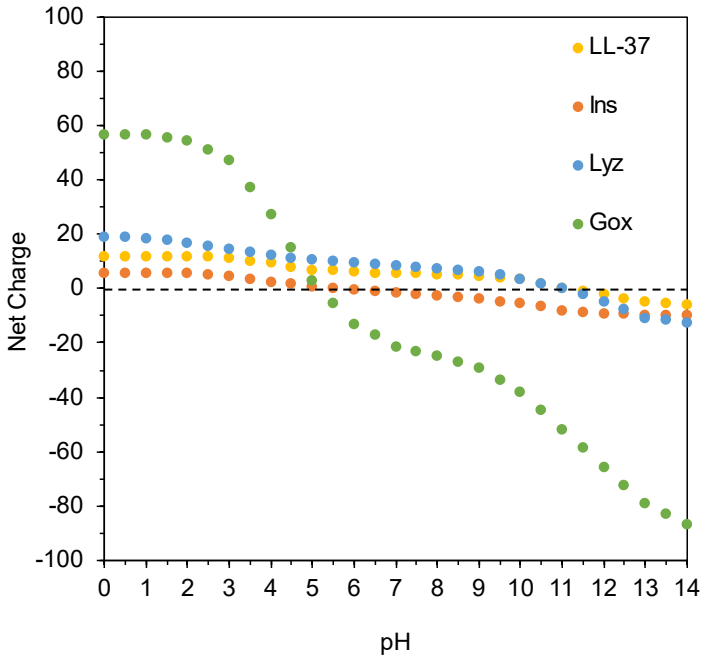

Figure IV-1. 1 – Net charge of LL-37 (PDB: 2K6O), Ins (PDB: 3I40), Lyz (PDB: 1HEL), and Gox (PDB: 1GAL) as a function of pH. The protein net charge was computed using the PDB2PQR Server.[63]

Figure IV-1. 2 shows an example of PPCs formation, here by mixing Lyz with Hep. The conditions used for PPCs formation are summarized in Table IV-1. 1.

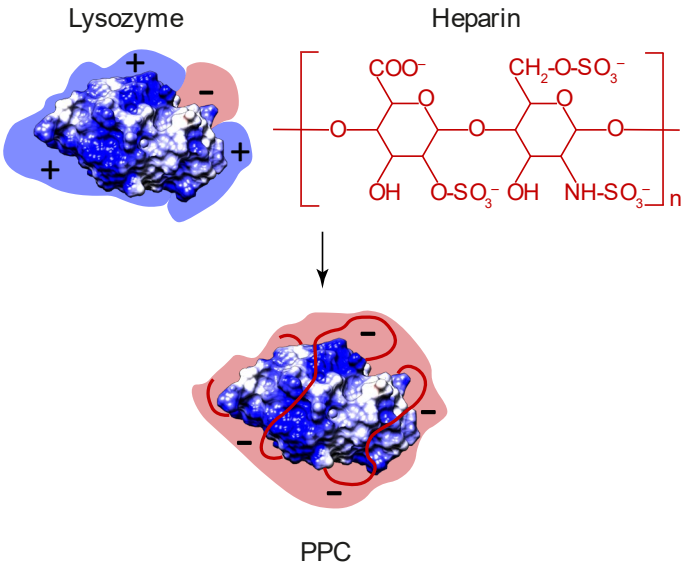

Figure IV-1. 2 – Schematic representation of Lyz-Hep complex formation. Hep is negative and represented by red lines. Lyz is a polyampholyte with the surface potential resulting from positive and negative residues, respectively, colored in blue and red (at pH 3.5). The molecular structure and the surface potential coloring were produced using the UCSF Chimera package.[68]

Table IV-1. 1 – Solution pH as a function of the protein and the PE used to form PPCs.

	LL-37	Ins	Lyz	Gox
Alg	pH 5	pH 3.5	pH 5	pH 3.5
PSS_I	pH 5	pH 3.5	pH 5	pH 3.5
Hep	pH 3.5	pH 3.5	pH 3.5	pH 3.5
PAH	/	pH 7.5	/	pH 7.5

A_{450} as a function of PE-to-protein charge ratio is presented in Figure IV-1. 3a, Figure IV-1. S1-S3, and Figure IV-1. 3c. In all cases, the turbidity increases as the PE is added to the protein solution until it reaches a plateau.[65] This turbidity plateau, *i.e.*, the charge ratio threshold value beyond which the turbidity does not increase, allows the PE-to-protein charge ratio *e* to be determined. This ratio can be related to the minimal amount of PE needed

to fully displace the equilibrium toward PPCs formation (Figure IV-1. 3a). This suggests that, beyond this value, all proteins are in PPCs with a core-corona structure with a neutral internal domain and a PE-charged corona.[69] In a view to further alternate the adsorption of PPCs with an oppositely-charged PE, knowing this *e* value is essential. Indeed, once the *e* value is reached, the overall PPCs charge is dictated by the excess of charge brought by the PE (either positive or negative).[70] The measured *e* values for LL-37, Ins, Lyz and Gox complexed with Hep at pH 3.5, Ins and Gox complexed with Alg and PSS_I at pH 3.5 and finally LL-37 and Lyz complexed with Alg and PSS_I at pH 5 are summarized in Figure IV-1. 3b. Finally, the A_{450} values for the different PE-to-protein combinations at a (-)/(+net) charge ratio of 2 are presented in Figure IV-1. 3c. From this Figure IV-1. 3c, it appears that the turbidimetry is strongly different depending on the PPCs and is between 0.02 and 0.3. Globally, when considering the results by protein, we note that the turbidimetry of PPCs is lower when the proteins are complexed with PSS_I than Hep. The turbidimetry being the highest when the proteins are complexed with Alg. When analyzing the results by PE, the tendency is the same for all PEs. The turbidimetry is the lowest for LL-37-based PPCs and lower for Lyz-based PPCs than those with Ins and Gox.

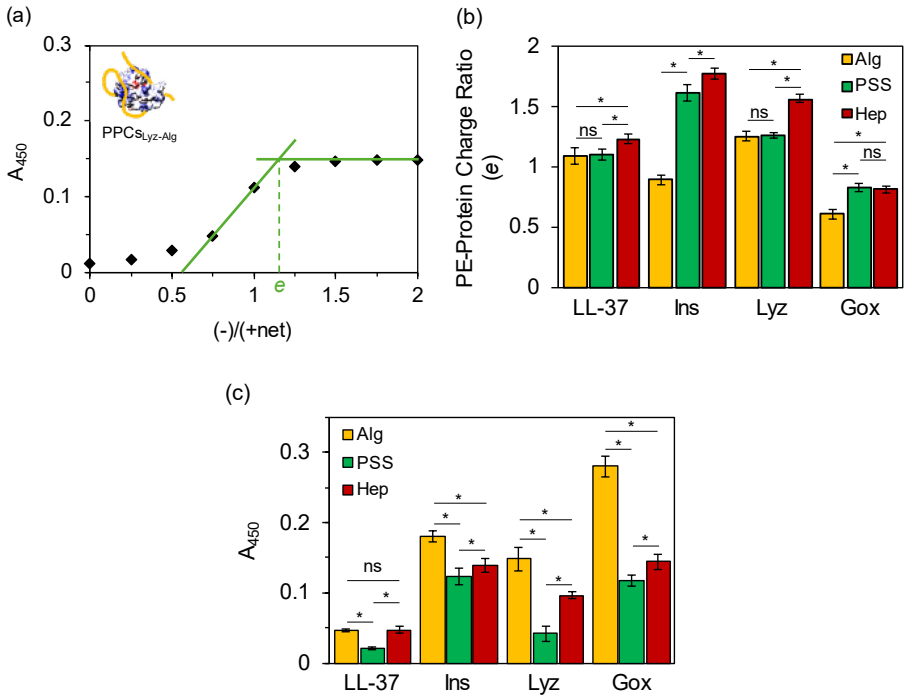

Figure IV-1. 3 – (a) Normalized A_{450} values of a Lyz solution undergoing Alg addition in such a way that (-)/(+net) charge ratio varies between 0 and 2 at pH 5 in ultrapure water. *e* represents the charge ratio at which protein charges are complexed. (b) (-)/(+net) PE-to-protein charge ratio at which the plateau is reached as an Alg, Hep or PSS_I solution is added to a LL-37, Ins, Lyz or Gox solution in ultrapure water. LL-37 and Lyz were complexed at pH 5 with Alg and PSS_I solutions, and the others were complexed at pH 3.5. The error bars represent the standard error (n = 3), and the asterisks indicate a statistically significant difference of the PE-to-protein charge ratio *e* ($p < 0.05$). (c) Normalized A_{450} of a LL-37, Ins, Lyz, and Gox solution undergoing Alg, PSS_I, and Hep addition in such a way that (-)/(+net) charge ratio is equal to 2 at pH 3.5 with Hep and at pH 5 with Alg and PSS_I in ultrapure water. The error bars represent the standard error (n = 3) and the asterisks indicate a statistically significant difference of the turbidity ($p < 0.05$).

For all pairs, the *e* value is found between 0.5 and 1.75. Interestingly, PPCs made with Alg, PSS_I, and Hep have, respectively, lower, intermediate, and higher *e* values. The *e* value thus scales with the PE charge density. Indeed, for high-charge-density PE such as Hep, all ionizable groups of the PE are unlikely to match and pair with those of the protein. Consequently, an excess of negative charges is needed to fully compensate the protein charge.

Though the latter latter scaling is consistent through all protein-PE pairs, the nature of the protein has the most influence on the *e* absolute value. At a given pH, from low to high, the *e* value order is the following: Gox, LL-37, Lyz, Ins. There is thus no relationship between the *e* value and protein size (see Figure IV-1. 4 for the size comparison). Using the Chimera software, the protein charge density and distribution at pH 3.5 were computed and are represented in Figure IV-1. 4. For LL-37, Ins, Lyz, and Gox, the net charges at pH 3.5 are, respectively, equal to +10.4, +3.6, +13.4, and +37.4, and at pH 5, they are respectively, equal to +7.02, +0.7, +10.5, and +2.9. The charges are homogeneously distributed on the Ins, Lyz and Gox molecules whereas LL-37 has a large positive domain.

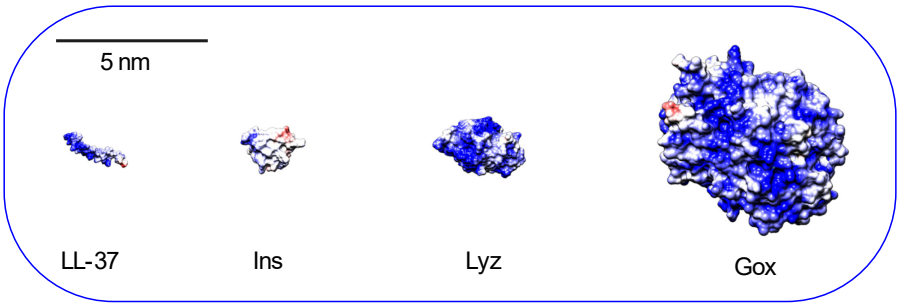

Figure IV-1. 4 – Molecular structure of LL-37 (PDB: 2K6O), Ins (PDB: 3I40), Lyz (PDB: 1HEL), and Gox (PDB: 1GAL). The electrostatic surface potentials were computed using the UCSF Chimera package.[68] The protein surface is colored in red for negative potential and in blue for positive potential. These molecular structures were produced considering a pH of 3.5.

The complexation of a protein with a net negative charge and a positively-charged PE was then studied. At pH 7.5, Ins and Gox have negative net charges of, respectively, -2.1 and -23.1. They were complexed with PAH. The turbidity was measured as a function of the effective (+)/(-net) charge ratio. Results are shown in Figure IV-1. 5. For both Ins and Gox, complexed with PAH, the *e* value equals 2. As for positively-charged proteins, these results show that negatively-charged proteins can be complexed with PE.

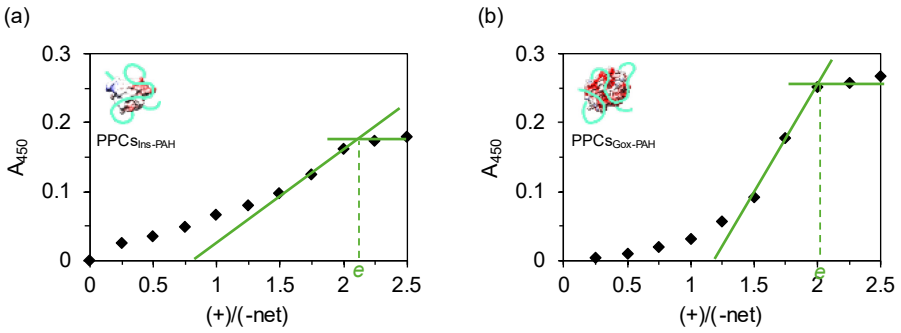

Figure IV-1. 5 – Normalized A_{450} of a (a) Ins and (b) Gox solution undergoing PAH addition in such a way that (+)/(-net) charge ratio varies between 0 and 2.5 at pH 7.5, in ultrapure water.

These results show that all proteins could be complexed with a PE by carefully computing their charge at a given pH and selecting the appropriate PE. Moreover, we found that, while protein size does not influence charge overcompensation, the latter scales with the PE charge density and the nature of the protein. PPCs charge overcompensation is critical to standardize the protein charge and facilitate its self-assembly in a LbL fashion.[49] These results will thus be used to identify the appropriate molar ratio to form PPCs to construct a multilayer by alternate adsorption of the latter with a second PE.

1.3.2 Protein-polyelectrolyte LbL assembly

In the following, PPCs formed with various proteins and PEs at a (-)/(+net) or (+)/(-net) charge ratio of 2 were assembled with oppositely-charged PEs using the LbL method. The LbL assembly of bare protein with PE, *i.e.*, the classical LbL assembly, was carried out for comparison. The same PE as the one used to complex the protein was alternately adsorbed with the bare protein to form a multilayer. Figure IV-1. 6 shows a schematic of films made with Lyz complexed with Hep or bare Lyz molecules assembled with, respectively, Chi and Hep. In all cases, two bilayers of PEs were constructed to screen the effect of the surface.[49] This anchoring layer is made of the PE used to integrate the PPCs in the multilayer and the PE used to complex the protein of interest. Then, five bilayers of PPCs or bare proteins and PEs were constructed.

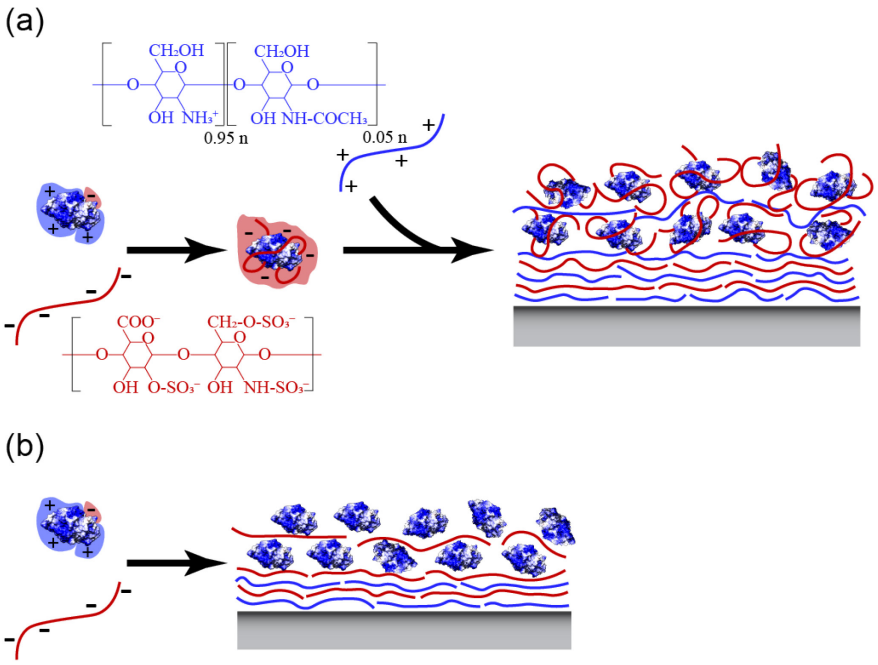

Figure IV-1. 6 – Schematic of the two different methods used to immobilize Lyz molecules. The red and blue lines represent, respectively, Hep and Chi. The different colors on Lyz suggest its heterogeneous charge distribution. First, an anchoring layer of two [Chi-Hep] bilayers was adsorbed on the surface. Then, (a) $PPCs_{Lyz\text{-}Hep}$ were adsorbed using Chi as the positive counter polyion, and (b) bare Lyz was adsorbed using Hep as the negative counter polyion in a classical LbL assembly.

The multilayer growth was monitored using QCM-D, and the results are expressed in adsorbed mass as a function of each adsorption step for each protein-PE combination (see Figure IV-1. S4-S9, and see *Part IV – 1.2 Experimental section* for details on the mass measurement). The adsorbed mass is calculated at the end of each adsorption step, when the steady state is reached. Figure IV-1. 7 and Figure IV-1. S10-S22 demonstrate that this equilibrium is reached at the end of each deposition step and of each rinsing step. Figure IV-1. 7 and Figure IV-1. S10-S22 represent the evolution of the frequency and dissipation as a function of time. Based on these graphs, the adsorbed mass was calculated via the Sauerbrey equation. However, it is important to keep in mind that this mass corresponds to the minimum mass adsorbed on the surface. Indeed, the use of Sauerbrey modeling can underestimate the real mass adsorbed, contrary to more complex models such as Johannsmann or Voinova modeling.

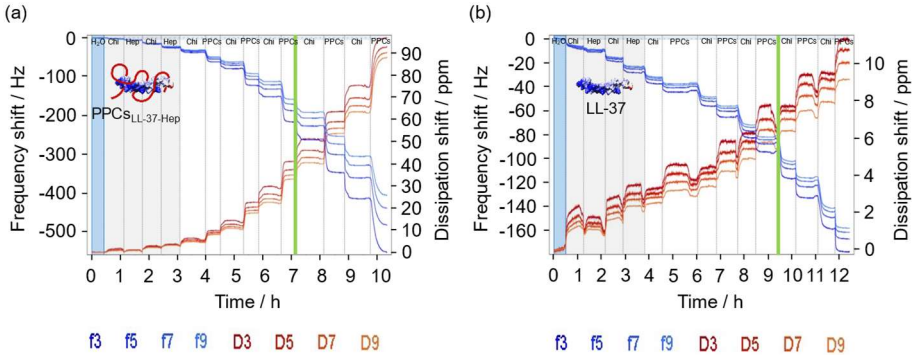

Figure IV-1. 7 – Evolution of the frequency and dissipation shift (3rd, 5th, 7th and 9th overtone) measured by QCM-D after adsorption of an anchoring layer of two Chi-Hep bilayers ([Chi-Hep]$_2$, shaded area) followed by five adsorption steps of either (a) Chi and PPCs ([Chi-PPCs$_{LL\text{-}37\text{-}Hep}$]$_5$) or (b) bare proteins and Hep ([LL-37-Hep]$_5$), at pH 3.5 in ultrapure water.

A typical result is shown in Figure IV-1. 8 for Gox complexed with Hep (PPCs$_{Gox\text{-}Hep}$) and assembled with Chi ([Chi-PPCs$_{Gox\text{-}Hep}$]) or PAH ([PAH-PPCs$_{Gox\text{-}Hep}$]), and for Gox bare molecules assembled with Hep ([Gox-Hep]). In this case, the classical LbL assembly [Gox-Hep] on either a [Chi-Hep]$_2$ or a [PAH-Hep]$_2$ anchoring layer led to an increase of mass of, respectively, 6 µg cm^{-2} (Figure IV-1. 8a) and 5 µg cm^{-2} (Figure IV-1. 8b) after deposition of five bilayers on the anchoring layer. When PPCs$_{Gox\text{-}Hep}$ are assembled with Chi or PAH, the mass increased by, respectively, 17 and 25 µg cm^{-2} after five bilayers (Figure IV-1. 8). This result confirms that PPCs with a (-)/(+net) charge ratio of 2 can be used to build multilayers. It also suggests that these PPCs are negatively charged since they can self-assemble with a polycation. Interestingly, a sawtooth adsorption profile is observed for the [PAH-PPCs$_{Gox\text{-}Hep}$] multilayer. At each PPCs$_{Gox\text{-}Hep}$ adsorption step, the total mass increases, while at each PAH adsorption step, the total mass decreases. These results suggest that material is removed from the multilayer upon PAH adsorption. From these results, we find that (1) the multilayer mass after five layers of protein deposition and (2) the magnitude of the desorption upon PE adsorption can inform the growth of a selected system. These data will thus be extracted from QCM-D results and discussed hereunder for all of the multilayers that were built.

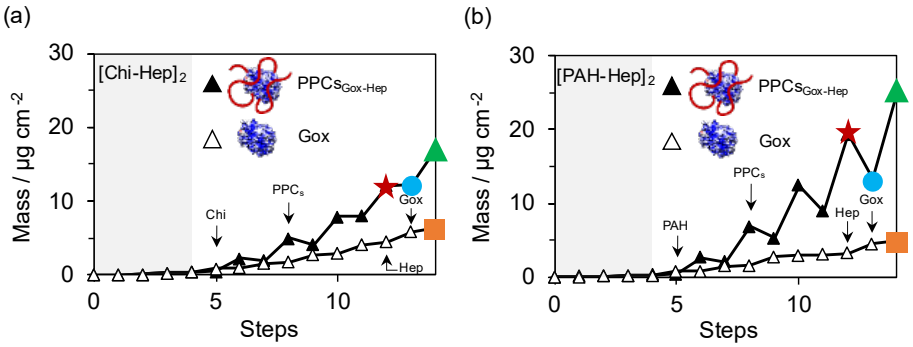

Figure IV-1. 8 – (a) Adsorbed mass measured by QCM-D after the adsorption of two bilayers of Chi-Hep ([Chi-Hep]$_2$) (shaded area) followed by five bilayers of either Chi and Gox-based PPCs (plain triangle) [Chi-PPCs$_{Gox-Hep}$]$_5$ or bare Gox proteins and Hep (empty triangle) [Gox-Hep]$_5$, at pH 3.5 in ultrapure water. (b) Adsorbed mass measured by QCM-D after the adsorption of two bilayers of PAH-Hep ([PAH-Hep]$_2$) (shaded area) followed by five bilayers of either PAH and Gox-based PPCs (plain triangle) [PAH-PPCs$_{Gox-Hep}$]$_5$ or bare Gox proteins and Hep (empty triangle) [Gox-Hep]$_5$, at pH 3.5 in ultrapure water.

For each of the 32 different self-assembled films that were built, the multilayer masses after five PPCs or bare proteins adsorption steps were extracted and are presented as a heat map in Figure IV-1. 9a. For example, for [Chi-PPCs$_{Gox-Hep}$]$_5$ and [PAH-PPCs$_{Gox-Hep}$]$_5$, the values in the heat map (Figure IV-1. 9a) correspond to the values of the green triangles and the orange squares in Figure IV-1. 8**.** To better capture the mass difference, *i.e.*, the improved protein adsorption when PPCs are used, the mass increase compared to classical LbL assembly was computed for each protein-PE combination. Results are presented in Figure IV-1. 9b and show the mass increase in percent for each of the 16 protein-PE couples tested. For example, for [Chi-PPCs$_{Gox-Hep}$]$_5$ *vs.* [LL-37-Hep]$_5$ and [PAH-PPCs$_{Gox-Hep}$]$_5$ *vs.* [LL-37-Hep]$_5$, the values in the heat map (Figure IV-1. 9b) correspond to the difference, in percent, between the green triangles and the orange squares in Figure IV-1. 8. From these results, it appears that except for Ins and one condition with Lyz ([Chi-PPCs$_{Lyz-Hep}$]), all multilayers grow to higher masses when using PPCs rather than bare protein molecules. These results confirm that PPCs can be used to immobilize a wide variety of protein and PEs in multilayers. Interestingly, the total adsorbed mass scales with the molecular weight of proteins for both types of self-assemblies and most of the protein-

PE combinations. Since all PEs used are identical and adsorption is carried out in identical pH and I conditions, this suggests that the mass difference is due to the presence of protein in the multilayer, or a difference in the multilayer architecture, *e.g.*, more water in the film. Therefore, the mass difference could be interpreted as an increased protein adsorption, or a more hydrated multilayer when PPCs are used compared to bare protein molecules. Both are of great interest since it has been shown that the biological activity increases with the increase in protein concentration[71] and a higher hydrated film can improve the biological activity of proteins. Importantly, previous works showed that $PPCs_{Lyz\text{-}PAH}$ immobilize Lyz that have 75% more enzymatic activity than bare Lyz molecules.[48,49]

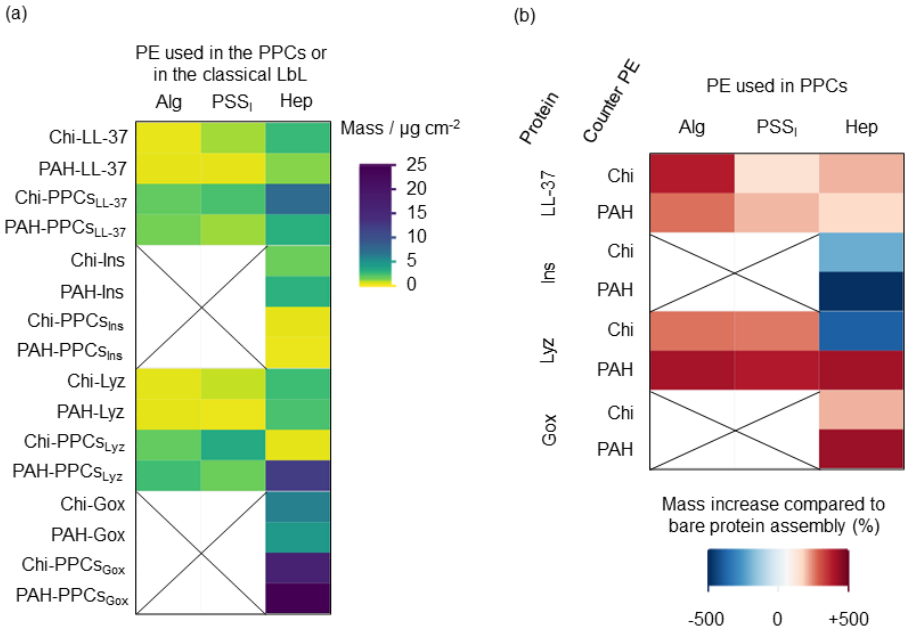

Figure IV-1. 9 – (a) Heat map representing the total mass adsorbed after the adsorption of an anchoring layer of two bilayers of PEs and five bilayers of PEs and either PPCs or bare proteins. (b) Heat map representing the mass increase when PPCs are used compared to bare proteins. Results with PPCs are expressed in percent of the total mass adsorbed after adsorption of an anchoring layer and five adsorption steps of PEs and bare proteins.

For the multilayers integrating [$Chi\text{-}PPCs_{LL\text{-}37\text{-}Hep}$] and [LL-37-Hep], the ratio between the dissipation shift (ΔD) and the frequency shift (Δf) obtained for the seventh overtone ($\Delta D_7/(-\Delta f_7/7)$) were calculated. These QCM-D

measurements are presented in Figure IV-1. 10a. Ratios calculated at the beginning, when the anchoring layer is adsorbed, are highly fluctuating, because dissipation and frequency shifts are both very low and close to zero (data not shown). Ratios obtained during the adsorption of PPCs and bare proteins are below the value of $\Delta D_7/(-\Delta f_7/7) = 4 \times 10^{-7}$ Hz^{-1}, proposed by Reviakine *et al.* as the threshold between rigid and soft films.[72] Figure IV-1. 10b represents, for the 16 studied systems, the $\Delta D_7/(-\Delta f_7/7)$ difference between the PPCs and the bare protein multilayers after the third adsorption step of PPCs. For example, for the [Chi-$PPCs_{LL\text{-}37\text{-}Hep}$] and [LL-37-Hep] multilayers, the Δf_7 and ΔD_7 values were taken at the green lines in Figure IV-1. 7. For all the systems, ratios are greater when PPCs are integrated into the multilayers than bare proteins. This suggests that multilayers with PPCs are more hydrated than the multilayers with bare proteins.

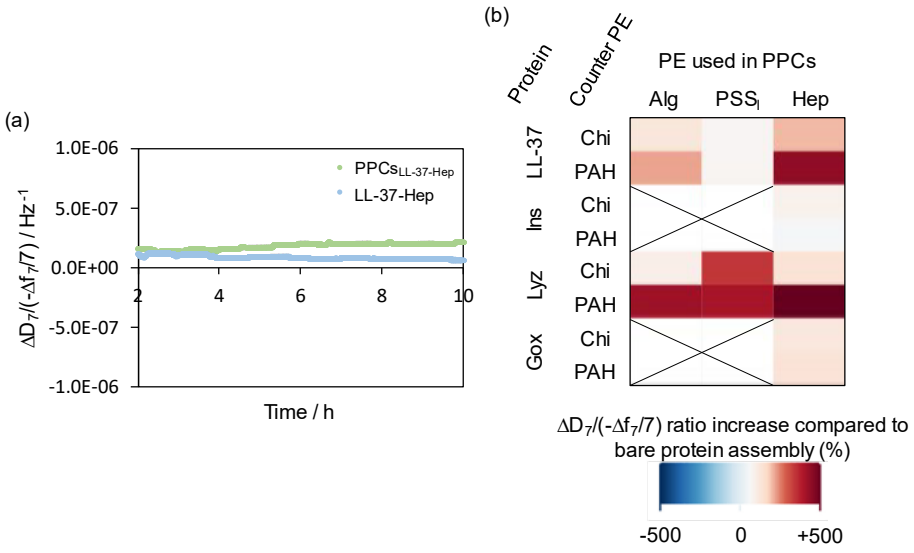

Figure IV-1. 10 – (a) Typical ratios between ΔD_7 and Δf_7 obtained under the adsorption steps using the QCM-D. (b) Heat map representing the $\Delta D_7/(-\Delta f_7/7)$ ratio increase when PPCs are used compared to bare proteins. Results with PPCs are expressed in percent of the $\Delta D_7/(-\Delta f_7/7)$ ratio of bare protein assembly, after the third adsorption step of the PPCs.

The second parameter that was extracted from the multilayer growth is the magnitude of desorption upon PE adsorption in the PPCs-based multilayers. This value was expressed as a percentage of the multilayer mass before and

after the last adsorption step of Chi or PAH and is represented as a heat map for each LbL assembly in Figure IV-1. 11. For example, for $[Chi\text{-}PPCs_{Gox\text{-}Hep}]_5$ and $[PAH\text{-}PPCs_{Gox\text{-}Hep}]_5$, the values in the heat map (Figure IV-1. 11) correspond to the difference, in percent, between the blue circles and the red stars (Figure IV-1. 8).

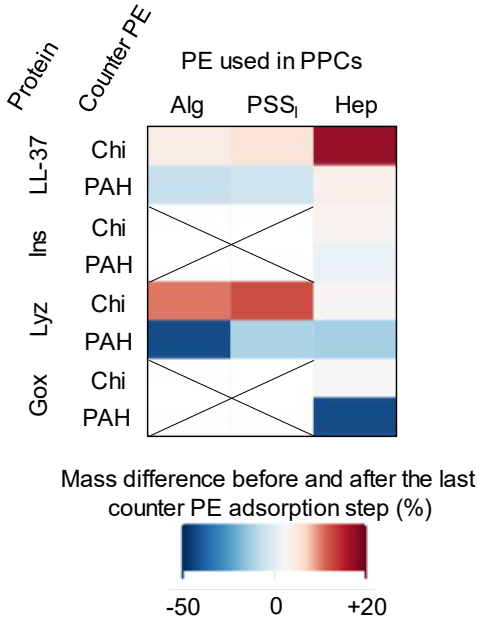

Figure IV-1. 11 – Heat map representing the desorption (blue) and the adsorption (red) into the multilayer after the last Chi or PAH adsorption step. Results are expressed in percent of the total mass adsorbed before the last addition step of Chi or PAH.

Interestingly, these results show that desorption is almost systematically observed upon PAH adsorption on a layer of PPCs. On the contrary, Chi adsorption never causes desorption. Desorption is thus observed when a PE with a high charge density is adsorbed on a PPCs layer. On the other hand, no decrease in mass is observed when a PE with a lower charge density, such as Chi, is used (less ionizable groups per unit of length, deacetylation degree of 95%, and lower pKa). When it comes to the difference between proteins, the adsorption of PAH on a PPCs layer that contains Lyz or Gox leads to a stronger desorption than when it is adsorbed on a PPCs layer that contains LL-37. The desorption is thus less pronounced with a protein that has a high charge density, such as LL-37 (Figure IV-1. S4-S9). We have recently

demonstrated that PPCs-based multilayers are highly dynamic self-assemblies. It means that a reorganization of the entire film can occur upon each adsorption step. In the section *Part IV – Results and discussion – Chapter 3*, the hydrodynamic radius of $PPCs_{LL\text{-}37\text{-}Hep}$ was measured and values in the range of 10-1000 nm were obtained. Figure IV-1. S23 depicts the evolution of the thickness of [Chi-$PPCs_{LL\text{-}37\text{-}Hep}$] and [LL-37-Hep]. The difference between the size of the $PPCs_{LL\text{-}37\text{-}Hep}$ and the increase in multilayer thickness at each stage of $PPCs_{LL\text{-}37\text{-}Hep}$ immobilization (up to 20 nm in the final adsorption stage) suggests that PPCs do not adsorb directly onto the surface in their native state; otherwise, the increase in multilayer thickness would be significantly greater. Moreover, we have also shown that when a PE is adsorbed on a PPCs layer, it can complex the PE of the PPCs, which releases the free protein and thus can cause a decrease of the multilayer mass.[73] This disassembly relies on associative forces rather than on the alteration of the protein-PE coupling strength. Similar phenomena have been reported in PEMs, especially for systems containing small molecules, where typical stepwise curves in a sawtooth profile (adsorption-desorption steps) were observed.[74] In a previous study, we suggested that this mechanism is a function of the PE-PE ion-pairing strength compared to the protein-PE pairing strength.[73] This hypothesis is in line with the difference in desorption observed for PAH compared to Chi, and for LL-37 compared to Ins and Gox. Indeed, PAH has a strong ion-pairing with Alg, PSS_I and Hep; hence, it can displace proteins from PPCs. Since LL-37 has a higher charge density than Ins and Gox, its pairing with Alg, PSS_I and Hep is stronger. The result is that PAH adsorption displaces less LL-37 from the PPCs than Ins and Gox. Our results thus confirm that the desorption from the multilayer is the result of a trade-off between PE-PE and protein-PE pairing strengths.

The stability of multilayers to environmental conditions was also investigated. To do so, QCM-D and XPS measurements were performed, by submitting $[Chi\text{-}Hep]_2$-$[Chi\text{-}PPCs_{LL\text{-}37\text{-}Hep}]_6$ samples to a Mueller Hinton broth (MHB), NaCl (pH 9 and I = 150 mM) or sodium dodecyl sulfate (SDS) solution. QCM-D analyses enable to account for potential desorption of the films due to contact of the multilayers with the solutions and the XPS analyses inform whether the surface chemical composition of the films is modified or not after such contact. Contact of $[Chi\text{-}Hep]_2$-$[Chi\text{-}PPCs_{LL\text{-}37\text{-}Hep}]_6$ multilayer with NaCl and SDS solutions leads to a mass loss attributed to partial desorption

of the film (data not shown). It could suggest a film deconstruction due to a change in pH and I.[75,76] The XPS analysis of Ti 2p peaks indicates that a partial but not complete film desorption has occurred (Figure IV-1. S24). No mass increase or decrease was observed after the immersion of the film in the MHB solution, suggesting a higher stability of the multilayer in this medium. By analyzing N 1s and C 1s XPS peaks (Figure IV-1. S24), it seems that the effect of sample treatment with a solution of MHB and NaCl on the surface elemental composition is relatively limited. Indeed, there is almost no difference in comparison with the untreated [Chi-PPCs$_{LL\text{-}37\text{-}Hep}$]$_6$ sample. However, the addition of SDS modified the multilayer composition, indicating desorption of the film and suggesting adsorption of SDS molecules on the surface of the sample. Rahim *et al.* also observed desorption of [PAH-PSS] PEMs upon the addition of SDS, which was proven to be chemically adsorbed into the multilayers.[77] Therefore the stability of LbL films is found to be highly dependent on the medium and the PEs.

To further study the LbL assembly of PPCs, multilayers were built using positively-charged PPCs. To do so, PPCs$_{Ins\text{-}PAH}$ and PPCs$_{Gox\text{-}PAH}$ were integrated into multilayers with Hep at pH 7.5. The total masses after five bare proteins or PPCs adsorption steps were extracted and are presented in Figure IV-1. S25. From these results, it appears that the multilayers do not grow when PPCs are used even though the PPCs are well formed (Figure IV-1. 5). On the contrary, a multilayer constructed with bare Ins and Gox, respectively, reaches masses of 0.7 and 1.8 µg cm^{-2}. This difference can be explained by the use of PAH and Hep as PEs. As shown before, the PE-PE ion-pairing strength dictates the multilayer growth. For this system, Hep has the highest charge density that exists among naturally-occurring PEs.[58] Thus, it seems that Hep is able to displace Gox and Ins from the PPCs. However, we do not explain this by the lack of charge of PAH, which is not fully ionized at pH 7.5 since we constructed multilayers of PPCs$_{Lyz\text{-}PSSI}$ integrated with PAH at pH 7.5.[48,49] Studies, more focused on the interactions between these species, should be conducted to understand the non-construction of multilayers when proteins are complexed with PAH.

We have thus shown that the difference between films integrating PPCs and those integrating bare proteins is noteworthy. The use of PPCs leads to an increase, by up to 4 times, of the protein mass and/or the hydration in the multilayer. Importantly, the PEs need to be carefully selected to avoid their

pairing and subsequent protein release from the film. Once this is accounted for, PPCs can be used as a more generalizable tool for protein surface immobilization.

1.3.3 PPCs LbL assembly to combine different proteins

To date, the studied systems included only one type of protein. The immobilization of several proteins at interfaces to create multifunctional multilayers is topical for various fields of research as drug release, tissue engineering, and regenerative medicine approaches.[78] The purpose of studying the assembly of PPCs based on different types of proteins is twofold. First, the possibility of incorporating several proteins, independently of each other, will be analyzed. Second, the parameters governing this integration will be compared to the ones of bare proteins. To do so, the assembly of mixed layers based on $PPCs_{LL\text{-}37\text{-}Alg}$ and $PPCs_{LL\text{-}37\text{-}PSSI}$, as well as on $PPCs_{Lyz\text{-}Alg}$ and $PPCs_{Lyz\text{-}PSSI}$ was monitored. The PPCs, which are negatively charged, were integrated with PAH at pH 5. The total masses after five PPCs or bare proteins adsorption steps (three with LL-37 and two with Lyz) were extracted from QCM-D data and presented in Figure IV-1. 12. Regarding the classical LbL assemblies that integrate LL-37 and Lyz, with either Alg or PSS_I, no building of the layers was observed. For Alg-based PPCs and PSS_I-based PPCs assembled with PAH, the mass increased by, respectively, 2 and 1.4 µg cm^{-2} after five bilayers. These results suggest that the multilayers grow to higher masses when using PPCs rather than bare protein molecules. As was the case for multilayers with a single type of proteins, dissipation values (data not shown) indicate that PPCs-based films are more hydrated. Similarly, a desorption step was systematically observed upon PAH adsorption on PPCs layers. Interestingly, the nature of the selected molecules guides again dictates the film growth. Indeed, for the Alg-based PPCs, a greater mass is adsorbed with $PPCs_{Lyz}$ than with $PPCs_{LL\text{-}37}$ and the magnitude of desorption upon PAH adsorption is larger with $PPCs_{Lyz}$ than with $PPCs_{LL\text{-}37}$, which stabilizes very quickly. This result is in line with that observed when a single type of protein was self-assembled into multilayers (Figure IV-1. S6-S7). The trend is also maintained for both PSS_I-based PPCs types (Figure IV-1. S8-S9). These results highlight that it is possible to integrate several types of proteins by PPCs self-assemblies within the same multilayer. However, the PE and the

protein in the PPCs as well as the counter PE largely influence the multilayer formation. Depending on the species involved in the multilayers, the adsorption profile is quite different.

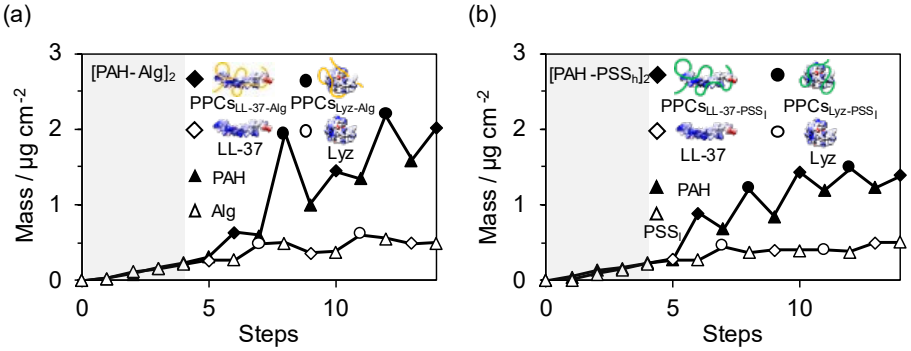

Figure IV-1. 12 – (a) Adsorbed mass measured by QCM-D after the adsorption of two bilayers of PAH-Alg ([PAH-Alg]$_2$) (shaded area) followed by either five bilayers of PAH (plain triangle), three of PPCs$_{LL-37-Alg}$ (plain square) and two of PPCs$_{Lyz-Alg}$ (plain circle) or five bilayers of Alg (empty triangle), three of bare LL-37 (empty square) and two of bare Lyz (empty circle), at pH 5 in ultrapure water. (b) Adsorbed mass measured by QCM-D after the adsorption of two bilayers of PAH-PSS$_h$ ([PAH-PSS$_h$]$_2$) (shaded area) followed by either five bilayers of PAH (plain triangle), three of PPCs$_{LL-37-PSSl}$ (plain square) and two of PPCs$_{Lyz-PSSl}$ (plain circle) or five bilayers of PSS$_l$ (empty triangle), three of bare LL-37 (empty square) and two of bare Lyz (empty circle), at pH 5 in ultrapure water.

1.4 Conclusion

In this chapter, we demonstrated that PPCs are versatile building blocks for the LbL assembly of proteins. PPCs were obtained by complexation of LL-37, Ins, Lyz and Gox with Alg, PSS$_l$, Hep, and PAH. We showed that the PE-to-protein charge ratio *e*, *i.e.*, the minimal amount of PE needed to fully displace the equilibrium toward PPCs formation, is reached at a charge ratio below 2 for all of them. PPCs with a PE-to-protein charge ratio of 2 were then assembled into multilayers using Chi, PAH, and Hep. Compared to the use of bare protein molecules, using PPCs generally allows a better multilayer growth, ranging from two to four times higher mass. We show that this difference in mass is due to a higher hydration level of multilayers integrating PPCs and/or a higher mass of proteins. Finally, we evidenced that the nature

of the protein and PE of the PPCs, and the nature of the counter PE used to build the films play a key role in the ability to self-assemble. Indeed, protein-PE and PE-PE pairing strengths are critical in that respect.

Such self-assembled PPCs are thus promising as versatile building blocks since it is possible to fine-tune the nature of the multilayer and therefore potentially its functionality. PPCs are of major importance for the development of bioactive interphases since they provide a higher protein and/or hydration level than the use of bare proteins.

1.5 Take-home messages

- All proteins could be complexed with a PE by carefully computing their charge at a given pH and selecting the appropriate PE.
- The nature of the protein has the most influence on the PE-to-protein charge ratio.
- Multilayers grow to higher masses when using PPCs rather than bare protein molecules. This mass difference could be interpreted as an increase of the proteins and/or PEs adsorbed, or a more hydrated multilayer.
- Desorption is observed when a PE with a high charge density is adsorbed on a PPCs layer. It is less pronounced with a protein that has a high charge density, such as LL-37. The desorption from the multilayer is the result of a trade-off between PE-PE and protein-PE pairing strengths.

In this *Chapter 1*, we demonstrated that PPCs are versatile building blocks for the LbL assembly of proteins. In the remainder of this work, our focus will be on the immobilization of LL-37 on surfaces to develop antibacterial coatings. To achieve this, we will use Chi, which offers improved multilayer stability by reducing desorption compared to PAH, and Hep. A key limitation of QCM-D is its inability to distinguish the specific nature of the adsorbed compounds. Therefore, we will first perform XPS analysis to identify the compounds incorporated into the multilayers.

1.6 Supporting information

1.6.1 Monitoring the PPCs formation under the addition of an alginate solution

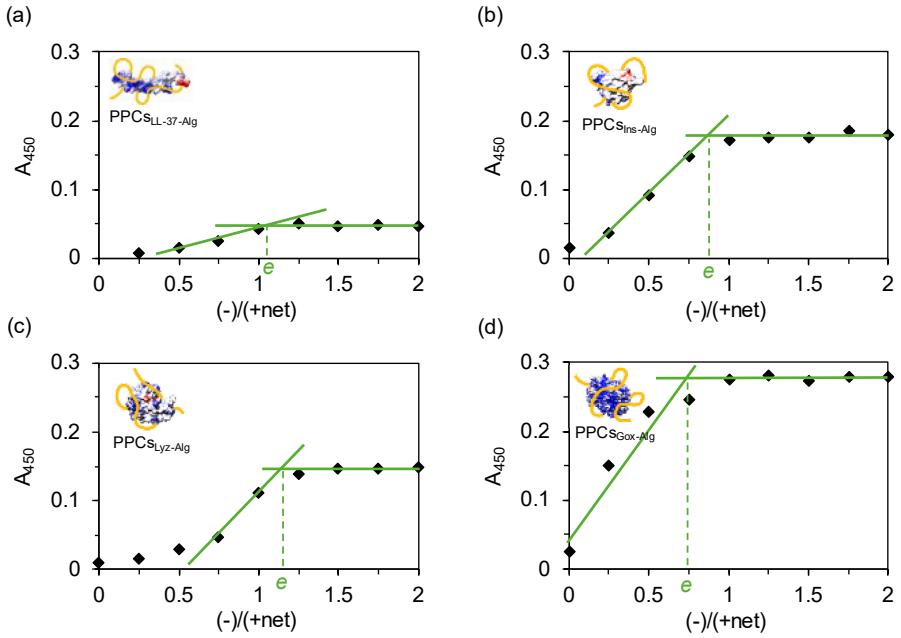

Figure IV-1. S1 – Normalized A_{450} of a (a) LL-37, (b) Ins, (c) Lyz, and (d) Gox solution undergoing Alg addition in such a way that (-)/(+net) charge ratio varies between 0 and 2 at pH 5 for LL-37 and Lyz and at pH 3.5 for Ins and Gox, in ultrapure water.

1.6.2 Monitoring the PPCs formation under the addition of a poly(styrenesulfonate) solution

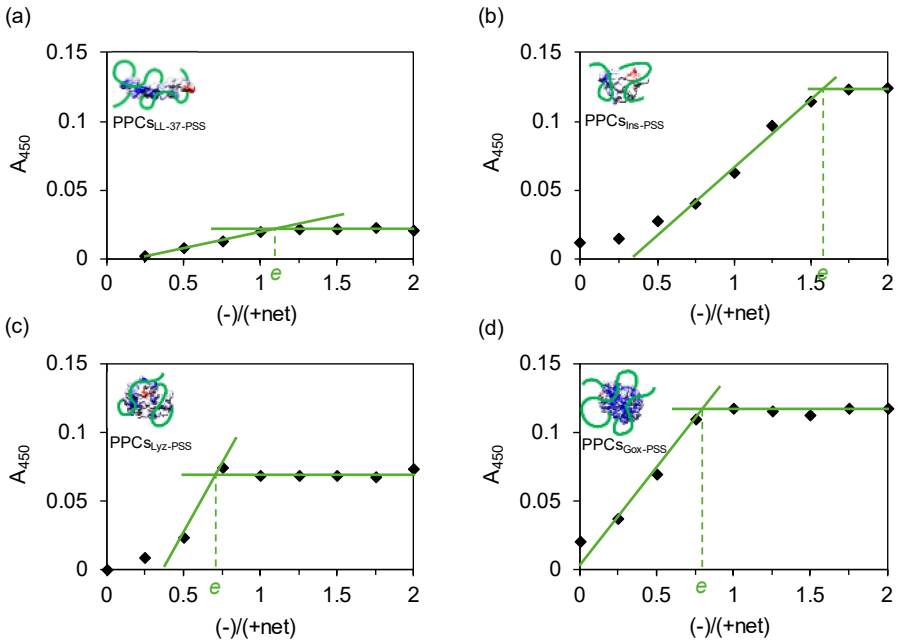

Figure IV-1. S2 – Normalized A_{450} of a (a) LL-37, (b) Ins, (c) Lyz, and (d) Gox solution undergoing PSS_I addition in such a way that (-)/(+net) charge ratio varies between 0 and 2 at pH 5 for LL-37 and Lyz and at pH 3.5 for Ins and Gox, in ultrapure water.

1.6.3 Monitoring the PPCs formation under the addition of a heparin solution

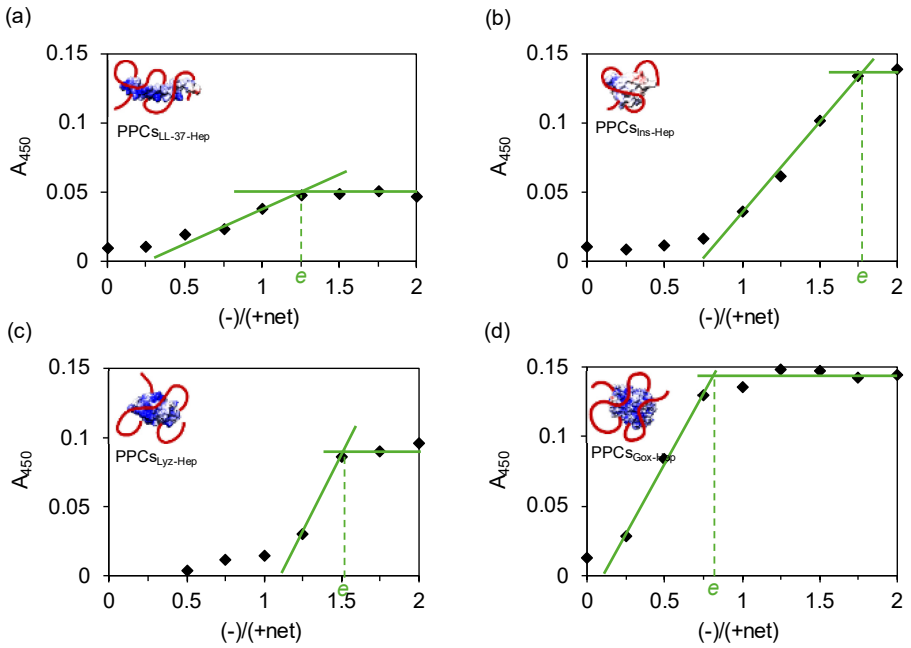

Figure IV-1. S3 – Normalized A_{450} of a (a) LL-37, (b) Ins, (c) Lyz, and (d) Gox solution undergoing Hep addition in such a way that (-)/(+net) charge ratio varies between 0 and 2 at pH 3.5, in ultrapure water.

1.6.4 Evolution of the adsorbed mass of a multilayer either made up of Chi and proteins complexed with Hep or made up of bare proteins and Hep

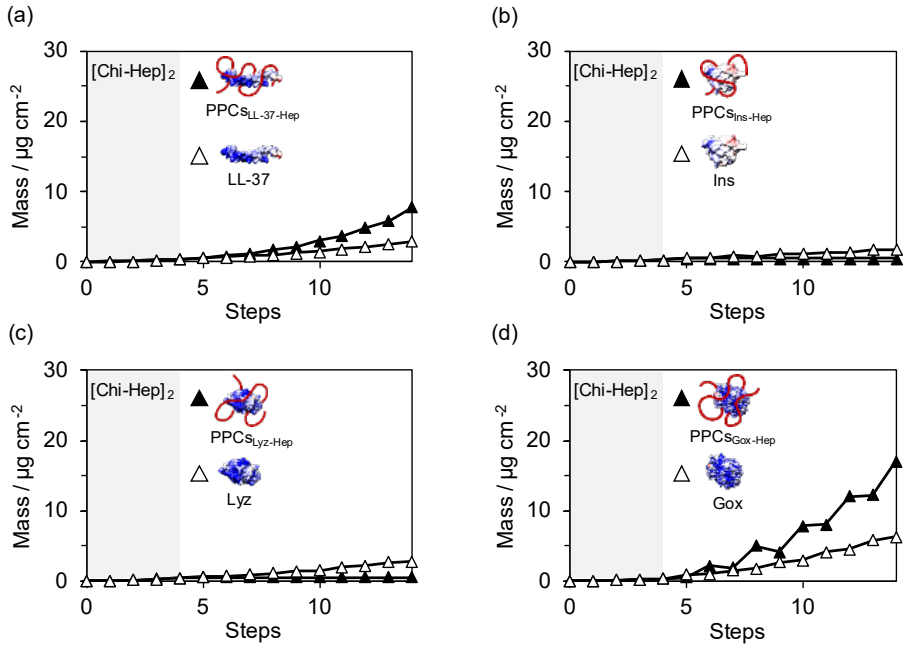

Figure IV-1. S4 – Mass adsorbed measured by QCM-D after adsorption of an anchoring layer of two Chi-Hep bilayers ($[Chi\text{-}Hep]_2$, shaded area) followed by five adsorption steps of either Chi and PPCs or bare proteins and Hep. (a) $[Chi\text{-}PPCs_{LL\text{-}37\text{-}Hep}]_5$ or $[LL\text{-}37\text{-}Hep]_5$, (b) $[Chi\text{-}PPCs_{Ins\text{-}Hep}]_5$ or $[Ins\text{-}Hep]_5$, (c) $[Chi\text{-}PPCs_{Lyz\text{-}Hep}]_5$ or $[Lyz\text{-}Hep]_5$ or (d) $[Chi\text{-}PPCs_{Gox\text{-}Hep}]_5$ or $[Gox\text{-}Hep]_5$, at pH 3.5 in ultrapure water.

1.6.5 Evolution of the adsorbed mass of a multilayer either made up of PAH and proteins complexed with Hep or made up of bare proteins and Hep

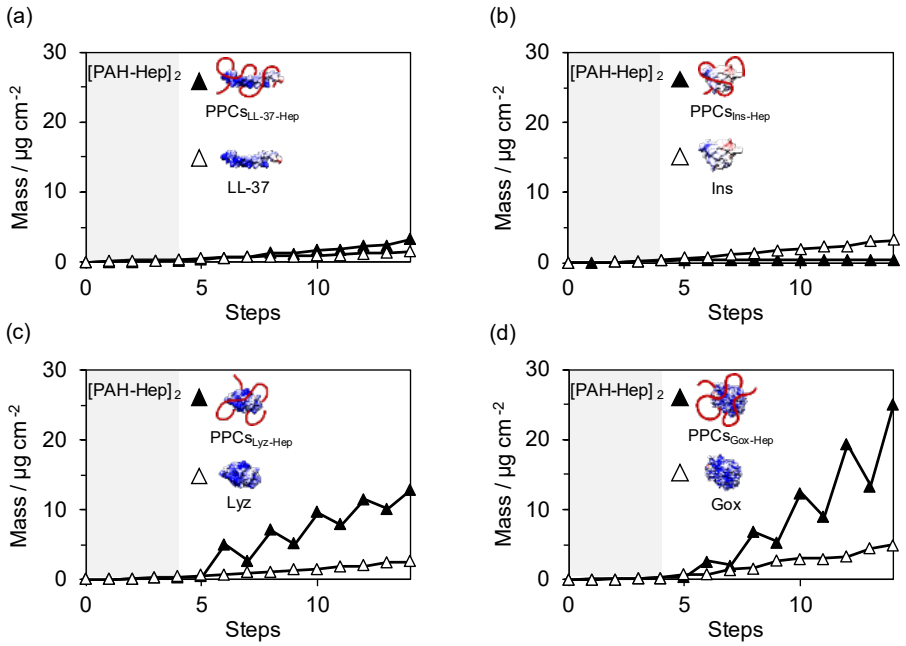

Figure IV-1. S5 – Mass adsorbed measured by QCM-D after adsorption of an anchoring layer of two PAH-Hep bilayers ($[PAH\text{-}Hep]_2$, shaded area) followed by five adsorption steps of either PAH and PPCs or bare proteins and Hep. (a) $[PAH\text{-}PPCs_{LL\text{-}37\text{-}Hep}]_5$ or $[LL\text{-}37\text{-}Hep]_5$, (b) $[PAH\text{-}PPCs_{Ins\text{-}Hep}]_5$ or $[Ins\text{-}Hep]_5$, (c) $[PAH\text{-}PPCs_{Lyz\text{-}Hep}]_5$ or $[Lyz\text{-}Hep]_5$ or (d) $[PAH\text{-}PPCs_{Gox\text{-}Hep}]_5$ or $[Gox\text{-}Hep]_5$, at pH 3.5 in ultrapure water.

1.6.6 Evolution of the adsorbed mass of a multilayer either made up of Chi and proteins complexed with Alg or made up of bare proteins and Alg

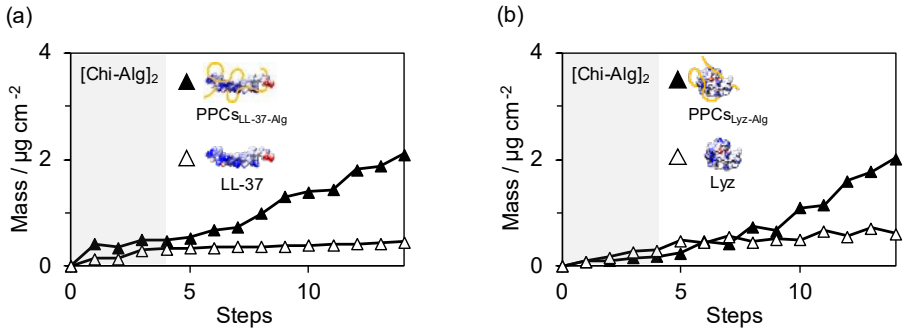

Figure IV-1. S6 – Mass adsorbed measured by QCM-D after adsorption of an anchoring layer of two Chi-Alg bilayers ($[Chi\text{-}Alg]_2$, shaded area) followed by five adsorption steps of either Chi and PPCs or bare proteins and Alg. (a) $[Chi\text{-}PPCs_{LL\text{-}37\text{-}Alg}]_5$ or $[LL\text{-}37\text{-}Alg]_5$, (b) $[Chi\text{-}PPCs_{Lyz\text{-}Alg}]_5$ or $[Lyz\text{-}Alg]_5$, at pH 5 in ultrapure water.

1.6.7 Evolution of the adsorbed mass of a multilayer either made up of PAH and proteins complexed with Alg or made up of bare proteins and Alg

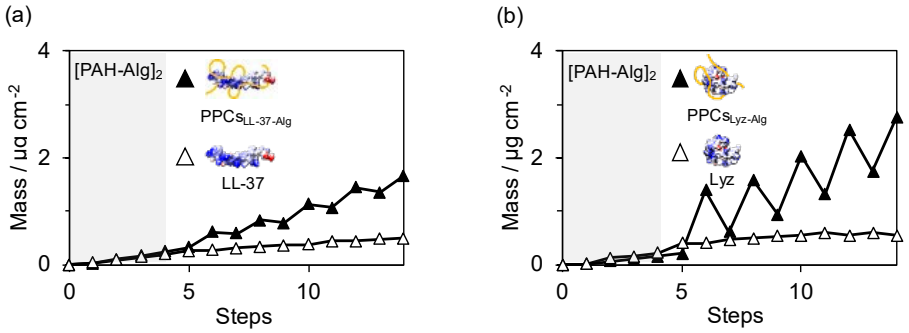

Figure IV-1. S7 – Mass adsorbed measured by QCM-D after adsorption of an anchoring layer of two PAH-Alg bilayers ($[PAH\text{-}Alg]_2$, shaded area) followed by five adsorption steps of either PAH and PPCs or bare proteins and Alg. (a) $[PAH\text{-}PPCs_{LL\text{-}37\text{-}Alg}]_5$ or $[LL\text{-}37\text{-}Alg]_5$, (b) $[PAH\text{-}PPCs_{Lyz\text{-}Alg}]_5$ or $[Lyz\text{-}Alg]_5$, at pH 5 in ultrapure water.

1.6.8 Evolution of the adsorbed mass of a multilayer either made up of Chi and proteins complexed with PSS or made up of bare proteins and PSS

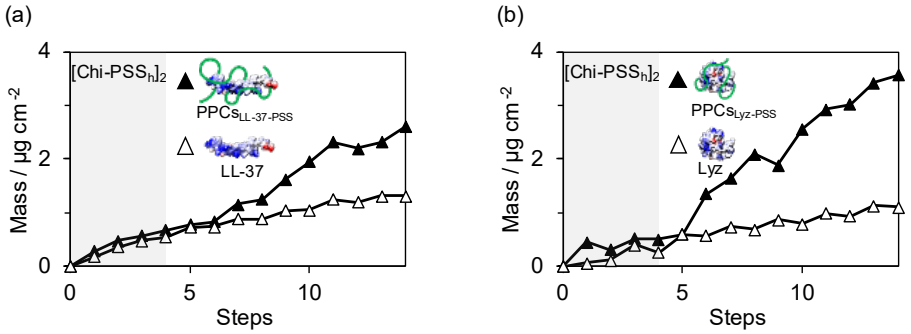

Figure IV-1. S8 – Mass adsorbed measured by QCM-D after adsorption of an anchoring layer of two Chi-PSS_h bilayers ($[Chi\text{-}PSS_h]_2$, shaded area) followed by five adsorption steps of either Chi and PPCs or bare proteins and PSS_l. (a) $[Chi\text{-}PPCs_{LL\text{-}37\text{-}PSSl}]_5$ or $[LL\text{-}37\text{-}PSS_l]_5$, (b) $[Chi\text{-}PPCs_{Lyz\text{-}PSSl}]_5$ or $[Lyz\text{-}PSS_l]_5$, at pH 5 in ultrapure water.

1.6.9 Evolution of the adsorbed mass of a multilayer either made up of PAH and proteins complexed with PSS or made up of bare proteins and PSS

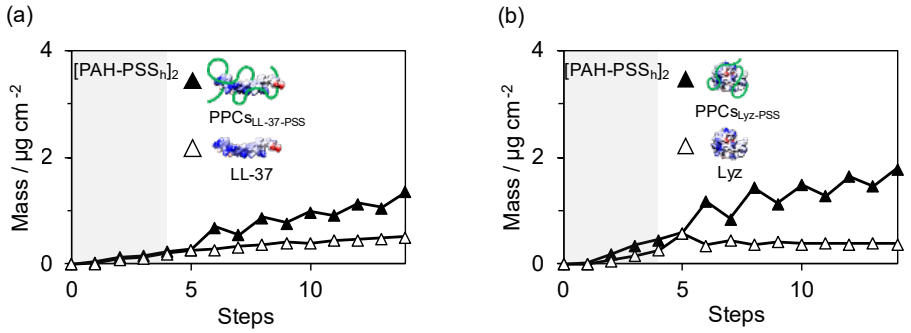

Figure IV-1. S9 – Mass adsorbed measured by QCM-D after adsorption of an anchoring layer of two PAH-PSS_h bilayers ($[PAH\text{-}PSS_h]_2$, shaded area) followed by five adsorption steps of either PAH and PPCs or bare proteins and PSS_l. (a) $[PAH\text{-}PPCs_{LL\text{-}37\text{-}PSSl}]_5$ or $[LL\text{-}37\text{-}PSS_l]_5$, (b) $[PAH\text{-}PPCs_{Lyz\text{-}PSSl}]_5$ or $[Lyz\text{-}PSS_l]_5$, at pH 5 in ultrapure water.

1.6.10 Evolution of the frequency and dissipation shifts of a multilayer either made up of Chi and LL-37 complexed with Hep or made up of bare LL-37 and Hep

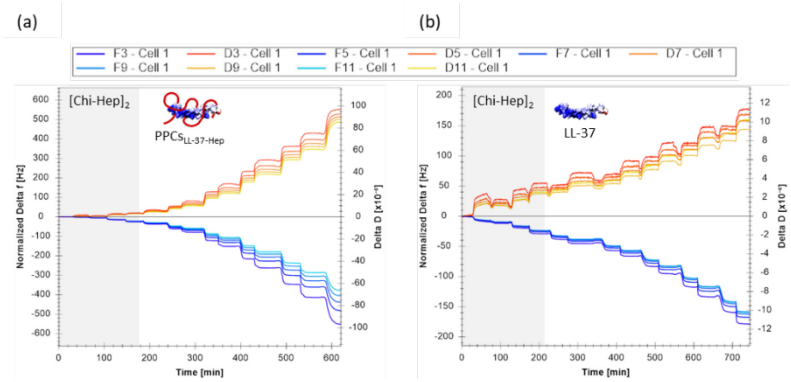

Figure IV-1. S10 – Evolution of the frequency and dissipation shift (3rd, 5th, 7th, 9th and 11th overtone) measured by QCM-D after adsorption of an anchoring layer of two Chi-Hep bilayers ($[Chi\text{-}Hep]_2$, shaded area) followed by five adsorption steps of either (a) Chi and PPCs ($[Chi\text{-}PPCs_{LL\text{-}37\text{-}Hep}]_5$) or (b) bare proteins and Hep ($[LL\text{-}37\text{-}Hep]_5$), at pH 3.5 in ultrapure water.

1.6.11 Evolution of the frequency and dissipation shifts of a multilayer either made up of Chi and Ins complexed with Hep or made up of bare Ins and Hep

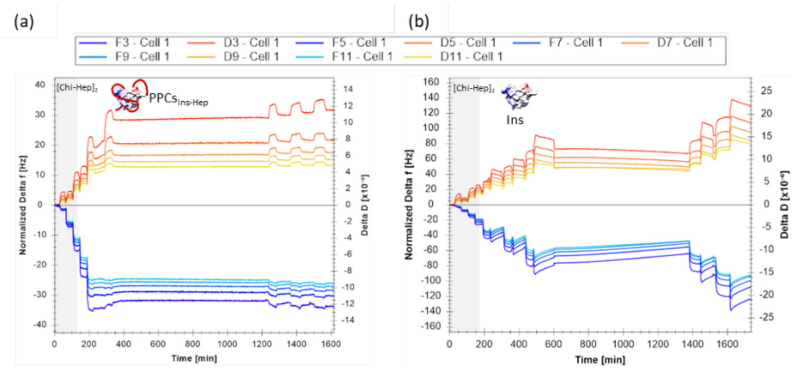

Figure IV-1. S11 – Evolution of the frequency and dissipation shift (3rd, 5th, 7th, 9th and 11th overtone) measured by QCM-D after adsorption of an anchoring layer of two Chi-Hep bilayers ($[Chi\text{-}Hep]_2$, shaded area) followed by five adsorption steps of either (a) Chi and PPCs ($[Chi\text{-}PPCs_{Ins\text{-}Hep}]_5$) or (b) bare proteins and Hep ($[Ins\text{-}Hep]_5$), at pH 3.5 in ultrapure water.

1.6.12 Evolution of the frequency and dissipation shifts of a multilayer either made up of Chi and Lyz complexed with Hep or made up of bare Lyz and Hep

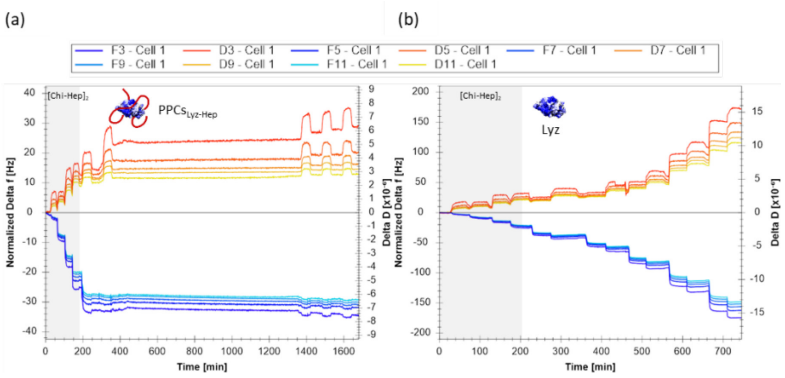

Figure IV-1. S12 – Evolution of the frequency and dissipation shift (3rd, 5th, 7th, 9th and 11th overtone) measured by QCM-D after adsorption of an anchoring layer of two Chi-Hep bilayers ($[Chi\text{-}Hep]_2$, shaded area) followed by five adsorption steps of either (a) Chi and PPCs ($[Chi\text{-}PPCs_{Lyz\text{-}Hep}]_5$) or (b) bare proteins and Hep ($[Lyz\text{-}Hep]_5$), at pH 3.5 in ultrapure water.

1.6.13 Evolution of the frequency and dissipation shifts of a multilayer either made up of Chi and Gox complexed with Hep or made up of bare Gox and Hep

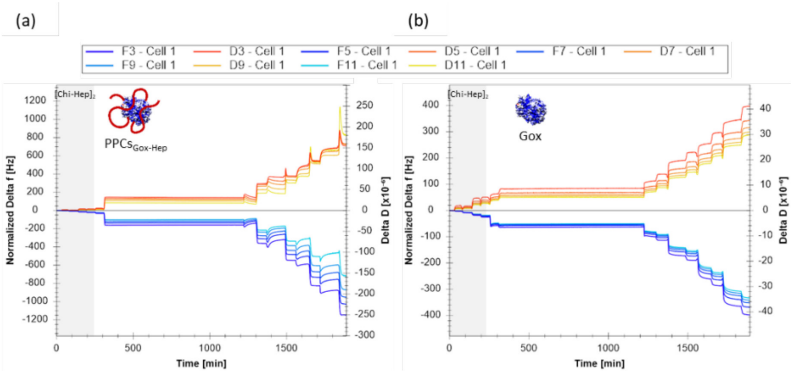

Figure IV-1. S13 – Evolution of the frequency and dissipation shift (3rd, 5th, 7th, 9th and 11th overtone) measured by QCM-D after adsorption of an anchoring layer of two Chi-Hep bilayers ($[Chi\text{-}Hep]_2$, shaded area) followed by five adsorption steps of either (a) Chi and PPCs ($[Chi\text{-}PPCs_{Gox\text{-}Hep}]_5$) or (b) bare proteins and Hep ($[Gox\text{-}Hep]_5$), at pH 3.5 in ultrapure water.

1.6.14 Evolution of the frequency and dissipation shifts of a multilayer either made up of PAH and LL-37 complexed with Hep or made up of bare LL-37 and Hep

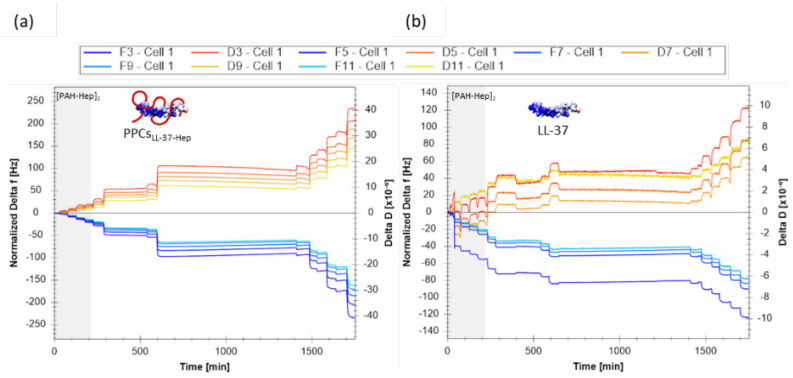

Figure IV-1. S14 – Evolution of the frequency and dissipation shift (3rd, 5th, 7th, 9th and 11th overtone) measured by QCM-D after adsorption of an anchoring layer of two PAH-Hep bilayers ($[PAH\text{-}Hep]_2$, shaded area) followed by five adsorption steps of either (a) PAH and PPCs ($[PAH\text{-}PPCs_{LL\text{-}37\text{-}Hep}]_5$) or (b) bare proteins and Hep ($[LL\text{-}37\text{-}Hep]_5$), at pH 3.5 in ultrapure water.

1.6.15 Evolution of the frequency and dissipation shifts of a multilayer either made up of PAH and Ins complexed with Hep or made up of bare Ins and Hep

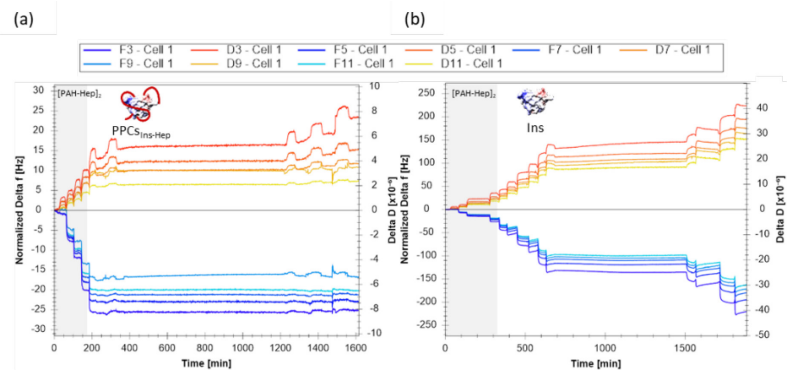

Figure IV-1. S15 – Evolution of the frequency and dissipation shift (3rd, 5th, 7th, 9th and 11th overtone) measured by QCM-D after adsorption of an anchoring layer of two PAH-Hep bilayers ($[PAH\text{-}Hep]_2$, shaded area) followed by five adsorption steps of either (a) PAH and PPCs ($[PAH\text{-}PPCs_{Ins\text{-}Hep}]_5$) or (b) bare proteins and Hep ($[Ins\text{-}Hep]_5$), at pH 3.5 in ultrapure water.

1.6.16 Evolution of the frequency and dissipation shifts of a multilayer either made up of PAH and Lyz complexed with Hep or made up of bare Lyz and Hep

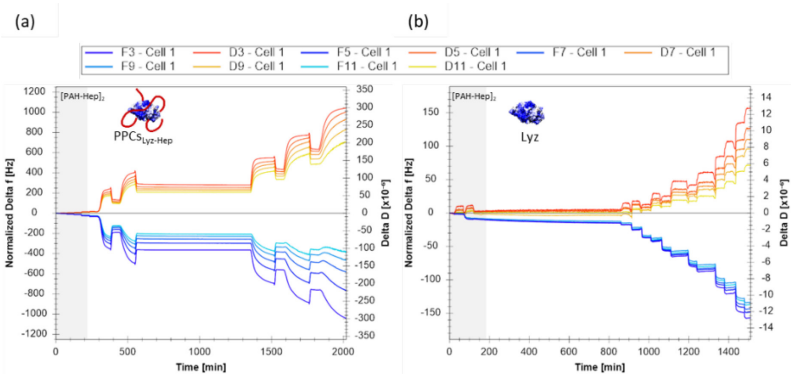

Figure IV-1. S16 – Evolution of the frequency and dissipation shift (3rd, 5th, 7th, 9th and 11th overtone) measured by QCM-D after adsorption of an anchoring layer of two PAH-Hep bilayers ($[PAH\text{-}Hep]_2$, shaded area) followed by five adsorption steps of either (a) PAH and PPCs ($[PAH\text{-}PPCs_{Lyz\text{-}Hep}]_5$) or (b) bare proteins and Hep ($[Lyz\text{-}Hep]_5$), at pH 3.5 in ultrapure water.

1.6.17 Evolution of the frequency and dissipation shifts of a multilayer either made up of PAH and Gox complexed with Hep or made up of bare Gox and Hep

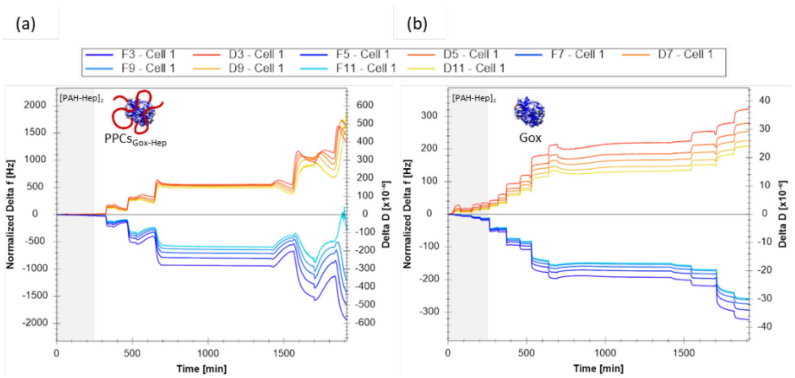

Figure IV-1. S17 – Evolution of the frequency and dissipation shift (3rd, 5th, 7th, 9th and 11th overtone) measured by QCM-D after adsorption of an anchoring layer of two PAH-Hep bilayers ($[PAH\text{-}Hep]_2$, shaded area) followed by five adsorption steps of either (a) PAH and PPCs ($[PAH\text{-}PPCs_{Gox\text{-}Hep}]_5$) or (b) bare proteins and Hep ($[Gox\text{-}Hep]_5$), at pH 3.5 in ultrapure water.

1.6.18 Evolution of the frequency and dissipation shifts of a multilayer either made up of Chi and LL-37 complexed with Alg or made up of bare LL-37 and Alg

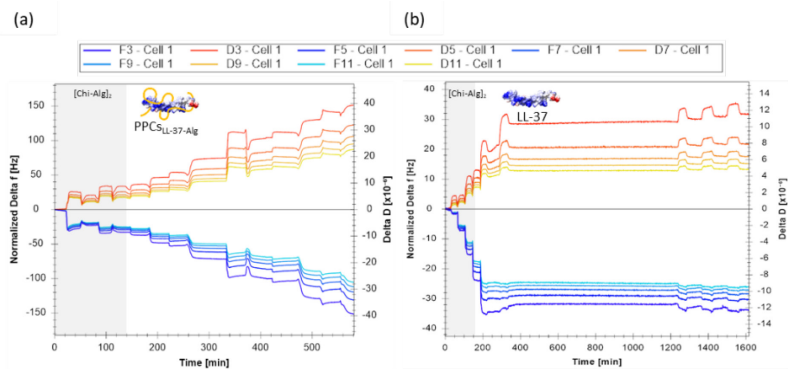

Figure IV-1. S18 – Evolution of the frequency and dissipation shift (3rd, 5th, 7th, 9th and 11th overtone) measured by QCM-D after adsorption of an anchoring layer of two Chi-Alg bilayers ($[Chi\text{-}Alg]_2$, shaded area) followed by five adsorption steps of either (a) Chi and PPCs ($[Chi\text{-}PPCs_{LL\text{-}37\text{-}Alg}]_5$) or (b) bare proteins and Alg ($[LL\text{-}37\text{-}Alg]_5$), at pH 5 in ultrapure water.

1.6.19 Evolution of the frequency and dissipation shifts of a multilayer either made up of Chi and Lyz complexed with Alg or made up of bare Lyz and Alg

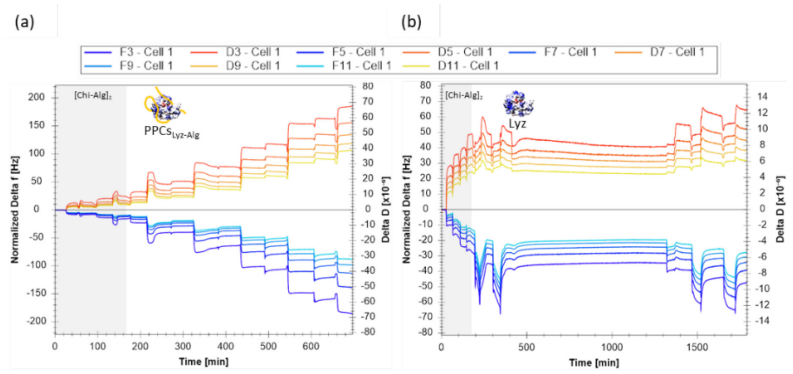

Figure IV-1. S19 – Evolution of the frequency and dissipation shift (3rd, 5th, 7th, 9th and 11th overtone) measured by QCM-D after adsorption of an anchoring layer of two Chi-Alg bilayers ($[Chi\text{-}Alg]_2$, shaded area) followed by five adsorption steps of either (a) Chi and PPCs ($[Chi\text{-}PPCs_{Lyz\text{-}Alg}]_5$) or (b) bare proteins and Alg ($[Lyz\text{-}Alg]_5$), at pH 5 in ultrapure water.

1.6.20 Evolution of the frequency and dissipation shifts of a multilayer either made up of Chi and LL-37 complexed with PSS or made up of bare LL-37 and PSS

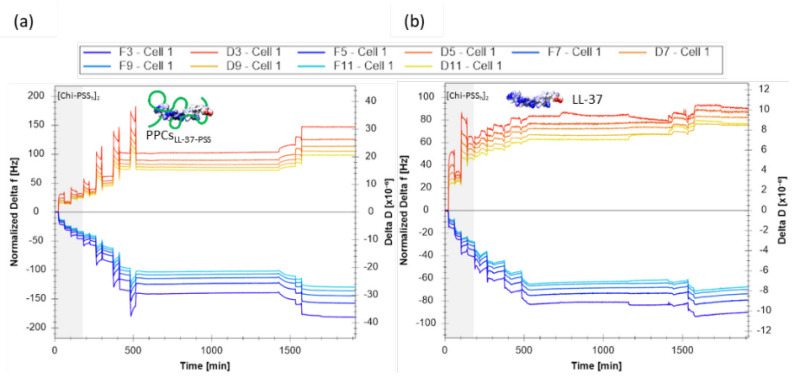

Figure IV-1. S20 – Evolution of the frequency and dissipation shift (3rd, 5th, 7th, 9th and 11th overtone) measured by QCM-D after adsorption of an anchoring layer of two Chi-PSS_h bilayers ($[Chi\text{-}PSS_h]_2$, shaded area) followed by five adsorption steps of either (a) Chi and PPCs ($[Chi\text{-}PPCs_{LL\text{-}37\text{-}PSS_l}]_5$) or (b) bare proteins and PSS_l ($[LL\text{-}37\text{-}PSS_l]_5$), at pH 5 in ultrapure water.

1.6.21 Evolution of the frequency and dissipation shifts of a multilayer either made up of Chi and Lyz complexed with PSS or made up of bare Lyz and PSS

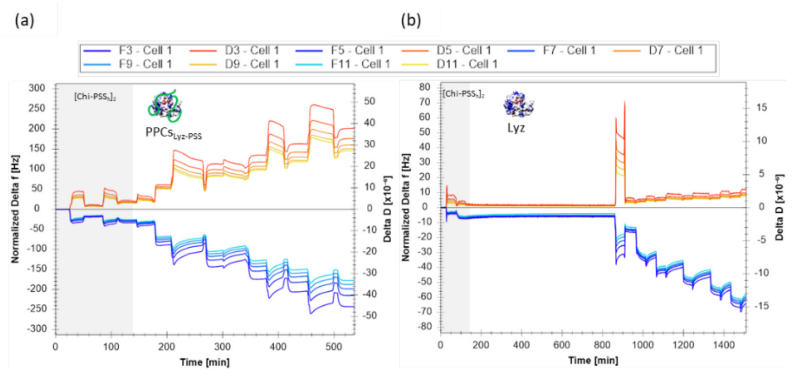

Figure IV-1. S21 – Evolution of the frequency and dissipation shift (3rd, 5th, 7th, 9th and 11th overtone) measured by QCM-D after adsorption of an anchoring layer of two Chi-PSS_h bilayers ($[Chi\text{-}PSS_h]_2$, shaded area) followed by five adsorption steps of either (a) Chi and PPCs ($[Chi\text{-}PPCs_{Lyz\text{-}PSS_l}]_5$) or (b) bare proteins and PSS_l ($[Lyz\text{-}PSS_l]_5$), at pH 5 in ultrapure water.

1.6.22 Evolution of the frequency and dissipation shifts of a multilayer either made up of PAH and Lyz complexed with PSS or made up of bare Lyz and PSS

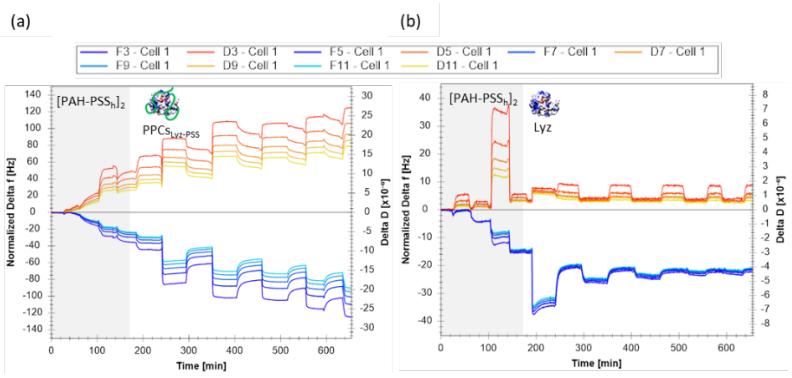

Figure IV-1. S22 – Evolution of the frequency and dissipation shift (3rd, 5th, 7th, 9th and 11th overtone) measured by QCM-D after adsorption of an anchoring layer of two PAH-PSS_h bilayers ($[PAH\text{-}PSS_h]_2$, shaded area) followed by five adsorption steps of either (a) PAH and PPCs ($[PAH\text{-}PPCs_{Lyz\text{-}PSSl}]_5$) or (b) bare proteins and PSS_l ($[Lyz\text{-}PSS_l]_5$), at pH 5 in ultrapure water.

1.6.23 Evolution of the thickness of a multilayer either made up of Chi and LL-37 complexed with Hep or made up of bare LL-37 and Hep

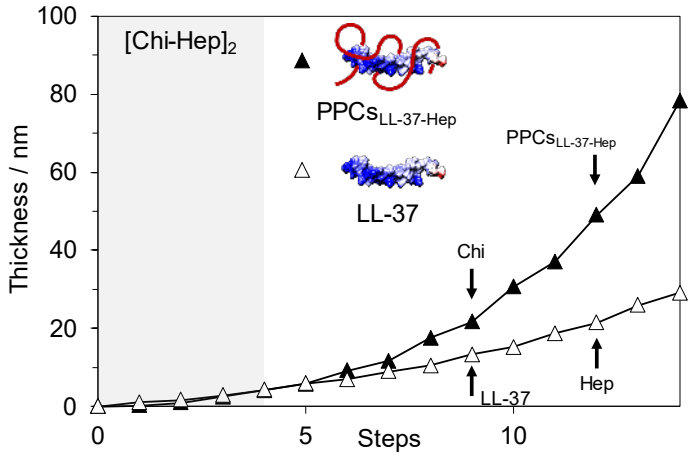

Figure IV-1. S23 – Thickness measured by QCM-D after adsorption of an anchoring layer of two Chi-Hep bilayers ($[Chi\text{-}Hep]_2$, shaded area) followed by five adsorption steps of either Chi and $PPCs_{LL\text{-}37\text{-}Hep}$ ($[Chi\text{-}PPCs_{LL\text{-}37\text{-}Hep}]_5$) or bare LL-37 and Hep ($[LL\text{-}37\text{-}Hep]_5$), at pH 3.5 in ultrapure water.

1.6.24 X-ray photoelectron spectroscopy

The sequential adsorption of $PPCs_{LL\text{-}37\text{-}Hep}$ with a charge ratio (-)/(+net) = 2 with Chi enables multilayer construction. In order to assess the stability of these multilayered systems, XPS experiments were performed on a SSI X probe spectrometer (SSI 100, Surface Science Laboratories, Mountain View, CA, USA) using the procedure described elsewhere.[79] Bare titanium surface were first analyzed by XPS as control a sample (Figure IV-1. S24a). The following assemblies were then built on a Chi-Hep bilayer cushion (Figure IV-1. S24b): $[Chi\text{-}PPCs_{LL\text{-}37\text{-}Hep}]_6$ (Figure IV-1. S24c), $[Chi\text{-}PPCs_{LL\text{-}37\text{-}Hep}]_6$ followed by immersion in MHB (Figure IV-1. S24d), $[Chi\text{-}PPCs_{LL\text{-}37\text{-}Hep}]_6$ followed by immersion in a NaCl solution at pH 9 and I = 150 mM (Figure IV-1. S24e) and $[Chi\text{-}PPCs_{LL\text{-}37\text{-}Hep}]_6$ followed by immersion in SDS (Figure IV-1. S24f). Ti 2p, N 1s and C 1s spectra are presented in Figure IV-1. S24 for all these conditions. For Ti 2p, the two main peaks at 458.8 and 464.5 eV correspond to Ti at an oxidation state of +IV. The smaller peak at 454.04 eV stands for the metallic titanium. The decrease in intensity of the TiO_2 peak from the Ti sample to the two bilayers cushion sample ($[Chi\text{-}Hep]_2$) until it becomes undetectable in the next samples shows clearly that the substrate is progressively covered by the growing layers. No difference between $[Chi\text{-}PPCs_{LL\text{-}37\text{-}Hep}]_6$ sample (Figure IV-1. S24c) and $[Chi\text{-}PPCs_{LL\text{-}37\text{-}Hep}]_6$ samples immersed in different solutions (d, e and f in Figure IV-1. S24) were observed for the Ti 2p spectra. It seems that MHB, NaCl and SDS solutions do not lead to a total multilayer desorption. However, it does not mean that there is no destabilization or reorganization within the multilayer. N 1s spectra depicts the N peaks for each sample, which can be divided in two main peaks. The first one is located around 401.7 eV and corresponds to the NH_3^+ shift. A second peak occurs around 399.8 eV and can be attributed to three different functions of the N atom, which are NH_2, N-SO_3 and the amide function (C=O)-NH. C 1s spectra can be split into four different peaks attributed to different C functions: 289.0 eV correspond to the O=C-O function, 288.0 eV for the N-C=O function, 287.8 eV for the O-C-O function, 286.5 for the C-(O, N) function and finally, 284.8 eV correspond to the C-(C, H) function. In order to study the resulting films stability, after immersion of $[Chi\text{-}PPCs_{LL\text{-}37\text{-}Hep}]_6$ multilayers in MHB, NaCl and SDS solutions, the differences between the N 1s and C 1s peaks were analyzed for the 4 conditions (c, d, e and f in Figure IV-1. S24).

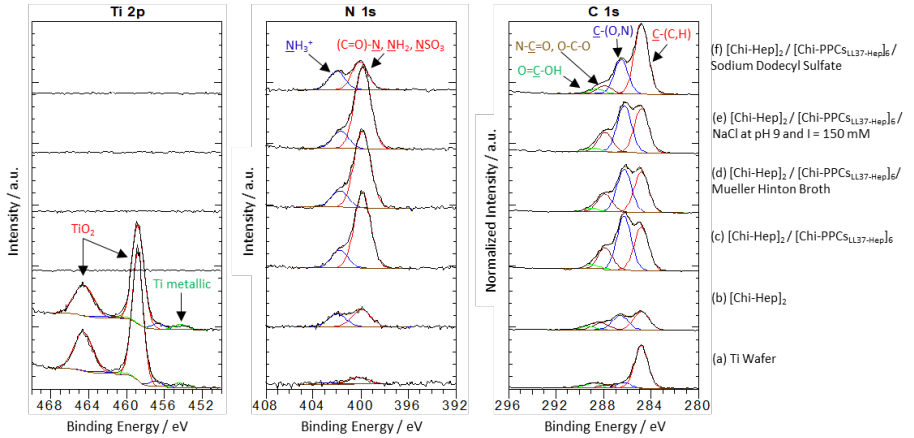

Figure IV-1. S24 – Ti 2p, N 1s, and C 1s peaks recorded by XPS for Ti surfaces coated with (a) nothing, (b) $[Chi\text{-}Hep]_2$ cushion followed by (c) $[Chi\text{-}PPCs_{LL\text{-}37\text{-}Hep}]_6$, (d) $[Chi\text{-}PPCs_{LL\text{-}37\text{-}Hep}]_6$ followed by immersion in a Mueller Hinton Broth solution, (e) $[Chi\text{-}PPCs_{LL\text{-}37\text{-}Hep}]_6$ followed by immersion in a NaCl solution at pH 5 and I = 0 mM and (f) $[Chi\text{-}PPCs_{LL\text{-}37\text{-}Hep}]_6$ followed by immersion in a Sodium dodecyl sulfate solution. Spectra are presented with their respective decomposition in components or doublets. The C 1s peaks were normalized in such a way that their maxima, *i.e.*, C-(C-H) component, have the same height. The peak intensity can thus not be directly compared.

1.6.25 Evolution of the adsorbed mass of a multilayer either made up of Hep and proteins complexed with PAH or made up of bare proteins and PAH

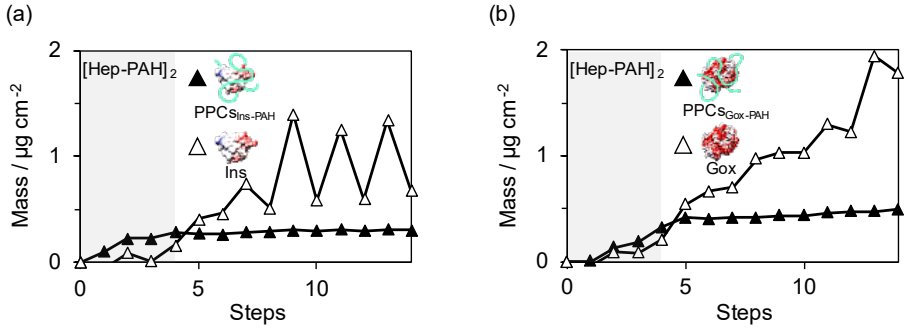

Figure IV-1. S25 – Mass adsorbed measured by QCM-D after adsorption of an anchoring layer of two Hep-PAH bilayers ($[PAH\text{-}Hep]_2$, shaded area) followed by five adsorption steps of either Hep and Ins-based PPCs (plain triangle) $[Hep\text{-}PPCs_{Ins\text{-}PAH}]_5$ or bare Ins proteins and PAH (empty triangle) $[Ins\text{-}PAH]_5$, at pH 7.5 in ultrapure water. (b) Mass adsorbed measured by QCM-D after adsorption of an anchoring layer of two Hep-PAH bilayers ($[PAH\text{-}Hep]_2$, shaded area) followed by five adsorption steps of either Hep and Gox-based PPCs (plain triangle) $[Hep\text{-}PPCs_{Gox\text{-}PAH}]_5$ or bare Gox proteins and PAH (empty triangle) $[Gox\text{-}PAH]_5$, at pH 7.5 in ultrapure water.

1.7 References

1. Han, C. & Guo, W. Fluorescent Noble Metal Nanoclusters Loaded Protein Hydrogel Exhibiting Anti-Biofouling and Self-Healing Properties for Electrochemiluminescence Biosensing Applications. *Small* **16**, 2002621 (2020).
2. Teanphonkrang, S. & Schulte, A. Automated Quantitative Enzyme Biosensing in 24-Well Microplates. *Anal Chem* **89**, 5261–5269 (2017).
3. Büscher, N. *et al.* Biocatalyst Immobilization by Anchor Peptides on an Additively Manufacturable Material. *Org Process Res Dev* **23**, 1852–1859 (2019).
4. Zhang, G., Johnston, T., Quin, M. B. & Schmidt-Dannert, C. Developing a Protein Scaffolding System for Rapid Enzyme Immobilization and Optimization of Enzyme Functions for Biocatalysis. *ACS Synth Biol* **8**, 1867–1876 (2019).
5. Schoeller, J. *et al.* pH-responsive chitosan/alginate polyelectrolyte complexes on electrospun PLGA nanofibers for controlled drug release. *Nanomaterials* **11**, 1850 (2021).
6. Lu, Y., Aimetti, A. A., Langer, R. & Gu, Z. Bioresponsive materials. *Nat Rev Mater* **2**, 16075 (2016).
7. Kitsara, M. *et al.* Polysaccharide–Protein Multilayers Based on Chitosan–Fibrinogen Assemblies for Cardiac Cell Engineering. *Macromol Biosci* **22**, e2100346 (2021).
8. Zander, N. E., Orlicki, J. A., Rawlett, A. M. & Beebe, T. P. Quantification of protein incorporated into electrospun polycaprolactone tissue engineering scaffolds. *ACS Appl Mater Interfaces* **4**, 2074–2081 (2012).
9. Richardson, J. J., Björnmalm, M. & Caruso, F. Technology-driven layer-by-layer assembly of nanofilms. *Science* **348**, 411–422 (2015).
10. Faccio, G. From protein features to sensing surfaces. *Sensors (Switzerland)* **18**, 1204 (2018).
11. Roach, P., Farrar, D. & Perry, C. C. Interpretation of protein adsorption: Surface-induced conformational changes. *J Am Chem Soc* **127**, 8168–8173 (2005).

12. Li, T., Hao, L., Li, J., Du, C. & Wang, Y. Insight into vitronectin structural evolution on material surface chemistries: The mediation for cell adhesion. *Bioact Mater* **5**, 1044–1052 (2020).
13. Jain, A. *et al.* Modulating the biological function of protein by tailoring the adsorption orientation on nanoparticles. *J Colloid Interface Sci* **587**, 150–161 (2021).
14. Yong, K. W., Yuen, D., Chen, M. Z., Porter, C. J. H. & Johnston, A. P. R. Pointing in the Right Direction: Controlling the Orientation of Proteins on Nanoparticles Improves Targeting Efficiency. *Nano Lett* **19**, 1827–1831 (2019).
15. Latour, R. A. Fundamental Principles of the Thermodynamics and Kinetics of Protein Adsorption to Material Surfaces. *Colloids Surf B Biointerfaces* **191**, 110992 (2020).
16. Norde, W., Buijs, J. & Lyklema, H. Adsorption Of Globular Proteins. *Fundamentals of Interface and Colloid Science* **5**, 3.1-3.59 (2005).
17. Langmuir, I. & Schaefer, V. J. Properties and structure of protein monolayers. *Chem Rev* **24**, 181–202 (1939).
18. Weltz, J. S., Kienle, D. F., Schwartz, D. K. & Kaar, J. L. Reduced Enzyme Dynamics upon Multipoint Covalent Immobilization Leads to Stability-Activity Trade-off. *J Am Chem Soc* **142**, 3463–3471 (2020).
19. Ogorzalek, T. L. *et al.* Molecular-Level Insights into Orientation-Dependent Changes in the Thermal Stability of Enzymes Covalently Immobilized on Surfaces. *Langmuir* **31**, 6145–6153 (2015).
20. Decher, G., Hong, J. D. & Schmitt, J. Buildup of ultrathin multilayer films by a self-assembly process: III. Consecutively alternating adsorption of anionic and cationic polyelectrolytes on charged surfaces. *Thin Solid Films* **210–211**, 831–835 (1992).
21. Schlenoff, J. B., Ly, H. & Li, M. Charge and mass balance in polyelectrolyte multilayers. *J Am Chem Soc* **120**, 7626–7634 (1998).
22. Decher, G. Fuzzy Nanoassemblies: Toward Layered Polymeric Multicomposites. *Science* **277**, 1232–1237 (1997).
23. Hammond, P. T. Recent explorations in electrostatic multilayer thin film assembly. *Curr Opin Colloid Interface Sci* **4**, 430–442 (1999).
24. Borges, J. & Mano, J. F. Molecular interactions driving the layer-by-layer assembly of multilayers. *Chem Rev* **114**, 8883–8942 (2014).

25. Ariga, K., Lvov, Y. & Decher, G. There is still plenty of room for layer-by-layer assembly for constructing nanoarchitectonics-based materials and devices. *Physical Chemistry Chemical Physics* **24**, 4097–4115 (2022).
26. Kleinfeld, E. R. & Ferguson, G. S. Stepwise Formation of Multilayered Nanostructural Films from Macromolecular Precursors. *Science* **265**, 370–373 (1994).
27. de Lucena, N. C., Miyazaki, C. M., Shimizu, F. M., Constantino, C. J. L. & Ferreira, M. Layer-by-layer composite film of nickel phthalocyanine and montmorillonite clay for synergistic effect on electrochemical detection of dopamine. *Appl Surf Sci* **436**, 957–966 (2018).
28. Lvov, Y., Hass, H., Decher, G. & Möhwald, H. Successive Deposition of Alternate Layers of Polyelectrolytes and a Charged Virus. *Langmuir* **10**, 4232–4236 (1994).
29. Watanabe, S. & Regen, S. L. Dendrimers as Building Blocks for Multilayer Construction. *J Am Chem Soc* **116**, 8855–8856 (1994).
30. Yoshida, K. *et al.* Adsorption and release of rose bengal on layer-by-layer films of poly(vinyl alcohol) and poly(amidoamine) dendrimers bearing 4-carboxyphenylboronic acid. *Polymers (Basel)* **12**, 1854 (2020).
31. Jiang, Y., Shen, Y. & Wu, P. Self-assembly of multilayer films containing gold nanoparticles via hydrogen bonding. *J Colloid Interface Sci* **319**, 398–405 (2008).
32. Yuehui, W. & Xing, Y. High-reflection optical thin films based on SiO2/TiO2 nanoparticles multilayers by dip coating. *Micro Nano Lett* **13**, 1349–1351 (2018).
33. Lvov, Y., Decher, G. & Sukhorukov, G. Assembly of thin films by means of successive deposition of alternate layers of DNA and poly(allylamine). *Macromolecules* **26**, 5396–5399 (1993).
34. Mauquoy, S. & Dupont-Gillain, C. Combination of collagen and fibronectin to design biomimetic interfaces: Do these proteins form layer-by-layer assemblies? *Colloids Surf B Biointerfaces* **147**, 54–64 (2016).
35. Delechiave, G. *et al.* Tuning protein delivery from different architectures of layer-by-layer assemblies on polymer films. *Mater Adv* **1**, 2043–2056 (2020).

36. Lvov, Y., Ariga, K., Ichinose, I. & Kunitake, T. Assembly of Multicomponent Protein Films by Means of Electrostatic Layer-by-Layer Adsorption. *J Am Chem Soc* **117**, 6117–6123 (1995).
37. Vigier-Carrière, C. *et al.* Bioactive Seed Layer for Surface-Confined Self-Assembly of Peptides. *Angewandte Chemie - International Edition* **54**, 10198–10201 (2015).
38. Rodon Fores, J. *et al.* Localized Supramolecular Peptide Self-Assembly Directed by Enzyme-Induced Proton Gradients. *Angewandte Chemie - International Edition* **56**, 15984–15988 (2017).
39. Vigier-Carrière, C. *et al.* Control of Surface-Localized, Enzyme-Assisted Self-Assembly of Peptides through Catalyzed Oligomerization. *Langmuir* **33**, 8267–8276 (2017).
40. Rodon Fores, J. *et al.* Supported Catalytically Active Supramolecular Hydrogels for Continuous Flow Chemistry. *Angewandte Chemie - International Edition* **58**, 18817–18822 (2019).
41. Silva, R. A., Urzúa, M. D., Petri, D. F. S. & Dubin, P. L. Protein adsorption onto polyelectrolyte layers: Effects of protein hydrophobicity and charge anisotropy. *Langmuir* **26**, 14032–14038 (2010).
42. Becker, A. L., Henzler, K., Welsch, N., Ballauff, M. & Borisov, O. Proteins and polyelectrolytes: A charged relationship. *Curr Opin Colloid Interface Sci* **17**, 90–96 (2012).
43. Sukhishvili, S. A., Kharlampieva, E. & Izumrudov, V. Where polyelectrolyte multilayers and polyelectrolyte complexes meet. *Macromolecules* **39**, 8873–8881 (2006).
44. Ariga, K., Onda, M., Lvov, Y. & Kunitake, T. Alternate Layer-by-Layer Assembly of Organic Dyes and Proteins is Facilitated by Pre-mixing with Linear Polyions. *Chem Lett* **26**, 25–26 (1997).
45. Jin, W., Shi, X. & Caruso, F. High Activity Enzyme Microcrystal Multilayer Films. *J Am Chem Soc* **123**, 8121–8122 (2001).
46. Xia, J. & Dubin, P. L. Protein-Polyelectrolyte Complexes. In: Dubin P., Bock J., Davis R., Schulz D.N., Thies C. in *Macromolecular Complexes in Chemistry and Biology* (ed. Springer) 247–271 (Berlin, Heidelberg, 1994).

47. Cooper, C. L., Dubin, P. L., Kayitmazer, A. B. & Turksen, S. Polyelectrolyte–protein complexes. *Curr Opin Colloid Interface Sci* **10**, 52–78 (2005).
48. vander Straeten, A. *et al.* Protein–polyelectrolyte complexes to improve the biological activity of proteins in layer-by-layer assemblies. *Nanoscale* **9**, 17186–17192 (2017).
49. vander Straeten, A., Bratek-Skicki, A., Jonas, A. M., Fustin, C.-A. & Dupont-Gillain, C. Integrating Proteins in Layer-by-Layer Assemblies Independently of their Electrical Charge. *ACS Nano* **12**, 8372–8381 (2018).
50. Vandamme, D., Landuyt, B., Luyten, W. & Schoofs, L. A comprehensive summary of LL-37, the factoctum human cathelicidin peptide. *Cell Immunol* **280**, 22–35 (2012).
51. Comune, M., Rai, A., Palma, P., TondaTuro, C. & Ferreira, L. Antimicrobial and pro-angiogenic properties of soluble and nanoparticle-immobilized LL37 peptides. *Biomater Sci* **9**, 8153–8159 (2021).
52. Chipman, D. M., Grisaro, V. & Sharon, N. The binding of oligosaccharides containing N-acetylglucosamine and N-acetylmuramic acid to lysozyme. The specificity of binding subsites. *Journal of Biological Chemistry* **242**, 4388–4394 (1967).
53. Vermassen, A. *et al.* Cell wall hydrolases in bacteria: Insight on the diversity of cell wall amidases, glycosidases and peptidases toward peptidoglycan. *Front Microbiol* **10**, 00331 (2019).
54. Wang, Z., Liu, S., Wu, P. & Cai, C. Detection of glucose based on direct electron transfer reaction of glucose oxidase immobilized on highly ordered polyaniline nanotubes. *Anal Chem* **81**, 1638–1645 (2009).
55. Haug, A. Composition and Properties of Alginates. *Norwegian Institute of Seaweed Research*, (Trondheim, Norway, 1964).
56. Sun, J. & Tan, H. Alginate-Based Biomaterials for Regenerative Medicine Applications. *Materials* **6**, 1285–1309 (2013).
57. Xu, M. *et al.* Alginate microgels as delivery vehicles for cell-based therapies in tissue engineering and regenerative medicine. *Carbohydr Polym* **266**, 118128 (2021).
58. Salmivirta, M., Lidholt, K. & Lindahl, U. Heparan sulfate: a piece of information. *The FASEB Journal* **10**, 1270–1279 (1996).

59. Domard, A. pH and c.d. measurements on a fully deacetylated chitosan: application to CuII—polymer interactions. *Int J Biol Macromol* **9**, 98–104 (1987).
60. Li, J. & Zhuang, S. Antibacterial activity of chitosan and its derivatives and their interaction mechanism with bacteria: Current state and perspectives. *Eur Polym J* **138**, 109984 (2020).
61. Castleberry, S. A. *et al.* Self-Assembled Wound Dressings Silence MMP-9 and Improve Diabetic Wound Healing in Vivo. *Advanced Materials* **28**, 1809–1817 (2016).
62. Choi, J. & Rubner, M. F. Influence of the Degree of Ionization on Weak Polyelectrolyte Multilayer Assembly. *Macromolecules* **38**, 116–124 (2005).
63. Dolinsky, T. J., Nielsen, J. E., McCammon, J. A. & Baker, N. A. PDB2PQR: An automated pipeline for the setup of Poisson-Boltzmann electrostatics calculations. *Nucleic Acids Res* **32**, 665–667 (2004).
64. Buchhammer, H. M., Mende, M. & Oelmann, M. Preparation of monodisperse polyelectrolyte complex nanoparticles in dilute aqueous solution. *Prog Colloid Polym Sci* **124**, 98–102 (2004).
65. Kayitmazer, A. B., Seeman, D., Minsky, B. B., Dubin, P. L. & Xu, Y. Protein-polyelectrolyte interactions. *Soft Matter* **9**, 2553–2583 (2013).
66. Seyrek, E., Dubin, P. L., Tribet, C. & Gamble, E. A. Ionic strength dependence of protein-polyelectrolyte interactions. *Biomacromolecules* **4**, 273–282 (2003).
67. Gao, S., Holkar, A. & Srivastava, S. Protein – Polyelectrolyte Complexes and Micellar Assemblies. *Polymers (Basel)* **11**, 1097 (2019).
68. Pettersen, E. F. *et al.* UCSF Chimera - A visualization system for exploratory research and analysis. *J Comput Chem* **25**, 1605–1612 (2004).
69. Cousin, F., Gummel, J., Combet, S. & Boué, F. The model Lysozyme-PSSNa system for electrostatic complexation: Similarities and differences with complex coacervation. *Adv Colloid Interface Sci* **167**, 71–84 (2011).
70. Amaduzzi, F. *et al.* Chitosan-DNA complexes: Charge inversion and DNA condensation. *Colloids Surf B Biointerfaces* **114**, 1–10 (2014).

71. Gupta, A. Enzymes. In: *Comprehensive Biochemistry for Dentistry*. (Springer, Singapore, 2019).
72. Reviakine, I., Johannsmann, D. & Richter, R. P. Hearing What You Cannot See and Visualizing What You Hear. *Anal Chem* **83**, 8838–8848 (2011).
73. vander Straeten, A. & Dupont-Gillain, C. Self-Reorganizing Multilayer to Release Free Proteins from Self-Assemblies. *Langmuir* **36**, 972–978 (2019).
74. Cheng, M., Jiang, C., Luo, C., Zhang, Y. & Shi, F. Investigating Zigzag Film Growth Behaviors in Layer-by-Layer Self-Assembly of Small Molecules through a High-Gravity Technique. *ACS Appl Mater Interfaces* **7**, 18824–18831 (2015).
75. Hoogeveen, N. G., Cohen Stuart, M. A., Fleer, G. J. & Böhmer, M. R. Formation and stability of multilayers of polyelectrolytes. *Langmuir* **12**, 3675–3681 (1996).
76. Dubas, S. T., Farhat, T. R. & Schlenoff, J. B. Multiple Membranes from 'True' Polyelectrolyte Multilayers. *J Am Chem Soc* **123**, 5368–5369 (2001).
77. Rahim, M. A., Choi, W. S., Lee, H. J. & Jeon, I. C. Ionic surfactant-triggered renewal of the structures and properties of polyelectrolyte multilayer films. *Langmuir* **26**, 4680–4686 (2010).
78. Casanova, M. R., Reis, R. L., Martins, A. & Neves, N. M. Surface biofunctionalization to improve the efficacy of biomaterial substrates to be used in regenerative medicine. *Mater Horiz* **7**, 2258–2275 (2020).
79. Art, J. F., vander Straeten, A. & Dupont-Gillain, C. C. NaCl strongly modifies the physicochemical properties of aluminum hydroxide vaccine adjuvants. *Int J Pharm* **517**, 226–233 (2017).

2 Chemical composition of LL-37-based layer-by-layer films revealed by X-ray photoelectron spectroscopy

Cédric Vranckx[1*], Alix Mertens de Wilmars[1], Pierre Eloy[1], Olivier Cornu[2,3], and Christine Dupont-Gillain[1*]

[1]Institute of Condensed Matter and Nanosciences, Bio-and Soft Matter, Université catholique de Louvain, Place Louis Pasteur, 1 bte L4.01.10, B-1348 Louvain-la-Neuve, Belgium
[2]Neuro-Musculo-Skeletal Pole, Experimental and Clinical Research Institute, Université catholique de Louvain, 1200 Brussels, Belgium
[3]Orthopaedic and Trauma Department, Cliniques Universitaires Saint-Luc, Université catholique de Louvain, 1200 Brussels, Belgium

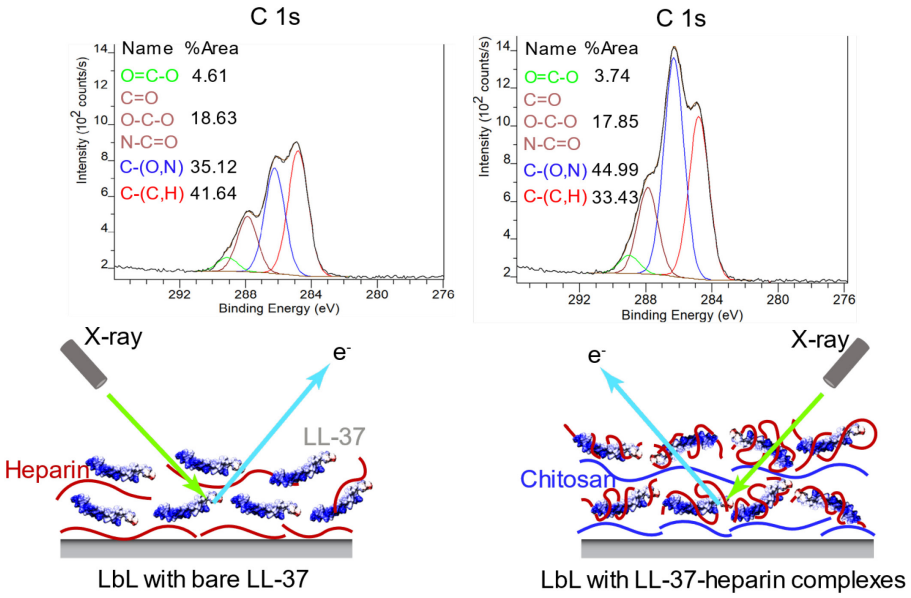

Abstract

To develop antibacterial coatings, the surface immobilization of LL-37, an antimicrobial peptide, represents a potentially valuable approach. This chapter aims to exploit X-ray photoelectron spectroscopy (XPS) data, in depth, to study LL-37-based multilayers assembled using the layer-by-layer (LbL) technique. Through immobilization of LL-37 in its bare form with heparin (Hep) and in its Hep-complexed ($PPCs_{LL\text{-}37\text{-}Hep}$) form with chitosan (Chi), differences have been highlighted in the proportions of Hep, Chi, and LL-37 within the multilayers, depending on the assembly approach. Based on the theoretical degrees of protonation (α) of the nitrogen groups of Hep, Chi and LL-37, and the recognition of sulfur as an indicator of Hep presence in the assemblies, the composition of the coatings was modeled after careful peak decomposition using the stoichiometry of Hep, Chi and LL-37. However, through this approach, it has been observed that the model did not fit with the signal measured by XPS. The measurement conditions inherent to XPS analysis (*i.e.*, multilayer drying, ultra-high vacuum environment, X-ray bombardment, etc.) induced differences between theoretical and observed α values. Therefore, based on α values determined empirically, the composition of [LL-37-Hep] and [Chi-$PPCs_{LL\text{-}37\text{-}Hep}$] multilayers was modeled again with better outcome. The results highlight that more LL-37 is integrated in the multilayers at pH 3.5 than at pH 5, and when using bare LL-37 compared to PPCs. XPS is shown here to be a powerful tool for determining the composition of LbL films integrating several compounds. Together with other analytical methods, it could contribute to the understanding of the organization of such complex coatings.

2.1 Introduction

The immobilization of active biomolecules is topical in different fields such as biosensing,[1,2] heterogeneous biocatalysis,[3,4] drug delivery,[5,6] and tissue engineering.[7,8] Layer-by-layer (LbL) self-assembly is a powerful technique to fabricate functional thin films by immobilizing biomolecules of interest at interfaces.[9] The principle of LbL is based on the surface charge inversion, *i.e.*, the multilayer is built through the successive deposition of positively- and negatively-charged species.[10,11] In this way, multilayers of various compounds or particles can be produced in any number of layers and any desired sequence.[12] Given the vast number of charged entities available, this technique can thus be applied to a wide variety of materials.[12] However, the forces involved in LbL assembly are not limited to electrostatic interactions as other forces such as hydrophobic interactions and hydrogen bonding also participate.[13,14] Hence, the LbL assembly method shows significant promise for designing biofunctionalized materials with diverse architectures.[15]

A commonly used method for determining the chemical composition of such LbL assemblies is X-ray photoelectron spectroscopy (XPS),[16] a technique that discloses not only the atomic composition but also the chemical environment of the outermost first nanometers of a material surface (5-10 nm in thickness).[16] It is thus a suitable technique for providing an overview of the main classes of compounds present in an adsorbed organic layer. In an assembly of biomacromolecules, the analyze of elements largely present, such as C, O, and N and to a lesser extent S and P, is of great interest. Indeed, through the exploitation of chemical shifts (*i.e.*, shifts in the core-level binding energies induced by the immediate chemical environment of an atom) and stoichiometry of these elements, it is possible to confirm the formation of LbL multilayers, examine their composition, and even assess their thickness and homogeneity.[17,18] Maachou *et al.* used XPS to analyze the surface composition and determine the mass concentration of relevant compounds in the surface layer of chitosan-hydroxyapatite biomaterials.[19] In the same vein, Yang *et al*. used XPS to make quantitative comparisons of the chemical compositions of layers formed at the surface of materials as a result of contact with solutions containing extracellular polymeric substances involving different bacterial strains.[20] In both studies, the methodology followed was guided by stoichiometry and charge balance concepts.

However, one of the major limitations of this technique is the use of an ultra-high vacuum for the analysis. Indeed, as the multilayers of biomacromolecules assembled using the LbL technique are highly hydrated structures,[21] analysis under ultra-high vacuum could disturb and thus modify the film organization and architecture. Moreover, it could also affect the charge state of the molecules,[22] which is a crucial parameter in a view of quantitative analysis.

LL-37 is the only human cathelicidin antimicrobial peptide. This 37-amino acids peptide (4.5 kDa) is positively charged (+6) under physiological conditions. It is widely studied for its immunomodulatory functions such as chemotaxis,[23] modulation of pro- and anti-inflammatory responses,[24] influence on cell proliferation and differentiation,[25] promotion of wound healing,[26] angiogenesis,[27] and antibacterial properties.[28] Its immobilization on biomaterial surface is thus of great interest with the goal to design wound-healing and antibacterial coatings. LbL thin films incorporating LL-37 molecules were developed according to two different strategies, as described in our previous study.[29] First, multilayers were designed at pH 3.5 and 5 by assembling LL-37 molecules with heparin (Hep), to form [LL-37-Hep] multilayers. Due to its positive charge, LL-37 can be assembled with Hep, which has the highest negative charge density of any known biological polyanion due to the presence of one carboxyl and three sulfonate groups per repeating unit.[30] Secondly, LL-37 was assembled in the form of a pre-formed complex with Hep. Indeed, as all proteins and peptides, the polyampholyte character and charge anisotropy of LL-37 can disturb its LbL assembly.[31] Therefore, peptide-polyelectrolyte complexes (PPCs) have been recently introduced as new building blocks for the LbL assembly of proteins and peptides.[29,32,33] The negatively-charged $PPCs_{LL\text{-}37\text{-}Hep}$ were thus assembled with chitosan (Chi) as a positively-charged polyelectrolyte (PE) to form [Chi-$PPCs_{LL\text{-}37\text{-}Hep}$] multilayers. Chi is a polysaccharide derived from chitin, which is also known for its antibacterial activity.[34] In our previous work, the successful growth of both $[LL\text{-}37\text{-}Hep]_n$ and $[Chi\text{-}PPCs_{LL\text{-}37\text{-}Hep}]_n$ films has been demonstrated, with higher adsorbed mass in the case of the $[Chi\text{-}PPCs_{LL\text{-}37\text{-}Hep}]_n$ multilayer.[29] However, this study did not provide information regarding the composition of these multilayers, and did not ascertain whether the increased mass adsorbed in the [Chi-$PPCs_{LL\text{-}37\text{-}Hep}$] multilayer results from the

immobilization of a higher amount of LL-37. The increased mass could indeed be due to more Chi and/or Hep deposition or a higher water content.

In this work, potential differences in chemical composition generated by these two assembly strategies are investigated and the presence of LL-37 in these films is evaluated through XPS analyses and in-depth data treatment, including careful peak decomposition. Moreover, the influence of the last adsorbed layer on the XPS signal is studied, *i.e.*, what is the effect on the signal when the last adsorbed layer is Hep instead of LL-37 or Chi instead of $PPCs_{LL\text{-}37\text{-}Hep}$? To do so, the composition of the multilayers was modeled starting from the chemical formula of Chi, Hep and LL-37. To distinguish Hep from Chi and LL-37, sulfur can be used as a marker. Therefore, all the S signal measured by XPS can be attributed to Hep. However, distinguishing between LL-37 and Chi is more challenging, as there is no specific chemical group that can serve as a marker to differentiate the signals originating from LL-37 and Chi. The stoichiometry of the compounds and their degree of protonation (α) were both exploited to reach the final aim of this analytical work: unravelling the composition of multilayers formed at pH 3.5 and 5, emphasizing the differences between $[LL\text{-}37\text{-}Hep]_n$ and $[Chi\text{-}PPCs_{LL\text{-}37\text{-}Hep}]_n$ films and the influence of the final adsorbed layer. An increased knowledge of such films is essential to better understand their potential antibacterial properties.

2.2 Experimental section

2.2.1 Materials

Chi, M_W = 10,000-50,000 g mol^{-1} and deacetylation degree (DD) of 95% was purchased from Heppe Medical Chitosan Gmbh (Halle, Germany). Chi is not soluble in ultrapure water. Therefore, Chi solution was prepared by first dissolving 50 mg of Chi in approximately 25 mL of ultrapure water and 60 µL of HCl 37% (VWR, Leuven, Belgium) at 60°C for 1 h. Then, pH was adjusted to a value of 3.5 or 5 with NaOH 10 M (Sigma Aldrich, Steinheim, Germany) and the volume was brought to exactly 100 mL. Finally, the Chi solution was filtered with successively 5 and 0.2 µm filters to remove small impurities and non-dissolved particles. Hep sodium salt, 5 000 I.E./mL, was obtained from B.Braun (Melsungen, Germany). LL-37, 98.05% pure (peptide sequence: LLGDFFRKSKEKIGKEFKRIVQRIKDFLRNLVPRTES, theoretical molecular mass of

4493.26 Da) was bought from Proteogenix (Schiltigheim, France). Hep and LL-37 solutions were prepared at an ionic strength (I) ≈ 0 mM, in ultrapure water (Elga Purelab Chorus 1, 18.2 MΩ.cm, Veolia, United Kingdom), with only the ions necessary for pH adjustment (3.5 or 5 with NaOH 10 M or HCl 37%). For Chi solution, as Chi must be dissolved in acidic conditions, I cannot be equal to 0 mM. I was kept as low as possible, with only the ions necessary for Chi dissolution and pH adjustment and is around 10 mM. The pH value was measured with a pH-indicator strip (MQuant, Merck, Darmstadt, Germany).

Gold-coated silicon wafers were purchased from Winfab (Louvain-la-Neuve, Belgium). The coating is made of an intermediate Ti layer (10 nm) and an outermost Au layer (250 nm). These wafers were cut into 1 cm x 1 cm pieces. Before use, these pieces were sonicated in acetone for 30 min then dried with N_2. Finally, they were exposed to UV-ozone (UVO Cleaner 42-220, Jelight Company, Irvine, USA) for 15 min.

2.2.2 Formation of $PPCs_{LL\text{-}37\text{-}Hep}$

Since electrostatic interactions drive $PPCs_{LL\text{-}37\text{-}Hep}$ formation, the PE-to-peptide molar ratio used to prepare the complexes is usually expressed as the PE-to-peptide charge ratio. The charge ratio was calculated as the ratio of PE net charge to the peptide net structural charge at pH 3.5 and 5. Due to its sulfonate groups, Hep was considered as fully negatively charged (4 negative charges per Hep repeating unit). The LL-37 charge was computed as a function of pH, based on its amino acid sequence and structure (PDB file: 2K6O), using the PDB2PQR Server.[35] The LL-37 net charge is +10.4 and +7 at, respectively, pH 3.5 and 5. For example, $PPCs_{LL\text{-}37\text{-}Hep}$ at a (-)/(+net) charge ratio of 1.5 were prepared by mixing 3 volumes of Hep solution at 0.5 mM negative charge with 10 volumes of LL-37 solution at 0.1 mM net positive charge. Therefore, the LL-37 and Hep concentrations used to prepare $PPCs_{LL\text{-}37\text{-}Hep}$ with a charge ratio of 1.5, are, respectively, 0.08 and 0.12 mM positive and negative net charge. This constitutes a theoretical charge ratio and taking into account the fact that part of Hep and LL-37 molecules could remain free, *i.e.*, would not be integrated in complexes, the actual charge ratio of the formed $PPCs_{LL\text{-}37\text{-}Hep}$ may differ from this theoretical ratio.

2.2.3 Multilayer construction

Multilayers were constructed on Au wafers by successive adsorption steps, with all steps performed either at pH 3.5 or 5. For all experiments, an anchoring layer of two bilayers of Chi alternately adsorbed with Hep ($[Chi\text{-}Hep]_2$) was constructed from Chi and Hep solutions (0.5 g L^{-1}). Then, two different multilayer systems were built on this anchoring layer: bare LL-37 molecules directly assembled with Hep ($[LL\text{-}37\text{-}Hep]_n$), and $PPCs_{LL\text{-}37\text{-}Hep}$ assembled with Chi ($[Chi\text{-}PPCs_{LL\text{-}37\text{-}Hep}]_n$). The following solutions were used: Chi (0.5 g L^{-1}), Hep (0.5 g L^{-1}) and LL-37 (0.08 mM positive net charge), as well as a suspension of $PPCs_{LL\text{-}37\text{-}Hep}$ prepared as described in the *Part IV – 2.2.2 Formation of $PPCs_{LL\text{-}37\text{-}Hep}$*. Au-coated wafers were placed in 24-well polystyrene Cellstar® plates (Greiner Bio-One, Kremsmünster, Austria) and each adsorption step, that lasted for 20 min, was carried out in static conditions with 300 µL of solution, and was followed by three consecutive rinsing steps with ultrapure water adjusted at pH 3.5 or 5.

2.2.4 X-ray photoelectron spectroscopy

X-ray photoelectron spectroscopy (XPS) measurements on multilayers built on Au-coated wafers were carried out using a SSI X probe spectrometer (SSI 100, Surface Science Laboratories, Mountain View, CA, USA) equipped with a monochromatized Al-Kα radiation source (1486 eV). Samples were fixed on an insulating home-made ceramic carousel by using a piece of double-sided insulating tape. The pressure in the analysis chamber was around 10^{-6} Pa and the direction of photoelectrons collection was 55° to the sample surface. The analyzed area was approximately 1.4 mm² and the used pass energy was set at 50 eV. The C-(C,H) component of the C 1s peak was fixed to 284.8 eV to set the binding energy scale. XPS measurements for every sample consisted of the following steps: (a) recording the survey spectra, (b) recording C 1s, O 1s, N 1s, S 2p and Au 4f spectra, and (c) recording the C 1s spectra again to check the charge stability as a function of time and the absence of sample degradation during the analyses. Data treatment was performed with the CasaXPS program (Casa Software Ltd., United Kingdom). Some spectra were decomposed using the least squares fitting routine provided by the software with a Gaussian/Lorentzian (85/15) product function and after subtraction of a non-linear baseline. Molar fractions (%) of each component were

calculated using peak areas normalized based on acquisition parameters and sensitivity factors provided by the manufacturer.

2.3 Results and discussion

2.3.1 Determination of the thickness of the layer probed by XPS

The thickness of the surface layer probed by XPS was computed, based on the exponential decrease of the signal as a function of depth. 95% of this signal originates from a layer with a thickness of 3λcosθ, where θ represents the angle of photoelectron collection with the normal to the surface of the sample and λ is the inelastic mean free path of the electrons, which is the average distance between inelastic collisions.[16] λ depends on different parameters, including the kinetic energy of the electrons, the molar mass of the species, the number of valence electrons, the band gap and the density of the film. These parameters were retrieved for each species composing the multilayer. The band gap is defined as the minimum energy that is required to excite an electron up to a state in the conduction band where it can participate in conduction. No references were found for Chi, Hep and LL-37 but a value of 7.5 eV was used after comparison with similar systems integrating organic insulating molecules. Regarding the density of the film, literature reports values between 1 and 1.5 g cm^{-3} with an average value at 1.33 g cm^{-3} for LL-37. The density of Chi and Hep in multilayers was assessed by Lundin et *al*. and found to be about 1.2 g cm^{-3}.[36] Consequently, λ values were computed for each species at 1, 1.33 and 1.5 g cm^{-3} and were found to be relatively close. The value at 1.33 g cm^{-3} was retained. Once these parameters were established, the electron mean free path was calculated for each species based on the equations developed by Tanuma *et al*.[37] The average of the obtained λ values was then taken to compute the probed thickness. For a θ angle of 55°, Table IV-2. 1 shows the final depth of the probed layer in function of the binding energy of different elements. This depth varies between 5.1 nm for O, the element with the lower kinetic energy, and 7.2 nm for S, the one with the higher kinetic energy.

Table IV-2. 1 – Inelastic mean free path of the electrons and probed thickness in function of the binding energy for a θ angle of 55°.

Element	O 1s	N 1s	C 1s	S 2p
Kinetic Energy (eV)	856	1087	1202	1319
λ (nm)	2.97	3.57	3.87	4.16
3λcosθ (nm)	**5.1**	**6.1**	**6.7**	**7.2**

2.3.2 Surface chemical composition of multilayers revealed by XPS

The sequential adsorption of bare LL-37 with Hep or of $PPCs_{LL\text{-}37\text{-}Hep}$ with Chi enables multilayer construction.[29] However, free Hep molecules from the $PPCs_{LL\text{-}37\text{-}Hep}$ suspension or released from $PPCs_{LL\text{-}37\text{-}Hep}$ upon assembly could participate to the [Chi-Hep] LbL assembly, which could result in the failure to immobilize LL-37. Therefore, identifying the compounds present in the multilayers is needed, and in particular assessing the presence of LL-37 is required. Bare gold surface and gold surfaces coated with a $[Chi\text{-}Hep]_2$ anchoring layer were first analyzed by XPS as control samples. The following LbL assemblies were then built at pH 3.5 and 5: $[LL\text{-}37\text{-}Hep]_{10}$, $[LL\text{-}37\text{-}Hep]_{10.5}$, $[Chi\text{-}PPCs_{LL\text{-}37\text{-}Hep}]_{10}$, and $[Chi\text{-}PPCs_{LL\text{-}37\text{-}Hep}]_{10.5}$. The influence of the last adsorbed layer (LL-37 or Hep and Chi or $PPCs_{LL\text{-}37\text{-}Hep}$) on the XPS signal is thus also investigated. Five elements were identified by analyzing the general spectrum. Au is the constituent element of the substrate used for assembly. C, O and N are the main elements of biomolecules and are found as expected for Chi, Hep and LL-37. The S signal originates from Hep molecules, which feature sulfonate groups in their structure. The theoretical compositions of Chi, Hep and LL-37 are depicted in Figure IV-2. S1-S3 and Table IV-2. S1-S3, and the surface composition measured by XPS for the different multilayers is shown in Table IV-2. 2. As determined in Table IV-2. 1, the thickness of the probed layer was found to be between 5 and 7 nm. Due to their number of layers and the thickness of $[LL\text{-}37\text{-}Hep]_{10}$, $[LL\text{-}37\text{-}Hep]_{10.5}$, $[Chi\text{-}PPCs_{LL\text{-}37\text{-}Hep}]_{10}$, and $[Chi\text{-}PPCs_{LL\text{-}37\text{-}Hep}]_{10.5}$ multilayers, which is close or greater than 7 nm since the Au signal is close to or below the detection limit (Table IV-2. 2), it has been assumed that the anchoring layer is not detected, and thus the signal coming from the Chi and Hep present in the anchoring layer is neglected.

Table IV-2. 2 – Surface chemical composition (in %, excluding H) obtained by XPS on gold surfaces coated with a $[Chi\text{-}Hep]_2$ anchoring layer followed by $[LL\text{-}37\text{-}Hep]_{10}$, $[LL\text{-}37\text{-}Hep]_{10.5}$, $[Chi\text{-}PPCs_{LL\text{-}37\text{-}Hep}]_{10}$, or $[Chi\text{-}PPCs_{LL\text{-}37\text{-}Hep}]_{10.5}$ at pH 3.5 and 5. bdl: below detection limit.

	O 1s	N 1s			C 1s					S 2p	Au 4f
	O-Me **O**-C **O**=C	**N**H$^+$-(C,H)	**N**-(C,H) C-**N**-SO_3 **N**-C=O	N_{tot}	O=**C**-O	**C**=O O-**C**-O N-**C**=O	**C**-(O,N)	**C**-(C,H)	C_{tot}	C-(O,N)-SO_3	
	$O^{532.4}$	$N^{401.7}$	$N^{399.8}$		$C^{289.0}$	$C^{287.9}$	$C^{286.3}$	$C^{284.8}$		$S^{168.3}$	$Au^{83.5}$
Au Wafer	10.5	bdl	bdl	bdl	1.4	1.7	4.8	25.0	32.9	bdl	56.6
$[Chi\text{-}Hep]_2$ pH 3.5	33.1	2.0	1.6	3.6	1.9	6.3	19.0	9.0	36.2	1.2	25.8
$[Chi\text{-}Hep]_2$ pH 5	36.8	2.0	2.8	4.8	1.9	7.7	23.4	9.2	42.2	1.1	15.1
$[Chi\text{-}Hep]_2$-$[LL37\text{-}Hep]_{10}$ pH 3.5	30.4	1.4	12.1	13.5	2.5	9.9	18.7	22.2	53.3	1.9	0.9
$[Chi\text{-}Hep]_2$-$[LL37\text{-}Hep]_{10}$ pH 5	23.8	0.9	15.7	16.6	1.1	11.8	17.7	28.1	58.6	1.0	0.1
$[Chi\text{-}Hep]_2$-$[LL37\text{-}Hep]_{10.5}$ pH 3.5	27.5	1.4	13.3	14.7	1.9	10.5	18.0	25.8	56.3	1.5	bdl
$[Chi\text{-}Hep]_2$-$[LL37\text{-}Hep]_{10.5}$ pH 5	23.4	0.9	15.6	16.5	0.7	11.7	17.3	29.5	59.2	0.9	bdl
$[Chi\text{-}Hep]_2$-$[Chi\text{-}PPCs_{LL\text{-}37\text{-}Hep}]_{10}$ pH 3.5	35.3	2.0	8.1	10.1	2.0	9.3	23.5	17.5	52.3	2.1	0.1
$[Chi\text{-}Hep]_2$-$[Chi\text{-}PPCs_{LL\text{-}37\text{-}Hep}]_{10}$ pH 5	38.3	2.2	5.3	7.4	1.5	9.0	29.3	11.8	51.5	1.9	0.9
$[Chi\text{-}Hep]_2$-$[Chi\text{-}PPCs_{LL\text{-}37\text{-}Hep}]_{10.5}$ pH 3.5	39.8	2.3	5.9	8.3	1.6	8.7	25.0	13.2	48.4	2.1	1.4
$[Chi\text{-}Hep]_2$-$[Chi\text{-}PPCs_{LL\text{-}37\text{-}Hep}]_{10.5}$ pH 5	38.5	1.9	5.0	6.9	1.2	8.2	27.7	15.4	52.5	1.4	0.6

Figure IV- 2. 1 depicts the N 1s and C 1s spectra for $[Chi\text{-}Hep]_2$, $[LL\text{-}37\text{-}Hep]_{10.5}$, and $[Chi\text{-}PPCs_{LL\text{-}37\text{-}Hep}]_{10}$ multilayers at pH 3.5 and 5, which correspond to the chemical composition represented in Table IV-2. 2. The peaks were decomposed into peak components. The N 1s peak component at 401.7 eV ($N^{401.7}$) is attributed to protonated amines and the peak component at 399.8 eV ($N^{399.8}$) to non-protonated amines and amide groups. The C 1s peak was decomposed in four components at 289.0 eV ($C^{289.0}$), 287.9 eV ($C^{287.9}$), 286.3 eV ($C^{286.3}$) and 284.8 eV ($C^{284.8}$), corresponding, respectively, to carboxyl groups O=**C**-O, amide groups N-**C**=O, O-**C**-O or **C**=O links, amine or alcohol groups **C**-(N,O) and aliphatic carbon chains **C**-(C,H).

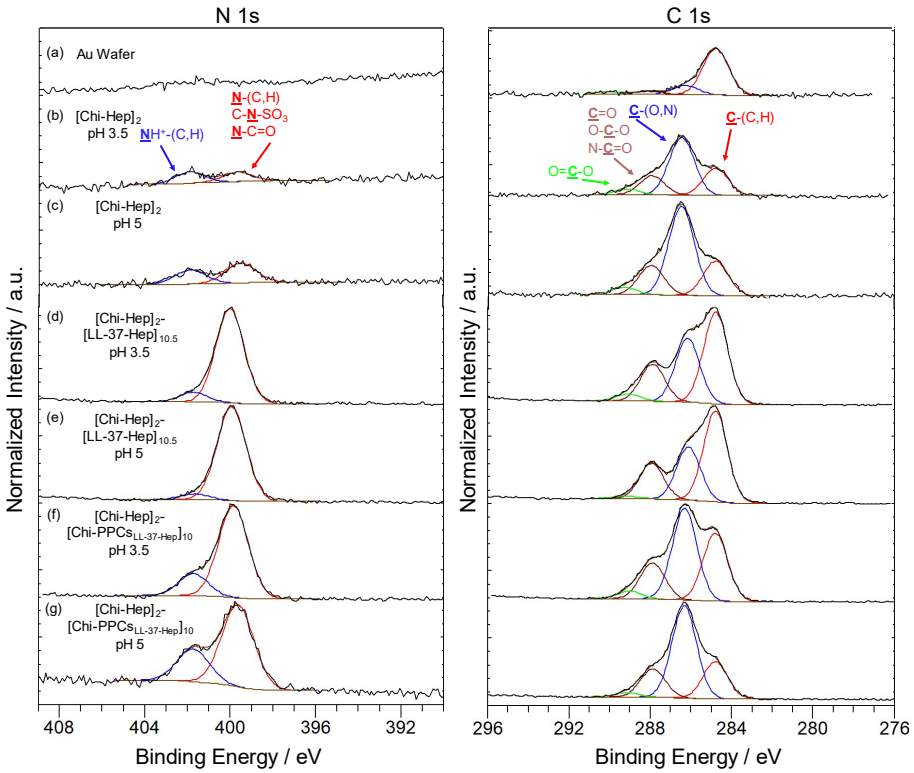

Figure IV-2. 1 – N 1s and C 1s peaks recorded by XPS for (a) gold surfaces coated with (b and c) a $[Chi\text{-}Hep]_2$ anchoring layer, followed by (d and e) $[LL\text{-}37\text{-}Hep]_{10.5}$ and (f and g) $[Chi\text{-}PPCs_{LL\text{-}37\text{-}Hep}]_{10}$, at pH 3.5 and 5. Spectra are presented with their respective decomposition in components.

For the naked Au-coated wafer, Figure IV-2. 1a shows a C 1s peak mainly attributed to aliphatic carbon chains, which can be explained by a contamination of the gold surface, as typically found on metallic surfaces. As expected, nitrogen is not detected on the naked gold surface.

Figure IV-2. 1b and Figure IV-2. 1c show spectra for the $[Chi\text{-}Hep]_2$ anchoring layer, built at pH 3.5 and 5. It appears that N 1s peaks are well detected. It confirms that the anchoring layer is well adsorbed on the surface at both pH. The detection of S 2p (Table IV-2. 2) confirms the presence of Hep. The higher $C^{286.3}$ content in the C 1s peak compared to the Au substrate indicates the presence of Chi and/or Hep, and the protonated nitrogen in the N 1s peak indicates that Chi is present in the anchoring layer. Since the S 2p signal is the same at both pH, the increase in $C^{287.9}$ and $C^{286.3}$ at pH 5 compared to pH 3.5

is attributed to Chi. Consequently, Chi being less charged at pH 5 than at pH 3.5, more Chi is present at the surface of the film at pH 5 to overcompensate the Hep charge, as also illustrated by the slightly higher N 1s signal.

For the $[Chi\text{-}Hep]_2$-$[LL\text{-}37\text{-}Hep]_{10}$ and $[Chi\text{-}Hep]_2$-$[LL\text{-}37\text{-}Hep]_{10.5}$ multilayers, a higher total nitrogen content compared to $[Chi\text{-}Hep]_2$ is observed at both pH (Table IV-2. 2). Figure IV-2. 1d and Figure IV-2. 1e highlight a shift in the contribution of N 1s peak, compared to the $[Chi\text{-}Hep]_2$ anchoring layer. The $N^{399.8}$ peak becomes much more important than the protonated nitrogen peak and represents more than 90% of the total N 1s signal (Table IV-2. 2). This rise suggests that the contribution of Chi is significantly reduced and is thus attributed to the presence of Hep, since sulfur is detected, and LL-37 in the multilayers. This is confirmed by the C 1s spectra analysis. Indeed, the $C^{286.3}$ was dominant in the $[Chi\text{-}Hep]_2$ anchoring layer, whereas in the $[Chi\text{-}Hep]_2$-$[LL\text{-}37\text{-}Hep]_{10 \text{ and } 10.5}$ multilayers, $C^{284.8}$ becomes the main C 1s contribution (more than 40% of the total C 1s signal), and a clear increase of the $C^{287.9}$ contribution is also observed. The high content in aliphatic carbons in the amino acid pending groups ($C^{284.8}$) and in amide carbons in the peptide bonds ($C^{287.9}$) are typical of protein adsorption, and thus, in our case, of the presence of LL-37 in the multilayers.[38–40] Interestingly, the XPS signal does not indicate an influence from the last adsorbed layer, as the compositions of the $[Chi\text{-}Hep]_2$-$[LL\text{-}37\text{-}Hep]_{10}$ and $[Chi\text{-}Hep]_2$-$[LL\text{-}37\text{-}Hep]_{10.5}$ multilayers are very similar at both pH values (Table IV-2. 2).

Finally, for the $[Chi\text{-}Hep]_2$-$[Chi\text{-}PPCs_{LL\text{-}37\text{-}Hep}]_{10}$ and $[Chi\text{-}Hep]_2$-$[Chi\text{-}PPCs_{LL\text{-}37\text{-}Hep}]_{10.5}$ multilayers, the S 2p signal also confirms that Hep is present in the multilayers (Table IV-2. 2). Figure IV-2. 1f, Figure IV-2. 1g and Table IV-2. 2 show that the $N^{399.8}$ contribution decreases to around 70-80% of the total N 1s signal, whereas it was more than 90% in the $[Chi\text{-}Hep]_2$-$[LL\text{-}37\text{-}Hep]_{10 \text{ and } 10.5}$ multilayers. Therefore, the $N^{399.8}$ contribution values are between those calculated for the $[Chi\text{-}Hep]_2$ anchoring layer and the $[Chi\text{-}Hep]_2$-$[LL\text{-}37\text{-}Hep]_{10 \text{ and } 10.5}$ multilayers. This N 1s peak pattern could be explained by the presence of both Chi and LL-37 in the multilayers. The C 1s spectra confirm this assumption. The $C^{284.8}$ peak, which is attributed to the LL-37 in the films, accounts for 23 to 33% of the total C 1s signal, depending on the nature of the final adsorbed layer and the pH (Table IV-2. 2). Again, the latter appears to exert minimal influence on the measured signal. Globally, the results suggest that less LL-37 is present in the $[Chi\text{-}Hep]_2$-$[Chi\text{-}PPCs_{LL\text{-}37\text{-}Hep}]_n$

multilayers at pH 5 than at pH 3.5. However, since the functional groups in the N 1s and C 1s spectra are present in Hep, Chi and LL-37, the raw results (Table IV-2. 2) do not allow to directly establish the proportions of each of these species in the multilayers.

2.3.3 Modeling the data to determine the composition of multilayer assemblies

$[Chi\text{-}Hep]_2$ anchoring layer

To assess the respective Chi, Hep and LL-37 contribution in the multilayered films, modeling of the composition was carried out based on the atomic composition of each species (Figure IV-2. S1-S3 and Table IV-2. S1-S3). Hep, Chi and LL-37 all contribute to the N 1s signal. The Hep contribution to the N 1s peaks was determined thanks to the sulfur marker. The following set of equations was used to compute the theoretical compositions in the $[Chi\text{-}Hep]_2$ anchoring layer:

$$N_{Hep} = N_{Hep}^{399.8} = S/3 \quad \text{(Equation IV-2. 1)}$$

$$N_{Chi} = N_{tot} - N_{Hep} \quad \text{(Equation IV-2. 2)}$$

$$N_{Chi}^{401.7} = \alpha * N_{Chi} \quad \text{(Equation IV-2. 3)}$$

$$N_{Chi}^{399.8} = (1-\alpha) * N_{Chi} \quad \text{(Equation IV-2. 4)}$$

Theoretically, since the pK_a of Chi is 6.5, it was assumed that all the amine groups of Chi are charged at pH 3.5 and 5, *i.e.*, α is equal to 0.95. Therefore, $N_{Chi}^{401.7}$ and $N_{Chi}^{399.8}$ represents, respectively, 95% and 5% of the total N_{Chi} signal. The contribution of Hep and Chi in the $[Chi\text{-}Hep]_2$ multilayers at pH 3.5 and 5 were modeled and compared to the total measured signal obtained by XPS measurements (Table IV-2. S4). After modeling, it is obvious that the $N^{401.7}$ contribution is overestimated while $N^{399.8}$ is underestimated. This is attributed to a value of α for Chi molecules that is not in agreement with its effective value, even though it was chosen according to the molecular structure and pH used for multilayers construction. The drying step of the multilayers, the analysis under ultra-high vacuum conditions, the exposure to X-rays, and the charge effect of the neighboring species may influence the charge distribution in the molecules.[22,41,42] It is well known that PEs and amino acids show a pH-dependent protonation of the functional groups and

will thereby be in different charge states depending on the environment.[43] Therefore, variations in conditions between sample preparation and analysis, due to the drying step and the analysis under ultra-high vacuum, could affect the charge state of the molecules.[22] Moreover, Zubavichus *et al.* demonstrated that exposure to X-rays could lead to some radiation-induced modifications, such as the deprotonation of originally protonated amino groups of zwitterionic amino acids.[44] Therefore, the α of the different species in the multilayers can be different from the theoretical one. Furthermore, the heterogeneity of the probed layer and the sensitivity factor of each element could also explain the differences between the modeled and the measured composition. Therefore, Equation IV-2. 3-4, with a theoretical α of 95%, should not be applied for further modeling (Table IV-2. S4). An empirical α was determined instead, based on the following procedure: for $[Chi\text{-}Hep]_2$ at pH 3.5, N_{tot} = 3.6% with $N^{401.7}$ = 2.0% and $N^{399.8}$ = 1.6%. Knowing that S = 1.2%, $N_{Hep}^{399.8}$ is modeled at 0.4% (Equation IV-2. 1) and thus, N_{Chi} is modeled at 3.2% (Equation IV-2. 2). Since $N_{Hep}^{401.7}$ = 0% and $N_{Hep}^{399.8}$ = 0.4%, to respect the measured values, $N_{Chi}^{401.7}$ = 2.0% and $N_{Chi}^{399.8}$ = 1.2%. In this way, an α value of 62.5% is found, instead of 95%, for Chi in the multilayer at pH 3.5 (Table IV-2. 3). The same procedure was used to calculate α for Chi in the multilayer at pH 5, and a value of 45.5% was determined (Table IV-2. 3).

Table IV-2. 3 – Modeling the percentage of each atom and functional group for Hep and Chi molecules in $[Chi\text{-}Hep]_2$ multilayers at pH 3.5 and 5, and determination of α for Chi.

		O 1s	N 1s			C 1s					S 2p	Au 4f
		$O^{532.4}$	$N^{401.7}$	$N^{399.8}$	N_{tot}	$C^{289.0}$	$C^{287.9}$	$C^{286.3}$	$C^{284.8}$	C_{tot}	$S^{168.3}$	$Au^{83.5}$
Au Wafer	Total measured composition	10.5	bdl	bdl	**bdl**	1.4	1.7	4.8	25.0	**32.9**	bdl	56.6
$[Chi\text{-}Hep]_2$ pH 3.5	Modeled Hep composition	7.8	0.0	0.4	**0.4**	0.4	0.8	3.7	0.0	**4.9**	1.2	/
	Modeled Chi composition	13.0	2.0	1.2	**3.2**	0.0	3.4	16.0	0.2	**19.6**	0.0	/
	Total modeled composition	20.8	2.0	1.6	**3.6**	0.4	4.2	19.7	0.2	**24.5**	1.2	/
62.5% Protonated 37.5% Non-protonated	Total measured composition	33.1	2.0	1.6	**3.6**	1.9	6.3	19.0	9.0	**36.2**	1.2	25.8
$[Chi\text{-}Hep]_2$ pH 5	Modeled Hep composition	6.8	0.0	0.4	**0.4**	0.4	0.7	3.2	0.0	**4.3**	1.1	/
	Modeled Chi composition	17.9	2.0	2.4	**4.4**	0.0	4.6	22.1	0.2	**26.9**	0.0	/
	Total modeled composition	24.7	2.0	2.8	**4.8**	0.4	5.3	25.3	0.2	**31.2**	1.1	/
45.5% Protonated 54.5% Non-protonated	Total measured composition	36.8	2.0	2.8	**4.8**	1.9	7.7	23.4	9.2	**42.2**	1.1	15.1

The theoretical O 1s and C 1s compositions for Hep and Chi were also modeled in Table IV-2. 3 from the N 1s and S 2p compositions, according to the following equations, in line with Hep and Chi stoichiometry:

$$O_{Hep} = 19 * N_{Hep} \quad \text{(Equation IV-2. 5)}$$
$$O_{Chi} = 4.05 * N_{Chi} \quad \text{(Equation IV-2. 6)}$$
$$C_{Hep} = 4 * S \quad \text{(Equation IV-2. 7)}$$
$$C_{Chi} = 6.1 * N_{Chi} \quad \text{(Equation IV-2. 8)}$$
$$C_{Hep}^{284.8} = 0 * C_{Hep} \quad \text{(Equation IV-2. 9)}$$
$$C_{Hep}^{286.3} = (3/4) * C_{Hep} \quad \text{(Equation IV-2. 10)}$$
$$C_{Hep}^{287.9} = (1/6) * C_{Hep} \quad \text{(Equation IV-2. 11)}$$
$$C_{Hep}^{289.0} = (1/12) * C_{Hep} \quad \text{(Equation IV-2. 12)}$$
$$C_{Chi}^{284.8} = (0.05/6.1) * C_{Chi} \quad \text{(Equation IV-2. 13)}$$
$$C_{Chi}^{286.3} = (5/6.1) * C_{Chi} \quad \text{(Equation IV-2. 14)}$$
$$C_{Chi}^{287.9} = (1.05/6.1) * C_{Chi} \quad \text{(Equation IV-2. 15)}$$
$$C_{Chi}^{289.0} = 0 * C_{Chi} \quad \text{(Equation IV-2. 16)}$$

For $[Chi\text{-}Hep]_2$, at both pH, there is a good fit between the modeled and the measured signal for $C^{286.3}$. For the other C 1s components and for the O 1s signal, the modeled composition is underestimated compared to the measured signal. Since the thickness of the multilayers is rather thin (< 5nm, as an Au signal is measured), the difference could be explained by a contamination of the surface as observed on the Au substrate (Table IV-2. 2), especially for $C^{284.8}$. For O 1s, the difference could be explained by an inaccurate sensitivity coefficient, which could overestimate the concentration.

$[Chi\text{-}Hep]_2$-$[LL\text{-}37\text{-}Hep]_{10}$ and $[Chi\text{-}Hep]_2$-$[LL\text{-}37\text{-}Hep]_{10.5}$ multilayers

The same approach was used to determine the signal of LL-37 and Hep in the $[Chi\text{-}Hep]_2$-$[LL\text{-}37\text{-}Hep]_{10 \text{ and } 10.5}$ multilayers. Theoretically, at pH 3.5 and 5, α of nitrogen groups for LL-37 is 0.2 at pH 3.5 and 5 (Table IV-2. S3). This identical α value at both pH is attributable to the nitrogen groups having pKa values substantially higher than 5, ensuring that their protonation states remain largely unchanged within this acidic pH range. Therefore, $N_{LL\text{-}37}^{401.7}$ and $N_{LL\text{-}37}^{399.8}$ represents, respectively, 20% and 80% of the total $N_{LL\text{-}37}$ signal. Due to the thickness of the films, it was assumed that Chi from the anchoring

layer is not detected and thus that only LL-37 and Hep contribute to the signal. Therefore, the following equations should be applied, in agreement with the stoichiometry of LL-37 and Hep:

$$N_{LL\text{-}37} = N_{tot} - N_{Hep} \quad \text{(Equation IV-2. 17)}$$

$$N_{LL\text{-}37}^{401.7} = \alpha * N_{LL\text{-}37} \quad \text{(Equation IV-2. 18)}$$

$$N_{LL\text{-}37}^{399.8} = (1-\alpha) * N_{LL\text{-}37} \quad \text{(Equation IV-2. 19)}$$

However, due to a lack of fit for the N 1s components (Table IV-2. S5), an empirical α was calculated at both pH, following the same approach as in Table IV-2. 3. Analyzing the modeled data for the $[Chi\text{-}Hep]_2\text{-}[LL\text{-}37\text{-}Hep]_{10}$ and $[Chi\text{-}Hep]_2\text{-}[LL\text{-}37\text{-}Hep]_{10.5}$ multilayers shows that the α values for LL-37 are similar, with 10% at pH 3.5 and 5.5% at pH 5 (Table IV-2. 4). These results also suggest that the last adsorbed layer does not strongly affect the value of α. Equations IV-2. 7-16 were used to model the C 1s components, and Table IV-2. 4 highlights the excellent fit between the modeled and the measured signals. The surface composition for $[Chi\text{-}Hep]_2\text{-}[LL\text{-}37\text{-}Hep]_{10 \text{ and } 10.5}$ multilayers will thus be extracted from this modeling approach (see hereunder).

Table IV-2. 4 – Modeling the percentage of each atom and functional group for Hep and LL-37 molecules in $[Chi\text{-}Hep]_2\text{-}[LL\text{-}37\text{-}Hep]_{10 \text{ and } 10.5}$ multilayers at pH 3.5 and 5, and determination of α for LL-37.

		O 1s	N 1s			C 1s					S 2p	Au 4f
		$O^{532.4}$	$N^{401.7}$	$N^{399.8}$	N_{tot}	$C^{289.0}$	$C^{287.9}$	$C^{286.3}$	$C^{284.8}$	C_{tot}	$S^{168.3}$	$Au^{83.5}$
$[Chi\text{-}Hep]_2\text{-}[LL\text{-}37\text{-}Hep]_{10}$ pH 3.5	Modeled Hep composition	11.9	0.0	0.6	**0.6**	0.6	1.3	5.6	0.0	**7.5**	1.9	/
	Modeled LL-37 composition	11.3	1.4	11.5	**12.8**	1.3	9.2	11.1	22.3	**43.9**	0.0	/
	Total modeled composition	23.2	1.4	12.1	**13.5**	1.9	10.5	16.7	22.3	**51.4**	1.9	/
10.9% Protonated 89.1% Non-protonated	Total measured composition	30.4	1.4	12.1	**13.5**	2.5	9.9	18.7	22.2	**53.3**	1.9	0.9
$[Chi\text{-}Hep]_2\text{-}[LL\text{-}37\text{-}Hep]_{10}$ pH 5	Modeled Hep composition	6.5	0.0	0.3	**0.3**	0.3	0.7	3.1	0.0	**4.1**	1.0	/
	Modeled LL-37 composition	14.3	0.9	15.4	**16.3**	1.6	11.6	14.1	28.1	**55.4**	0.0	/
	Total modeled composition	20.8	0.9	15.7	**16.6**	1.9	12.3	17.2	28.1	**59.5**	1.0	/
5.5% Protonated 94.5% Non-protonated	Total measured composition	23.8	0.9	15.7	**16.6**	1.1	11.8	17.7	28.1	**58.6**	1.0	0.1
$[Chi\text{-}Hep]_2\text{-}[LL\text{-}37\text{-}Hep]_{10.5}$ pH 3.5	Modeled Hep composition	9.2	0.0	0.5	**0.5**	0.5	1.0	4.4	0.0	**5.9**	1.5	/
	Modeled LL-37 composition	12.5	1.4	12.8	**14.2**	1.4	10.2	12.3	24.6	**48.5**	0.0	/
	Total modeled composition	21.7	1.4	13.3	**14.6**	1.9	11.2	16.7	24.6	**54.4**	1.5	/
9.9% Protonated 90.1% Non-protonated	Total measured composition	27.5	1.4	13.3	**14.7**	1.9	10.5	18.0	25.8	**56.3**	1.5	bdl
$[Chi\text{-}Hep]_2\text{-}[LL\text{-}37\text{-}Hep]_{10.5}$ pH 5	Modeled Hep composition	5.7	0.0	0.3	**0.3**	0.3	0.6	2.7	0.0	**3.6**	0.9	/
	Modeled LL-37 composition	14.3	0.9	15.3	**16.2**	1.6	11.6	14.1	28.1	**55.4**	0.0	/
	Total modeled composition	20.0	0.9	15.6	**16.5**	1.9	12.2	16.8	28.1	**59.0**	0.9	/
5.6% Protonated 94.4% Non-protonated	Total measured composition	23.4	0.9	15.6	**16.5**	0.7	11.7	17.3	29.5	**59.2**	0.9	bdl

$[Chi\text{-}Hep]_2$-$[Chi\text{-}PPCs_{LL\text{-}37\text{-}Hep}]_{10}$ and $[Chi\text{-}Hep]_2$-$[Chi\text{-}PPCs_{LL\text{-}37\text{-}Hep}]_{10.5}$ multilayers

Finally, for $[Chi\text{-}Hep]_2$-$[Chi\text{-}PPCs_{LL\text{-}37\text{-}Hep}]_{10 \text{ and } 10.5}$ multilayers at pH 3.5 and 5, in a preliminary approach, a model considering the presence of two of the three compounds used to build the multilayers was applied (Table IV-2. S6), based on the empirical α values for Chi and LL-37, obtained from $[Chi\text{-}Hep]_2$ (Table IV-2. 3) and $[Chi\text{-}Hep]_2$-$[LL\text{-}37\text{-}Hep]_{10 \text{ and } 10.5}$ (Table IV-2. 4) multilayers. Independently of the pH value, an α value of 55% and 10% was considered for Chi and LL-37, respectively. Due to the significant discrepancy between the modeled and the measured composition (Table IV-2. S6), it can be concluded that a model considering only Chi and Hep, only LL-37 and Hep or only Chi and LL-37 in the multilayers is not sufficient to explain the XPS data. This already indicates that the three compounds are incorporated in the multilayers upon build-up. Therefore, a model considering the presence of the three compounds in the multilayers should be applied. Although S 2p can again be used as a marker for Hep, there is no marker atom or chemical group that would enable the differentiation between Chi and LL-37. Consequently, a model was constructed by assembling the contribution of each species to both $N^{399.8}$ and $N^{401.7}$ peak components and considering the empirical α values identified above (55% for Chi and 10% for LL-37). A system of two equations can be written as follows:

$$N^{401.7} = 0.1 * N_{LL\text{-}37} + 0.55 * N_{Chi} \quad \text{(Equation IV-2. 20)}$$

$$N^{399.8} = N_{Hep} + 0.9 * N_{LL\text{-}37} + 0.45 * N_{Chi} \quad \text{(Equation IV-2. 21)}$$

Using Equations IV-2. 5-16 and 20-21, the O, N and C peak component contributions were calculated and are shown in Table IV-2. 5. The model aligns well with the measured data, apart from the discrepancies in the values for O and $C^{284.8}$. These lower values may be attributed to an underestimation of LL-37 in the multilayers or to a contamination of the outermost surface layer.

Table IV-2. 5 – Modeling the percentage of each atom and functional group for Hep, Chi and LL-37 molecules in $[Chi\text{-}Hep]_2\text{-}[Chi\text{-}PPCs_{LL\text{-}37\text{-}Hep}]_{10 \text{ and } 10.5}$ multilayers at pH 3.5 and 5, considering empirical α for Chi and LL-37.

		O 1s	N 1s			C 1s					S 2p	Au 4f
		$O^{532.4}$	$N^{401.7}$	$N^{399.8}$	N_{tot}	$C^{289.0}$	$C^{287.9}$	$C^{286.3}$	$C^{284.8}$	C_{tot}	$S^{168.3}$	$Au^{83.5}$
$[Chi\text{-}Hep]_2\text{-}[Chi\text{-}PPCs_{LL\text{-}37\text{-}Hep}]_{10}$ pH 3.5	Modeled Hep composition	13.5	0.0	0.7	**0.7**	0.7	1.4	6.4	0.0	**8.5**	2.1	/
	Modeled Chi composition	9.4	1.3	1.0	**2.3**	0.0	2.4	11.6	0.1	**14.1**	0.0	/
	Modeled LL-37 composition	6.3	0.7	6.4	**7.1**	0.7	5.1	6.1	12.3	**24.2**	0.0	/
	Total modeled composition	29.2	2.0	8.1	**10.1**	1.4	8.9	24.1	12.4	**46.8**	2.1	/
	Total measured composition	35.3	2.0	8.1	**10.1**	2.0	9.3	23.5	17.5	**52.3**	2.1	0.1
$[Chi\text{-}Hep]_2\text{-}[Chi\text{-}PPCs_{LL\text{-}37\text{-}Hep}]_{10}$ pH 5	Modeled Hep composition	12.1	0.0	0.6	**0.6**	0.6	1.3	5.7	0.0	**7.6**	1.9	/
	Modeled Chi composition	13.5	1.8	1.5	**3.3**	0.0	3.5	16.7	0.2	**20.3**	0.0	/
	Modeled LL-37 composition	3.1	0.3	3.1	**3.5**	0.3	2.5	3.0	6.0	**11.8**	0.0	/
	Total modeled composition	28.7	2.2	5.3	**7.4**	0.9	7.3	25.4	6.2	**39.8**	1.9	/
	Total measured composition	38.3	2.2	5.3	**7.4**	1.5	9.0	29.3	11.8	**51.5**	1.9	0.9
$[Chi\text{-}Hep]_2\text{-}[Chi\text{-}PPCs_{LL\text{-}37\text{-}Hep}]_{10.5}$ pH 3.5	Modeled Hep composition	13.1	0.0	0.7	**0.7**	0.7	1.4	6.2	0.0	**8.3**	2.1	/
	Modeled Chi composition	14.2	1.9	1.6	**3.5**	0.0	3.7	17.6	0.2	**21.4**	0.0	/
	Modeled LL-37 composition	3.6	0.4	3.7	**4.1**	0.4	2.9	3.5	7.0	**13.9**	0.0	/
	Total modeled composition	31.0	2.3	5.9	**8.3**	1.1	8.0	27.3	7.2	**43.6**	2.1	/
	Total measured composition	39.8	2.3	5.9	**8.3**	1.6	8.7	25.0	13.2	**48.4**	2.1	1.4
$[Chi\text{-}Hep]_2\text{-}[Chi\text{-}PPCs_{LL\text{-}37\text{-}Hep}]_{10.5}$ pH 5	Modeled Hep composition	9.0	0.0	0.5	**0.5**	0.5	1.0	4.3	0.0	**5.7**	1.4	/
	Modeled Chi composition	11.0	1.5	1.2	**2.7**	0.0	2.9	13.6	0.1	**16.6**	0.0	/
	Modeled LL-37 composition	3.3	0.4	3.3	**3.7**	0.4	2.7	3.2	6.4	**12.7**	0.0	/
	Total modeled composition	23.3	1.9	5.0	**6.9**	0.9	6.6	21.1	6.5	**35.0**	1.4	/
	Total measured composition	38.5	1.9	5.0	**6.9**	1.2	8.2	27.7	15.4	**52.5**	1.4	0.6

Modeling multilayer composition

All the values obtained after modeling according to the stoichiometry of Chi, Hep and LL-37 must be considered with caution since the outermost layer contributes more to the XPS signal than underlying layers, which induces an overrepresentation of the extreme surface layer in the data and thus a distorted composition compared to the one of the entire film. Data treatment and modeling were performed considering that the analyzed volume is homogeneous, which may not be the case given the sequential deposition method. Yet, considering the good agreement between the modeled and measured values presented above, the proportions of the repeating unit of Hep, Chi and LL-37 in the multilayered films were calculated, and results are depicted in Table IV-2. 6.

Table IV-2. 6 – Proportion of the repeating unit of Hep, Chi and LL-37, calculated using the modeled N 1s contribution or the $C^{287.9}$ component in the multilayered films.

	N 1s			$C^{287.9}$		
	Hep	Chi	LL-37	Hep	Chi	LL-37
$[Chi\text{-}Hep]_2$ pH 3.5	1	7.80	-	1	8.10	-
$[Chi\text{-}Hep]_2$ pH 5	1	12.40	-	1	12.52	-
$[Chi\text{-}Hep]_2\text{-}[LL37\text{-}Hep]_{10}$ pH 3.5	1	-	0.36	1	-	0.33
$[Chi\text{-}Hep]_2\text{-}[LL37\text{-}Hep]_{10}$ pH 5	1	-	0.91	1	-	0.77
$[Chi\text{-}Hep]_2\text{-}[LL37\text{-}Hep]_{10.5}$ pH 3.5	1	-	0.47	1	-	0.47
$[Chi\text{-}Hep]_2\text{-}[LL37\text{-}Hep]_{10.5}$ pH 5	1	-	0.90	1	-	0.90
$[Chi\text{-}Hep]_2\text{-}[Chi\text{-}PPCs_{LL\text{-}37\text{-}Hep}]_{10}$ pH 3.5	1	3.29	0.17	1	3.27	0.17
$[Chi\text{-}Hep]_2\text{-}[Chi\text{-}PPCs_{LL\text{-}37\text{-}Hep}]_{10}$ pH 5	1	5.50	0.10	1	5.13	0.09
$[Chi\text{-}Hep]_2\text{-}[Chi\text{-}PPCs_{LL\text{-}37\text{-}Hep}]_{10.5}$ pH 3.5	1	5.00	0.10	1	5.03	0.10
$[Chi\text{-}Hep]_2\text{-}[Chi\text{-}PPCs_{LL\text{-}37\text{-}Hep}]_{10.5}$ pH 5	1	5.40	0.12	1	5.52	0.13

To achieve this, the total N 1s fraction or the $C^{287.9}$ component assigned to each compound (Hep, Chi and LL-37 in Table IV-2. 3-5) were used. For the N 1s fraction, the values were divided by the number of N atoms per repeating unit, *i.e.*, 1 for Hep, 1 for Chi, and 60 for LL-37, (Figure IV-2. S1-S2 and Table IV-2. S1) to relate the signal to one repeating unit. The same approach was applied for the $C^{287.9}$ component and the values were divided by 2 for Hep, 1.05 for Chi, and 43 for LL-37. First, the $[Chi\text{-}Hep]_2$ anchoring layer exhibits a higher proportion of Chi, in comparison to Hep, at pH 5 than at pH 3.5. This observation had already been made through the analysis of the raw data (Table IV-2. 2 and Figure IV-2. 1). Given that Chi is less charged at pH 5 than at pH 3.5, the higher proportion of Chi in the film at pH 5 allows to overcompensate the Hep charge. Similarly, for $[Chi\text{-}Hep]_2\text{-}[LL\text{-}37\text{-}Hep]_{10\text{ and }10.5}$ multilayers, since LL-37 is less positively charged at pH 5 than at pH 3.5, the proportion of LL-37 at the surface is higher in order to overcompensate the Hep charge. Indeed, although the α of the nitrogen groups in LL-37 is identical

at both pH, the higher overall positive charge observed at pH 3.5 is due to the protonation of carboxyl groups, which are less negatively charged at pH 3.5 than at pH 5. By modeling the composition, it seems that there is a weak effect of the last adsorbed layer. Indeed, the modeled proportions of Hep and LL-37 in $[Chi\text{-}Hep]_2\text{-}[LL\text{-}37\text{-}Hep]_{10 \text{ and } 10.5}$ are quite similar. Finally, for $[Chi\text{-}Hep]_2\text{-}[Chi\text{-}PPCs_{LL\text{-}37\text{-}Hep}]_{10 \text{ and } 10.5}$, $PPCs_{LL\text{-}37\text{-}Hep}$ were immobilized after being formed at a theoretical (-)/(+net) charge ratio of 1.5. After integration into the multilayers, a (-)/(+net) charge ratio of 2.3 and 3.9 is calculated at pH 3.5 for $[Chi\text{-}Hep]_2\text{-}[Chi\text{-}PPCs_{LL\text{-}37\text{-}Hep}]_{10}$ and $[Chi\text{-}Hep]_2\text{-}[Chi\text{-}PPCs_{LL\text{-}37\text{-}Hep}]_{10.5}$, respectively. These ratios were calculated based on the proportions of the N 1s fraction of the repeating unit of Hep and LL-37 in the multilayer (Table IV-2. 6) and considering 4 negative charges for Hep and 10.4 positive charges for LL-37. It suggests that the multilayer undergoes molecular rearrangement after Chi addition. This is even more striking at pH 5 (4 negative charges for Hep and 7 positive charges for LL-37), with a (-)/(+net) charge ratio of 6.3 and 4.4 for $[Chi\text{-}Hep]_2\text{-}[Chi\text{-}PPCs_{LL\text{-}37\text{-}Hep}]_{10}$ and $[Chi\text{-}Hep]_2\text{-}[Chi\text{-}PPCs_{LL\text{-}37\text{-}Hep}]_{10.5}$, respectively. It shows that the proportion of LL-37 in the films is lower at pH 5 than at pH 3.5.

Interestingly, our analysis shows that there is proportionally less LL-37 in the $PPCs_{LL\text{-}37\text{-}Hep}$-based multilayers than in the bare LL-37-based multilayers. When the positively-charged Chi is adsorbed onto $PPCs_{LL\text{-}37\text{-}Hep}$, it could substitute LL-37 from the latter, which releases some of the LL-37 molecules from the multilayer. vander Straeten *et al*. have already highlighted this phenomenon of reorganization and our results are consistent with that observation. They demonstrated that when poly(allylamine hydrochloride) (PAH) is adsorbed on a layer of lysozyme-poly(styrenesulfonate) complexes ($PPCs_{Lyz\text{-}PSS}$), PAH can complex PSS, resulting in the release of free Lyz from $PPCs_{Lyz\text{-}PSS}$.[21,45]

Even if the results must be considered with caution, due to the exacerbation of the extreme surface signal, the analysis under ultra-high vacuum, the sensitivity factors, the decomposition error, etc., it seems clear that, in the first few nanometers of the films, there is proportionally less LL-37 in the bare LL-37 based-multilayers at pH 3.5 than at pH 5, and in the PPCs-based multilayers than in the bare LL-37-based multilayers. The proportions were calculated based on the total fraction of N 1s or the $C^{287.9}$ contribution of the different multilayers. Figure IV-2. 2 illustrates the Chi and LL-37 proportions,

as outlined in Table IV-2. 6 (with the Hep proportion fixed at 1) and indicates that modeling based on N 1s or $C^{287.9}$ results in comparable proportions. This consistency supports the robustness of the modeling approach. Specifically, the closer the data points align with the reference line, the more consistent the proportions calculated from both contributions.

Hence, for achieving high LL-37 adsorption to design antimicrobial or wound-healing surfaces, the optimal approach appears to be the immobilization of bare LL-37, using Hep as the counter polyanion.

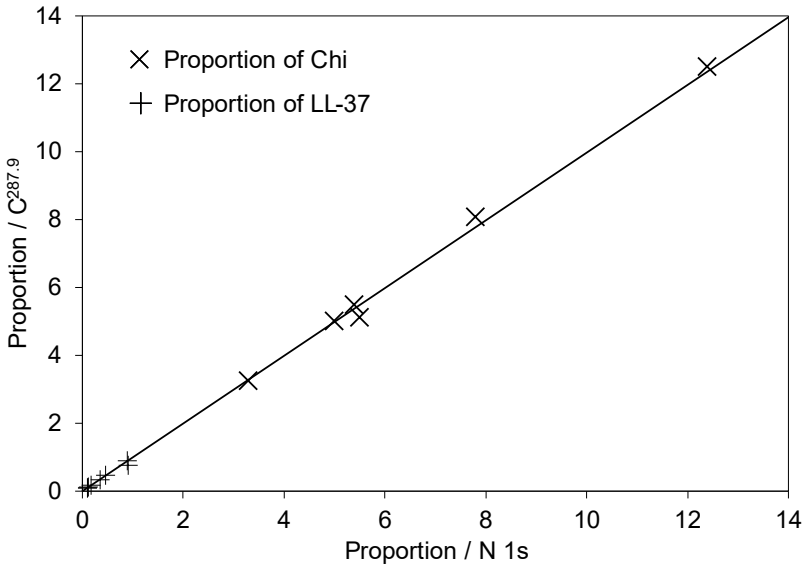

Figure IV-2. 2 – Proportion of Chi and LL-37 repeating units relative to one Hep repeating unit in the different multilayers determined from the modeled total N 1s fraction or the modeled $C^{287.9}$ component.

2.4 Conclusion

In this study, XPS analysis and in-depth data treatment were used to investigate the composition of LL-37-based multilayers formed via the LbL technique at pH 3.5 and 5. Our goal was to determine the proportion of Chi, Hep and LL-37 within the $[Chi\text{-}Hep]_2\text{-}[LL\text{-}37\text{-}Hep]_{10 \text{ and } 10.5}$ and $[Chi\text{-}Hep]_2\text{-}[Chi\text{-}PPCs_{LL\text{-}37\text{-}Hep}]_{10 \text{ and } 10.5}$ multilayers. To assess the contributions of Chi, Hep and LL-37, the composition was modeled based on their stoichiometry. This was possible through the determination of empirical protonation degrees α for

Chi and LL-37, for which values of 55% and 10% were found, respectively, to be compared to the theoretical degrees of 95% for Chi and 20% for LL-37. This difference can be attributed to the measurement conditions inherent to XPS analysis. Interestingly, we found that more Chi is present in the [Chi-Hep]$_2$ anchoring layer at pH 5 than at pH 3.5 to overcompensate the Hep charge. Similarly, in the [Chi-Hep]$_2$-[LL-37-Hep]$_{10 \text{ and } 10.5}$ multilayers, LL-37 exhibited reduced charge at pH 5, leading to a decreased amount of Hep needed to counterbalance LL-37's charge than at pH 3.5. Additionally, we found proportionally less LL-37 in the PPCs$_{LL\text{-}37\text{-}Hep}$-based multilayers compared to the bare LL-37-based multilayers, likely due to molecular rearrangement after Chi addition to the PPCs$_{LL\text{-}37\text{-}Hep}$ layer, and thus a potential release of some LL-37 molecules. In conclusion, our XPS study provides the composition of the extreme surface of multilayers through the exploitation of peak decomposition and compounds stoichiometry, highlighting the interest of this technique and in particular of data treatment and modeling to obtain molecular information.

2.5 Take-home messages

- XPS analysis enables the determination of the composition within the first 5-7 nm of the films.
- XPS analysis influences the degree of protonation of the nitrogen groups in the compounds, as the empirical α are lower than the theoretical ones.
- The PPCs$_{LL\text{-}37\text{-}Hep}$-based multilayers contain a lower proportion of LL-37 compared to the bare LL-37-based multilayers.

In this *Chapter 2*, the Chi, Hep and LL-37 contribution has been assessed by modeling the atomic composition of each species in order to determine their proportion in the multilayered films. Although XPS analysis confirmed the presence of the compounds in the multilayers, the results should be considered with caution due to the measurement conditions inherent to XPS analysis, *i.e.*, multilayer drying, ultra-high vacuum environment, X-ray bombardment, extreme surface signal, decomposition error, etc. Consequently, in the following, the quantification of LL-37 within the entire multilayers will be conducted using a more direct method, specifically the

bicinchoninic acid assay. This will allow us to evaluate the consistency of these measurements with the results obtained from XPS. Furthermore, the evaluation of the hydration level of multilayers assembled via the LbL method is of significant interest and cannot be assessed using XPS. To obtain this information, QCM-D and ellipsometry measurements can be performed.

2.6 Supporting Information

2.6.1 Chitosan

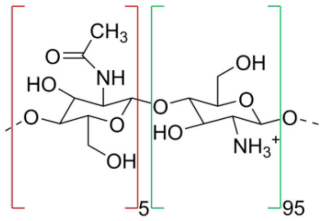

		O	N				C									S	H
	Number		(CN)=O	C-NH	Sum N	O=C-O	N-C=O N-C-N C=N O-C-O	C-O	C-N	C-S	C-H_3	C-H_2	C-H	C-C-C	Sum C		
Acetylated chitosan	0.05	5	0	1	1	0	2	4	1	0	1	0	0	0	8	0	13
Deacetylated chitosan	0.95	4	0	1	1	0	1	4	1	0	0	0	0	0	6	0	11
Total	1	4.05	0	1	1	0	1.05	4	1	0	0.05	0	0	0	6.1	0	11.1

$$C_{6.1}O_{4.05}N_1H_{11.1}$$

Figure IV-2. S1 – Structure and chemical formula of chitosan. The table gives the theoretical composition, and the chemical groups present in a 95% deacetylated chitosan.

2.6.2 Heparin

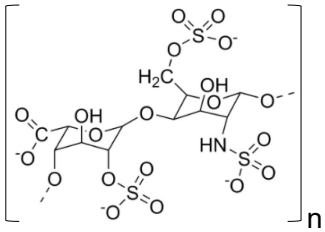

	O	N				C									S	H
		(CN)=O	C-NH	N-SO_3	Sum N	O=C-O	N-C=O N-C-N C=N O-C-O	C-O	C-N	C-S	C-H_3	C-H_2	C-H	C-C-C	Sum C		
Heparin	19	0	0	1	1	1	2	8	1	0	0	0	0	0	12	3	19

$$C_{12}O_{19}N_1S_3H_{19}$$

Figure IV-2. S2 – Structure and chemical formula of heparin. The table gives the theoretical composition, and the chemical groups.

2.6.3 LL-37

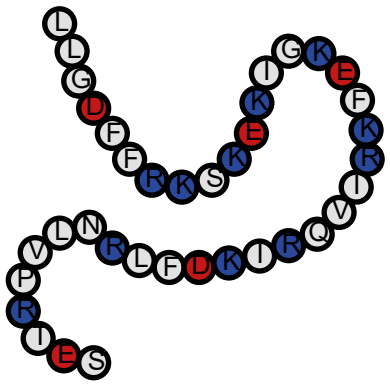

Figure IV-2. S3 – Primary structure of LL-37.

2.6.4 Chemical composition of LL-37

Table IV-2. S1 – Chemical composition of LL-37 based on the amino acid residues of its primary structure.

			Number of atoms in amino acid residues					Number of atoms in LL -37				
Amino acid	Aka	Number	C	O	N	S	H	C	O	N	S	H
Alanine (Ala)	A	0	3	1	1	0	5	0	0	0	0	0
Arginine (Arg)	R	5	6	1	4	0	12	30	5	20	0	60
Asparagine (Asn)	N	1	4	2	2	0	6	4	2	2	0	6
Aspartic acid (Asp)	D	2	4	3	1	0	5	8	6	2	0	10
Cysteine (Cys)	C	0	3	1	1	1	5	0	0	0	0	0
Glutamic acid (Glu)	E	3	5	3	1	0	7	15	9	3	0	21
Glutamine (Gln)	Q	1	5	2	2	0	8	5	2	2	0	8
Glycine (Gly)	G	2	2	1	1	0	3	4	2	2	0	6
Histidine (His)	H	0	6	1	3	0	7	0	0	0	0	0
Isoleucine (Ile)	I	3	6	1	1	0	11	18	3	3	0	33
Leucine (Leu)	L	4	6	1	1	0	11	24	4	4	0	44
Lysine (Lys)	K	6	6	1	2	0	12	36	6	12	0	72
Methionine (Met)	M	0	5	1	1	1	9	0	0	0	0	0
Phenylalanine (Phe)	F	4	9	1	1	0	9	36	4	4	0	36
Proline (Pro)	P	1	5	1	1	0	7	5	1	1	0	7
Serine (Ser)	S	2	3	2	1	0	5	6	4	2	0	10
Tryptophan (Trp)	W	0	11	1	2	0	10	0	0	0	0	0
Threonine (Thr)	T	1	4	2	1	0	7	4	2	1	0	7
Tyrosine (Tyr)	Y	0	9	2	1	0	9	0	0	0	0	0
Valine (Val)	V	2	5	1	1	0	9	10	2	2	0	18
Chain ends			0	1	0	0	2	0	1	0	0	2
Total		37	107	30	29	2	159	205	53	60	0	340
Theoretical composition revealed by XPS								64.47%	16.67%	18.87%	0%	0%

2.6.5 Carbon groups in LL-37

Table IV-2. S2 – Carbon groups present in amino acid residues constituting the LL-37 molecule.

Amino acid	Aka	Number	Number of carbon groups in amino acid residues										Number of carbon groups in LL- 37							
			O=C-O	N-C=O N-C-N C=N O-C-O	C-O	C-N	C-S	C-H$_3$	C-H$_2$	C-H	C-C-C	O=C-O	N-C=O N-C-N C=N O-C-O	C-O	C-N	C-S	C-H$_3$	C-H$_2$	C-H	C-C-C	Sum C
Alanine	A	0	0	1	0	1	0	1	0	0	0	0	0	0	0	0	0	0	0	0	0
Arginine	R	5	0	2	0	2	0	0	2	0	0	0	10	0	10	0	0	10	0	0	30
Asparagine	N	1	0	2	0	1	0	0	1	0	0	0	2	0	1	0	0	1	0	0	4
Aspartic acid	D	2	1	1	0	1	0	0	1	0	0	2	2	0	2	0	0	2	0	0	8
Cysteine	C	0	0	1	0	1	1	0	0	0	0	0	0	0	0	0	0	0	0	0	0
Glutamic acid	E	3	1	1	0	1	0	0	2	0	0	3	3	0	3	0	0	6	0	0	15
Glutamine	Q	1	0	2	0	1	0	0	2	0	0	0	2	0	1	0	0	2	0	0	5
Glycine	G	2	0	1	0	1	0	0	0	0	0	0	2	0	2	0	0	0	0	0	4
Histidine	H	0	0	2	0	3	0	0	1	0	0	0	0	0	0	0	0	0	0	0	0
Isoleucine	I	3	0	1	0	1	0	2	1	1	0	0	3	0	3	0	6	3	3	0	18
Leucine	L	4	0	1	0	1	0	2	1	1	0	0	4	0	4	0	8	4	4	0	24
Lysine	K	6	0	1	0	2	0	0	3	0	0	0	6	0	12	0	0	18	0	0	36
Methionine	M	0	0	1	0	1	2	0	1	0	0	0	0	0	0	0	0	0	0	0	0
Phenylalanine	F	4	0	1	0	1	0	0	1	5	1	0	4	0	4	0	0	4	20	4	36
Proline	P	1	0	1	0	2	0	0	2	0	0	0	1	0	2	0	0	2	0	0	5
Serine	S	2	0	1	1	1	0	0	0	0	0	0	2	2	2	0	0	0	0	0	6
Tryptophan	W	0	0	1	0	3	0	0	1	4	2	0	0	0	0	0	0	0	0	0	0
Threonine	T	1	0	1	1	1	0	1	0	0	0	0	1	1	1	0	1	0	0	0	4
Tyrosine	Y	0	0	1	1	1	0	0	1	4	1	0	0	0	0	0	0	0	0	0	0
Valine	V	2	0	1	0	1	0	2	0	1	0	0	2	0	2	0	4	0	2	0	10
Chain ends												1	-1								
Total		37										6	43	3	49	0	19	52	29	4	205

2.6.6 Nitrogen groups in LL-37

Table IV-2. S3 – (a) Nitrogen groups present in amino acid residues constituting the LL-37 molecule. (b) The theoretical protonation ratio of nitrogen groups of the N 1s core-level were calculated.

(a)

			Number of nitrogen groups in amino acid residues		Number of nitogen groups in LL-37		
Amino acid	Aka	Number	(CN)=O	C-NH	(CN)=O	C-NH	Sum C
Alanine (Ala)	A	0	1	0	0	0	0
Arginine (Arg)	R	5	1	3	5	15	20
Asparagine (Asn)	N	1	2	0	2	0	2
Aspartic acid (Asp)	D	2	1	0	2	0	2
Cysteine (Cys)	C	0	1	0	0	0	0
Glutamic acid (Glu)	E	3	1	0	3	0	3
Glutamine (Gln)	Q	1	2	0	2	0	2
Glycine (Gly)	G	2	1	0	2	0	2
Histidine (His)	H	0	1	2	0	0	0
Isoleucine (Ile)	I	3	1	0	3	0	3
Leucine (Leu)	L	4	1	0	4	0	4
Lysine (Lys)	K	6	1	1	6	6	12
Methionine (Met)	M	0	1	0	0	0	0
Phenylalanine (Phe)	F	4	1	0	4	0	4
Proline (Pro)	P	1	1	0	1	0	1
Serine (Ser)	S	2	1	0	2	0	2
Tryptophan (Trp)	W	0	1	1	0	0	0
Threonine (Thr)	T	1	1	0	1	0	1
Tyrosine (Tyr)	Y	0	1	0	0	0	0
Valine (Val)	V	2	1	0	2	0	2
Chain ends					-1	1	
Total		37			38	22	60

(b)

Ratio of N groups in LL-37 at pH 3.5 and 5

Protonated amine	Ratio of C-NH	Number
Arginine (R)	1/3	5
Lysine (K)	1	6
End chain	1	1
Non-protonated amine	Ratio of C-NH	Number
Arginine (R)	2/3	10
Amide	Ratio of (CN)=O	Number
	1	38
	Ratio	Peak
(Amide + non-protonated amine) / N_{tot}	0.8	399.8 eV
Protonated amine / N_{tot}	0.2	401.7 eV

2.6.7 Comparison between the theoretical composition and the composition measured by XPS of $[Chi\text{-}Hep]_2$ multilayers

For $[Chi\text{-}Hep]_2$ at pH 3.5, 1.2% of the total signal comes from S. Therefore, the N signal coming from Hep ($N^{399.8}$) is modeled at 0.4% of the total signal (Equation IV-2. 1). Knowing that the rest of the N signal is due to the presence of Chi (Equation IV-2. 2), it is modeled at 3.2%, of which 3.0% are attributed to the $N^{401.7}$ component (Equation IV-2. 3) and 0.2% to the $N^{399.8}$ component (Equation IV-2. 4).

Table IV-2. S4 – Modeling the percentage of each atom and functional group for Hep and Chi molecules in $[Chi\text{-}Hep]_2$ multilayers at pH 3.5 and 5.

		O 1s	N 1s			C 1s					S 2p	Au 4f
		$O^{532.4}$	$N^{401.7}$	$N^{399.8}$	N_{tot}	$C^{289.0}$	$C^{287.9}$	$C^{286.3}$	$C^{284.8}$	C_{tot}	$S^{168.3}$	$Au^{83.5}$
Au Wafer	Total measured composition	10.5	bdl	bdl	**bdl**	1.4	1.7	4.8	25.0	**32.9**	bdl	56.6
$[Chi\text{-}Hep]_2$ pH 3.5	Modeled Hep composition	7.8	0.0	0.4	**0.4**	0.4	0.8	3.7	0.0	**4.9**	1.2	/
	Modeled Chi composition	13.0	3.0	0.2	**3.2**	0.0	3.4	16.0	0.2	**19.6**	0.0	/
	Total modeled composition	20.8	3.0	0.6	**3.6**	0.4	4.2	19.7	0.2	**24.5**	1.2	/
	Total measured composition	33.1	2.0	1.6	**3.6**	1.9	6.3	19.0	9.0	**36.2**	1.2	25.8
$[Chi\text{-}Hep]_2$ pH 5	Modeled Hep composition	6.8	0.0	0.4	**0.4**	0.4	0.7	3.2	0.0	**4.3**	1.1	/
	Modeled Chi composition	17.9	4.2	0.2	**4.4**	0.0	4.6	22.1	0.2	**26.9**	0.0	/
	Total modeled composition	24.7	4.2	0.6	**4.8**	0.4	5.3	25.3	0.2	**31.2**	1.1	/
	Total measured composition	36.8	2.0	2.8	**4.8**	1.9	7.7	23.4	9.2	**42.2**	1.1	15.1

2.6.8 Comparison between the theoretical composition and the composition measured by XPS of [Chi-Hep]$_2$-[LL-37-Hep]$_{10 \text{ and } 10.5}$ multilayers

For [Chi-Hep]$_2$-[LL-37-Hep]$_{10}$ at pH 3.5, 1.9% of the total signal comes from S. Therefore, the N signal coming from Hep ($N^{399.8}$) is modeled at 0.6% of the total signal (Equation IV-2. 1). We assume that Chi of the anchoring layer is not detected due to the thickness of the film (> 5-7 nm, since almost no Au signal is detected). Therefore, the rest of the N signal comes from LL-37 molecules (Equation IV-2. 17), and it is modeled at 12.8%. 2.6% are attributed to the $N^{401.7}$ component (Equation IV-2. 18) and 10.3% to the $N^{399.8}$ component (Equation IV-2. 19).

Table IV-2. S5 – Modeling the percentage of each atom and functional group for Hep and LL-37 molecules in [Chi-Hep]$_2$-[LL-37-Hep]$_{10 \text{ and } 10.5}$ multilayers at pH 3.5 and 5.

		O 1s	N 1s			C 1s					S 2p	Au 4f
		$O^{532.4}$	$N^{401.7}$	$N^{399.8}$	N_{tot}	$C^{289.0}$	$C^{287.9}$	$C^{286.3}$	$C^{284.8}$	C_{tot}	$S^{168.3}$	$Au^{83.5}$
[Chi-Hep]$_2$-[LL-37-Hep]$_{10}$ pH 3.5	Modeled Hep composition	11.9	0.0	0.6	**0.6**	0.6	1.3	5.6	0.0	**7.5**	1.9	/
	Modeled LL-37 composition	11.3	2.6	10.3	**12.8**	1.3	9.2	11.1	22.3	**43.9**	0.0	/
	Total modeled composition	23.2	2.6	10.9	**13.5**	1.9	10.5	16.7	22.3	**51.4**	1.9	/
	Total measured composition	30.4	1.4	12.1	**13.5**	2.5	9.9	18.7	22.2	**53.3**	1.9	0.9
[Chi-Hep]$_2$-[LL-37-Hep]$_{10}$ pH 3.5	Modeled Hep composition	6.5	0.0	0.3	**0.3**	0.3	0.7	3.1	0.0	**4.1**	1.0	/
	Modeled LL-37 composition	14.3	3.2	13.0	**16.2**	1.6	11.6	14.1	28.1	**55.4**	0.0	/
	Total modeled composition	20.8	3.2	13.3	**16.6**	1.9	12.3	17.2	28.1	**59.5**	1.0	/
	Total measured composition	23.8	0.9	15.7	**16.6**	1.1	11.8	17.7	28.1	**58.6**	1.0	0.1
[Chi-Hep]$_2$-[LL-37-Hep]$_{10.5}$ pH 3.5	Modeled Hep composition	9.2	0.0	0.5	**0.5**	0.5	1.0	4.4	0.0	**5.9**	1.5	/
	Modeled LL-37 composition	12.5	2.8	11.3	**14.2**	1.4	10.2	12.3	24.6	**48.5**	0.0	/
	Total modeled composition	21.7	2.8	11.8	**14.6**	1.9	11.2	16.7	24.6	**54.4**	1.5	/
	Total measured composition	27.5	1.4	13.3	**14.7**	1.9	10.5	18.0	25.8	**56.3**	1.5	bdl
[Chi-Hep]$_2$-[LL-37-Hep]$_{10.5}$ pH 5	Modeled Hep composition	5.7	0.0	0.3	**0.3**	0.3	0.6	2.7	0.0	**3.6**	0.9	/
	Modeled LL-37 composition	14.3	3.2	13.0	**16.2**	1.6	11.6	14.1	28.1	**55.4**	0.0	/
	Total modeled composition	20.0	3.2	13.3	**16.5**	1.9	12.2	16.8	28.1	**59.0**	0.9	/
	Total measured composition	23.4	0.9	15.6	**16.5**	0.7	11.7	17.3	29.5	**59.2**	0.9	bdl

2.6.9 Comparison between the modeled composition and the XPS measured composition of $[Chi\text{-}Hep]_2\text{-}[Chi\text{-}PPCs_{LL\text{-}37\text{-}Hep}]_{10}$ and 10.5 multilayers considering a model with two of the three compounds integrated into the multilayers

Table IV-2. S6 – Modeling the percentage of each atom and functional group for Hep, Chi and LL-37 molecules in $[Chi\text{-}Hep]_2\text{-}[Chi\text{-}PPCs_{LL\text{-}37\text{-}Hep}]_{10 \text{ and } 10.5}$ multilayers at pH 3.5 and 5, considering the presence of two of the three compounds in the multilayers.

		O 1s	N 1s			C 1s					S 2p	Au 4f
		$O^{532.4}$	$N^{401.7}$	$N^{399.8}$	N_{tot}	$C^{289.0}$	$C^{287.9}$	$C^{286.3}$	$C^{284.8}$	C_{tot}	$S^{168.3}$	$Au^{83.5}$
$[Chi\text{-}Hep]_2\text{-}[Chi\text{-}PPCs_{LL\text{-}37\text{-}Hep}]_{10}$ pH 3.5	Modeled Hep composition	13.5	0.0	0.7	**0.7**	0.7	1.4	6.4	0.0	**8.5**	2.1	/
	Modeled Chi composition	38.1	5.2	4.2	**9.4**	0.0	9.9	47.0	0.5	**57.4**	0.0	/
	Total Chi-Hep modeled composition	51.6	5.2	4.9	**10.1**	0.7	11.3	53.4	0.5	**65.9**	2.1	/
	Modeled Hep composition	13.5	0.0	0.7	**0.7**	0.7	1.4	6.4	0.0	**8.5**	2.1	/
	Modeled LL-37 composition	8.3	0.9	8.5	**9.4**	0.9	6.7	8.1	16.3	**32.0**	0.0	/
	Total LL-37-Hep modeled composition	21.8	0.9	9.2	**10.1**	1.6	8.1	14.5	16.3	**40.5**	2.1	/
	Modeled Chi composition	-0.2	-0.1	0.0	**-0.1**	0.0	-0.1	-0.3	0.0	**-0.3**	0.0	/
	Modeled LL-37 composition	9.0	1.0	9.2	**10.2**	1.0	7.3	8.8	17.6	**34.7**	0.0	/
	Total Chi -LL-37 modeled composition	8.2	0.9	9.2	**10.1**	1.0	7.2	8.5	17.6	**34.4**	0.0	/
	Total measured composition	35.3	2.0	8.1	**10.1**	2.0	9.3	23.5	17.5	**52.3**	2.1	0.1
$[Chi\text{-}Hep]_2\text{-}[Chi\text{-}PPCs_{LL\text{-}37\text{-}Hep}]_{10}$ pH 5	Modeled Hep composition	12.1	0.0	0.6	**0.6**	0.6	1.3	5.7	0.0	**7.6**	1.9	/
	Modeled Chi composition	27.5	3.7	3.1	**6.8**	0.0	7.1	34.0	0.3	**41.4**	0.0	/
	Total Chi- Hep modeled composition	39.6	3.7	3.7	**7.4**	0.6	8.4	39.7	0.3	**49.0**	1.9	/
	Modeled Hep composition	12.1	0.0	0.6	**0.6**	0.6	1.3	5.7	0.0	**7.6**	1.9	/
	Modeled LL-37 composition	6.0	0.7	6.1	**6.8**	0.7	4.9	5.9	11.8	**23.3**	0.0	/
	Total LL-37-Hep modeled composition	18.1	0.7	6.7	**7.4**	1.3	6.2	11.6	11.8	**30.9**	1.9	/
	Modeled Chi composition	3.7	0.5	0.4	**0.9**	0.0	1.0	4.6	0.0	**5.6**	0.0	/
	Modeled LL-37 composition	5.7	0.7	5.8	**6.5**	0.7	4.7	5.6	11.3	**22.2**	0.0	/
	Total Chi -LL-37 modeled composition	9.5	1.2	6.2	**7.4**	0.7	5.7	10.2	11.3	**27.8**	0.0	/
	Total measured composition	38.3	2.2	5.3	**7.4**	1.5	9.0	29.3	11.8	**51.5**	1.9	0.9
$[Chi\text{-}Hep]_2\text{-}[Chi\text{-}PPCs_{LL\text{-}37\text{-}Hep}]_{10.5}$ pH 3.5	Modeled Hep composition	13.1	0.0	0.7	**0.7**	0.7	1.4	6.2	0.0	**8.3**	2.1	/
	Modeled Chi composition	30.7	4.2	3.4	**7.6**	0.0	8.0	37.9	0.4	**46.3**	0.0	/
	Total Chi- Hep modeled composition	43.8	4.2	4.1	**8.3**	0.7	9.4	44.1	0.4	**54.6**	2.1	/
	Modeled Hep composition	13.1	0.0	0.7	**0.7**	0.7	1.4	6.2	0.0	**8.3**	2.1	/
	Modeled LL-37 composition	6.7	0.8	6.8	**7.6**	0.8	5.4	6.6	13.1	**25.9**	0.0	/
	Total LL-37-Hep modeled composition	19.8	0.8	7.5	**8.3**	1.5	6.8	12.8	13.1	**34.2**	2.1	/
	Modeled Chi composition	3.7	0.5	0.4	**0.9**	0.0	1.0	4.6	0.0	**5.6**	0.0	/
	Modeled LL-37 composition	6.5	0.7	6.7	**7.4**	0.7	5.3	6.4	12.7	**25.1**	0.0	/
	Total Chi -LL-37 modeled composition	10.2	1.2	7.1	**8.3**	0.7	6.3	11.0	12.7	**30.7**	0.0	/
	Total measured composition	39.8	2.3	5.9	**8.3**	1.6	8.7	25.0	13.2	**48.4**	2.1	1.4
$[Chi\text{-}Hep]_2\text{-}[Chi\text{-}PPCs_{LL\text{-}37\text{-}Hep}]_{10.5}$ pH 5	Modeled Hep composition	9.0	0.0	0.5	**0.5**	0.5	1.0	4.3	0.0	**5.8**	1.4	/
	Modeled Chi composition	26.0	3.5	2.9	**6.4**	0.0	6.8	32.2	0.3	**39.3**	0.0	/
	Total Chi- Hep modeled composition	35.0	3.5	3.4	**6.9**	0.5	7.8	36.5	0.3	**45.1**	1.4	/
	Modeled Hep composition	9.0	0.0	0.5	**0.5**	0.5	1.0	4.3	0.0	**5.8**	1.4	/
	Modeled LL-37 composition	5.7	0.6	5.8	**6.4**	0.6	4.6	5.6	11.1	**21.9**	0.0	/
	Total LL-37-Hep modeled composition	14.7	0.6	6.3	**6.9**	1.1	5.6	9.9	11.1	**27.7**	1.4	/
	Modeled Chi composition	2.6	0.3	0.3	**0.6**	0.0	0.7	3.2	0.0	**3.9**	0.0	/
	Modeled LL-37 composition	5.5	0.6	5.7	**6.3**	0.6	4.5	5.4	10.9	**21.4**	0.0	/
	Total Chi -LL-37 modeled composition	8.1	0.9	6.0	**6.9**	0.6	5.2	8.6	10.9	**25.3**	0.0	/
	Total measured composition	38.5	1.9	5.0	**6.9**	1.2	8.2	27.7	15.4	**52.5**	1.4	0.6

2.7 References

1. Han, C. & Guo, W. Fluorescent Noble Metal Nanoclusters Loaded Protein Hydrogel Exhibiting Anti-Biofouling and Self-Healing Properties for Electrochemiluminescence Biosensing Applications. *Small* **16**, e2002621 (2020).
2. Teanphonkrang, S. & Schulte, A. Automated Quantitative Enzyme Biosensing in 24-Well Microplates. *Anal Chem* **89**, 5261–5269 (2017).
3. Büscher, N. *et al.* Biocatalyst Immobilization by Anchor Peptides on an Additively Manufacturable Material. *Org Process Res Dev* **23**, 1852–1859 (2019).
4. Zhang, G., Johnston, T., Quin, M. B. & Schmidt-Dannert, C. Developing a Protein Scaffolding System for Rapid Enzyme Immobilization and Optimization of Enzyme Functions for Biocatalysis. *ACS Synth Biol* **8**, 1867–1876 (2019).
5. Schoeller, J. *et al.* pH-responsive chitosan/alginate polyelectrolyte complexes on electrospun PLGA nanofibers for controlled drug release. *Nanomaterials* **11**, 1850 (2021).
6. Lu, Y., Aimetti, A. A., Langer, R. & Gu, Z. Bioresponsive materials. *Nat Rev Mater* **2**, 16075 (2016).
7. Kitsara, M. *et al.* Polysaccharide–Protein Multilayers Based on Chitosan–Fibrinogen Assemblies for Cardiac Cell Engineering. *Macromol Biosci* **22**, 2100346 (2021).
8. Zander, N. E., Orlicki, J. A., Rawlett, A. M. & Beebe, T. P. Quantification of protein incorporated into electrospun polycaprolactone tissue engineering scaffolds. *ACS Appl Mater Interfaces* **4**, 2074–2081 (2012).
9. Ariga, K., Song, J. & Kawakami, K. Layer-by-layer designer nanoarchitectonics for physical and chemical communications in functional materials. *Chemical Communications* **60**, 2152–2167 (2024).
10. Decher, G., Hong, J. D. & Schmitt, J. Buildup of ultrathin multilayer films by a self-assembly process: III. Consecutively alternating adsorption of anionic and cationic polyelectrolytes on charged surfaces. *Thin Solid Films* **210–211**, 831–835 (1992).

11. Schlenoff, J. B., Ly, H. & Li, M. Charge and mass balance in polyelectrolyte multilayers. *J Am Chem Soc* **120**, 7626–7634 (1998).
12. Decher, G. Fuzzy Nanoassemblies: Toward Layered Polymeric Multicomposites. *Science* **277**, 1232–1237 (1997).
13. Hammond, P. T. Recent explorations in electrostatic multilayer thin film assembly. *Curr Opin Colloid Interface Sci* **4**, 430–442 (1999).
14. Borges, J. & Mano, J. F. Molecular interactions driving the layer-by-layer assembly of multilayers. *Chem Rev* **114**, 8883–8942 (2014).
15. Ariga, K., Lvov, Y. & Decher, G. There is still plenty of room for layer-by-layer assembly for constructing nanoarchitectonics-based materials and devices. *Physical Chemistry Chemical Physics* **24**, 4097–4115 (2022).
16. Genet, M. J., Dupont-Gillain, C. C. & Rouxhet, P. G. XPS analysis of biosystems and biomaterials. in *Medical Applications of Colloids* (ed. Matijevic, E.) 177–307 (New York, 2008).
17. Boddohi, S., Killingsworth, C. E. & Kipper, M. J. Polyelectrolyte Multilayer Assembly as a Function of pH and Ionic Strength Using the Polysaccharides Chitosan and Heparin. *Biomacromolecules* **9**, 2021–2028 (2008).
18. Almodóvar, J., Place, L. W., Gogolski, J., Erickson, K. & Kipper, M. J. Layer-by-Layer Assembly of Polysaccharide-Based Polyelectrolyte Multilayers: A Spectroscopic Study of Hydrophilicity, Composition, and Ion Pairing. *Biomacromolecules* **12**, 2755–2765 (2011).
19. Maachou, H., Genet, M. J., Aliouche, D., Dupont-Gillain, C. C. & Rouxhet, P. G. XPS analysis of chitosan–hydroxyapatite biomaterials: from elements to compounds. *Surface and Interface Analysis* **45**, 1088–1097 (2013).
20. Yang, Y. *et al.* Proteins dominate in the surface layers formed on materials exposed to extracellular polymeric substances from bacterial cultures. *Biofouling* **32**, 95–108 (2016).
21. vander Straeten, A. & Dupont-Gillain, C. Highly Hydrated Thin Films Obtained via Templating of the Polyelectrolyte Multilayer Internal Structure with Proteins. *ACS Appl Polym Mater* **2**, 2602–2611 (2020).
22. Chang, T. M., Prell, J. S., Warrick, E. R. & Williams, E. R. Where's the Charge? Protonation Sites in Gaseous Ions Change with Hydration. *J Am Chem Soc* **134**, 15805–15813 (2012).

23. Niyonsaba, F. *et al.* A cathelicidin family of human antibacterial peptide LL-37 induces mast cell chemotaxis. *Immunology* **106**, 20–26 (2002).
24. Hemshekhar, M., Choi, K. Y. G. & Mookherjee, N. Host defense peptide LL-37-mediated chemoattractant properties, but not anti-inflammatory cytokine IL-1RA production, is selectively controlled by Cdc42 Rho GTPase via G protein-coupled receptors and JNK mitogen-activated protein kinase. *Front Immunol* **9**, 17 (2018).
25. Milhan, N. V. M. *et al.* The Antimicrobial Peptide LL-37 as a Possible Adjunct for the Proliferation and Differentiation of Dental Pulp Stem Cells. *J Endod* **43**, 2048–2053 (2017).
26. Ramos, R. *et al.* Wound healing activity of the human antimicrobial peptide LL37. *Peptides* **32**, 1469–1476 (2011).
27. Comune, M., Rai, A., Palma, P., TondaTuro, C. & Ferreira, L. Antimicrobial and pro-angiogenic properties of soluble and nanoparticle-immobilized LL37 peptides. *Biomater Sci* **9**, 8153–8159 (2021).
28. Dürr, U. H. N., Sudheendra, U. S. & Ramamoorthy, A. LL-37, the only human member of the cathelicidin family of antimicrobial peptides. *Biochimica et Biophysica Acta (BBA) - Biomembranes* **1758**, 1408–1425 (2006).
29. Vranckx, C. *et al.* Layer-by-Layer Nanoarchitectonics Using Protein-Polyelectrolyte Complexes toward a Generalizable Tool for Protein Surface Immobilization. *Langmuir* **38**, 5579–5589 (2022).
30. Salmivirta, M., Lidholt, K. & Lindahl, U. Heparan sulfate: a piece of information. *The FASEB Journal* **10**, 1270–1279 (1996).
31. Silva, R. A., Urzúa, M. D., Petri, D. F. S. & Dubin, P. L. Protein adsorption onto polyelectrolyte layers: Effects of protein hydrophobicity and charge anisotropy. *Langmuir* **26**, 14032–14038 (2010).
32. vander Straeten, A. *et al.* Protein–polyelectrolyte complexes to improve the biological activity of proteins in layer-by-layer assemblies. *Nanoscale* **9**, 17186–17192 (2017).
33. vander Straeten, A., Bratek-Skicki, A., Jonas, A. M., Fustin, C.-A. & Dupont-Gillain, C. Integrating Proteins in Layer-by-Layer Assemblies

Independently of their Electrical Charge. *ACS Nano* **12**, 8372–8381 (2018).

34. Li, J. & Zhuang, S. Antibacterial activity of chitosan and its derivatives and their interaction mechanism with bacteria: Current state and perspectives. *Eur Polym J* **138**, 109984 (2020).
35. Dolinsky, T. J., Nielsen, J. E., McCammon, J. A. & Baker, N. A. PDB2PQR: An automated pipeline for the setup of Poisson-Boltzmann electrostatics calculations. *Nucleic Acids Res* **32**, 665–667 (2004).
36. Lundin, M., Solaqa, F., Thormann, E., Macakova, L. & Blomberg, E. Layer-by-Layer Assemblies of Chitosan and Heparin: Effect of Solution Ionic Strength and pH. *Langmuir* **27**, 7537–7548 (2011).
37. Tanuma, S., Powell, C. J. & Penn, D. R. Calculation of electron inelastic mean free paths (IMFPs) VII. Reliability of the TPP-2M IMFP predictive equation. *Surface and Interface Analysis* **35**, 268–275 (2003).
38. Lebugle, A., Subirade, M. & Gueguen, J. Structural characteristics of a globular protein investigated by X-ray photoelectron spectroscopy: comparison between a legumin film and a powdered legumin. *Biochimica et Biophysica Acta (BBA) - Protein Structure and Molecular Enzymology* **1248**, 107–114 (1995).
39. Deligianni, D. D. *et al.* Effect of surface roughness of the titanium alloy Ti–6Al–4V on human bone marrow cell response and on protein adsorption. *Biomaterials* **22**, 1241–1251 (2001).
40. Vanea, E. & Simon, V. XPS study of protein adsorption onto nanocrystalline aluminosilicate microparticles. *Appl Surf Sci* **257**, 2346–2352 (2011).
41. Bozack, M. J., Zhou, Y. & Worley, S. D. Structural modifications in the amino acid lysine induced by soft x-ray irradiation. *J Chem Phys* **100**, 8392–8398 (1994).
42. Taucher, T. C., Hehn, I., Hofmann, O. T., Zharnikov, M. & Zojer, E. Understanding Chemical versus Electrostatic Shifts in X-ray Photoelectron Spectra of Organic Self-Assembled Monolayers. *Journal of Physical Chemistry C* **120**, 3428–3437 (2016).
43. Herboth, R., Gopakumar, G., Caleman, C. & Wohlert, M. Charge State Dependence of Amino Acid Propensity at Water Surface: Mechanisms Elucidated by Molecular Dynamics Simulations. *Journal of Physical Chemistry A* **125**, 4705–4714 (2021).

44. Zubavichus, Y. *et al.* Soft X-Ray-Induced Decomposition of Amino Acids: An XPS, Mass Spectrometry, and NEXAFS Study. *Radiat Res* **161**, 346–358 (2004).
45. vander Straeten, A. & Dupont-Gillain, C. Self-Reorganizing Multilayer to Release Free Proteins from Self-Assemblies. *Langmuir* **36**, 972–978 (2019).

3 Unraveling the nanoarchitecture of LL-37-based layer-by-layer self-assembled multilayered structures depending on the conditions and the pathway of assembly

Cédric Vranckx[1*], Olivier Cornu[2,3], and Christine Dupont-Gillain[1*]

[1]Institute of Condensed Matter and Nanosciences, Bio-and Soft Matter, Université catholique de Louvain, Place Louis Pasteur, 1 bte L4.01.10, B-1348 Louvain-la-Neuve, Belgium

[2]Neuro-Musculo-Skeletal Pole, Experimental and Clinical Research Institute, Université catholique de Louvain, 1200 Brussels, Belgium

[3]Orthopaedic and Trauma Department, Cliniques Universitaires Saint-Luc, Université catholique de Louvain, 1200 Brussels, Belgium

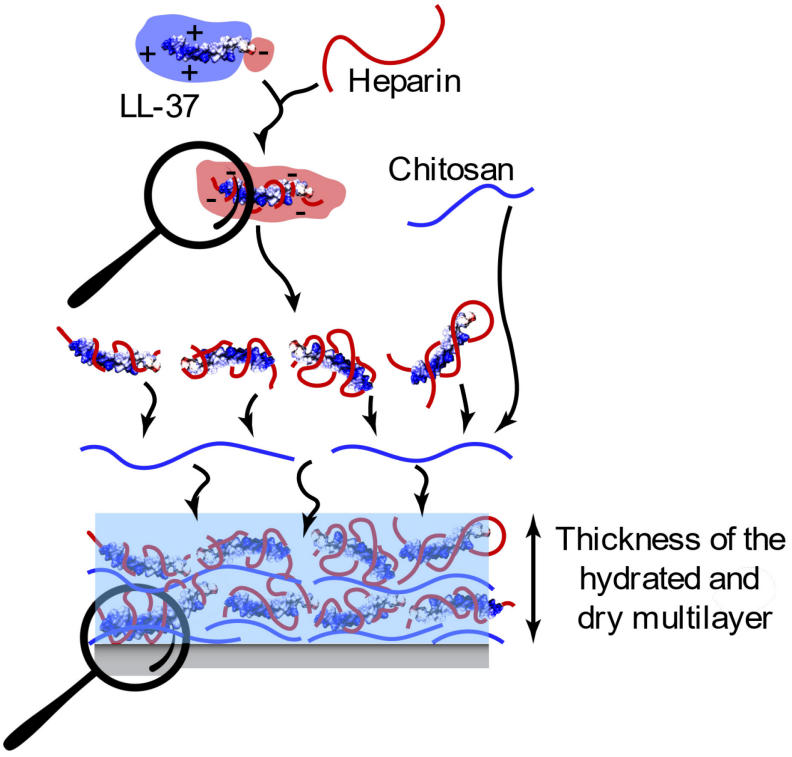

Abstract

Here, we demonstrate the self-assembly of the antimicrobial human LL-37 peptide onto the surface and that controlling the way in which LL-37 molecules are immobilized at surfaces allows designing self-assemblies whose architecture depends on the selected construction pathway. An investigation of the self-assembly pathways holds promises in endowing the resultant assemblies with diverse organizations. LL-37 molecules were self-assembled with heparin (Hep) and chitosan (Chi) using the layer-by-layer (LbL) method. On the one hand, LL-37 was complexed with Hep, and the resulting peptide-polyelectrolyte complex ($PPC_{LL\text{-}37\text{-}Hep}$) was alternately adsorbed with Chi, and, on the other hand, bare LL-37 molecules were directly immobilized using Hep. A deep analytical study of the obtained nanofilms was conducted to unravel their architecture. The wet and dry thicknesses were determined using quartz crystal microbalance with dissipation monitoring (QCM-D) and ellipsometry, enabling the assessment of viscoelasticity and hydration level of the multilayers. It appears that nanoassemblies obtained via $PPCs_{LL\text{-}37\text{-}Hep}$ are thicker, more viscoelastic, and more hydrated than the ones designed with bare LL-37 molecules. Moreover, it has been highlighted that the pH of assembly also plays a crucial role in the nanofilm architecture. Polyelectrolytes adopt a more extended conformation at pH 3.5 and a more random one at pH 5, giving a more viscoelastic character to films assembled at pH 5. Altogether, the findings of this study provide a way to tune the architecture of LL-37-containing nanoassemblies, with the goal to design antibacterial surfaces on medical devices and biomaterials and thus to deal with medical implant-related infections issue.

3.1 Introduction

The last decades have seen the number of antimicrobial-resistant bacteria rising, and a delayed development of new therapeutic options, which could have catastrophic consequences.[1,2] The World Health Organization has declared antimicrobial resistance as one of the biggest threats to humanity. Moreover, nosocomial diseases are linked, in more than 50% of cases, to the presence of a medical device (catheters, implants, etc.).[3] To address this issue, more and more studies are focusing on the design of antimicrobial coatings to improve the biomaterial performances.[4–6]

Among these strategies, antimicrobial peptides (AMPs) constitute a promising avenue.[7] These innate system components exhibit a broad-spectrum antimicrobial activity and can be used efficiently to kill Gram-negative and -positive bacteria,[8,9] viruses,[10] fungi,[11] and cancerous cells.[12] Besides their antimicrobial activity, these host defense molecules are able to modulate the immune response and boost infection-resolving immunity, making them good candidates as therapeutic agents.[13,14] Several AMPs have been identified, of which cathelicidins and defensins have been the most studied.[15]

There is only one cathelicidin antimicrobial peptide (CAMP) gene identified in humans.[16] This gene encodes the small amphipathic LL-37 peptide, which is 37-amino-acid-long (4.5 kDa) and may take an α-helical conformation, depending on its concentration, the solution pH, and the ionic strength (I).[17] Importantly, the LL-37 antimicrobial activity is conformation-dependent since the α-helices create pores in the bacterial membrane, causing leakage from the bacterial cells.[18] LL-37 antibiofilm activity was also demonstrated for *P. aeruginosa* and *S. aureus*.[19,20] Finally, LL-37 exerts different immunomodulatory functions such as chemotaxis,[21] modulation of pro- and anti-inflammatory responses,[22] influence on cell proliferation and differentiation,[23] promotion of wound healing,[24] and angiogenesis.[25]

Despite all these benefits, LL-37 suffers from several limitations, that can make it difficult to use as therapeutic agent, such as high cost, lower activity in physiological environments,[26] susceptibility to proteolytic degradation,[27] and toxicity to human cells[17,28]. Depending on the type of eukaryotic cells, the cytotoxic concentration of LL-37 *in vitro* was reported to be 13-25 µM,

and the cytotoxicity gradually increases at higher concentrations.[17] However, this value is reported to be strongly affected by factors present in human serum, which attenuate the cytotoxic effect of LL-37.[17] The minimum inhibitory concentration (MIC) of LL-37 is strongly related to the bacteria strains. Values from 0.1 µM to more than 56 µM of LL-37 were reported for Gram-positive and -negative bacteria.[25,29–31] These values are strongly dependent on the experimental conditions under which the analyses were performed, *e.g.*, the medium, the salt concentration, the pH and the presence of serum.

Many systems that aim at exploiting LL-37 biological activity were already proposed. As the LL-37 antimicrobial activity is highly sensitive to environmental conditions, research has focused on the immobilization of LL-37 onto biomaterial surfaces.[26,32,33] However, it remains a challenge to obtain functional layers and little is known about LL-37 properties after immobilization. Gabriel *et al.* demonstrated that LL-37 grafted on titanium surfaces retain its antibacterial activity.[34] More recently, it was shown that LL-37 can be loaded in poly(lactic-co-glycolic acid)-nanoparticles and its release promoted wound healing while antibacterial activity was maintained.[35] LL-37 synthetic derivatives were also incorporated in a polymer-lipid encapsulation matrix coating allowing controlled released. Such coating displayed promising performances to prevent biomaterial-associated infections.[36] Collagen/hyaluronic acid polyelectrolyte multilayers (PEMs) were modified with LL-37 by physisorption and chemical immobilization. The presence of the peptide led to a significantly decrease of microbial adhesion on the surface, which has been related to the amount of immobilized LL-37. No cytotoxicity was observed for up to 16 µM LL-37.[37] More recently, it was shown that LL-37 conjugated to gold nanoparticles is less cytotoxic to endothelial cells than soluble LL-37, while retaining its antibacterial and pro-angiogenic activities.[25] As an alternative to reduce the LL-37 cytotoxicity, Quemé-Peña *et al.* associated LL-37 non-covalently with suramin to form LL-37-suramin complexes.[38] The results showed that suramin significantly reduced LL-37 cytotoxicity. However, the impact of suramin on LL-37 antibacterial activity was not studied.[38] Yoshida *et al.* also proposed to use the complexation method to lower mammalian cytotoxic activity while maintaining a sufficient bactericidal effect on some bacteria strains.[39] In this way, they have shown that, using LL-37-heparin complexes,

the cytotoxicity on human dental pulp cells and MG-63 cells could be lowered while keeping a significant antibacterial activity against Gram-positive and -negative bacteria.[39] Additionally, it is anticipated that LL-37-heparin complexes could protect LL-37 from protease action the same way as self-DNA is protected from DNases degradation in self-DNA/LL-37 complexes.[40] Therefore, the surface immobilization of LL-37 could decrease its cytotoxic effect while keeping its antimicrobial properties.

Since LL-37 forms complexes with Hep, which is reported to maintain its bacterial activity,[39] the method developed in our previous work, which consists in layer-by-layer (LbL) adsorption of proteins through protein-polyelectrolyte complexes (PPCs), may prove particularly helpful with respect to LL-37 immobilization.[41] LbL self-assembly technique is a well-known surface immobilization technique based on successive adsorption steps of different compounds, usually through electrostatic interactions.[42] Multilayer build-up involves the successive deposition of positively- and negatively-charged species from aqueous solutions to shape an interpenetrated-charged network.[43] This technique does not require the use of any chemical reactions and offers many advantages compared to other surface modification methods, including simplicity and versatility. While this "build-to-order" technique is easily applied to homopolyelectrolytes, the LbL assembly of peptides is however challenging due to their polyampholyte character and charge anisotropy.[44] To circumvent this issue, PPCs have been recently introduced as new building blocks for the LbL assembly of proteins and peptides.[41,45,46]

In this study, as depicted in Figure IV-3. 1, LL-37-heparin complexes ($PPCs_{LL-37-Hep}$) have been first synthesized at pH 3.5 and 5. The negatively-charged Hep has been added to the positively-charged LL-37 to yield negatively-charged $PPCs_{LL-37-Hep}$. The obtained $PPCs_{LL-37-Hep}$ have been assembled using the LbL method with Chi, which is positively charged at a pH below its pK_a value, approximately 6.5.[47] The constructed multilayers will thus also benefit from the antimicrobial and wound healing properties of Chi.[48] As a matter of comparison, LL-37 was immobilized using the classical method, *i.e.*, bare LL-37 directly assembled with Hep. Both LbL assembly methods were compared in terms of LbL growth, organization, and architecture to gain a better understanding of the obtained multilayers, and thus to design, *in fine*, new valuable coatings for antimicrobial and biomedical applications.

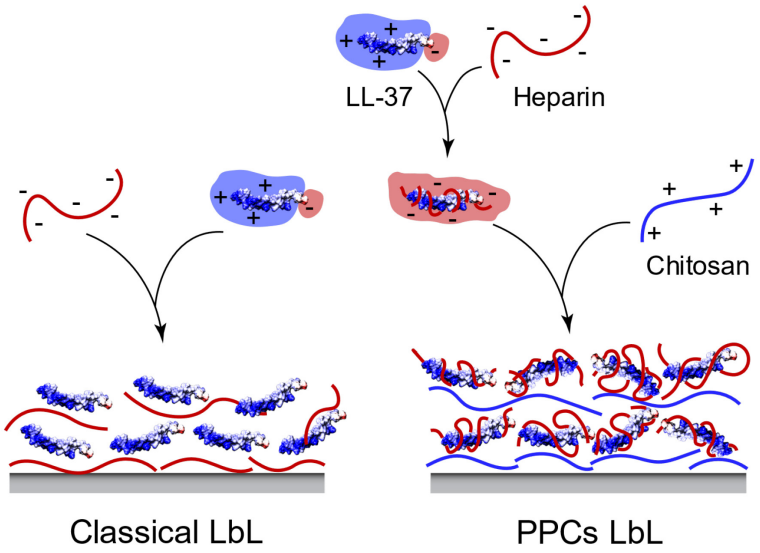

Figure IV-3. 1 – Schematic representation of the two immobilization strategies studied in this work.

3.2 Experimental section

3.2.1 Materials

Chi, M_W = 10,000-50,000 g mol^{-1} and deacetylation degree (DD) of 95% was purchased from Heppe Medical Chitosan Gmbh (Halle, Germany). Chi is not soluble in ultrapure water. Therefore, Chi solution was prepared by first dissolving 50 mg of Chi in approximately 25 mL of ultrapure water and 60 µL of HCl 37% (VWR, Leuven, Belgium) at 60°C for 1 h. Then, pH was adjusted to a value of 3.5 or 5 with NaOH 10 M (Sigma Aldrich, Steinheim, Germany) and the volume was brought to exactly 100 mL. Finally, the Chi solution was filtered with successively 5 and 0.2 µm filters to remove small impurities and non-dissolved particles. Hep sodium salt, 5 000 I.E./mL, was obtained from B.Braun (Melsungen, Germany). LL-37, 98.05% pure (peptide sequence: LLGDFFRKSKEKIGKEFKRIVQRIKDFLRNLVPRTES, theoretical molecular mass of 4493.26 Da) was bought from Proteogenix (Schiltigheim, France). Hep and LL-37 solutions were prepared at I ≈ 0 mM, in ultrapure water (Elga Purelab Chorus 1, 18.2 MΩ.cm, Veolia, United Kingdom), with only the ions necessary for pH adjustment (3.5 or 5 with NaOH 10 M or HCl 37%). For Chi solution, as Chi must be dissolved in acidic conditions, I cannot be equal to 0 mM. I was

kept as low as possible, with only the ions necessary for Chi dissolution and pH adjustment and is around 10 mM. The pH value was measured using a pH-indicator strip (MQuant, Merck, Darmstadt, Germany).

Silicon (Si) wafers of 1 cm² were cleaned, prior to use, for 15 min in a piranha solution, H_2O_2/H_2SO_4 1:3 (v:v) (Prolabo, VWR, Leuven, Belgium), and then thoroughly rinsed with ultrapure water then ethanol, dried under nitrogen flow, and further treated under UV/O_3 (UVO Cleaner 42-220, Jelight Company, Irvine, USA) during 15 min.

3.2.2 Formation of $PPCs_{LL\text{-}37\text{-}Hep}$

Since electrostatic interactions drive $PPCs_{LL\text{-}37\text{-}Hep}$ formation, the polyelectrolyte (PE)-to-peptide molar ratio in the complexes is usually expressed as the PE-to-peptide charge ratio. The charge ratio was calculated as the ratio of PE net charge to the peptide net structural charge at pH 3.5 and 5. Due to its sulfonate groups, Hep was considered as fully negatively charged. LL-37 charge was computed as a function of pH based on its amino acid sequence and structure (PDB file: 2K6O), using the PDB2PQR Server.[49] The LL-37 net charge is +10.4 and +7 at, respectively, pH 3.5 and 5. For example, $PPCs_{LL\text{-}37\text{-}Hep}$ at a (-)/(+net) charge ratio of 1.5 were prepared by mixing 3 volumes of Hep solution (0.5 mM negative charge) with 10 volumes of LL-37 solution (0.1 mM net positive charge). Therefore, the LL-37 and Hep concentrations in the $PPCs_{LL\text{-}37\text{-}Hep}$ with a charge ratio of 1.5 are, respectively, 0.08 and 0.12 mM positive and negative net charge. This constitutes a theoretical charge ratio and, taking into account the fact that part of Hep and LL-37 molecules could remain free, *i.e.*, would not be integrated in complexes, the actual charge ratio of the formed $PPCs_{LL\text{-}37\text{-}Hep}$ may differ from this theoretical ratio. For turbidity measurements, the Hep solution was added to the LL-37 solution in such a way that (-)/(+net) charge ratio varied between 0 and 3, *e.g.*, 0.4 mL of Hep solution was added to 1 mL of LL-37 solution to reach a (-)/(+net) charge ratio of 2.

3.2.3 Turbidimetry

Previous data showed that the turbidity value can be used to estimate the charge ratio at which the protein charge is overcompensated by the added

PE.[41,45] This informs on the charge ratio (or molar ratio) necessary to obtain PPCs that can be assembled with the LbL method.[50] In the following, turbidity measurements were thus used to monitor $PPCs_{LL\text{-}37\text{-}Hep}$ formation as Hep is added to the LL-37 solution. The turbidimetry at λ = 450 nm (A_{450}) of the suspension was measured at pH 3.5 and 5, using a multi-mode microplate reader (SpectraMaxiD3, Molecular Device, USA). The A_{450} values were normalized by the dilution factor according to the Beer-Lambert law. Measurements were all performed at 25°C and were made in independent triplicate. Results are presented with their standard deviation.

3.2.4 Zeta potential measurement

The electrophorectic mobility of $PPCs_{LL\text{-}37\text{-}Hep}$ was determined by a Laser Doppler Velocimetry technique. Measurements were made at pH 3.5 and 5 using a Malvern Zetasizer NanoZS instrument (Worcestershire, UK). Each measurement was performed in independent triplicate and results are presented with their standard deviation.

3.2.5 Dynamic light scattering

Measurements were performed at 25°C and at an angle of 90° using a Malvern CGS-3 apparatus (Langen, Germany) equipped with a He-Ne laser with a wavelength of 632.8 nm. The experimental intensity autocorrelation function was measured and analyzed by the CONTIN routine as described by Brown.[51] Dynamic light scattering (DLS) measurements were repeated ten times (n=10) and the experiment was performed three times (N=3). The results are presented together as a mean of the 30 values with their standard deviation. Hydrodynamic radius (R_h) refers to the mean apparent hydrodynamic radius calculated for each population in the CONTIN histogram.

3.2.6 LL-37 quantification in $PPCs_{LL\text{-}37\text{-}Hep}$ using bicinchoninic acid assay

LL-37 amount within the $PPCs_{LL\text{-}37\text{-}Hep}$ was assessed by bicinchoninic acid assay (BCA, ThermoFisher Scientific, Waltham, MA, USA). 20 µL of $PPCs_{LL\text{-}37\text{-}Hep}$ solution was added in wells of a 96-well microplate (Greiner Bio-One,

Kremsmünster, Austria). The working reagent (200 µL, reagent A:reagent B, 50:1, v:v) was then added and incubated 60 min at 60°C. The absorbance was measured at 562 nm (A_{562}) using a multi-mode microplate reader (SpectraMaxiD3, Molecular Device, USA). LL-37 amount was determined based on a calibration curve obtained with known LL-37 amounts.

3.2.7 Multilayer construction

Multilayers were constructed by successive adsorption steps on Si wafers. For all experiments, an anchoring layer of two bilayers of Chi alternately adsorbed with Hep ($[Chi\text{-}Hep]_2$) was constructed from Chi and Hep solutions (0.5 g L^{-1}). Then, two different multilayer systems were built on this anchoring layer: bare LL-37 molecules directly assembled with Hep ([LL-37-Hep]), and $PPCs_{LL\text{-}37\text{-}Hep}$ assembled with Chi ($[Chi\text{-}PPCs_{LL\text{-}37\text{-}Hep}]$). The following solutions were used: Chi (0.5 g L^{-1}), Hep (0.5 g L^{-1}) and LL-37 (0.08 mM positive net charge), as well as a suspension of $PPCs_{LL\text{-}37\text{-}Hep}$ prepared as described in *Part IV – 3.2.2 Formation of $PPCs_{LL\text{-}37\text{-}Hep}$*. Si wafers were placed in 24-well polystyrene Cellstar® plates (Greiner Bio-One, Kremsmünster, Austria) and each adsorption step, that lasted for 20 min, was carried out in static conditions with 300 µL of solution and was followed by three consecutive rinsing steps with ultrapure water adjusted at pH 3.5 or 5.

3.2.8 Quartz crystal microbalance with dissipation monitoring

To study the thin films formation, commercially available 4.95 MHz AT-cut gold-coated quartz sensors (Q-sense, Stockholm, Sweden) were purchased. These sensors were washed with piranha solution (H_2O_2/H_2SO_4 1:3 (v:v)), and successively rinsed with water and ethanol, then exposed to UV/O_3 for 15 min. Layer growth on gold-coated sensors was monitored using a quartz crystal microbalance with dissipation (QCM-D) monitoring system (Q-sense E4 system, Q-Sense, Stockholm, Sweden). The solution flow rate and the temperature were respectively set at 20 µL min^{-1} and 20°C. Layers were constructed by successive adsorption steps as described in the *Part IV – 3.2.7 Multilayer construction* section. The adsorption time for each compound is not fixed. The solutions pass through the QCM-D cells until stabilization of the frequency and dissipation shifts. Each adsorption step was followed by a

rinsing step of 10 min with ultrapure water adjusted to pH 3.5 or 5. The frequency and dissipation shifts were recorded for the third to the eleventh overtones and the results for the seventh one are presented here. The adsorbed mass (µg cm^{-2}) was assessed for the 7^{th} overtone, based on two different models. First, the Voinova model that is usually used for multilayers considered as viscoelastic.[52] Second, the Sauerbrey equation: $\Delta m = -\Delta f_7 \, C \, 7^{-1}$, where Δm is the shift of adsorbed mass (µg cm^{-2}), Δf_7 the frequency shift measured for the seventh overtone (Hz), C the mass sensitivity constant, equal to 17.7 ng cm^{-2} Hz^{-1} for a 5 MHz crystal and 7 the overtone number.[53] Reviakine et *al.* suggested that $|\Delta D_n/(-\Delta f_n/n)| << 4\times10^{-7}$ Hz^{-1}, for a 5 MHz crystal, indicates a film that can be approximated to be as rigid as the sensor, and thus the Sauerbrey equation may be used to extract the areal mass density of the film.[53,54] Importantly, the Sauerbrey model is more straightforward to apply, but it provides the minimum value for the mass adsorbed on the surface, and thus can underestimate the real mass adsorbed.

3.2.9 Spectroscopic ellipsometry

The dry thickness of LbL multilayers on Si wafers was monitored by spectroscopic ellipsometry (EP3 ellipsometer, Accurion). The measurement was performed at an incidence angle of 65° in a wavelength range from 400 to 800 nm. The collected data were analyzed by using the EP4 Model software with a three-layer model. In this model, the complex refractive index (n+jk) of Si substrate is (3.840-j0.016), and the refractive index of native SiO_2 layer is 1.46. The thickness of the SiO_2 layer was first measured by ellipsometry on the bare wafers just after piranha solution treatment. A thickness of 1.9 nm was determined by fitting, based on a two-layer optical model (without peptide and PE layer on top). The SiO_2 thickness was subsequently fixed to 1.9 nm during the fitting of the LbL film in a three-layer model wherein the multilayer thickness and complex refractive index are the sole unknowns, assuming a homogeneous and isotropic layer. The thickness of the LbL films were modeled by a Cauchy dispersion law by fixing the refractive index at 1.46.[55]

3.3 Results and discussion

3.3.1 Formation of $PPCs_{LL\text{-}37\text{-}Hep}$

$PPCs_{LL\text{-}37\text{-}Hep}$ were formed in ultrapure water at pH 3.5 and 5 by adding Hep to LL-37. The $PPCs_{LL\text{-}37\text{-}Hep}$ obtained by complexation are represented in Figure IV-3. 2. The addition of Hep is expressed as a function of (-)/(+net) charge ratio, which is defined as the structural charge ratio, where LL-37 charge is +10.4 and +7 at, respectively, pH 3.5 and 5, and Hep charge is equal to -4 per repeating unit.[49]

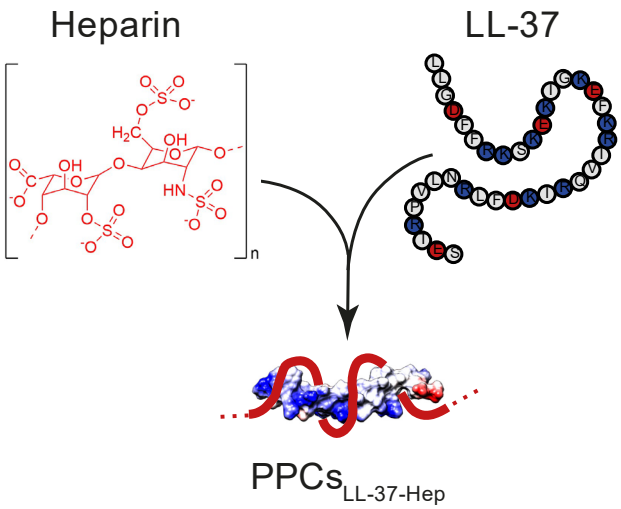

Figure IV-3. 2 – Schematic representation of LL-37-Hep complex formation. Hep is negatively-charged and represented by red line, while LL-37 is a polyampholyte with uncharged (grey), positively-charged (blue) and negatively-charged (red) residues. The molecular structure of LL-37 was produced using the UCSF Chimera package.[56]

The formation of $PPCs_{LL\text{-}37\text{-}Hep}$ was monitored by turbidimetry measurement at 450 nm (A_{450}), as a function of (-)/(+net) charge ratio (Figure IV-3. 3a). As the (-)/(+net) charge ratio increases, *i.e.*, with Hep addition, an increase of A_{450} is observed, until it reaches a plateau between (-)/(+net) = 1.25 and 1.5. A_{450} values follow the same trend at both tested pH values but are a bit higher at pH 3.5 compared to pH 5. The complexation was further investigated by centrifugation, followed by LL-37 BCA-dosage (Figure IV-3. 3b). The fraction of LL-37 found in the supernatant and in the pellet, after centrifugation at

12,000 g, was measured at pH 3.5 and 5. At pH 3.5, when the (-)/(+net) charge ratio increases, the fraction of LL-37 in the pellet increases, until it reaches a maximum at a (-)/(+net) charge ratio of 1. Beyond this value, when there is an excess of Hep, an increase of the fraction of LL-37 in the supernatant is observed. At pH 5, results are slightly different, with the LL-37 fraction that increases in the pellet until (-)/(+net) charge ratio of 1, then almost all the LL-37 is found in the pellet beyond this charge ratio value. The $PPCs_{LL\text{-}37\text{-}Hep}$ surface charge, as a function of the (-)/(+net) charge ratio, was monitored using zeta potential measurements (Figure IV-3. 3c). It appears that the LL-37 surface charge compensation by Hep occurs around (-)/(+net) = 1 and 1.25 at, respectively, pH 3.5 and 5. Except for this slight difference of charge reversal, the positive and negative potential values recorded, respectively, at low and high charge ratio are very similar at both tested pH. Regarding $PPCs_{LL\text{-}37\text{-}Hep}$ size, DLS measurements were performed (Figure IV-3. 3d) and three populations with different sizes were observed after Hep addition to LL-37, with apparent R_h around 10 nm, 100 nm and 1000 nm. No significant difference was observed neither according to the charge ratio ((-)/(+net) = 1.5 or 2) nor according to pH (3.5 or 5).

As expected, $PPCs_{LL\text{-}37\text{-}Hep}$ take an increasingly negative charge as Hep is further added. The (-)/(+net) charge ratio of 1.25-1.5 at the onset of the turbidimetry plateau can be related to the minimal amount of Hep vs LL-37 needed to displace the equilibrium towards $PPCs_{LL\text{-}37\text{-}Hep}$ formation. These data are consistent with the ones obtained for other systems such as $PPCs_{Lyz\text{-}PSS}$.[45,46,57] This suggests that, beyond a (-)/(+net) charge ratio of 1.25, the LL-37 charges are compensated by Hep and the $PPCs_{LL\text{-}37\text{-}Hep}$ take a core-corona structure with a neutral internal domain and negatively-charged Hep chains dangling outside, explaining zeta potential reversal.[58] The size and the polydispersity of $PPCs_{LL\text{-}37\text{-}Hep}$ suspension can be explained by the mechanism of PPCs formation proposed by Tsuboi *et al*.[59] First, upon addition of Hep to LL-37, the LL-37 molecules bind to Hep via Coulomb attraction, resulting in the formation of intrapolymer complexes, in which the Hep charges are balanced by LL-37 charges of the opposite sign. These intrapolymer complexes are neutral, and subsequently associate with one another to shape aggregates (AG_1). Further addition of Hep leads to an increase in the concentration of AG_1 (without a change in its size), and finally to the formation of larger aggregates (AG_2) formed through association of AG_1. The

formation of PPCs being a highly dynamic process, at a (-)/(+net) charge ratio of 1.5 and 2, the three forms would be present in the suspension, at different proportions. An excess of Hep can lead to complete redissolution of the PPCs.[50,60] In our case, the total redissolution is not reached, but more soluble PPCs are present at pH 3.5 than at pH 5, at a (-)/(+net) charge ratio of 1.5 and 2, as revealed by centrifugation. It can be explained by the pH-dependent behavior of the $PPCs_{LL\text{-}37\text{-}Hep}$ formation. At a given (-)/(+net) charge ratio, the Hep/LL-37 molar ratio is greater at pH 3.5 than at pH 5, which may explain the redissolution of $PPCs_{LL\text{-}37\text{-}Hep}$ at pH 3.5. Xu et *al.* demonstrated, for several proteins, that protein-Hep binding affinity, and thus PPCs formation, is a function of pH, I, and protein charge anisotropy.[61] They showed that this binding affinity is directly correlated to the strength of protein-Hep interaction, *i.e.*, the ability to lead to the formation of soluble complexes. This is consistent with our observations.[61]

Therefore, to obtain $PPCs_{LL\text{-}37\text{-}Hep}$ suitable for further LbL assembly, with a Hep-negatively charged crown sufficient to screen the LL-37 charge, $PPCs_{LL\text{-}37\text{-}Hep}$ must be formed at a (-)/(+net) charge ratio of 1.25-1.5 at both pH.

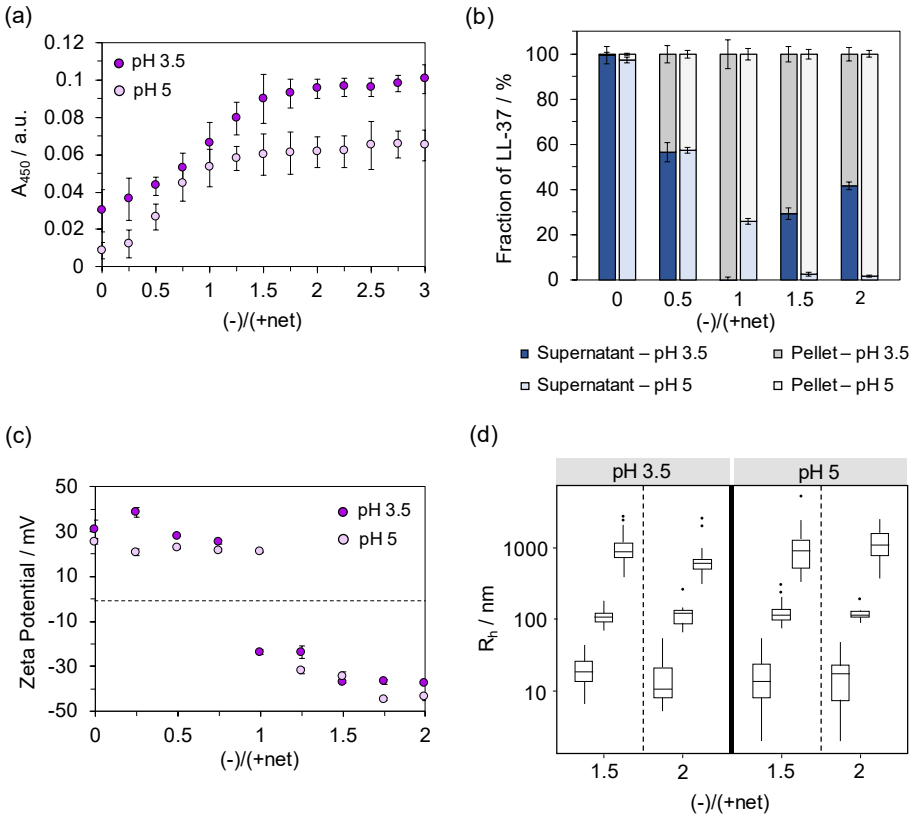

Figure IV-3. 3 – (a) Turbidimetry measurements of LL-37 undergoing Hep addition in such a way that (-)/(+net) charge ratio varies between 0 and 3. The dark and light blue circles represent the A_{450} values at, respectively, pH 3.5 and pH 5. Error bars represent the standard deviation (n=3). (b) Fraction of LL-37 assessed by BCA measurement in the pellet and in the supernatant, at pH 3.5 and 5, respectively, after PPCs centrifugation at 12,000 g. (c) Zeta potential measurements of LL-37 undergoing Hep addition in such a way that (-)/(+net) charge ratio varies between 0 and 2. The dark and light blue circles represent the values at pH 3.5 and pH 5, respectively. Error bars show the standard deviation (n=3). (d) Hydrodynamic radius (R_h) of PPCs at (-)/(+net) net charge ratio of 1.5 and 2 measured by DLS. Box plots show the R_h values for 30 measurements (n=10 and N=3).

3.3.2 Construction and properties of LL-37-containing multilayers monitored by QCM-D

With the goal to immobilize LL-37 at surface, negatively-charged $PPCs_{LL\text{-}37\text{-}Hep}$ were integrated into multilayers using the LbL assembly technique. In order

to assess the $PPCs_{LL\text{-}37\text{-}Hep}$ immobilization and to confirm that it is well governed by electrostatic interactions, $PPCs_{LL\text{-}37\text{-}Hep}$ with either a theoretical (-)/(+net) charge ratio of 0.5 ($PPCs_{LL\text{-}37\text{-}Hep}^{0.5}$) (used as a control), 1.5 ($PPCs_{LL\text{-}37\text{-}Hep}^{1.5}$) and 2 ($PPCs_{LL\text{-}37\text{-}Hep}^{2}$) were assembled with Chi as polycation to form three-compounds multilayers. As a matter of comparison, the LbL assembly of bare LL-37 with Hep and of Chi with Hep, *i.e.,* the classical two-compounds LbL assembly, was carried out. The multilayer growth was monitored by QCM-D at pH 3.5 and 5. The frequency and dissipation shifts of the 7th overtone ($\Delta f_7/7$ and ΔD_7) of the QCM-D sensors as a function of the adsorption steps are depicted in Figure IV-3. 4. For all experiments, an anchoring layer made of two bilayers of Chi and Hep ($[Chi\text{-}Hep]_2$) was first deposited to minimize the influence of the substrate and to favor further assembly (grey area in Figure IV-3. 4).[62] The adsorption of five bilayers of Chi-$PPCs_{LL\text{-}37\text{-}Hep}$ (at a theoretical (-)/(+net) charge ratio of 0.5, 1.5 and 2, $[Chi\text{-}PPCs_{LL\text{-}37\text{-}Hep}]_5$), five bilayers of LL-37-Hep ($[LL\text{-}37\text{-}Hep]_5$) or five bilayers of Chi-Hep ($[Chi\text{-}Hep]_5$) was then monitored.

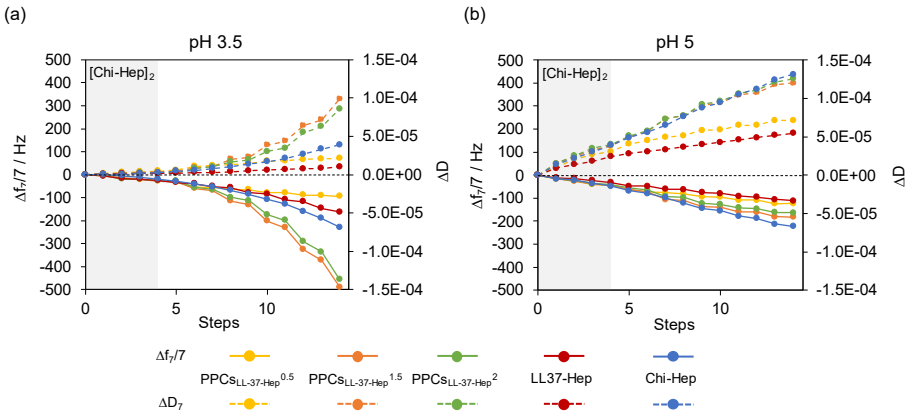

Figure IV-3. 4 – Evolution of the 7th overtone frequency and dissipation of a QCM-D gold sensor after adsorption of an anchoring layer of two Chi-Hep bilayers ($[Chi\text{-}Hep]_2$, grey area) followed by either Chi-$PPCs_{LL\text{-}37\text{-}Hep}$ with (-)/(+net)=0.5 ($[Chi\text{-}PPCs_{LL\text{-}37\text{-}Hep}^{0.5}]_5$, yellow), Chi-$PPCs_{LL\text{-}37\text{-}Hep}$ with (-)/(+net)=1.5 ($[Chi\text{-}PPCs_{LL\text{-}37\text{-}Hep}^{1.5}]_5$, orange), Chi-$PPCs_{LL\text{-}37\text{-}Hep}$ with (-)/(+net)=2 ($[Chi\text{-}PPCs_{LL\text{-}37\text{-}Hep}^{2}]_5$, green), $[LL\text{-}37\text{-}Hep]_5$ (red) and $[Chi\text{-}Hep]_5$ (blue) in ultrapure water at (a) pH 3.5 and (b) pH 5.

Regarding layers integrating $PPCs_{LL\text{-}37\text{-}Hep}^{0.5}$ at pH 3.5 and 5, the frequency shift is quite small after the adsorption of the five bilayers: 94 Hz and 123 Hz, at pH 3.5 and 5, respectively. As expected, the positively-charged $PPCs_{LL\text{-}37\text{-}}$

$_{Hep}^{0.5}$ cannot assemble through electrostatic interactions with Chi, which is also positively charged. The slight frequency shift could be explained by other forces, such as hydrophobic and van der Waals interactions, and hydrogen bonds. The classical LbL assembly that integrates LL-37, *i.e.*, $[LL\text{-}37\text{-}Hep]_5$, led to a final frequency shift of 162 Hz and 111 Hz, respectively, at pH 3.5 and 5. These low frequency shifts could be explained by the amphipathic character of LL-37 and thus its low adsorption. The difference between the two pH values can be attributed to the higher charge of LL-37 at pH 3.5 (+10.4) than at pH 5 (+7). As LL-37 is more charged, electrostatic interactions with Hep are favored, resulting in better multilayer growth. For LL-37-free assembly of Chi with Hep, *i.e.*, $[Chi\text{-}Hep]_5$, the frequency shift is 229 Hz at pH 3.5 and 222 Hz at pH 5. Despite a similar frequency shift after the adsorption of five bilayers, the construction profile appears to be different. At pH 3.5, the growth follows an exponential profile whereas it is linear at pH 5. Finally, for $PPCs_{LL\text{-}37\text{-}Hep}^{1.5}$ and $PPCs_{LL\text{-}37\text{-}Hep}^{2}$ assembled with Chi, the final frequency shift, after five bilayers, reaches ~470 Hz and ~170 Hz, respectively, at pH 3.5 and 5. It confirms that $PPCs_{LL\text{-}37\text{-}Hep}^{1.5}$ and $PPCs_{LL\text{-}37\text{-}Hep}^{2}$ are negatively charged, interact favorably with the positively-charged Chi and are successfully integrated within the multilayer systems. At pH 3.5, the frequency shift is three-fold higher for multilayers integrating $PPCs_{LL\text{-}37\text{-}Hep}^{1.5}$ and $PPCs_{LL\text{-}37\text{-}Hep}^{2}$ than for the $[LL\text{-}37\text{-}Hep]_5$ classical LbL. At pH 5, the frequency shift with $PPCs_{LL\text{-}37\text{-}Hep}^{1.5}$ and $PPCs_{LL\text{-}37\text{-}Hep}^{2}$ is much lower than at pH 3.5 and similar to the frequency shift with $[LL\text{-}37\text{-}Hep]_5$ at pH 5. It demonstrates that the adsorption profile is different for Hep-complexed vs bare LL-37, and that the multilayer architecture is also pH-dependent. Based on QCM-D analyses, it appears that the best adsorption of LL-37 at the surface occurs at pH 3.5 when it is integrated in multilayers from $PPCs_{LL\text{-}37\text{-}Hep}$ at a (-)/(+net) charge ratio of 1.5 or 2. However, these data do not allow to determine whether these frequency shifts are due to the adsorption of LL-37, Hep and/or Chi within the multilayers or even to the hydration state of these multilayers, which can influence their physical properties. Our previous data, based on X-ray photoelectron spectroscopy (XPS) experiments (see in *Part IV – Results and discussion – Chapter 2*), showed that there are proportionally fewer LL-37 at the surface of the $PPCs_{LL\text{-}37\text{-}Hep}$-based multilayers than at the surface of the bare LL-37-based multilayers. It suggests thus a higher hydration level for the $PPCs_{LL\text{-}37\text{-}Hep}$-based multilayers. Ellipsometry measurements were further

conducted to assess the dry thickness and subsequently, in combination with QCM-D data, to determine the multilayer hydration level. This approach aimed to validate the hypothesis of a higher hydration level in $PPCs_{LL\text{-}37\text{-}Hep}$-based multilayers (see *Part IV – 3.3.3 Film thickness and hydration level*).

QCM-D data interpretation allows to determine the physical nature of the films. By tracking the dissipation factor, it is possible to observe changes in energy dissipation that are related to the viscoelastic properties of the thin film. As already explained in the *Part IV – 3.2 Experimental section*, if the film can be approximated to be as rigid as the sensor, the Sauerbrey equation may be used to extract the areal mass density of the film.[53,54] Otherwise, a viscoelastic modeling, such as Johannsmann or Voinova modeling, should be used.[52,63,64] The $\Delta D_7/(-\Delta f_7/7)$ values were calculated for the different conditions and results are presented as a function of time in Figure IV-3. 5. For all conditions, the $\Delta D_7/(-\Delta f_7/7)$ values are slightly lower than 4×10^{-7} Hz^{-1} at pH 3.5, and higher at pH 5. The total mass adsorbed on the QCM-D sensors was calculated using both Sauerbrey and Voinova modeling at pH 3.5 and 5 in Figure IV-3. S1. In this way, we can compare the two models at both pH, and we can clearly note that the total mass adsorbed on the QCM-D sensors calculated using the Sauerbrey equation is closer to the one calculated using the Voinova modeling at pH 3.5 than at pH 5. This was expected according to the evolution of the $\Delta D_7/(-\Delta f_7/7)$ ratio, revealing more rigid layers at pH 3.5 compared to pH 5. It leads to assume that the use of Sauerbrey equation is more suitable at pH 3.5 than at pH 5. Overall, the total mass adsorbed on the surface is higher at pH 5. Finally, concerning the $PPCs_{LL\text{-}37\text{-}Hep}$ films, they are more viscoelastic than the LL-37-bare multilayers. In other words, more energy is dissipated in the PPCs-based multilayers and in the multilayers built at pH 5. The rigid/viscoelastic behavior of the Chi-$PPCs_{LL\text{-}37\text{-}Hep}$ films at pH 3.5 and 5, respectively, can be explained by Chi conformation. At pH 3.5, the ionization degree of Chi is high, the electrostatic repulsion between charged segments along the chain is stronger, leading to increased chain stiffness. The PE chains take a more extended configuration. At pH 5, and thus lower charge density, the Chi chains may exhibit more random ('loops and tails') configurations, which favor the water uptake, resulting in a more viscous behavior of the constructed layers.[65] This 'loop and tail'. Likewise, for the [LL-37-Hep] multilayers, the difference in the physical nature of the films could be explained by a higher water content in the films at pH 5 compared to pH

3.5. To clarify the hydration level of multilayers, the dissipation shift recorded by QCM can be further studied.

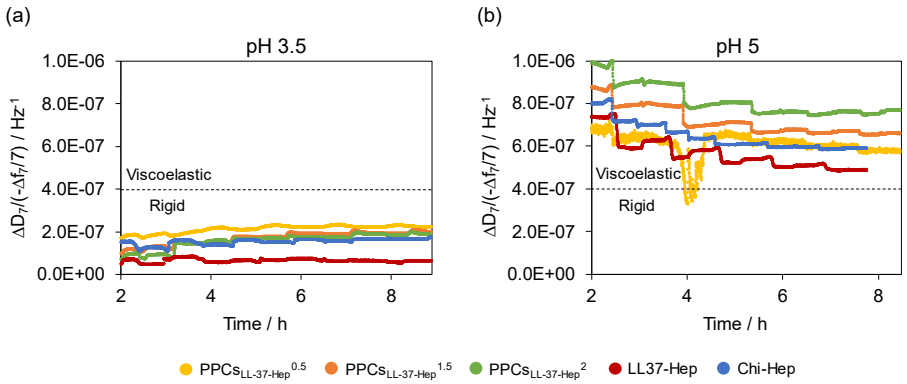

Figure IV-3. 5 – Evolution of the $\Delta D_7/(-\Delta f_7/7)$ ratio as a function of time of a QCM-D gold sensor during the adsorption of an anchoring layer of two Chi-Hep bilayers ($[Chi\text{-}Hep]_2$) followed by either Chi-$PPCs_{LL\text{-}37\text{-}Hep}$ with (-)/(+net)=0.5 ($[Chi\text{-}PPCs_{LL\text{-}37\text{-}Hep}^{0.5}]_5$, yellow), Chi-$PPCs_{LL\text{-}37\text{-}Hep}$ with (-)/(+net)=1.5 ($[Chi\text{-}PPCs_{LL\text{-}37\text{-}Hep}^{1.5}]_5$, orange), Chi-$PPCs_{LL\text{-}37\text{-}Hep}$ with (-)/(+net)=2 ($[Chi\text{-}PPCs_{LL\text{-}37\text{-}Hep}^{2}]_5$, green), $[LL\text{-}37\text{-}Hep]_5$ (red) and $[Chi\text{-}Hep]_5$ (blue), in ultrapure water at (a) pH 3.5 and (b) pH 5.

The dissipation (D) shift measured by QCM-D, after the adsorption of five bilayers are, respectively, 8.6×10^{-5}, 9.9×10^{-5}, 1.0×10^{-5} and 3.9×10^{-5} for $[Chi\text{-}PPCs_{LL\text{-}37\text{-}Hep}^{2}]_5$, $[Chi\text{-}PPCs_{LL\text{-}37\text{-}Hep}^{1.5}]_5$, $[LL\text{-}37\text{-}Hep]_5$, and $[Chi\text{-}Hep]_5$ at pH 3.5 (Figure IV-3. 4a). At pH 5, those D shifts are 1.3×10^{-4}, 1.2×10^{-4}, 5.5×10^{-5} and 1.3×10^{-4} for, respectively, $[Chi\text{-}PPCs_{LL\text{-}37\text{-}Hep}^{2}]_5$, $[Chi\text{-}PPCs_{LL\text{-}37\text{-}Hep}^{1.5}]_5$, $[LL\text{-}37\text{-}Hep]_5$, and $[Chi\text{-}Hep]_5$ (Figure IV-3. 4b). In general, an increase of the dissipation shift observed by QCM-D indicates a higher hydration level (percentage of water within the multilayer) or a multilayer that is softer. It thus could suggest that the hydration level of assemblies built with $PPCs_{LL\text{-}37\text{-}Hep}$ is higher than the ones built with bare LL-37 molecules. It would explain why the $PPCs_{LL\text{-}37\text{-}Hep}$ films are more viscoelastic than the ones built with bare LL-37. However, it is important to consider that the relationship between ΔD and the hydration level is influenced by environmental factors. Therefore, it is necessary to carefully analyze and interpret the ΔD in conjunction with other measurements and observations to draw meaningful conclusions about the hydration level. To do so, ellipsometry measurements were performed in dry conditions. By combining the information from both

techniques, complementary insights into the hydration level of the thin films may be obtained.

3.3.3 Film thickness and hydration level

Ellipsometry is a powerful technique for characterizing surfaces and thin film thickness. It assumes that the material being studied is homogeneous and that the layers are planar and uniform. In the case of thin layers, such as LbL films, there is often a discontinuity in the homogeneity. The analysis may thus be less accurate. Moreover, in this study, the multilayers are constructed from three different compounds. This introduces another uncertainty regarding the actual refractive index value of the layers. Therefore, ellipsometry measurements will give a general and comparative idea about the thickness of the multilayers. Indeed, a variation in the refractive index value will lead to a variation in the measured thickness of the layer. Figure IV-3. 6 depicts the LbL evolution of the film thickness ([Chi-Hep]$_2$-[LL-37-Hep]$_5$ and [Chi-Hep]$_2$-[Chi-PPCs$_{LL\text{-}37\text{-}Hep}^{1.5}$] at pH 3.5 and 5) considering a refractive index of 1.46 for the LbL film. This value was chosen based on the work of Lundin *et al.* who studied LbL assemblies of Chi and Hep.[55] The dry film thickness, after the adsorption of the anchoring layer and five bilayers, was, respectively, 2.5 and 7.2 nm for [LL-37-Hep]$_5$ at pH 3.5 and 5, and, respectively, 4.1 and 6.7 nm for [Chi-PPCs$_{LL\text{-}37\text{-}Hep}^{1.5}$]$_5$ at pH 3.5 and 5 (Figure IV-3. 6).

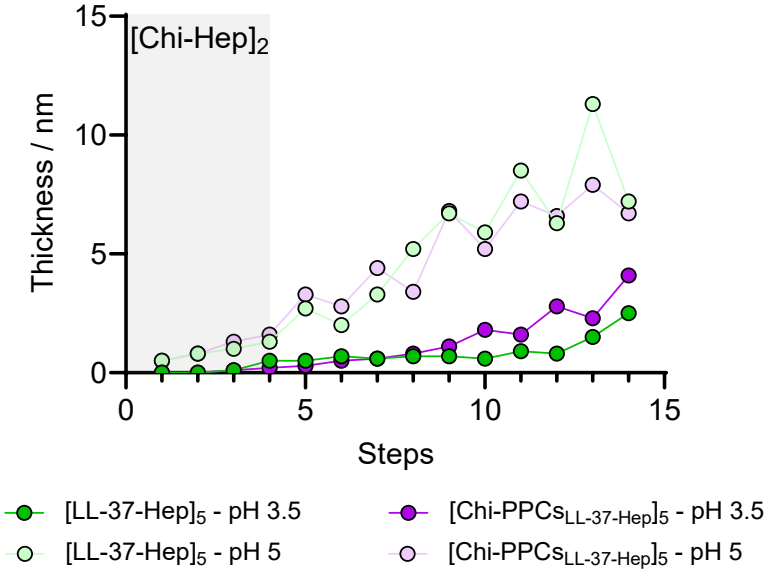

Figure IV-3. 6 – Evolution of the dry film thickness on Si wafers measured by ellipsometry. After the adsorption of an anchoring layer of two Chi-Hep bilayers ($[Chi\text{-}Hep]_2$, grey area), either five bilayers of Chi-$PPCs_{LL\text{-}37\text{-}Hep}$ with (-)/(+net)=1.5 ($[Chi\text{-}PPCs_{LL\text{-}37\text{-}Hep}{}^{1.5}]_5$) or LL-37-Hep ($[LL\text{-}37\text{-}Hep]_5$) were adsorbed in ultrapure water at pH 3.5 and 5. The films were dried with N_2 before the measurement.

It is noteworthy that the difference in dry thickness between classical LbL films and those integrating $PPCs_{LL\text{-}37\text{-}Hep}$ is less pronounced compared to mass disparities recorded with the QCM-D analysis. To highlight this, the wet thickness of the multilayer assemblies, derived from QCM-D measurements and assuming a film density of 1 (determined using the Voinova model, see Figure IV-3. S1), was compared with their dry thickness. Figure IV-3. 7 shows the wet and dry thicknesses after the construction of the anchoring layer and five bilayers of [LL-37-Hep] or [Chi-$PPCs_{LL\text{-}37\text{-}Hep}$], at pH 3.5 and 5. At pH 3.5, the film thickness determined by QCM-D for the $PPCs_{LL\text{-}37\text{-}Hep}$-based multilayer is 3.7 times greater compared to that for the bare LL-37-based multilayer, while ellipsometry measurements show only a 1.6-fold difference. Similarly, at pH 5, QCM-D measurements indicate that the film thickness for the $PPCs_{LL\text{-}37\text{-}Hep}$-based multilayer is 1.6 times greater than the one for bare LL-37 molecules, whereas ellipsometry results reveal a 1.1-fold decrease. This discrepancy is hypothesized to be attributed, at least in part, to the hydration level (relation between the wet film and the dry film) of the

multilayered films. All the films have a hydration level in the 91% to 97% range, confirming that the main constituent of multilayer assemblies is water. Comparatively, $PPCs_{LL\text{-}37\text{-}Hep}$ are more hydrated than the bare LL-37-based LbL assemblies. It is well known that a more hydrated environment improves protein activity, confirming the interest of these LbL assemblies. The differences between the viscoelastic properties of [LL-37-Hep] and [Chi-$PPCs_{LL\text{-}37\text{-}Hep}{}^{1.5}$] at pH 3.5 and pH 5 may thus be attributed to the hydration of the multilayers and the ionization degree of the compounds.

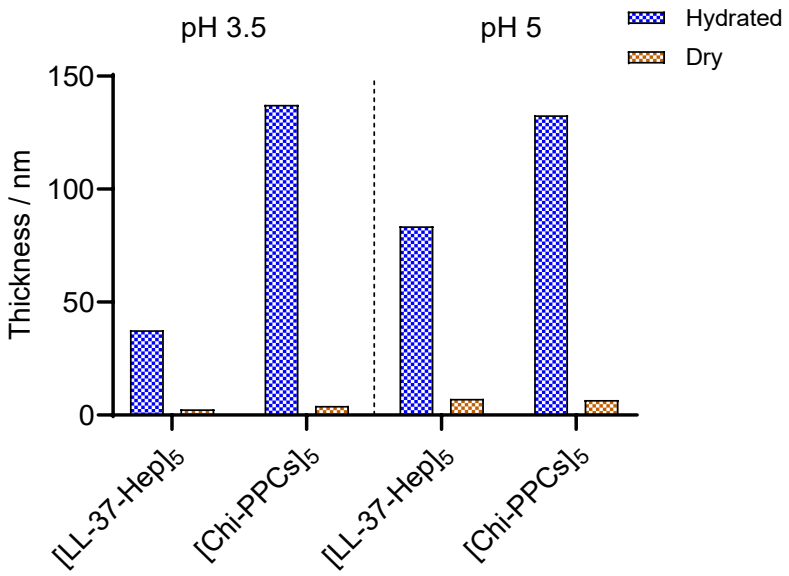

Figure IV-3. 7 – Thickness of wet and dry multilayer assemblies after the adsorption of the $[Chi\text{-}Hep]_2$ anchoring layer and five bilayers integrating bare LL-37 ($[LL\text{-}37\text{-}Hep]_5$) or $PPCs_{LL\text{-}37\text{-}Hep}$ ($[Chi\text{-}PPCs]_5$) at pH 3.5 and 5.

Basically, as well depicted in the literature, pH clearly influences the organization and architecture of multilayer assemblies.[66] The films are more viscoelastic at pH 5 than at pH 3.5. The hydrated mass/thickness of $PPCs_{LL\text{-}37\text{-}Hep}$-based multilayers is higher than the ones of bare LL-37 films, and thus the multilayers integrating the $PPCs_{LL\text{-}37\text{-}Hep}$ contain more water than the classical LbL systems. Importantly, even though a three-component system (Chi-$PPCs_{LL\text{-}37\text{-}Hep}$) is compared to a two-component system (LL-37-Hep), the observed differences in adsorbed mass and film viscosity underscore that distinct successive adsorption steps yield different states. This could suggest that equilibrium is not achieved, and that the environmental conditions and

assembly pathway have a major effect on the nanoarchitecture and organization of self-assembling multilayers.

QCM-D provides a global view of the multilayer hydrated mass but does not give any information on the amount of each compound of interest in the multilayers as it is not an identification method. It is impossible to confirm the presence of LL-37, Hep or Chi in the multilayer by only using this method. However, previous XPS analyses confirmed the presence of the three compounds in [Chi-$PPCs_{LL\text{-}37\text{-}Hep}$] systems, and of the two compounds in the [LL-37-Hep] systems (see in *Part IV – Results and discussion – Chapter 2*).

3.3.4 Global view of the multilayers' nanoarchitecture

Despite all the systems studied exhibit a hydration level exceeding 90%, indicating that water is the primary constituent of the multilayers, the results show that [LL-37-Hep] and [Chi-$PPCs_{LL\text{-}37\text{-}Hep}$] systems have different growth patterns, which enables different LbL coatings with well-controlled architecture and properties to be obtained. Interestingly, our findings demonstrated that assemblies constructed with $PPCs_{LL\text{-}37\text{-}Hep}$ exhibit higher hydration levels compared to those composed of bare LL-37 molecules. This increased hydration likely contributes to the higher viscoelasticity observed in $PPCs_{LL\text{-}37\text{-}Hep}$-based multilayers. Regarding the effect of the pH on the film properties, we highlighted that more rigid multilayers are formed at pH 3.5 compared to pH 5, due to the ionization degree of the species and the water content. Moreover, our previous findings, based on XPS analyses, demonstrated that a lower proportion of LL-37 was present at the surface of the $PPCs_{LL\text{-}37\text{-}Hep}$-based multilayers than at the surface of the bare LL-37-based multilayers (see in *Part IV – Results and discussion – Chapter 2*). Two hypotheses have been proposed to account for the lower proportion of LL-37 in the $PPCs_{LL\text{-}37\text{-}Hep}$ multilayers. The adsorption of Chi onto $PPCs_{LL\text{-}37\text{-}Hep}$ led to the release of some LL-37 molecules from the multilayer; or the immediate adsorption of Hep, excluding a part of LL-37, due to an instability of $PPCs_{LL37\text{-}Hep}$, upon adsorption on a Chi layer. These different characteristics are summarized in Figure IV-3. 8 which illustrates the different nano-architectures and organizations that could be obtained depending on the pH and the strategy of assembly.

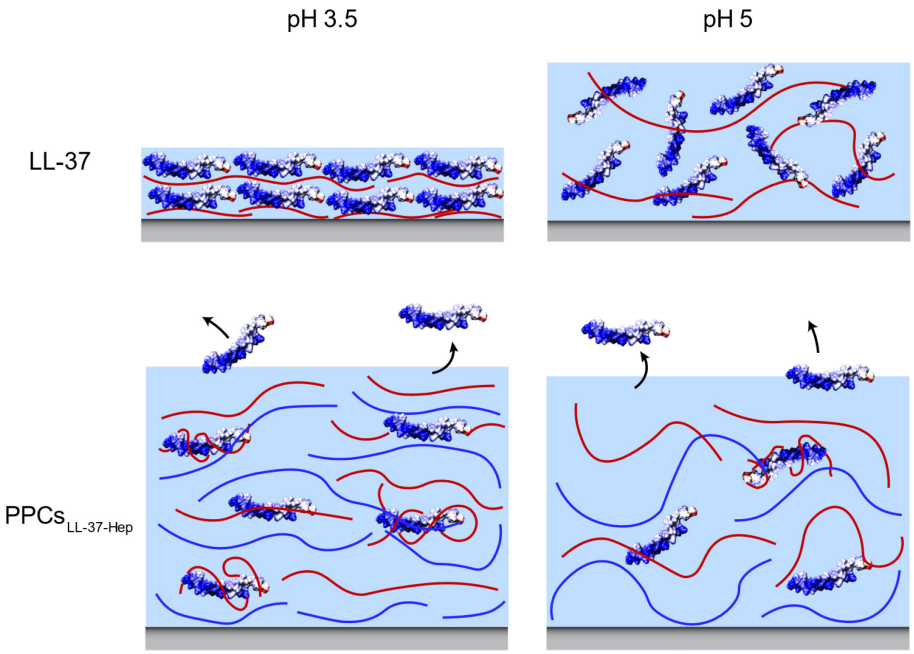

Figure IV-3. 8 – Schematic representation of the nanoarchitecture and organization of LL-37-based multilayers depending on the assembly strategy and pH.

3.4 Conclusion

In conclusion, [LL-37-Hep] and [Chi-PPCs$_{LL-37-Hep}$] multilayered films were constructed at pH 3.5 and 5. The data from this study, combined with previous XPS analysis results, indicate that varying viscoelastic properties, structural organization and architecture, and proportion of each compound are achieved depending on the multilayer assembly strategy and pH conditions. On the one hand, [Chi-PPCs$_{LL-37-Hep}$] multilayers are dynamic, thick, and highly hydrated films. On the other hand, [LL-37-Hep] multilayers are thinner but more stable and seem to integrate more LL-37 molecules. These films are also very hydrated but less than those immobilizing the PPCs$_{LL-37-Hep}$. Besides that, pH also plays a key role in the architecture of these films. Due to the more random 'loops and tails' configuration of the PEs and the LL-37's lower charge, multilayers are more viscoelastic at higher pH. It shows the importance of the path followed to immobilized molecules and the conditions in which they are assembled, allowing the construction of nanosystems featuring particular architectures which may, *in fine*, lead to

different functionalities. It thus provides a way to tune the hydration state of LbL assemblies depending on the field of interest, which is topical for biomedical applications.

3.5 Take-home messages

- $PPCs_{LL\text{-}37\text{-}Hep}$ are well formed with a Hep-negatively charged crown sufficient to screen the LL-37 charge at a theoretical (-)/(+net) charge ratio of 1.25-1.5 at pH 3.5 and 5. These $PPCs_{LL\text{-}37\text{-}Hep}$ can thus be immobilized with positively-charged Chi using the LbL technique.
- $PPCs_{LL\text{-}37\text{-}Hep}$-based multilayers have a higher hydration level than bare LL-37-based multilayers, which contributes to their higher viscoelastic character.
- More rigid multilayers are obtained at pH 3.5 compared to pH 5. This can be explained by the hydration of the multilayers and the ionization degree of the compounds.

In this *Chapter 3*, we showed that different nanoarchitectures and structural organizations could be achieved depending on the pH and the assembly approach. However, the analytical techniques used do not provide insight into the multilayer composition. The amount of LL-37 immobilized on the surface is not determined, which is a key factor for designing coatings intended to inhibit biofilm formation. Therefore, in the subsequent parts of this work, BCA analyses are performed to quantify the LL-37 content in the multilayers and to assess the kinetics of its release from these multilayers.

3.6 Supporting Information

3.6.1 Determination of the mass adsorbed on a QCM-D gold sensor using the Sauerbrey and the Voinova modeling

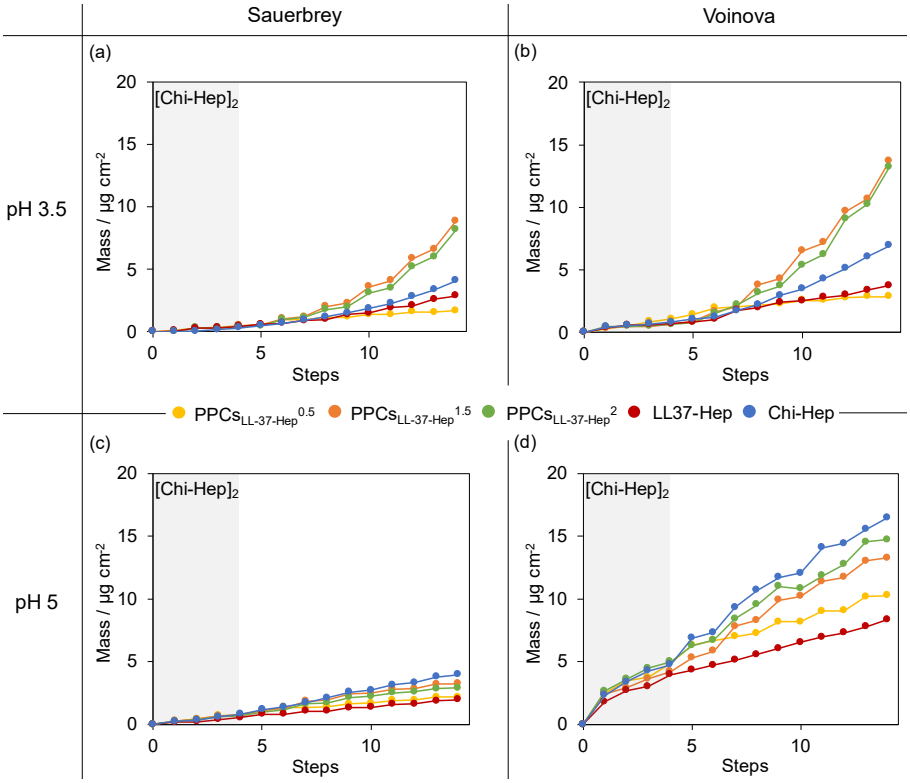

Figure IV-3. S1 – Evolution of the mass adsorbed on a QCM-D gold sensor after adsorption of an anchoring layer of two Chi-Hep bilayers ($[Chi\text{-}Hep]_2$, grey area) followed by either Chi-$PPCs_{LL\text{-}37\text{-}Hep}$ with (-)/(+net)=0.5 ($[Chi\text{-}PPCs_{LL\text{-}37\text{-}Hep}^{0.5}]_5$ (in yellow), Chi-$PPCs_{LL\text{-}37\text{-}Hep}$ with (-)/(+net)=1.5 ($[Chi\text{-}PPCs_{LL\text{-}37\text{-}Hep}^{1.5}]_5$ (in orange), Chi-$PPCs_{LL\text{-}37\text{-}Hep}$ with (-)/(+net)=2 ($[Chi\text{-}PPCs_{LL\text{-}37\text{-}Hep}^{2}]_5$ (in green), $[LL\text{-}37\text{-}Hep]_5$ (in red) and $[Chi\text{-}Hep]_5$ (in blue) (a) in ultrapure water at pH 3.5, using the Sauerbrey equation, (b) in ultrapure water at pH 3.5, using the Voinova modeling, (c) in ultrapure water at pH 5, using the Sauerbrey equation, and (d) in ultrapure water at pH 5, using the Voinova modeling.

3.7 References

1. Murray, C. J. *et al.* Global burden of bacterial antimicrobial resistance in 2019: a systematic analysis. *The Lancet* **399**, (2022).
2. World Health Organization. Antimicrobial Resistance: Global Report on Surveillance. (2014).
3. Guggenbichler, J. P., Assadian, O., Boeswald, M. & Kramer, A. Incidence and clinical implication of nosocomial infections associated with implantable biomaterials - catheters, ventilator-associated pneumonia, urinary tract infections. *GMS Krankenhaushygiene interdisziplin* **6**, (2011).
4. Mutschler, A. *et al.* Unexpected Bactericidal Activity of Poly(arginine)/Hyaluronan Nanolayered Coatings. *Chemistry of Materials* **28**, 8700–8709 (2016).
5. Geissel, F. J. *et al.* Antibiofilm activity of nanosilver coatings against *Staphylococcus aureus*. *J Colloid Interface Sci* **608**, 3141–3150 (2022).
6. Nazi, N., Marguier, A., Debiemme-Chouvy, C. & Humblot, V. Optimization and Antibacterial Response of N-Halamine Coatings Based on Polydopamine. *Colloids and Interfaces* **6**, 9 (2022).
7. Hancock, R. E. W. & Sahl, H. G. Antimicrobial and host-defense peptides as new anti-infective therapeutic strategies. *Nat Biotechnol* **24**, 1551–1557 (2006).
8. Chileveru, H. R. *et al.* Visualizing attack of *Escherichia coli* by the antimicrobial peptide human defensin 5. *Biochemistry* **54**, 1767–1777 (2015).
9. Malanovic, N. & Lohner, K. Antimicrobial Peptides Targeting Gram-Positive Bacteria. *Pharmaceuticals* **9**, 59 (2016).
10. He, M. *et al.* Cathelicidin-derived antimicrobial peptides inhibit Zika virus through direct inactivation and interferon pathway. *Front Immunol* **9**, 722 (2018).
11. Oard, S. V. & Enright, F. M. Expression of the antimicrobial peptides in plants to control phytopathogenic bacteria and fungi. *Plant Cell Rep* **25**, 561–572 (2006).
12. Tornesello, A. L., Borrelli, A., Buonaguro, L., Buonaguro, F. M. & Tornesello, M. L. Antimicrobial Peptides as Anticancer Agents:

Functional Properties and Biological Activities. *Molecules* **25**, 2850 (2020).

13. Hancock, R. E. W. & Lehrer, R. Cationic peptides: A new source of antibiotics. *Trends Biotechnol* **16**, 82–88 (1998).
14. Lande, R. *et al.* Plasmacytoid dendritic cells sense self-DNA coupled with antimicrobial peptide. *Nature* **449**, 564–569 (2007).
15. Pachón-Ibáñez, M. E., Smani, Y., Pachón, J. & Sánchez-Céspedes, J. Perspectives for clinical use of engineered human host defense antimicrobial peptides. *FEMS Microbiol Rev* **41**, 323–342 (2017).
16. Larrick, J. W. *et al.* Human CAP18: A novel antimicrobial lipopolysaccharide-binding protein. *Infect Immun* **63**, 1291–1297 (1995).
17. Johansson, J., Gudmundsson, G. H., Rottenberg, M. E., Berndt, K. D. & Agerberth, B. Conformation-dependent antibacterial activity of the naturally occurring human peptide LL-37. *Journal of Biological Chemistry* **273**, 3718–3724 (1998).
18. Sancho-Vaello, E. *et al.* The structure of the antimicrobial human cathelicidin LL-37 shows oligomerization and channel formation in the presence of membrane mimics. *Sci Rep* **10**, 17356 (2020).
19. Overhage, J. *et al.* Human host defense peptide LL-37 prevents bacterial biofilm formation. *Infect Immun* **76**, 4176–4182 (2008).
20. Dean, S. N., Bishop, B. M. & van Hoek, M. L. Natural and synthetic cathelicidin peptides with anti-microbial and anti-biofilm activity against Staphylococcus aureus. *BMC Microbiol* **11**, 114 (2011).
21. Niyonsaba, F. *et al.* A cathelicidin family of human antibacterial peptide LL-37 induces mast cell chemotaxis. *Immunology* **106**, 20–26 (2002).
22. Hemshekhar, M., Choi, K. Y. G. & Mookherjee, N. Host defense peptide LL-37-mediated chemoattractant properties, but not anti-inflammatory cytokine IL-1RA production, is selectively controlled by Cdc42 Rho GTPase via G protein-coupled receptors and JNK mitogen-activated protein kinase. *Front Immunol* **9**, 17 (2018).
23. Milhan, N. V. M. *et al.* The Antimicrobial Peptide LL-37 as a Possible Adjunct for the Proliferation and Differentiation of Dental Pulp Stem Cells. *J Endod* **43**, 2048–2053 (2017).

24. Ramos, R. *et al.* Wound healing activity of the human antimicrobial peptide LL37. *Peptides* **32**, 1469–1476 (2011).
25. Comune, M., Rai, A., Palma, P., TondaTuro, C. & Ferreira, L. Antimicrobial and pro-angiogenic properties of soluble and nanoparticle-immobilized LL37 peptides. *Biomater Sci* **9**, 8153–8159 (2021).
26. Song, D. W. *et al.* Multi-biofunction of antimicrobial peptide-immobilized silk fibroin nanofiber membrane: Implications for wound healing. *Acta Biomater* **39**, 146–155 (2016).
27. Kilsgård, O. *et al.* Peptidylarginine deiminases present in the airways during tobacco smoking and inflammation can citrullinate the host defense peptide LL-37, resulting in altered activities. *Am J Respir Cell Mol Biol* **46**, 240–248 (2012).
28. Oren, Z., Lerman, J. C., Gudmundsson, G. H., Agerberth, B. & Shai, Y. Structure and organization of the human antimicrobial peptide LL-37 in phospholipid membranes: Relevance to the molecular basis for its non-cell-selective activity. *Biochemical Journal* **341**, 501–513 (1999).
29. Turner, J., Cho, Y., Dinh, N. N., Waring, A. J. & Lehrer, R. I. Activities of LL-37, a cathelin-associated antimicrobial peptide of human neutrophils. *Antimicrob Agents Chemother* **42**, 2206–2214 (1998).
30. Geitani, R., Ayoub Moubareck, C., Touqui, L. & Karam Sarkis, D. Cationic antimicrobial peptides: Alternatives and/or adjuvants to antibiotics active against methicillin-resistant *Staphylococcus aureus* and multidrug-resistant *Pseudomonas aeruginosa*. *BMC Microbiol* **19**, 12 (2019).
31. Friberg, C. *et al.* Human antimicrobial peptide, LL-37, induces non-inheritable reduced susceptibility to vancomycin in *Staphylococcus aureus*. *Sci Rep* **10**, 8 (2020).
32. Rapsch, K., Bier, F. F., Tadros, M. & Von Nickisch-Rosenegk, M. Identification of antimicrobial peptides and immobilization strategy suitable for a covalent surface coating with biocompatible properties. *Bioconjug Chem* **25**, 308–319 (2014).
33. Ye, H. *et al.* Regulation of MSC and macrophage functions in bone healing by peptide LL-37-loaded silk fibroin nanoparticles on a titanium surface. *Biomater Sci* **7**, 5492–5505 (2019).

34. Gabriel, M., Nazmi, K., Veerman, E. C., NieuwAmerongen, A. V & Zentner, A. Preparation of LL-37-grafted titanium surfaces with bactericidal activity. *Bioconjug Chem* **17**, 548–550 (2006).
35. Chereddy, K. K. *et al.* PLGA nanoparticles loaded with host defense peptide LL37 promote wound healing. *Journal of Controlled Release* **194**, 138–147 (2014).
36. Riool, M. *et al.* Controlled Release of LL-37-Derived Synthetic Antimicrobial and Anti-Biofilm Peptides SAAP-145 and SAAP-276 Prevents Experimental Biomaterial-Associated *Staphylococcus aureus* Infection. *Adv Funct Mater* **27**, 11 (2017).
37. Cassin, M. E., Ford, A. J., Orbach, S. M., Saverot, S. E. & Rajagopalan, P. The design of antimicrobial LL37-modified collagen-hyaluronic acid detachable multilayers. *Acta Biomater* **40**, 119–129 (2016).
38. Quemé-Peña, M. *et al.* Old Polyanionic Drug Suramin Suppresses Detrimental Cytotoxicity of the Host Defense Peptide LL-37. *ACS Pharmacol Transl Sci* **4**, 155–167 (2021).
39. Yoshida, K. *et al.* Heparin–LL 37 complexes are less cytotoxic for human dental pulp cells and have undiminished antimicrobial and LPS -neutralizing abilities. *Int Endod J* **52**, 1327–1343 (2019).
40. Gilliet, M. & Lande, R. Antimicrobial peptides and self-DNA in autoimmune skin inflammation. *Curr Opin Immunol* **20**, 401–407 (2008).
41. Vranckx, C. *et al.* Layer-by-Layer Nanoarchitectonics Using Protein-Polyelectrolyte Complexes toward a Generalizable Tool for Protein Surface Immobilization. *Langmuir* **38**, 5579–5589 (2022).
42. Decher, G. & Hong, J. D. Buildup of Ultrathin Multilayer Films by a Self-Assembly Process: II. Consecutive Adsorption of Anionic and Cationic Bipolar Amphiphiles and Polyelectrolytes on Charged Surfaces. *Berichte der Bunsengesellschaft für physikalische Chemie* **95**, 1430–1434 (1991).
43. Hammond, P. T. Recent explorations in electrostatic multilayer thin film assembly. *Curr Opin Colloid Interface Sci* **4**, 430–442 (1999).
44. Silva, R. A., Urzúa, M. D., Petri, D. F. S. & Dubin, P. L. Protein adsorption onto polyelectrolyte layers: Effects of protein hydrophobicity and charge anisotropy. *Langmuir* **26**, 14032–14038 (2010).

45. vander Straeten, A. *et al.* Protein–polyelectrolyte complexes to improve the biological activity of proteins in layer-by-layer assemblies. *Nanoscale* **9**, 17186–17192 (2017).
46. vander Straeten, A., Bratek-Skicki, A., Jonas, A. M., Fustin, C.-A. & Dupont-Gillain, C. Integrating Proteins in Layer-by-Layer Assemblies Independently of their Electrical Charge. *ACS Nano* **12**, 8372–8381 (2018).
47. Domard, A. pH and c.d. measurements on a fully deacetylated chitosan: application to CuII—polymer interactions. *Int J Biol Macromol* **9**, 98–104 (1987).
48. Wang, C. H. *et al.* Procoagulant and antimicrobial effects of chitosan in wound healing. *Int J Mol Sci* **22**, 7067 (2021).
49. Dolinsky, T. J., Nielsen, J. E., McCammon, J. A. & Baker, N. A. PDB2PQR: An automated pipeline for the setup of Poisson-Boltzmann electrostatics calculations. *Nucleic Acids Res* **32**, 665–667 (2004).
50. Kayitmazer, A. B., Seeman, D., Minsky, B. B., Dubin, P. L. & Xu, Y. Protein-polyelectrolyte interactions. *Soft Matter* **9**, 2553–2583 (2013).
51. Brown W. Dynamic Light Scattering: The method and some applications. (Clarendon, Oxford, 1993).
52. Voinova, M. V, Rodahl, M., Jonson, M. & Kasemo, B. Viscoelastic Acoustic Response of Layered Polymer Films at Fluid-Solid Interfaces: Continuum Mechanics Approach. *Phys Scr* **59**, 391–396 (1999).
53. Reviakine, I., Johannsmann, D. & Richter, R. P. Hearing What You Cannot See and Visualizing What You Hear. *Anal Chem* **83**, 8838–8848 (2011).
54. Sauerbrey, G. Verwendung von Schwingquarzen zur Wägung dünner Schichten und zur Mikrowägung. *Zeitschrift für Physik* **155**, 206–222 (1959).
55. Lundin, M., Solaqa, F., Thormann, E., Macakova, L. & Blomberg, E. Layer-by-Layer Assemblies of Chitosan and Heparin: Effect of Solution Ionic Strength and pH. *Langmuir* **27**, 7537–7548 (2011).
56. Pettersen, E. F. *et al.* UCSF Chimera - A visualization system for exploratory research and analysis. *J Comput Chem* **25**, 1605–1612 (2004).

57. Štajner, L., Požar, J. & Kovačević, D. Complexation between lysozyme and sodium poly(styrenesulfonate): The effect of pH, reactant concentration and titration direction. *Colloids Surf A Physicochem Eng Asp* **483**, 171–180 (2015).
58. Cousin, F., Gummel, J., Combet, S. & Boué, F. The model Lysozyme-PSSNa system for electrostatic complexation: Similarities and differences with complex coacervation. *Adv Colloid Interface Sci* **167**, 71–84 (2011).
59. Tsuboi, A. *et al.* Complexation of proteins with a strong polyanion in an aqueous salt-free system. *Langmuir* **12**, 6295–6303 (1996).
60. Cooper, C. L., Dubin, P. L., Kayitmazer, A. B. & Turksen, S. Polyelectrolyte–protein complexes. *Curr Opin Colloid Interface Sci* **10**, 52–78 (2005).
61. Xu, Y. *et al.* Effect of heparin on protein aggregation: Inhibition versus promotion. *Biomacromolecules* **13**, 1642–1651 (2012).
62. Lvov, Y. & Mohwald, H. Protein Architecture: Interfacing Molecular Assemblies and Immobilization Biotechnology. (CRC Press, 1999).
63. Johannsmann, D. Viscoelastic analysis of organic thin films on quartz resonators. *Macromol. Chem. Phys* **200**, 501–516 (1999).
64. Johannsmann, D. Viscoelastic, mechanical, and dielectric measurements on complex samples with the quartz crystal microbalance. *Physical Chemistry Chemical Physics* **10**, 4516–4534 (2008).
65. Rojas, O. J., Ernstsson, M., Neuman, R. D. & Claesson, P. M. Effect of polyelectrolyte charge density on the adsorption and desorption behavior on mica. *Langmuir* **18**, 1604–1612 (2002).
66. vander Straeten, A., Lefèvre, D., Demoustier-Champagne, S. & Dupont-Gillain, C. Protein-based polyelectrolyte multilayers. *Adv Colloid Interface Sci* **280**, 102161 (2020).

4 Development of layer-by-layer coatings for antibacterial applications: loading and release of LL-37

Cédric Vranckx[1*], Clément Guibert[2], Noémie de Suraÿ[1], Coralie Nerincx[1], Olivier Cornu[3,4], and Christine Dupont-Gillain[1*]

[1]Institute of Condensed Matter and Nanosciences, Bio-and Soft Matter, Université catholique de Louvain, Place Louis Pasteur, 1 bte L4.01.10, B-1348 Louvain-la-Neuve, Belgium

[2]Laboratoire de Réactivité de Surface (LRS), Sorbonne Université, CNRS, Paris, F-75005, France

[3]Neuro-Musculo-Skeletal Pole, Experimental and Clinical Research Institute, Université catholique de Louvain, 1200 Brussels, Belgium

[4]Orthopaedic and Trauma Department, Cliniques Universitaires Saint-Luc, Université catholique de Louvain, 1200 Brussels, Belgium

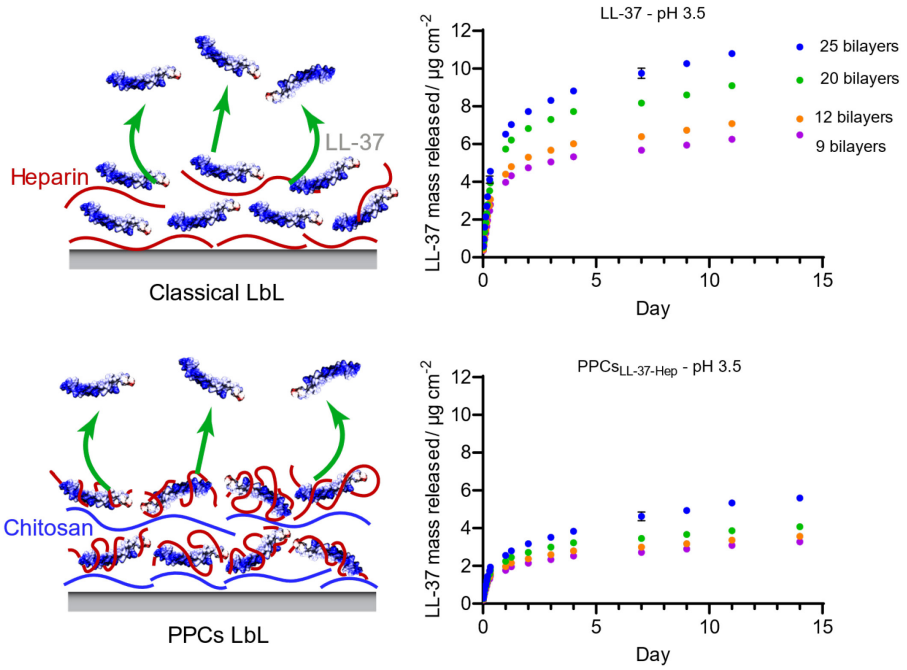

Abstract

This chapter explores the conformational, the adsorption behavior and the release kinetics of LL-37 immobilized into multilayers using the layer-by-layer (LbL) self-assembly technique. LL-37 was immobilized using two strategies. First, bare LL-37 was assembled with heparin (Hep) to design [LL-37-Hep] multilayers. Second, it was complexed with Hep to form peptide-polyelectrolyte complexes ($PPCs_{LL\text{-}37\text{-}Hep}$), which were then assembled with chitosan (Chi) into [Chi-$PPCs_{LL\text{-}37\text{-}Hep}$] multilayers. Before its adsorption into the multilayers, the conformation of LL-37 was study depending on its bare or complexed nature. Circular dichroism measurements highlighted that LL-37 adopts an α-helix conformation when complexed with Hep in water, unlike its random coil conformation under its bare form. Despite the charge homogenization of LL-37 through $PPCs_{LL\text{-}37\text{-}Hep}$ formation to facilitate its LbL assembly, our results demonstrate that the amount of LL-37 incorporated into the multilayers is 4 times higher when assembled in its bare form compared to its $PPCs_{LL\text{-}37\text{-}Hep}$ form. The $[LL\text{-}37\text{-}Hep]_{25}$ film built at pH 3.5 immobilize up to 20 µg cm^{-2} of LL-37. From this 20 µg cm^{-2} immobilized, release kinetics in PBS show an initial burst release of 6.5 µg cm^{-2} in 24 hours, followed by a gradual release of 4.5 µg cm^{-2} over 13 days. Therefore, after 14 days, 45% of the LL-37 still remains immobilized within the $[LL\text{-}37\text{-}Hep]_{25}$ multilayer. Interestingly, this percentage is dependent on the number of bilayers in the multilayers and the LbL assembly strategy. These findings suggest that such self-assemblies are promising for antimicrobial delivery systems, offering both immediate and sustained effects, thereby enhancing the potential of its antibacterial coatings.

4.1 Introduction

With the increasing issues of infections caused by antibiotic-resistant pathogens,[1,2] antimicrobial peptides (AMPs) are currently viewed as an interesting alternative due to their broad-spectrum antimicrobial activity and low resistance.[3] In the realm of biomaterials, preventing bacterial adhesion, and thus biofilm formation, is essential to avoid contamination of biomedical devices. Devices such as contact lenses, catheters and implants are commonly affected by bacterial contamination. Therefore, strategies that inhibit harmful bacteria from adhering to these materials are crucial for mitigating long-term health complications and high healthcare costs. To tackle this problem, an increasing number of studies are dedicated to developing antimicrobial coatings to enhance the performance of biomaterials.[4–6]

AMPs play a crucial role in the innate immunity system and are often referred to as natural antibiotics. Among them, LL-37 is the only human cathelicidin-derived AMP.[7] LL-37 is a cationic and amphipathic peptide, composed of 37 amino acids, and has a molecular weight of 4.5 kDa. This small positively-charged peptide (+6 under physiological conditions) may take an α-helical conformation, depending on its concentration, pH, and ionic strength (I).[8] It is present in the innate immune system as a first-line defense agent against bacteria, fungi, and viral pathogens.[9] Importantly, LL-37 exhibits a conformation-dependent antimicrobial activity. To play its antimicrobial role, LL-37 must take an α-helical conformation to interact with bacterial membranes. Sancho-Vaello *et al.* studied the interaction between the LL-37 and the bacterial cell wall, *in vitro* and in the presence of membrane-mimicking detergents and lipids, to propose a mechanistic model.[10] Basically, due to its cationic character, the LL-37 interacts electrostatically with bacteria, integrates into membranes as conducting channels, perforating them and finally leading to the breakdown of the transmembrane potential and thus to the bacterial death. An antibiofilm activity of LL-37 was also shown against *P. aeruginosa*, *S. aureus*, and *S. epidermidis*.[11–14] LL-37 also exerts different immunomodulatory functions such as modulation of pro-inflammatory response, chemotaxis, influence on cell proliferation and differentiation, promotion of wound healing and angiogenesis, etc.[7,9] Interestingly, Sancho-Vaello *et al.* also demonstrated that the effect of LL-37

on the cell wall was time and concentration dependent.[10] In blood plasma, LL-37 is secreted at physiological concentration around 0.2-0.4 µM (1-2 µg mL^{-1}), and up to 25 µM in the presence of infectious pathogens.[15] Data showed that LL-37 displayed eukaryotic cytotoxicity occurring at 13-25 µM *in vitro*.[8] Usually, the effect of an antimicrobial drug is determined using the minimum inhibitory concentration (MIC) measurement. This value is strongly related to the experimental conditions under which the analyses are performed, such as the culture medium, the presence of serum, etc., and to the bacteria strains. Values from 0.1 µM to more than 56 µM of LL-37 were reported for Gram-positive and -negative bacteria.[16–19]

Given that a certain degree of cytotoxicity could be induced by local high-concentration administration of LL-37, some studies have been directed towards immobilizing LL-37 on biomaterial surfaces. Nevertheless, achieving functional layers remains challenging. The C-terminal tail seems to play an essential role in the antibacterial activity of LL-37. Therefore, in case of chemical grafting, it is crucial to preserve this region to maintain the antibacterial character of LL-37.[20] Cassin *et al.* studied detachable polyelectrolyte multilayers (PEMs) composed of collagen and hyaluronic acid, which were modified with LL-37.[21] LL-37 was immobilized to the surface of these multilayers either by physical adsorption or by chemical immobilization using carbodiimide chemistry. Following the adsorption of LL-37, both the physically adsorbed and chemically immobilized group exhibited similar reduction in bacterial adhesion on the surface, which has been related to the amount of immobilized LL-37. The release of LL-37 from physisorbed multilayers was nearly up to 60% within 48h period. This prevented bacteria, present in the broth, from adhering to the multilayers.[21] Gomes *et al.* built PEM films using chitosan (Chi) and alginate over cotton gauzes, to load Cys-LC-LL-37.[22] They integrated about 8 µg mL^{-1} of Cys-LC-LL-37 in the multilayers, and showed that a burst released is obtained during the first 6h, followed by a stage of continuous decrease in release rate during the next 18h. After 24h, about 25% of the absorbed Cys-LC-LL-37 still remained in the functionalized cotton gauze. This burst release, within the few first hours, allows to eliminate a high number of bacteria that are present at the beginning of the infection.[23] Indeed, they demonstrated a reduction of more than 4log in the growth of *S. aureus* and *K. pneumoniae* bacteria, after 24h.[22]

Therefore, with the goal to prevent bacterial attachment on the surface of biomedical devices, it seems crucial to design multilayers incorporating enough LL-37 that can be released over a long period of time, to kill both bacteria in the early stages of infection and opportunistic pathogens beyond this period. Therefore, based on strategies that we already developed in our previous works; we designed multilayers integrating LL-37 using the layer-by-layer (LbL) self-assembly technique. LbL is a versatile bottom-up method based on alternate adsorption of positively- and negatively-charged compounds. Due to the surface charge reversal at each adsorption step, the process is self-limiting and highly repeatable.[24] The assembling procedure can be performed in mild aqueous medium and does not require chemically harsh conditions. In addition, the LbL structures are less densely packed than those of Langmuir-Blodgett films,[25,26] which is advantageous for diffusion-drive release of drugs through the films,[27] which is very interesting in our case for the release of LL-37 molecules. Due to the polyampholyte character and charge anisotropy of LL-37, its LbL assembly could be challenging.[28] To address this challenge, peptide-polyelectrolyte complexes (PPCs) have been introduced as building blocks for the LbL assembly of proteins and peptides.[29–31]

The same strategies as in our previous studies were followed. In brief, LL-37 was first complexed with heparin (Hep) to form $PPCs_{LL\text{-}37\text{-}Hep}$. These $PPCs_{LL\text{-}37\text{-}Hep}$, which have a negative surface charge, due to the negatively-charged Hep chains dangling outside, were LbL assembled at pH 3.5 and 5 with Chi, which is positively charged at a pH below its pK_a value, approximately 6.5,[32] to obtain [Chi-$PPCs_{LL\text{-}37\text{-}Hep}$] multilayers. As a matter of comparison, LL-37 was immobilized using the classical method, *i.e.*, bare LL-37 assembled with Hep, to design [LL-37-Hep] multilayers. In both cases, the amount of LL-37 absorbed onto the surface and subsequently released into the medium, *i.e.*, the phosphate-buffered saline (PBS), have been determined. Moreover, before its adsorption on surface, the LL-37 conformation was monitored by circular dichroism (CD) analyses. Since the secondary structure of LL-37 depends on the experimental conditions, CD analyses should be performed in the same medium as the one used for bacterial experiments. However, these media are rich in proteins and other compounds that screen the LL-37 signal. Consequently, CD analyses were carried out in the same medium that the one used for the release kinetics analyses, the PBS, which simulates a

bacterial medium. In addition, the conformational changes of LL-37 due to complexation by Hep were also investigated using CD analyses.

4.2 Experimental section

4.2.1 Materials

Chi, M_W = 10,000-50,000 g mol^{-1} and deacetylation degree (DD) of 95% was purchased from Heppe Medical Chitosan Gmbh (Halle, Germany). Chi is not soluble in ultrapure water. Therefore, Chi solution was prepared by first dissolving 50 mg of Chi in approximately 25 mL of ultrapure water and 60 µL of HCl 37% (VWR, Leuven, Belgium) at 60°C for 1 h. Then, pH was adjusted to a value of 3.5 or 5 with NaOH 10 M (Sigma Aldrich, Steinheim, Germany) and the volume was brought to exactly 100 mL. Finally, the Chi solution was filtered with successively 5 and 0.2 µm filters to remove small impurities and non-dissolved particles. Hep sodium salt, 5 000 I.E./mL, was obtained from B.Braun (Melsungen, Germany). LL-37, 98.05% pure (peptide sequence: LLGDFFRKSKEKIGKEFKRIVQRIKDFLRNLVPRTES, theoretical molecular mass of 4493.26 Da), was bought from Proteogenix (Schiltigheim, France). Hep and LL-37 solutions were prepared at I ≈ 0 mM, in ultrapure water (Elga Purelab Chorus 1, 18.2 MΩ.cm, Veolia, United Kingdom), with only the ions necessary for pH adjustment (3.5 or 5 with NaOH 10 M or HCl 37%). For Chi solution, as Chi must be dissolved in acidic conditions, I cannot be equal to 0 mM. I was kept as low as possible, with only the ions necessary for Chi dissolution and pH adjustment, and is around 10 mM. The pH value was measured using a pH-indicator strip (MQuant, Merck, Darmstadt, Germany).

4.2.2 Formation of $PPCs_{LL\text{-}37\text{-}Hep}$

Since electrostatic interactions drive $PPCs_{LL\text{-}37\text{-}Hep}$ formation, the polyelectrolyte (PE)-to-peptide molar ratio used to prepare the complexes is usually expressed as the PE-to-peptide charge ratio. The charge ratio was calculated as the ratio of PE net charge to the peptide net structural charge at pH 3.5 and 5. Due to its sulfonate groups, Hep was considered as fully negatively charged (4 negative charges per Hep repeating unit). LL-37 charge was computed, as a function of pH, based on its amino acid sequence and structure (PDB file: 2K6O), using the PDB2PQR Server.[33] The LL-37 net charge

is +10.4 and +7 at, respectively, pH 3.5 and 5. For example, $PPCs_{LL\text{-}37\text{-}Hep}$ at a (-)/(+net) charge ratio of 1.5 were prepared by mixing 3 volumes of Hep solution at 0.5 mM negative charge with 10 volumes of LL-37 solution at 0.1 mM net positive charge. Therefore, the LL-37 and Hep concentrations in $PPCs_{LL\text{-}37\text{-}Hep}$ with a charge ratio of 1.5, are, respectively, 0.08 and 0.12 mM positive and negative net charge. This constitutes a theoretical charge ratio, and taking into account the fact that part of the Hep and LL-37 molecules could remain free, the actual charge ratio of the formed $PPCs_{LL\text{-}37\text{-}Hep}$ may differ from this theoretical ratio.

4.2.3 Circular dichroism spectroscopy

Far-UV CD spectroscopy is a valuable technique for characterizing protein secondary structures.[34] CD spectra were recorded with a Jasco J-815 spectrometer equipped with a Peltier temperature controller from 200 to 260 nm in ultrapure pure water (pH 3.5 and 5), ethanol (99%) and PBS (GibcoTM). The following solutions were used: Chi (0.5 g L^{-1}), Hep (0.5 g L^{-1}), LL-37 (0.08 mM positive net charge, at both pH), and $PPCs_{LL\text{-}37\text{-}Hep}$ (0.08 mM positive net charge of LL-37 at both pH, and 64 µg mL^{-1} of Hep). The sample chamber was purged with nitrogen at a flow rate of about 3 L min^{-1}. All spectra were acquired at 25°C in a quartz cell with 2 mm path length at a scan rate of 50 nm min^{-1}, with a 1 nm bandwidth and a 2 s data integration time (D.I.T.). The spectrum of the solvent used, *i.e.*, ultrapure water, ethanol (99%), or PBS was subtracted for all experiments.

4.2.4 Multilayer construction

Multilayers were constructed in 96-well polystyrene Cellstar® plates (Greiner Bio-One, Kremsmünster, Austria) by successive adsorption steps, with all steps performed either at pH 3.5 or 5. For all experiments, an anchoring layer (AL) of two bilayers of Chi alternately adsorbed with Hep ($[Chi\text{-}Hep]_2$) was constructed from Chi and Hep solutions (0.5 g L^{-1}). Then, two different multilayer systems were built on this anchoring layer: bare LL-37 molecules directly assembled with Hep ([LL-37-Hep]), and $PPCs_{LL\text{-}37\text{-}Hep}$ assembled with Chi ($[Chi\text{-}PPCs_{LL\text{-}37\text{-}Hep}]$). The following solutions were used: Chi (0.5 g L^{-1}), Hep (0.5 g L^{-1}), LL-37 and fluorescein isothiocyanate-marked LL-37 (FITC-LL-37)

(0.08 mM positive net charge, at both pH), as well as suspensions of $PPCs_{LL-37-Hep}$ and $PPCs_{FITC-LL-37-Hep}$ prepared as described in *Part IV – 4.2.2 Formation of $PPCs_{LL-37-Hep}$*. Each adsorption step, that lasted for 20 min, was carried out in static conditions with 100 µL of solution, and was followed by three consecutive rinsing steps with ultrapure water adjusted at pH 3.5 or 5.

4.2.5 Quantification of LL-37 in the multilayers using the bicinchoninic acid assay

Multilayers were constructed in 96-well polystyrene Cellstar® plates. After the adsorption of the $[Chi-Hep]_2$ anchoring layer, 1, 3, 5, 6, 9, 10, 12, 15, 20 or 25 bilayers of [LL-37-Hep] or $[Chi-PPCs_{LL-37-Hep}]$ were constructed at pH 3.5 and 5. The amount of LL-37 within the LbL assemblies was assessed by bicinchoninic acid assay (BCA, ThermoFisher Scientific, Waltham, MA, USA). 20 µL of sodium dodecyl sulfate (SDS, 1%, Merck, Darmstadt, Germany) was added to solubilize LL-37 molecules from multilayers before quantification. The working reagent (200 µL, reagent A:reagent B, 50:1, v:v) was then added and incubated 60 min at 60°C. The absorbance was measured at 562 nm (A_{562}) using a multi-mode microplate reader (SpectraMaxiD3, Molecular Device, USA). LL-37 amount was determined based on a calibration curve obtained with known LL-37 amounts. The high pH of the BCA buffer and the presence of SDS cause complete LL-37 and Chi deprotonation, which results in the complete dissolution of the film. Indeed, following a first BCA assay, a second one was conducted in the same wells, which yielded no measurable signal, suggesting the film had fully dissolved. In this work, the limit of quantification (LOQ) was calculated as ten times the standard deviation of the blank (raw data), which corresponds to a confidence level of 90%, and then transformed in micrograms using the calibration curves.[35]

4.2.6 Quantification of FITC-LL-37 in the multilayers by fluorescence

Multilayers were constructed in 96-well polystyrene Cellstar® plates. After the adsorption of the $[Chi-Hep]_2$ anchoring layer, 9, 12, 20 or 25 bilayers of [FITC-LL-37-Hep] or $[Chi-PPCs_{FITC-LL-37-Hep}]$ were constructed at pH 3.5 and 5. The amount of LL-37 within the LbL assemblies was thus assessed by recording the fluorescence of FITC-LL-37. Due to quenching, a direct

quantification of the immobilized amount of FITC-LL-37 in the multilayers was not possible (Figure IV-4. S1). Therefore, multilayers must be solubilized to allow FITC-LL-37 quantification. To do so, BCA reagent was used as solubilizing agent, and not for quantification purposes. 20 µL of SDS 1% and 200 µL of BCA working reagent were added and incubated 60 min at 60 °C to solubilize FITC-LL-37 molecules from multilayers. 200 µL were transferred in a 96-well polystyrene black Fluotrac™ plate (Greiner Bio-One, Kremsmünster, Austria). The fluorescence was measured with an excitation wavelength of 490 nm and an emission wavelength of 525 nm, using the multi-mode microplate reader. LL-37 amount was determined based on a calibration curve obtained with known LL-37 amounts.

4.2.7 Study of LL-37 release profile from the multilayers using FITC-LL-37

Multilayers were constructed in 96-well polystyrene Cellstar® plates. After the adsorption of the $[Chi\text{-}Hep]_2$ anchoring layer, 9, 12, 20 or 25 bilayers of [FITC-LL-37-Hep] or $[Chi\text{-}PPCs_{FITC\text{-}LL\text{-}37\text{-}Hep}]$ were constructed at pH 3.5 and 5. To study the LL-37 release profile, the coated wells were immersed in 250 µL of PBS. The space between wells was filled with water to saturate the air in water and avoid excessive evaporation from the wells. The plates were sealed with parafilm and left under agitation at 150 rpm and 37°C. The LL-37 released from the multilayers was evaluated after 30 min, 1, 2, 3, 4, 5, 7, 8, 24, and 30h, 2, 3, 4, 7, 9, 11, and 14 days. After each time interval, the total volume of each well was collected and transferred in Eppendorf tubes (Eppendorf Belgium, Aarschot, Belgium). One tube was used per condition. Tubes were stored at -25°C for future quantification. The emptied wells were refilled with 250 µL of PBS and plates were put back at 37°C under agitation. After the 14 days of release, 200 µL of each Eppendorf tube were transferred in a 96-well polystyrene black Fluotrac™ plate. The fluorescence was measured with an excitation wavelength of 490 nm and an emission wavelength of 525 nm, using the multi-mode microplate reader. LL-37 amount was determined based on a calibration curve obtained with known LL-37 amounts.

4.3 Results and discussion

$PPCs_{LL\text{-}37\text{-}Hep}$ were formed in ultrapure water at pH 3.5 and 5 by adding Hep to LL-37. The addition of Hep to LL-37 solution was expressed through the negative-to-positive (-)/(+net) charge ratio, termed as the theoretical charge ratio. In our previous work, we demonstrated, by turbidimetry measurements, that $PPCs_{LL\text{-}37\text{-}Hep}$ are effectively formed at a (-)/(+net) charge ratio of 1.25-1.5 (see *Part IV – Results and discussion – Chapter 3*). Beyond this value, the LL-37 charges are compensated by Hep and the $PPCs_{LL\text{-}37\text{-}Hep}$ take a core-corona structure with a neutral internal domain and negatively-charged Hep chains dangling outside. Therefore, to obtain $PPCs_{LL\text{-}37\text{-}Hep}$ suitable for further LbL assembly, with a Hep-negatively charged crown, sufficient to screen the LL-37 charge, $PPCs_{LL\text{-}37\text{-}Hep}$ must be formed at a (-)/(+net) charge ratio of 1.25-1.5 at 3.5 and 5.

4.3.1 Study of LL-37 conformation by circular dichroism spectroscopy

Since LL-37 exhibits a conformation-dependent antibacterial activity, CD measurements were first performed to assess the bare LL-37 conformation in ultrapure water and PBS and to monitor structural changes upon complexation with Hep.[8] CD spectra, *i.e.*, the ellipticity as a function of wavelength, were recorded for LL-37 and $PPCs_{LL\text{-}37\text{-}Hep}$ solutions in ultrapure water at pH 3.5 and 5, and in PBS, as illustrated in Figure IV-4. 1. First, the CD spectra of Hep and Chi were monitored and show no signal. Second, the CD spectrum of bare LL-37 was recorded in a solvent that promotes α-helix formation, *i.e.*, ethanol.[36] It shows the characteristic negative bands of α-helix at 208 and 222 nm.[34] The positive band, usually obtained at 193 nm for α-helical conformations, is not shown since measurements under 200 nm are not interpretable in ethanol and PBS (data not shown). With respect to LL-37 in ultrapure water at both pH, the CD spectra reveal a profile typical of disordered proteins, suggesting that bare LL-37 is in a random coil conformation, in agreement with previous findings.[8,34,37] In contrast with this observation for bare LL-37, the two negative bands of α-helixes, at 208 and 222 nm, are present for $PPCs_{LL\text{-}37\text{-}Hep}$ in ultrapure water. It suggests that LL-37 takes an α-helical conformation when it is complexed with Hep. This noteworthy feature, leading to structural

rearrangements, has previously been documented for LL-37-alginate mixtures, as well as for apocytochrome c complexed with poly(isobutylene-alt-maleic acid) and poly(1-tetradecene-alt-maleic acid).[38,39] It was suggested that the electrostatic and hydrophobic interactions between the peptide and the polyelectrolyte result in the exclusion of water molecules, thereby promoting the formation of hydrogen bonds conducive to the α-helical structure.

Importantly, previous studies have established that the α-helical conformation of LL-37 is anion-, pH-, I-, and concentration-dependent.[8,38,40] Therefore, CD measurements were performed at the same concentrations in LL-37 and Hep as for the quantification and release studies. Since the environmental conditions play a key role in the LL-37 conformation, CD measurements should be performed in physiological media to mimic the *in vivo* conditions as closely as possible. Pavani *et al.* reveal that efficacy of protein stabilization depends on type and concentration of buffer used.[41] With the goal to study the *in vitro* antimicrobial activity of LL-37, its conformation should be recorded in media typically used in bacterial experiments, *i.e.*, Mueller-Hinton broth (MHB), Roswell Park Memorial Institute (RPMI) medium, tryptic soy broth (TSB), etc. However, those media are complex in terms of composition. Subsequently, CD analysis in such media is impossible since the LL-37 signal would be embedded in those of all other proteins and compounds present in the medium. Therefore, to mimic bacterial analysis conditions, experiments were performed in PBS (pH 7.4 and I = 150 mM). In contrast with the observation in ultrapure water, bare LL-37 in PBS takes an α-helical conformation. That highlights that peptide conformation is pH-, I-, and composition-dependent. Furthermore, it illustrates the important role of PBS on stability of LL-37, and thus promoting the α-helical conformation, as previously demonstrated for lysozyme, stem bromelain, hemoglobin, and human serum albumin.[41] It should be emphasized that the conformation of $PPCs_{LL\text{-}37\text{-}Hep}$ in PBS was not investigated, considering the differing I and its potential impact on $PPCs_{LL\text{-}37\text{-}Hep}$ formation.

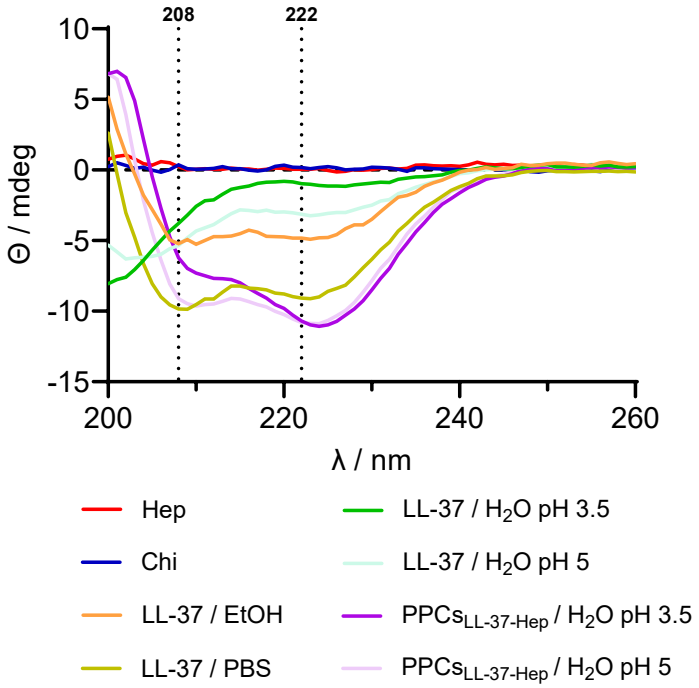

Figure IV-4. 1 – CD spectra obtained for bare LL-37 in ethanol (99%), ultrapure water at pH 3.5 and 5, and PBS and for $PPCs_{LL\text{-}37\text{-}Hep}$ at a (-)/(+net) = 1.5 suspended in ultrapure water at pH 3.5 and 5.

4.3.2 Quantification of LL-37 in the multilayers

Since LL-37 exhibits an amount-dependent antibacterial activity, BCA assays were performed to assess the amount of LL-37 immobilized in the multilayers. For the [Chi-$PPCs_{LL\text{-}37\text{-}Hep}$] multilayers, Chi interferes with the BCA assay due to the presence of an amide bond in its acetylated monomer residues (Figure IV-4. S2). To measure the extent of this interference, the BCA assay was calibrated using pure LL-37 and Chi solutions as presented in Figure IV-4. S3. It appears that, although only 5% of the Chi monomers are acetylated, Chi interferes with the BCA assay. The BCA assay selectivity coefficient for LL-37 in presence of Chi is 90%. This selectivity coefficient represents the ratio of responses at a specific mass (at a given mass, the LL-37 response divided by the Chi response equals 10, which means that if there are ten times, in terms of mass, as many Chi as LL-37 in the film, the same response will be obtained for both BCA assays). Note that Hep does not interfere in the BCA response. Since the BCA assay has a lower sensitivity to

Chi than LL-37, it has been assumed that most of the signal provided by the BCA assay is due to the presence of LL-37 in the multilayers and that the interference of Chi can be neglected. However, in our previous work, based on X-ray photoelectron spectroscopy (XPS) analyses (see *Part IV – Results and discussion – Chapter 2*), we clearly demonstrated that Chi is well immobilized at the surface of the [Chi-$PPCs_{LL\text{-}37\text{-}Hep}$]-based multilayers, which means that the LL-37 mass determined by BCA corresponds to the maximal amount of LL-37 that could be immobilized.

The quantity of LL-37 in the multilayered systems as a function of the number of bilayers has been investigated at pH 3.5 and 5 and the results are presented in terms of mass per cm² in Figure IV-4. 2. The dashed line corresponds to the LOQ of LL-37, which is equal to 0.7 µg cm^{-2}. Regarding the multilayers built at pH 3.5 (Figure IV-4. 2a), the amount of immobilized LL-37 increases as the number of bilayers increases. However, the mass growth profile of $PPCs_{LL\text{-}37\text{-}Hep}$-based multilayers is different from the one of LL-37-based multilayers. $PPCs_{LL\text{-}37\text{-}Hep}$-based multilayers grow linearly while LL-37-based multilayers tend to grow toward an exponential regime. Therefore, after 25 bilayers, the LL-37-based multilayer incorporates 19.7 ± 1.5 µg cm^{-2} of LL-37, *i.e.*, three times more than the $PPCs_{LL\text{-}37\text{-}Hep}$-based multilayer (6.3 ± 2.1 µg cm^{-2}). This exponential growth may be explained by the diffusion of species within the growing film, which act as a reservoir.[42,43] LL-37 molecules can diffuse throughout the multilayer down into the substrate after each new LL-37 adsorption step. Then, when the surface is in contact with the Hep solution, LL-37 diffuse toward the surface of the film. Since the LL-37 reaches the outer layer of the multilayer, it interacts with the incoming Hep, forming a new layer of [LL-37-Hep]. Hence, the amount of this new layer is proportional to the amount of LL-37 that diffuses out of the film during the buildup step. Thus, this regime not only involves a superposition of the two species, but also an 'in and out' diffusion process.[44] Concerning the films built at pH 5 (Figure IV-4. 2b), the mass growth profile for the two multilayer types is quite different from those at pH 3.5. For the $PPCs_{LL\text{-}37\text{-}Hep}$-based multilayers, almost no LL-37 is integrated into the films. For the bare LL-37-based films, the growth regime appears to be linear regarding the mass of adsorbed LL-37 until about 12 bilayers. Then, the amount of immobilized LL-37 seems to reach a plateau, suggesting that there is a saturation of LL-37 incorporation into the multilayers. After 25 bilayers, 1.1 ± 0.6 µg cm^{-2} of LL-37 are

integrated into the $PPCs_{LL\text{-}37\text{-}Hep}$-based multilayer, while 5.4 ± 2.1 µg cm^{-2} in the bare LL-37-based multilayer, *i.e.*, five times more. Gand *et al.* also observed a saturating growth profile during the LbL assembly of poly(L-lysine) with fibronectin.[45] They suggested that the suppression of the film assembly was due to a lack of surface charge reversal.[45] In our case, after 12 bilayers, we can hypothesize that the surface charge no longer modified by exposure to the polyion solutions, and thus the film growth seems terminated.

By comparing the results according to the pH, after 25 bilayers, more LL-37 is integrated in the multilayers at pH 3.5 than at pH 5. For the $PPCs_{LL\text{-}37\text{-}Hep}$-based films, that can be explained by the charge density. At pH 3.5, Chi is fully charged, while at pH 5, 4% of the amine groups are not protonated.[46] The higher charge density of Chi at pH 3.5 results in a stronger attraction of the $PPCs_{LL\text{-}37\text{-}Hep}$, leading to higher amount of LL-37 adsorbed per layer. For the bare LL-37-based multilayers, since Hep is considered to be fully charged at both pH, the difference in the amount of LL-37 immobilized may be explained by the higher charge density of LL-37 at pH 3.5 (+10.4) than at pH 5 (+7).[33] Since LL-37 is more charged, the electrostatic interactions are stronger, and thus more LL-37 can be adsorbed. This highlights the well-known importance of pH in the LbL film construction.

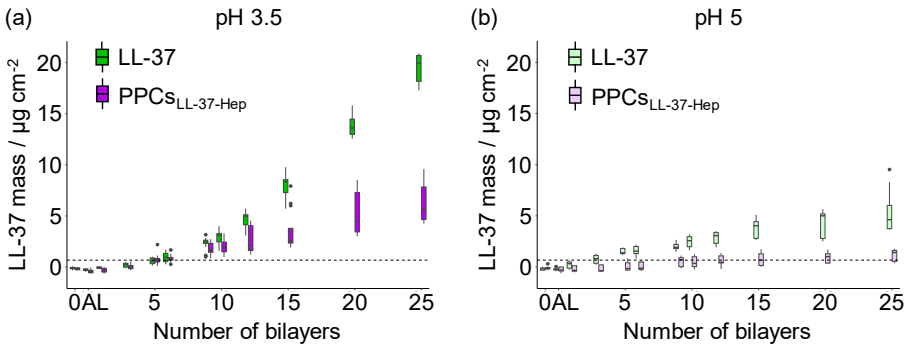

Figure IV-4. 2 – LL-37 mass immobilized on a $[Chi\text{-}Hep]_2$ anchoring layer, in a polystyrene well, after the adsorption of 1 to 25 bilayers of [LL-37-Hep] or [Chi-$PPCs_{LL\text{-}37\text{-}Hep}$] at (a) pH 3.5 and (b) pH 5. Box plots are presented for n=3 and N=4. Outliers were detected by Dixon's test.

Interestingly, it appears that the mass of LL-37 adsorbed in its bare form in the films is three to five times higher than in its $PPCs_{LL\text{-}37\text{-}Hep}$ form. Contrary to

what has been observed in previous studies with lysozyme,[47,48] $PPCs_{LL\text{-}37\text{-}Hep}$ formation, and thus homogenization of the LL-37 charge with Hep, does not increase the amount of LL-37 adsorbed on the surface. This difference between lysozyme- and LL-37-based multilayers could be found in the LL-37 structure. While lysozyme keeps a compact globular structure in ultrapure water,[49–51] LL-37 is a long chain with a disordered structure (Figure IV-4. 1). The complexation and thus, the homogenization of charge density of proteins/peptides by a counter-polyelectrolyte seems more appropriate in the case of globular proteins. Moreover, LbL assemblies are not stable, meaning that a permanent reorganization takes place within the multilayer. The addition of Chi as a third film component can disturb LL-37-Hep interactions. Indeed, in our previous work, based on XPS measurements (see *Part IV – Results and discussion – Chapter 2*), we already demonstrated that part of LL-37 may not be integrated in the film as it can be displaced by electrostatic interactions between Hep and Chi. The experimental results obtained from $PPCs_{LL\text{-}37\text{-}Hep}$, in this study, appear to support this trend. Moreover, vander Straeten *et al.* also demonstrated that once PPCs are incorporated into a bilayer, they do not retain their complexed form as a reorganization takes place.[52]

Therefore, bare LL-37-based multilayers built at pH 3.5 seem to be the most suitable design, in terms of adsorbed quantity. However, a larger immobilized amount of LL-37 does not guarantee better antimicrobial activity of the multilayer. It is of paramount importance that the peptide maintains its α-helix conformation. Moreover, the ability of LL-37 to be kept in the film or to be released will also affect the antimicrobial properties. Therefore, the LL-37 release profile has been studied in PBS. This medium is used because it provides physiological conditions and confers an α-helix conformation to LL-37 (Figure IV-4. 1). Due to the low amount of released LL-37, the BCA assay is not sufficiently sensitive to allow a study of release kinetics (LOQ = 0.7 $\mu g\ cm^{-2}$). Therefore, FITC-LL-37 was immobilized, and the release kinetics was monitored by fluorescence spectroscopy.

First, the quantity of LL-37 in the multilayered systems as a function of the number of bilayers has been investigated by fluorescence at pH 3.5 and 5, using a FITC-LL-37 calibration curve (Figure IV-4. S4) and the results are presented in terms of mass per cm^2 in Figure IV-4. 3. Interestingly, the quantity of FITC-LL-37 immobilized in the multilayers (Figure IV-4. 3) fits well

with the quantity of unlabeled LL-37 immobilized (Figure IV-4. 2), except for the following conditions: $[LL\text{-}37\text{-}Hep]_{9 \text{ and } 12}$ at both pH and $[Chi\text{-}PPCs_{LL\text{-}37\text{-}Hep}]_{20 \text{ and } 25}$ at pH 5. The difference could be explained by the hydrophobic and π-π stacking interactions that could occur between the aromatic groups of FITC moieties of LL-37 molecules, which could result in slightly greater adsorption of LL-37 when labeled.

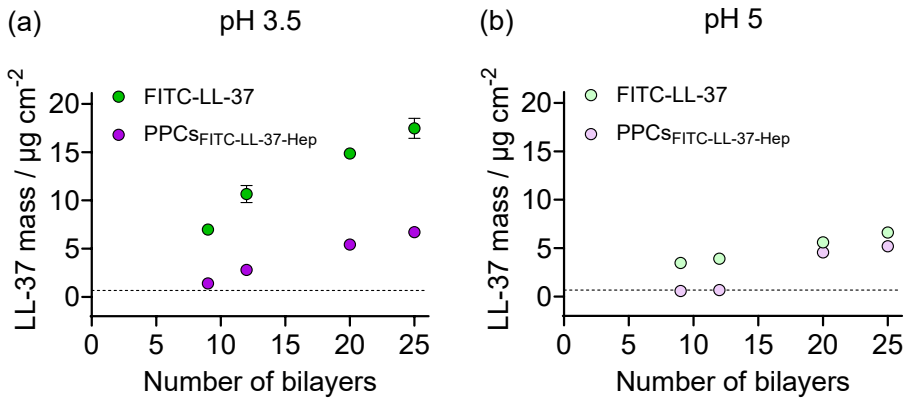

Figure IV-4. 3 – LL-37 mass immobilized on a $[Chi\text{-}Hep]_2$ anchoring layer, in a polystyrene well, after the adsorption of 9, 12, 20, or 25 bilayers of [FITC-LL-37-Hep] or $[Chi\text{-}PPCs_{FITC\text{-}LL\text{-}37\text{-}Hep}]$ at (a) pH 3.5 and (b) pH 5. Error bars show the standard deviation (n=3).

4.3.3 Study of LL-37 release profile from the multilayers using FITC-LL-37

The cumulative mass of released LL-37 has been investigated at pH 3.5 and 5 as a function of time and number of bilayers, using a FITC-LL-37 calibration curve in PBS (Figure IV-4. S5). The results are shown in Figure IV-4. S6. Whatever the assembly strategy and pH value, the cumulative amount of LL-37 released increases as the number of bilayers increases. This goes hand in hand with the amount of LL-37 immobilized in the multilayers (Figure IV-4. 3). The more layers deposited, the more LL-37 integrated in the film, and thus the more LL-37 released. It is worth noting that conducting this release profile experiment in a more representative culture medium, such as RPMI, rather than PBS, would provide additional insights.

While the released amount is quantified, it does not provide insight into the amount of LL-37 that remains integrated within the multilayers and that is thus not released. To do so, the remain LL-37 in the multilayers was

quantified and therefore the LL-37 cumulative percentage release was calculated. This LL-37 cumulative percentage release is related to the cumulative mass of released LL-37 for the [FITC-LL-37-Hep] and [Chi-$PPCs_{FITC\text{-}LL\text{-}37\text{-}Hep}$] multilayers integrating 25 bilayers at pH 3.5 and 5. Results are depicted in Figure IV-4. 4. The results for the multilayers integrating 9, 12, and 20 bilayers are shown in Figure IV-4. S7-S9. It appears that the release profile is divided in two regimes. A burst release is observed within the first 24h. Interestingly, less than 50% of the LL-37 immobilized is prone to burst release. Then, from day 1 to 14, a more gradual release follows. The advantage that the coated surface may offer through the release of LL-37 thus occurs during the first few hours to weeks. The results are promising, with the aim of developing implant-medical coatings with an antibacterial effect. It is of great interest to design coatings with burst release as the likelihood of bacterial contamination is the highest in the first few hours following surgery. However, burst release may miss the bactericidal time window for opportunistic pathogens. To avoid this, our coatings allow to ensure a long-term release beyond 14 days. Indeed, the $[LL\text{-}37\text{-}Hep]_{25}$ multilayer, which integrates the highest quantity of LL-37, released 11.1 µg cm^{-2} of LL-37 after 14 days. This accounts for only 54% of the total amount incorporated into the multilayer (Figure IV-4. 4a), which demonstrates that the coating is not depleted of its LL-37 content after the 14 days.

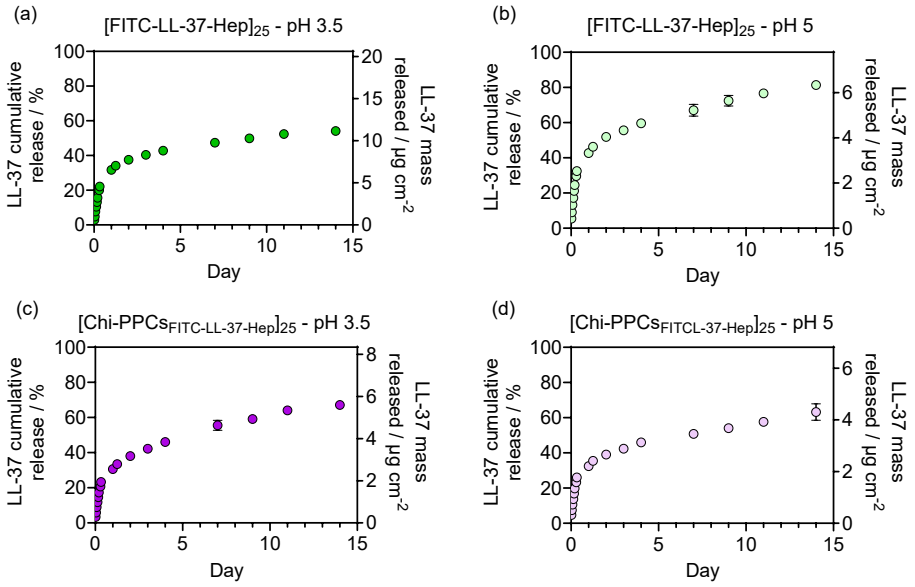

Figure IV-4. 4 – LL-37 release profile from $[Chi\text{-}Hep]_2$-$[FITC\text{-}LL\text{-}37\text{-}Hep]_{25}$ at (a) pH 3.5 and (b) pH 5 and $[Chi\text{-}Hep]_2$-$[Chi\text{-}PPCs_{FITC\text{-}LL\text{-}37\text{-}Hep}]_{25}$ at (c) pH 3.5 and (d) pH 5 coated polystyrene wells after 30 min, 1, 2, 3, 4, 5, 7, 8, 24, 30h, 2, 3, 4, 7, 9, 11 and 14 days. Error bars show the standard deviation (n=3).

The LL-37 content released and remaining after 14 days in the multilayers containing 9, 12, 20 and 25 bilayers are expressed in Figure IV-4. 5. A mass balance has been performed to determine whether the sum of the released and residual mass is equal to the integrated mass, which was determined in Figure IV-4. 3, and that is represented as the total mass in Figure IV-4. 5. In general, this mass balance is respected.

It can be noticed that the mass of LL-37 remaining in the multilayers is greater at pH 3.5 and a high number of bilayers than at pH 5 and a small number of bilayers. It can be pointed out that for bare LL-37-based multilayers, pH has a significant impact on the remaining amount of LL-37 (Figure IV-4. 5a-b). For [LL-37-Hep] multilayers at pH 5, only 15-20% of their LL-37 content remain after 14 days, regardless of the number of bilayers. For constructions at pH 3.5, the number of bilayers seems to play a role in percentage of LL-37 remaining, with a range between 30 and 45%. This difference could be explained by the organization of the films. The multilayers at pH 3.5 are more rigid and compact leading to more stable coatings (see *Part IV – Results and discussion – Chapter 3*). Consequently, in addition to immobilizing and

releasing more LL-37, the release of LL-37 from [LL-37-Hep] multilayers at pH 3.5 takes place over a longer period of time, and all the more so as the number of bilayers increases. This is a very promising result since even after 14 days the coating still contains LL-37. Cassin *et al*. physisorbed LL-37 on collagen/hyaluronic acid PEMs and studied the LL-37 release profile. After 4 days, all the LL-37 was released.[21] Regarding the $PPCs_{LL\text{-}37\text{-}Hep}$-based multilayers, the pH appears to have less impact on the percentage of LL-37 remaining in the assemblies (Figure IV-4. 5c-d). It could be explained by a reorganization of the films. The pH of release (7.4) is above the pKa of Chi (6.5). Hence, no matter the pH of the multilayer assembly, Chi becomes neutral, leading to a destabilization, a reorganization of the system, and thus a release of LL-37. In addition, the percentage of LL-37 released after 24h highlights the intensity of burst release. For all multilayers, this percentage is approximately half the total percentage released after 14 days.

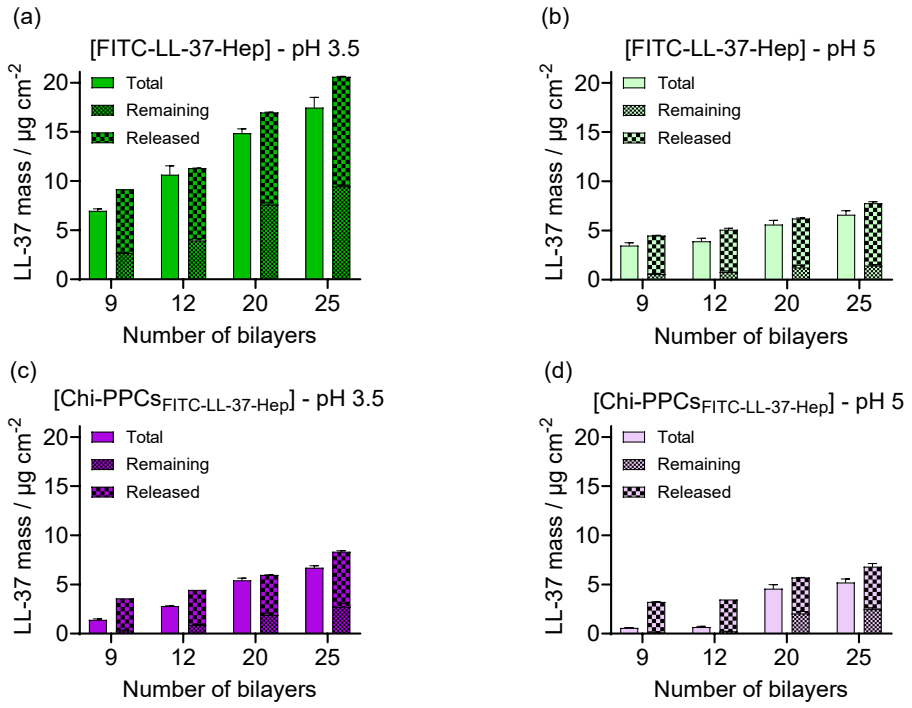

Figure IV-4. 5 – Amount of LL-37 released from and remaining in $[Chi\text{-}Hep]_2$-$[LL\text{-}37\text{-}Hep]_{9,\ 12,\ 20,\ or\ 25}$ multilayers at (a) pH 3.5 and (b) pH 5, and $[Chi\text{-}Hep]_2$-$[Chi\text{-}PPCs_{LL\text{-}37\text{-}Hep}]_{9,\ 12,\ 20,\ or\ 25}$ multilayers at (c) pH 3.5 and (d) pH 5 after 14 days in PBS solution. Error bars show the standard deviation (n=3). The comparison with the total mass integrated (Figure IV-4. 3) allows to carry out a mass balance.

With the goal to design antimicrobial coatings and thus to deal with medical implant-related infections issue, it seems critical to immobilize LL-37 molecules that could be released in the surrounding environment. The interest of LbL immobilization of bare LL-37 with Hep at pH 3.5 is twofold. First, it facilitates the immobilization of significant amounts of LL-37, forming a pool of active molecules, particularly with increasing bilayer numbers. Second, the release unfolds in two stages: an initial burst release lasting 24h, followed by a continuous release spanning over 14 days, ensuring a sustained effect over an extended period of time.

4.4 Conclusion

We have established that when LL-37 is complexed with Hep in ultrapure water, it adopts an α-helix conformation, which differs from the random coil conformation of bare LL-37. We suggest that the interactions between both compounds result in the formation of hydrogen bonds conducive to the α-helix structure.

However, differing from results demonstrated in other systems,[47,48] the integration of these $PPCs_{LL\text{-}37\text{-}Hep}$ in multilayers, by LbL assembly with a polycation (Chi), does not lead to a higher amount of LL-37 being adsorbed onto the surface. As already demonstrated in our previous works, the Chi, as a third component, disrupt the organization of the film, mainly establishing electrostatic interactions with Hep. The assembly of [LL-37-Hep] multilayers, especially at pH 3.5, enables the immobilization of as much as 20 µg cm^{-2} of LL-37. This is attributed to the mobility exhibited by bare LL-37, and thus its diffusion within the growing film. Consequently, we suggest that complexation of proteins/peptides and the subsequent homogenization of their charge are more suitable for globular molecules, like lysozyme, as opposed to elongated molecules, such as LL-37.[47,48]

From this reservoir, the release kinetics of LL-37 in PBS medium was investigated. Our study reveals a two-stage release pattern. First, a burst release: up to 6.5 µg cm^{-2} of LL-37 are released within the first 24 hours. Then, a continuous stage, gradually releasing up to 4.5 µg cm^{-2} over the subsequent 13 days. These results are very promising since the burst release represents less than 50% of the total amount of immobilized LL-37 and that the coating is not depleted of its LL-37 content after 14 days. Indeed, the remaining 9 µg

cm^{-2} will be released later, ensuring a sustained effect over an extended duration.

Taken together, our results show that such self-assemblies are promising in the design of systems that aim at delivering antimicrobial molecules in short and prolonged time periods and thus opens perspectives for future advances in the field of antibacterial coatings.

4.5 Take-home messages

- In PBS, the LL-37 peptide adopts an α-helical conformation, whereas in ultrapure water, it assumes a random coil structure. However, upon complexation with Hep in ultrapure water, LL-37 stabilizes into an α-helical structure.
- In the conditions tested in this work, in order to immobilize a large quantity of LL-37, the multilayer structure consisting of 25 bilayers of [LL-37-Hep], assembled at pH 3.5, seems to be the most suitable design. However, increasing the number of adsorbed bilayers will result in a greater immobilization of LL-37.
- Regarding LL-37 release kinetics from the multilayers, an initial burst release is observed within the first 24 hours, followed by a sustained release phase. After 14 days of release, the coating is not depleted of its LL-37 content. This profile of release is particularly interesting for targeting both bacteria in the early stages of infection and opportunistic pathogens beyond this period.

In this *Chapter 4*, we showed that the amount of LL-37 adsorbed is contingent upon both the immobilization strategy and the pH at which the multilayer is assembled. For *in vitro* studies of the antibiofilm efficacy of the coatings, we have chosen to focus on coatings incorporating bare LL-37 at pH 3.5, as these conditions yield the highest levels of LL-37 immobilization.

4.6 Supporting Information

4.6.1 Calibration curves of FITC-LL-37 in solution and adsorbed onto surface

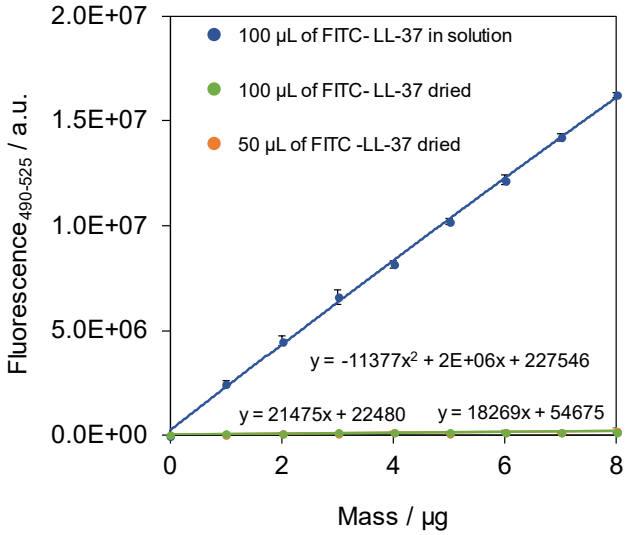

Figure IV-4. S1 – Calibration curve of FITC-LL-37 in ultrapure water (blue curve) and adsorbed onto surface after the vaporization of a 100 µL (green curve) or a 50 µL (orange curve) drop of different mass of FITC-LL-37 in ultrapure water.

To determine the optimal quantification method for surface-adsorbed FITC-LL-37, three distinct calibration protocols were developed. First, the fluorescence of varying concentrations of FITC-LL-37 in a 100 µL volume was measured. Second, droplets of 100 µL or 50 µL containing different concentrations of FITC-LL-37 were air-dried in the wells of a 96-well plate prior to fluorescence measurement. These calibration curves are presented in Figure IV-4. S1. The calibrations performed using air-dried LL-37 solutions present a low R^2 value and a low fluorescence signal probably due to some quenching with polystyrene occurring because marked LL-37 is in close contact with other molecules. Therefore, due to the significantly higher signal sensitivity of fluorescence measurements in solution, this method was selected to quantify surface-adsorbed LL-37.

4.6.2 Structure of Chi

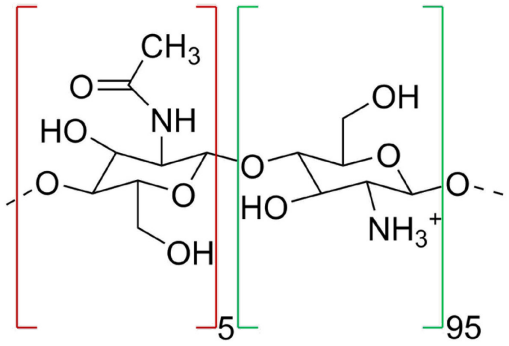

Figure IV-4. S2 – Structure of a 95% deacetylated Chi.

4.6.3 Calibration curve of BCA assay for LL-37, Chi and Hep

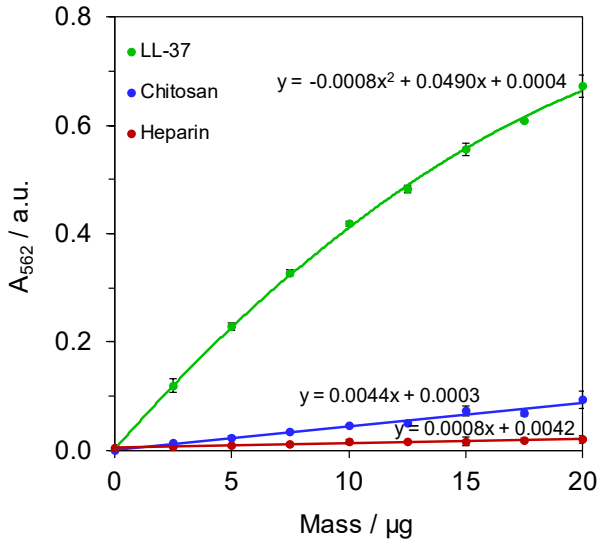

Figure IV-4. S3 – Calibration curve of BCA assay for LL-37 (green) and interfering responses of Chi (blue) and Hep (red).

4.6.4 Calibration curve of FITC-LL-37 in BCA working reagent

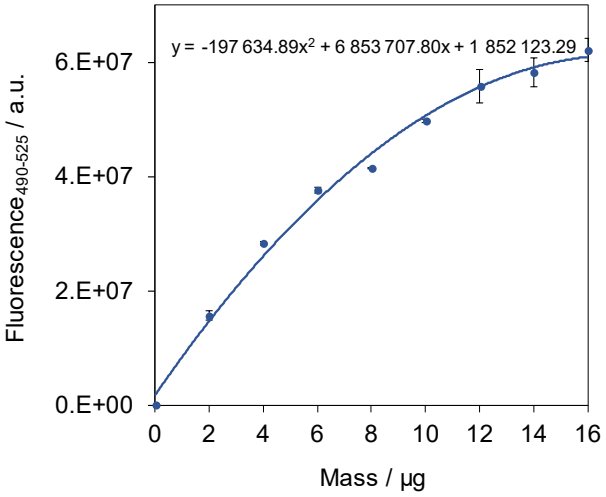

Figure IV-4. S4 – Calibration curve of FITC-LL-37 in BCA working reagent.

4.6.5 Calibration curve of FITC-LL-37 in PBS

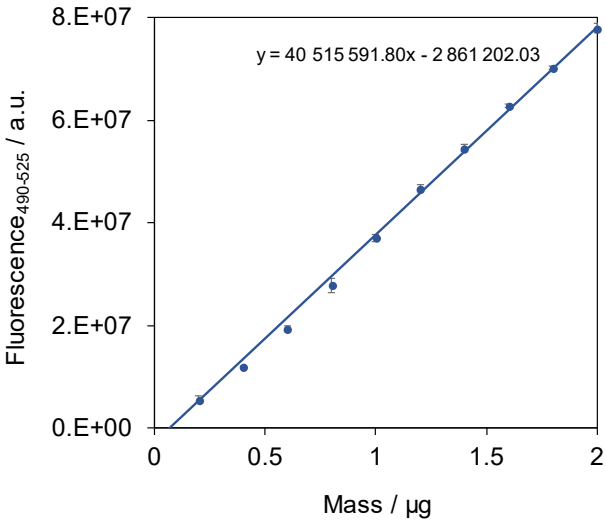

Figure IV-4. S5 – Calibration curve of FITC-LL-37 in PBS.

4.6.6 Cumulative mass of LL-37 released as a function of the LbL assembly strategy, the number of bilayers, and the pH

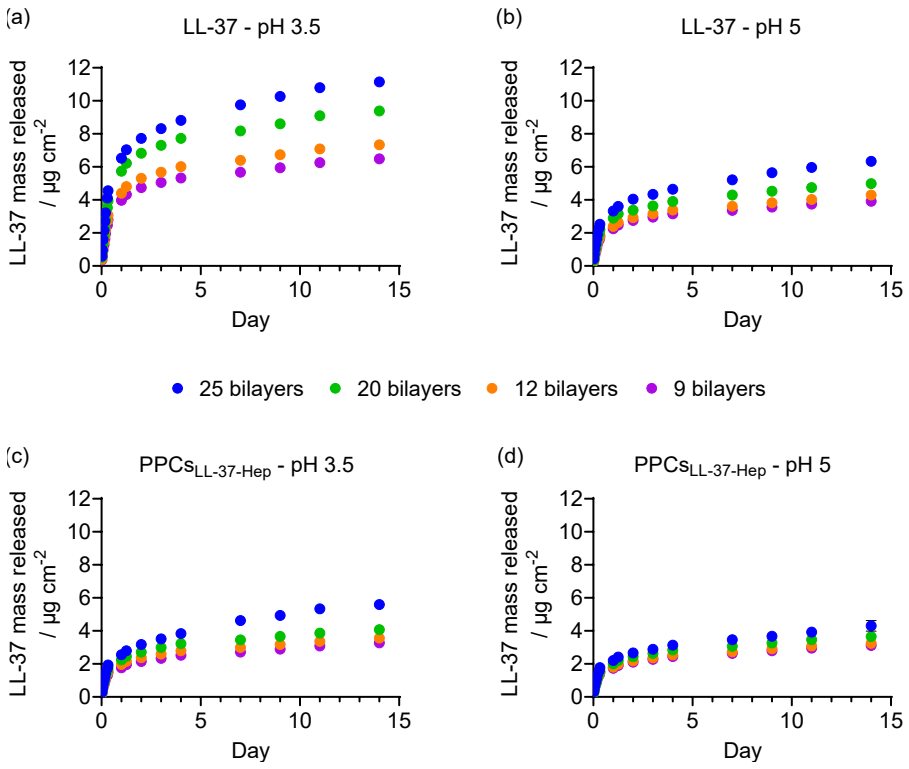

Figure IV-4. S6 – Cumulative mass of LL-37 released from $[Chi\text{-}Hep]_2$-[FITC-LL-37-$Hep]_{9,\ 12,\ 20,\ or\ 25}$ at (a) pH 3.5 and (b) pH 5, and $[Chi\text{-}Hep]_2$-$[Chi\text{-}PPCs_{FITC\text{-}LL\text{-}37\text{-}Hep}]_{9,\ 12,\ 20,\ or\ 25}$ at (c) pH 3.5 and (d) pH 5 coated polystyrene wells after 30 min, 1, 2, 3, 4, 5, 7, 8, 24, 30 h, 2, 3, 4, 7, 9, 11 and 14 days. Error bars show the standard deviation (n=3).

4.6.7 LL-37 release profiles as a function of the LbL assembly strategy, and the pH for multilayers designed with 9 bilayers

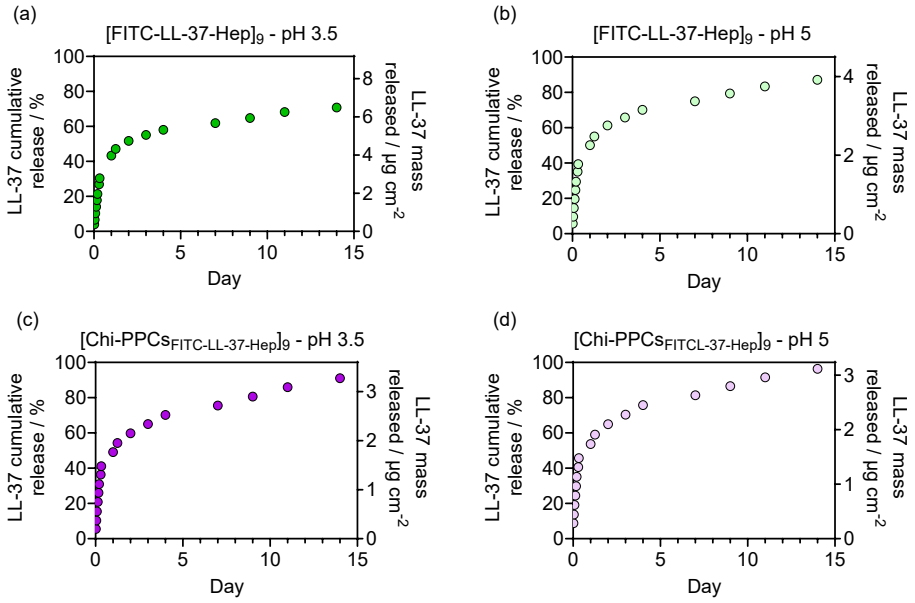

Figure IV-4. S7 – LL-37 release profile from $[Chi\text{-}Hep]_2$-$[FITC\text{-}LL\text{-}37\text{-}Hep]_9$ at (a) pH 3.5 and (b) pH 5, and $[Chi\text{-}Hep]_2$-$[Chi\text{-}PPCs_{FITC\text{-}LL\text{-}37\text{-}Hep}]_9$ at (c) pH 3.5 and (d) pH 5 coated polystyrene wells after 30 min, 1, 2, 3, 4, 5, 7, 8, 24, 30 h, 2, 3, 4, 7, 9, 11 and 14 days. Error bars show the standard deviation (n=3).

4.6.8 LL-37 release profiles as a function of the LbL assembly strategy, and the pH for multilayers designed with 12 bilayers

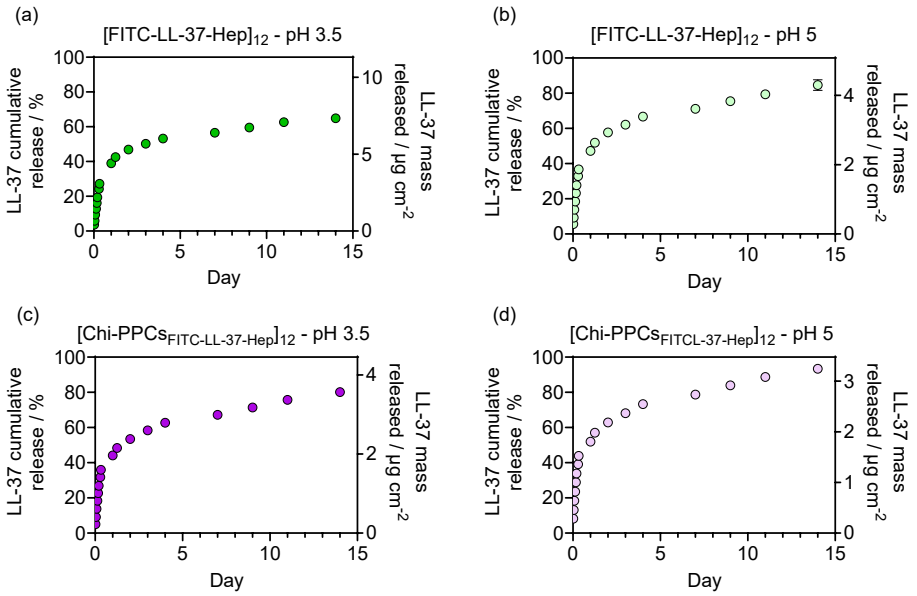

Figure IV-4. S8 – LL-37 release profile from $[Chi\text{-}Hep]_2$-$[FITC\text{-}LL\text{-}37\text{-}Hep]_9$ at (a) pH 3.5 and (b) pH 5, and $[Chi\text{-}Hep]_2$-$[Chi\text{-}PPCs_{FITC\text{-}LL\text{-}37\text{-}Hep}]_{12}$ at (c) pH 3.5 and (d) pH 5 coated polystyrene wells after 30 min, 1, 2, 3, 4, 5, 7, 8, 24, 30 h, 2, 3, 4, 7, 9, 11 and 14 days. Error bars show the standard deviation (n=3).

4.6.9 LL-37 release profiles as a function of the LbL assembly strategy, and the pH for multilayers designed with 20 bilayers

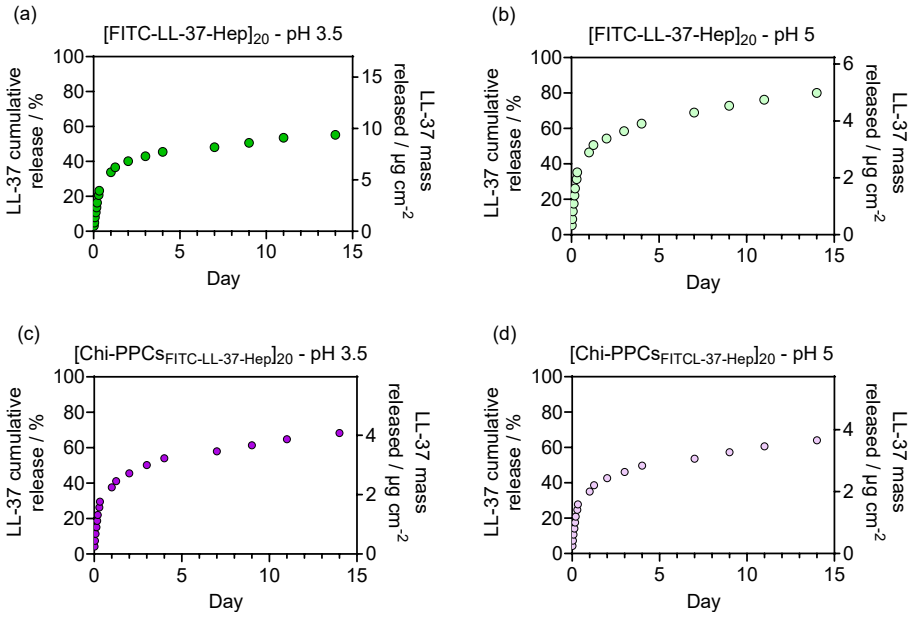

Figure IV-4. S9 – LL-37 release profile from $[Chi\text{-}Hep]_2$-$[FITC\text{-}LL\text{-}37\text{-}Hep]_9$ at (a) pH 3.5 and (b) pH 5, and $[Chi\text{-}Hep]_2$-$[Chi\text{-}PPCs_{FITC\text{-}LL\text{-}37\text{-}Hep}]_{20}$ at (c) pH 3.5 and (d) pH 5 coated polystyrene wells after 30 min, 1, 2, 3, 4, 5, 7, 8, 24, 30 h, 2, 3, 4, 7, 9, 11 and 14 days. Error bars show the standard deviation (n=3).

4.7 References

1. Murray, C. J. *et al.* Global burden of bacterial antimicrobial resistance in 2019: a systematic analysis. *The Lancet* **399**, (2022).
2. World Health Organization. Antimicrobial Resistance Surveillance in Europe 2023 - 2021 Data. (2023).
3. Hancock, R. E. W. & Sahl, H.-G. Antimicrobial and host-defense peptides as new anti-infective therapeutic strategies. *Nat Biotechnol* **24**, 1551–1557 (2006).
4. Mutschler, A. *et al.* Unexpected Bactericidal Activity of Poly(arginine)/Hyaluronan Nanolayered Coatings. *Chemistry of Materials* **28**, 8700–8709 (2016).
5. Geissel, F. J. *et al.* Antibiofilm activity of nanosilver coatings against *Staphylococcus aureus*. *J Colloid Interface Sci* **608**, 3141–3150 (2022).
6. Nazi, N., Marguier, A., Debiemme-Chouvy, C. & Humblot, V. Optimization and Antibacterial Response of N-Halamine Coatings Based on Polydopamine. *Colloids and Interfaces* **6**, 9 (2022).
7. Vandamme, D., Landuyt, B., Luyten, W. & Schoofs, L. A comprehensive summary of LL-37, the factotum human cathelicidin peptide. *Cell Immunol* **280**, 22–35 (2012).
8. Johansson, J., Gudmundsson, G. H., Rottenberg, M. E., Berndt, K. D. & Agerberth, B. Conformation-dependent Antibacterial Activity of the Naturally Occurring Human Peptide LL-37. *Journal of Biological Chemistry* **273**, 3718–3724 (1998).
9. Dürr, U. H. N., Sudheendra, U. S. & Ramamoorthy, A. LL-37, the only human member of the cathelicidin family of antimicrobial peptides. *Biochimica et Biophysica Acta (BBA) - Biomembranes* **1758**, 1408–1425 (2006).
10. Sancho-Vaello, E. *et al.* The structure of the antimicrobial human cathelicidin LL-37 shows oligomerization and channel formation in the presence of membrane mimics. *Sci Rep* **10**, 17356 (2020).
11. Overhage, J. *et al.* Human host defense peptide LL-37 prevents bacterial biofilm formation. *Infect Immun* **76**, 4176–4182 (2008).
12. Dean, S. N., Bishop, B. M. & van Hoek, M. L. Natural and synthetic cathelicidin peptides with anti-microbial and anti-biofilm activity against *Staphylococcus aureus*. *BMC Microbiol* **11**, 114 (2011).

13. Saporito, P., Vang Mouritzen, M., Løbner-Olesen, A. & Jenssen, H. LL-37 fragments have antimicrobial activity against *Staphylococcus epidermidis* biofilms and wound healing potential in HaCaT cell line. *Journal of Peptide Science* **24**, e3080 (2018).
14. Jacobsen, A. S. & Jenssen, H. Human cathelicidin LL-37 prevents bacterial biofilm formation. *Future Med Chem* **4**, 1587–1599 (2012).
15. Beaumont, P. E., Li, H. N. & Davidson, D. J. LL-37: An immunomodulatory Antimicrobial Host Defence Peptide. in *Antimicrobial Peptides and Innate Immunity.* 97–121 (Springer Basel, 2013).
16. Turner, J., Cho, Y., Dinh, N. N., Waring, A. J. & Lehrer, R. I. Activities of LL-37, a cathelin-associated antimicrobial peptide of human neutrophils. *Antimicrob Agents Chemother* **42**, 2206–2214 (1998).
17. Geitani, R., Ayoub Moubareck, C., Touqui, L. & Karam Sarkis, D. Cationic antimicrobial peptides: Alternatives and/or adjuvants to antibiotics active against methicillin-resistant *Staphylococcus aureus* and multidrug-resistant *Pseudomonas aeruginosa*. *BMC Microbiol* **19**, 12 (2019).
18. Friberg, C. *et al.* Human antimicrobial peptide, LL-37, induces non-inheritable reduced susceptibility to vancomycin in *Staphylococcus aureus*. *Sci Rep* **10**, 8 (2020).
19. Comune, M., Rai, A., Palma, P., TondaTuro, C. & Ferreira, L. Antimicrobial and pro-angiogenic properties of soluble and nanoparticle-immobilized LL37 peptides. *Biomater Sci* **9**, 8153–8159 (2021).
20. De Miguel Catalina, A. *et al.* The C-Terminal VPRTES Tail of LL-37 Influences the Mode of Attachment to a Lipid Bilayer and Antimicrobial Activity. *Biochemistry* **58**, 2447–2462 (2019).
21. Cassin, M. E., Ford, A. J., Orbach, S. M., Saverot, S. E. & Rajagopalan, P. The design of antimicrobial LL37-modified collagen-hyaluronic acid detachable multilayers. *Acta Biomater* **40**, 119–129 (2016).
22. Gomes, A. P., Mano, J. F., Queiroz, J. A. & Gouveia, I. C. Incorporation of antimicrobial peptides on functionalized cotton gauzes for medical applications. *Carbohydr Polym* **127**, 451–461 (2015).
23. Harrison-Balestra, C., Cazzaniga, A. L., Davis, S. C. & Mertz, P. M. A Wound-Isolated *Pseudomonas aeruginosa* Grows a Biofilm *In Vitro*

Within 10 Hours and Is Visualized by Light Microscopy. *Dermatologic Surgery* **29**, 631–635 (2003).

24. Decher, G. & Hong, J. D. Buildup of ultrathin multilayer films by a self-assembly process: II. Consecutive adsorption of anionic and cationic bipolar amphiphiles and polyelectrolytes on charged surfaces. *Berichte der Bunsengesellschaft für physikalische Chemie* **95**, 1430–1434 (1991).
25. Okahata, Y., Tsuruta, T., Ijiro, K. & Ariga, K. Langmuir-Blodgett Films of an Enzyme-Lipid Complex for Sensor Membranes. *Langmuir* **4**, 1373–1375 (1988).
26. Okahata, Y., Tsuruta, T., Ijiro, K. & Ariga, K. Preparations of Langmuir-Blodgett films of enzyme-lipid complexes: A glucose sensor membrane. *Thin Solid Films* **180**, 65–72 (1989).
27. Onda, M., Ariga, K. & Kunitake, T. Activity and stability of glucose oxidase in molecular films assembled alternately with polyions. *J Biosci Bioeng* **87**, 69–75 (1999).
28. Silva, R. A., Urzúa, M. D., Petri, D. F. S. & Dubin, P. L. Protein adsorption onto polyelectrolyte layers: Effects of protein hydrophobicity and charge anisotropy. *Langmuir* **26**, 14032–14038 (2010).
29. vander Straeten, A. *et al.* Protein–polyelectrolyte complexes to improve the biological activity of proteins in layer-by-layer assemblies. *Nanoscale* **9**, 17186–17192 (2017).
30. vander Straeten, A., Bratek-Skicki, A., Jonas, A. M., Fustin, C.-A. & Dupont-Gillain, C. Integrating Proteins in Layer-by-Layer Assemblies Independently of their Electrical Charge. *ACS Nano* **12**, 8372–8381 (2018).
31. Vranckx, C. *et al.* Layer-by-Layer Nanoarchitectonics Using Protein-Polyelectrolyte Complexes toward a Generalizable Tool for Protein Surface Immobilization. *Langmuir* **38**, 5579–5589 (2022).
32. Domard, A. pH and c.d. measurements on a fully deacetylated chitosan: application to CuII—polymer interactions. *Int J Biol Macromol* **9**, 98–104 (1987).
33. Dolinsky, T. J., Nielsen, J. E., McCammon, J. A. & Baker, N. A. PDB2PQR: An automated pipeline for the setup of Poisson-Boltzmann electrostatics calculations. *Nucleic Acids Res* **32**, 665–667 (2004).

34. Greenfield, N. J. Using circular dichroism spectra to estimate protein secondary structure. *Nat Protoc* **1**, 2876–2890 (2007).
35. Macdougall, D. & Crummett, W. B. Guidelines for Data Acquisition and Data Quality Evaluation in Environmental Chemistry. *Anal Chem* **52**, 2242–2249 (1980).
36. Hirota, N., Mizuno, K. & Goto, Y. Cooperative α-helix formation of β-lactoglobulin and melittin induced by hexafluoroisopropanol. *Protein Science* **6**, 416–421 (1997).
37. Al-Adwani, S. *et al.* Studies on citrullinated LL-37: detection in human airways, antibacterial effects and biophysical properties. *Sci Rep* **10**, 2376 (2020).
38. Toppazzini, M. *et al.* Can the interaction between the antimicrobial peptide LL-37 and alginate be exploited for the formulation of new biomaterials with antimicrobial properties? *Carbohydr Polym* **83**, 578–585 (2011).
39. Liang, L., Yao, P. & Jiang, M. Structural Transformation of Apocytochrome c Induced by Alternating Copolymers of Maleic Acid and Alkene. *Biomacromolecules* **6**, 2748–2755 (2005).
40. Wei, Z., Rolle, M. W. & Camesano, T. A. Characterization of LL37 Binding to Collagen through Peptide Modification with a Collagen-Binding Domain. *ACS Omega* **8**, 35370–35381 (2023).
41. Pavani, P., Kumar, K., Rani, A., Venkatesu, P. & Lee, M. J. The influence of sodium phosphate buffer on the stability of various proteins: Insights into protein-buffer interactions. *J Mol Liq* **331**, 115753 (2021).
42. V. Klitzing, R. Internal structure of polyelectrolyte multilayer assemblies. *Physical Chemistry Chemical Physics* **8**, 5012–5033 (2006).
43. Borges, J. & Mano, J. F. Molecular interactions driving the layer-by-layer assembly of multilayers. *Chem Rev* **114**, 8883–8942 (2014).
44. Picart, C. *et al.* Molecular basis for the explanation of the exponential growth of polyelectrolyte multilayers. *Proc Natl Acad Sci U S A* **99**, 12531–12535 (2002).
45. Gand, A. *et al.* Fibronectin-based multilayer thin films. *Colloids Surf B Biointerfaces* **156**, 313–319 (2017).
46. Lundin, M., Solaqa, F., Thormann, E., Macakova, L. & Blomberg, E. Layer-by-Layer Assemblies of Chitosan and Heparin: Effect of Solution Ionic Strength and pH. *Langmuir* **27**, 7537–7548 (2011).

47. vander Straeten, A. *et al.* Protein–polyelectrolyte complexes to improve the biological activity of proteins in layer-by-layer assemblies. *Nanoscale* **9**, 17186–17192 (2017).
48. vander Straeten, A., Bratek-Skicki, A., Jonas, A. M., Fustin, C.-A. & Dupont-Gillain, C. Integrating Proteins in Layer-by-Layer Assemblies Independently of their Electrical Charge. *ACS Nano* **12**, 8372–8381 (2018).
49. Nath, H., Sarmah, R. J. & Kundu, S. Langmuir monolayer of lysozyme at variable subphase pH conditions: a comprehensive study on structure, morphology and hysteresis behaviour. *RSC Adv* **13**, 22789–22799 (2023).
50. Sedov, I. A. & Magsumov, T. I. Molecular dynamics study of unfolding of lysozyme in water and its mixtures with dimethyl sulfoxide. *J Mol Graph Model* **76**, 466–474 (2017).
51. Lu, J. R., Su, T. J. & Howlin, B. J. The effect of solution pH on the structural conformation of lysozyme layers adsorbed on the surface of water. *Journal of Physical Chemistry B* **103**, 5903–5909 (1999).
52. vander Straeten, A. & Dupont-Gillain, C. Self-Reorganizing Multilayer to Release Free Proteins from Self-Assemblies. *Langmuir* **36**, 972–978 (2019).

5 Phages, antibiotics or antimicrobial coatings? Evaluating combined treatment approaches for the removal of staphylococcal biofilms on medical implantable devices

S. De Soir[1,2], C. Vranckx[3], (co-first authors) F. Van Bambeke[1], O. Cornu[4,5], C. Dupont-Gillain[3].

[1]Pharmacologie cellulaire et moléculaire, Louvain Drug Research Institute, Université catholique de Louvain, 1200 Brussels, Belgium
[2]Laboratory for Molecular and Cellular Technology of the Queen Astrid Military Hospital, 1120 Brussels, Belgium
[3]Institute of Condensed Matter and Nanosciences, Bio-and Soft Matter, Université catholique de Louvain, 1348 Louvain-la-Neuve, Belgium
[4]Neuro-Musculo-Skeletal Pole, Experimental and Clinical research Institute, Université catholique de Louvain, 1200 Brussels, Belgium
[5]Orthopaedic and Trauma Department, Cliniques Universitaires Saint-Luc, Université catholique de Louvain, 1200 Brussels, Belgium

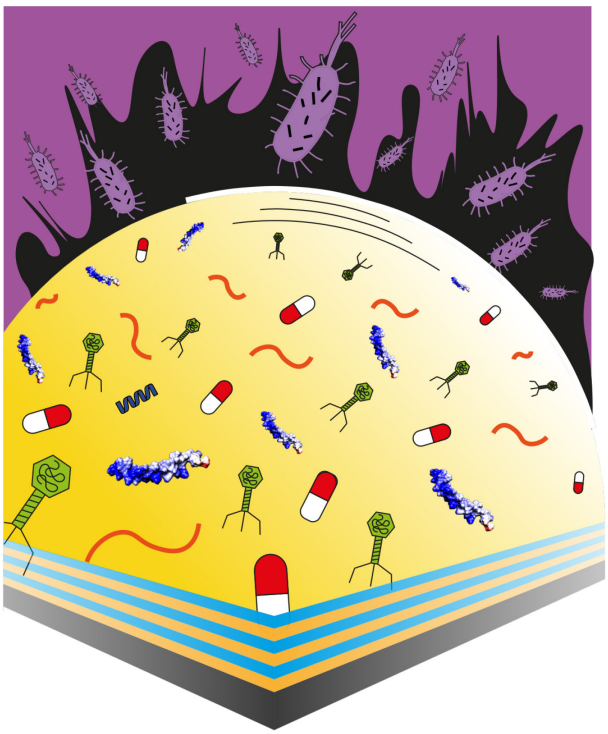

Abstract

The use of antibacterial agents is essential in the treatment of patients with bacterial infections. However, the last decades have seen the number of antimicrobial-resistant bacteria exponentially rise accompanied by a lack in the development of new therapeutic options with catastrophic consequences in the clinics. Antimicrobial resistance was identified by the World Health Organization as one of the biggest threats to humanity. Besides this problematic issue, bacterial adhesion and colonization on the surface of medical implantable devices, leading to biofilm formation, are causing serious complications most predominantly caused by staphylococcal populations. As the 'one-therapy fits all' approach is clearly falling short in the clinics, the present work aimed in evaluating the biofilm eradicating potential of a multifaceted approach for combatting biofilm-associated infections, combining a *de novo* isolated bacteriophage active against *S. epidermidis* along with routinely-used antibiotics and a LL-37-based antimicrobial coating. The antimicrobial coating generally decreased the biomass of biofilms formed by both reference and clinical *S. epidermidis* strains while the cultivable cell count and the bacterial metabolism were less affected. These latter were better addressed upon addition of either phage PSE1 or routinely-used antibiotics such as vancomycin, tobramycin, doxycycline, and linezolid. Results suggest that combining LL-37 with antibiotics targeting intracellular pathways is more efficient when compared to the combination with vancomycin. The use of phage PSE1 showed interesting effects on both biomass and cultivable cell count when combined with tobramycin, only on the clinical *S. epidermidis* strain and on 48h pre-formed biofilms. The results highlight that an approach combining a preventive coating and a treatment therapy is more effective in terms of biofilm destabilization than a stand-alone approach. However, depending on the timeframe of biofilm pre-growth and the strain used, clear differences can be observed in efficacy. This study underscores the challenges of treating biofilm-associated infections and recommends the use of a multifaceted approach that leverages all available antimicrobial weapons to overcome them.

5.1 Introduction

For most bacterial infections, not only the emergence of resistance mechanisms towards routinely-used antibiotics, but also the formation of so-called biofilms, is a major concern, especially on medical implantable devices. A lot of research has been performed on bacterial monocultures in suspension under laboratory conditions. Yet, in reality, biofilms are the most prevailing mode of life for bacterial populations and represent communities of microorganisms embedded in, and protected by, a self-produced extracellular matrix (ECM) composed of extracellular polymeric substances (EPS) including polysaccharides, proteins and lipids while also harboring cellular debris, extracellular DNA (eDNA), and other signaling molecules.[1]

The formation of such biofilms is generally observed on (a)biotic surfaces after initial adhesion followed by irreversible attachment and subsequent colonization. For medical implantable devices, this is especially happening upon implantation, and it is then referred to as surgical site infections, providing entry sites and a window of opportunity for opportunistic pathogenic bacteria.[2] To make matters worse, bacteria can adhere up to 10,000 times better to the material of which the orthopedic implant is made than to the native tissue surrounding it.[3]

Although the overall incidence of surgical site infections is only estimated to be around 2.5% globally,[4] treatment failure as a result of microbiological entities colonizing implant material is seen to be extremely high, with more than 50% of nosocomial infections being implant-associated bacterial infections.[5] Even after excessive antibiotic treatment, full bacterial eradication is proven to be an almost impossible feature. Moreover, although the implant could potentially be replaced, creating a new window for surgical site infections, recolonization by persistent bacteria still residing in the surrounding tissue often leads to repeated failure of medical implantable devices. Bacteria of the *Staphylococcus* species (*S. aureus* and *S. epidermidis*) are known to be the most common causative microorganisms when it comes to these biofilm-associated infections on implant material.[6–8] Both are among the bacteria constituting an individuals' healthy skin microbiome.[9] During surgery, these bacteria can thus easily be introduced into the wound bed thereby quickly colonizing implant material, forming biofilms and eventually resulting in recurrent infections.

Treatment failure due to implantable medical device-related infections was initially thought to be the result of antibiotic resistance. However, for biofilm-associated infections, there is more to the matter. Besides offering a functional environment and providing a structural stability, the EPS also enhance the biofilm's tolerance towards both antimicrobial agents and host defense systems.[10,11] As the antibiotic penetration is hindered by the biofilm structure, the bactericidal concentrations throughout the entire biofilm are not reaching sufficient levels to really affect it.[12]

On top of this, once bacteria have irreversibly attached and during maturation of the biofilm, they will undergo a metabolic shift, becoming 'dormant', or, in other words, metabolically inactive cells.[13] This bacterial metabolic shift is of huge importance as antibiotics routinely used in clinical practice usually target a metabolic pathway (protein or cell wall synthesis, DNA replication, etc.). These antimicrobial agents will thus lose their target and will no longer be as effective, causing biofilm bacteria to become up to 5,000 times more tolerant towards these antibiotics compared to their planktonic counterparts.[3] When pieces of the biofilm are dispersed, bacterial cells can re-activate their metabolism while entering the systemic circulation and reinitiate the formation of novel biofilms elsewhere. *The US National Institute of Health* estimated that microbial biofilms account for over 60% of all microbial infections in humans and 80% of all chronic infections.[14,15]

Despite increasing research interests and improved clinical focus along with the vastly growing demand for medical implantable devices (as life-expectancy has increasing drastically over the last few decades), treatment success rates have remained unchanged over the last few years.[16] Current treatment strategies to combat these biofilm-associated infections in different fields of medicine remain limited and new treatment options are therefore urgently needed. However, the pipeline of new drugs being developed or put on the market is drying up fast. At the moment, there is no drug clinically approved by *the US Food and Drug Administration* or any other equivalent regulatory authorities that can effectively treat biofilm-associated infections.[17] This resulted in the resurgence of alternative treatments such as phage therapy, which are bacteria-specific viruses leaving both human and non-targeted bacterial cells and thereby the commensal microbiome unharmed. Antimicrobial peptides (AMPs), which are cationic and amphiphilic short peptides playing a crucial role in innate immunity systems,

are also widely studied with the goal to fight against medical-related infections. However, the effectiveness of antibiotics cannot be overlooked. Therefore, various antibiotic repurposing efforts to try and evaluate multimodal approaches rather than individual monotherapies are of great interest.

In line with this, De Soir *et al.* reported the synergistic effects of several phage-antibiotic combinations on biofilms formed by *P. aeruginosa* PAO1 on orthopedic implants.[18] Bacteriophages entering biofilm cells will not be able to hijack the bacteria's machinery for the sole purpose of reproducing themselves as they rely on the same DNA and protein production, or translation systems inactivated upon the biofilm's metabolic shift. However, enzymatic activity of phage-related proteins such as depolymerases could act as virtual scissors on polymeric substances, comprising a large portion of the ECM, in the outskirts of the biofilm structure. This will force bacterial cells in the vicinity of these ruptures to re-activate their metabolism, enter the planktonic mode and thereby reintroduce the metabolic target for both antibiotics and phages, possibly explaining part of the observed synergisms. However, full eradication of biofilm structure is still seen to be virtually impossible.

Another interesting strategy, which could further increase treatment outcomes, involves the prevention of bacterial adhesion and subsequent colonization by creating an antiadhesive or bactericidal coating on implants, thereby interfering with the initial attachment of bacterial cells rather than trying to treat an almost incurable biofilm-associated infection. A wide variety of antimicrobial coatings has already been reported in literature for the prevention of biofilm formation, including polymeric antifouling,[19] polymeric bactericidal,[20] nanostructured surfaces,[21] bioactive glasses,[22] as long as coatings incorporating metal and metal oxide nanoparticles.[23] Although the use of such antimicrobial coatings applied on implant material have proven effective in reducing bacterial counts, full bacterial eradication remains a challenge.

With the multitude of complicating factors surrounding biofilm-related infections and limited effective treatment options remaining in the clinics, it is becoming more and more urgent to deal with this issue. Here, a multifaceted strategy was evaluated by investigating the possible synergy

effects when using several antimicrobial weapons. First, as a preventive strategy, a coating incorporating an AMP, *i.e.*, LL-37, was built using the layer-by-layer (LbL) assembly technique.[24,25] LL-37 has been chosen as the only human cathelicidin AMP,[26,27] with bactericidal, antibiofilm, and antifungal activities reported against all ESKAPE pathogens (*E. faecium, S. aureus, K. pneumoniae, A. baumannii, P. aeruginosa,* and *Enterobacter* species).[28–30] Second, as a therapeutic strategy, a *de novo* isolated bacteriophage active against *S. epidermidis* (PSE1) and routinely-used antibiotics (vancomycin (Van), tobramycin (Tob), doxycycline (Dox), and linezolid (Lin)) were used. This combined treatment approach was carried out to see if the treatment outcome for biofilm-related infections could be improved on staphylococcal biofilms *in vitro*. The global strategy is depicted in Figure IV-5. 1.

Although we previously reported the feasibility of incorporating LL-37 in LbL assemblies, this study is the first evaluating the antibiofilm potential against staphylococci of this specific antimicrobial coating, in combination with a *de novo* isolated bacteriophage and routinely-used antibiotics. Our study focused on coatings integrating the highest possible amount of LL-37. Therefore, the coatings were assembled using bare LL-37 molecules ([LL-37-Hep] multilayers) rather than $PPCs_{LL\text{-}37\text{-}Hep}$, at pH 3.5.

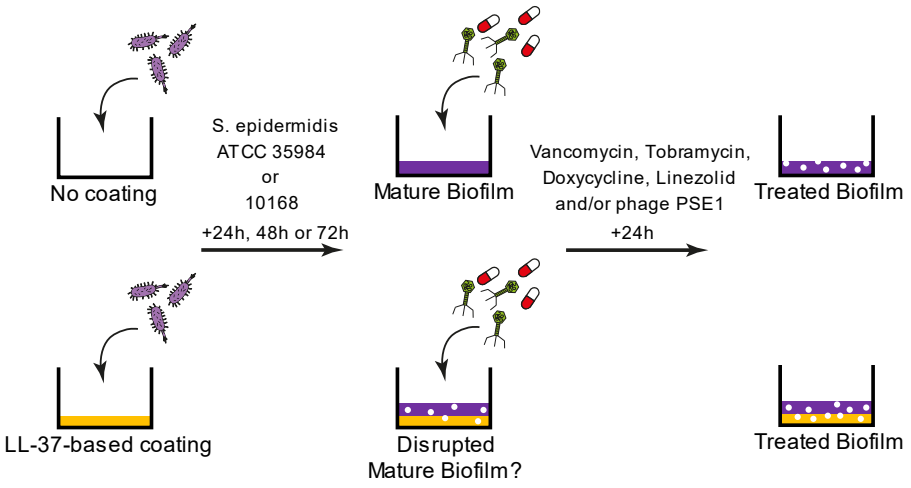

Figure IV-5. 1 – Schematic representation of the study's strategy. LL-37-based coating is designed under sterile conditions before incubating *S. epidermidis* strains during 24h, 48h, or 72h. Once the biofilm is formed, it is treated with antibiotics (Van, Tob, Dox, or Lin) and/or phage PSE1 for 24h.

5.2 Experimental section

5.2.1 Antimicrobial coating

5.2.1.1 Materials

Chitosan (Chi), M_W = 10,000-50,000 g mol^{-1} and a deacetylation degree (DD) of 95% was purchased from Heppe Medical Chitosan Gmbh (Halle, Germany). Chi is not soluble in ultrapure water. Therefore, Chi solution was prepared by first dissolving 50 mg of Chi in approximately 25 mL of ultrapure water and 60 µL of HCl 37% (VWR, Leuven, Belgium) at 60°C for 1h. Then, pH was adjusted to a value of 3.5 with NaOH 10 M (Sigma Aldrich, Steinheim, Germany) and the volume was brought to exactly 100 mL. Finally, the Chi solution was filtered with successively 5 and 0.2 µm filters to remove small impurities and non-dissolved particles. Heparin (Hep) sodium salt, 5,000 I.E./mL, was obtained from B. Braun (Melsungen, Germany). LL-37, 96.55% pure (peptide sequence: LLGDFFRKSKEKIGKEFKRIVQRIKDFLRNLVPRTES, theoretical molecular mass of 4493.26 Da) was bought from Proteogenix (Schiltigheim, France). LL-37 charge was computed, as a function of pH, based on its amino acid sequence and structure (PDB file: 2K6O), using the PDB2PQR Server.[31] The LL-37 net charge is +10.4 at pH 3.5. Hep and LL-37 solutions were prepared at ionic strength (I) ≈ 0 mM, in ultrapure water (Elga Purelab Chorus 1, 18.2 MΩ.cm, Veolia, United Kingdom), with only the ions necessary for pH adjustment at 3.5 with HCl 37%. For Chi solution, as Chi must be dissolved in acidic conditions, I cannot be equal to 0 mM. I was kept as low as possible, with only the ions necessary for Chi dissolution and pH adjustment, and is around 10 mM. The pH value was measured using a pH-indicator strip (MQuant, Merck, Darmstadt, Germany).

5.2.1.2 Coating construction

A multilayered structure was built in 96-well polystyrene Cellstar® plates (Greiner Bio-One, Kremsmünster, Austria), by successive adsorption steps, based on the LbL assembly technique previously described by our group.[25] In brief, for all experiments, an anchoring layer (AL), consisting of two bilayers of Chi alternately adsorbed with Hep ($[Chi\text{-}Hep]_2$), was constructed from Chi

and Hep solutions (0.5 g L^{-1}). Then, 15 bilayers of bare LL-37 molecules were adsorbed in alternance with Hep to obtain the $[Chi\text{-}Hep]_2$-$[LL\text{-}37\text{-}Hep]_{15}$ antibacterial coating. The following solutions were used: Chi (0.5 g L^{-1}), Hep (0.5 g L-1), LL-37 (0.08 mM positive net charge, *i.e.*, 36 µg mL^{-1}). Each adsorption step lasted for 20 min and was carried out with 200 µL of solution. It was followed by three consecutive rinsing steps with ultrapure water adjusted at pH 3.5.

5.2.2 Turbidimetry

Turbidimetry were used to monitor the turbidity of 0.5 g L^{-1} LL-37 solutions in commonly used bacterial culture media*, i.e.*, Mueller-Hinton broth (MHB; VWR, Leuven, Belgium), tryptic soy broth (TSB; VWR, Leuven, Belgium), Luria-Bertani (LB; VWR, Leuven, Belgium), and Roswell Park Memorial Institute 1640 (RPMI 1640; Gibco, Belgium). The turbidity at λ = 600 nm (A_{600}) was measured using a multi-mode microplate reader (SpectraMaxiD3, Molecular Device, USA). Measurements were all performed at 25°C in independent triplicate.

5.2.3 Isolation and purification of phage PSE1

A bacteriophage active against *S. epidermidis*, and referred to as phage PSE1, was isolated *de novo* from a biological water purification plant (purifying incoming waste water from two different hospitals) in Leuven (Belgium) following protocols previously described by De Soir *et al*.[18] In short, after an initial enrichment protocol, collected samples were centrifuged and filtered (0.45 µm pores) after which spot tests were performed on bait strains in order to define phage presence. Bacterial lysis zones were then cut out from these agar plates using inoculation loops and re-cultured in 3 mL liquid TSB with the respective host bacteria. Double agar overlays subsequently allowed for the visualization of individual phage plaques. Phage-specific plaques were subsequently picked up with pipette points and re-cultured with their bacterial host strain, after which new double agar overlays were performed. This process was repeated at least 10 times in order to obtain a pure phage solution. Phage PSE1 was subsequently propagated in high titers to allow for subsequent host range evaluation and genetic sequencing.

5.2.4 Bacterial strains and antibiotics

Two laboratory strains ATCC 33591 and ATCC 35984 were used as reference for methicillin-resistant *S. aureus* (MRSA) and methicillin-resistant *S. epidermidis* (MRSE), respectively. One clinical *S. epidermidis* 10168 strain, collected from a patient, suffering of an orthopedic device-related infection, via a swab of the infected wound (University Hospital of Lyon, Service des maladies infectieuses et tropicales du GHN, Lyon, France) was also studied. The clinical strain *S. epidermidis* 10168 is the host of *de novo* isolated phage PSE1. Antibiotics were obtained as microbiological standards, as follows: Van (potency 97.5%) was procured as generic drug branded products for human parenteral use distributed for clinical use in Belgium by Sandoz (Holzkirchen, Germany), Tob (potency, 100%) was from Galephar (Marche-en-Famenne, Belgium), Dox (potency: 90.2%) was purchased from Sigma-Aldrich (Steinheim, Germany), and Lin (potency, 99.2%) was from Rib-X Pharmaceuticals (Morristown, NJ, USA).

5.2.5 Susceptibility testing

Minimum inhibitory concentrations (MICs) were determined by broth microdilution in RPMI 1640 medium, supplemented with 50 mM of KH_2PO_4 (Sigma Aldrich, Steinheim, Germany), 74.1 mM of Na_2HPO_4 (Sigma Aldrich, Steinheim, Germany) and 1% (w/v) of glucose (VWR Chemical, Leuven, Belgium), and adjusted at pH 7.4. The MIC of antibiotics was determined for the *S. epidermidis* ATCC 35984 strain by following the standard procedures established by the *Clinical and Laboratory Standards Institute* (CLSI).[32] The MIC of LL-37 was also determined for the *S. epidermidis* ATCC 35984 strain in 96-well polypropylene plates (Greiner Bio-One, Kremsmünster, Austria), by following the recommendation of Wiegand *et al*.[33] MIC was defined as the lowest concentration at which no visual bacterial growth is observed.

5.2.6 Biofilm culture and treatments

Biofilm experiments were performed in 96-well plates coated or uncoated with the LL-37-based film. To start, bacterial cultures were pre-grown overnight on tryptic soy agar (TSA; VWR Chemical, Leuven, Belgium) plates. They were then suspended in phosphate-buffered saline (PBS) and adjusted

to a McFarland OD of 1.8. This bacterial suspension was subsequently diluted 1:40 in RPMI 1640 medium, supplemented with 50 mM of KH_2PO_4, 74.1 mM of Na_2HPO_4 and 1% (w/v) of glucose, and adjusted at pH 7.4. Coated and uncoated 96-well plates were then incubated for 24h, 48h or 72h at 37°C with 200 µL of bacterial suspension in RPMI per well. Every 24h, the RPMI medium, with the planktonic bacteria, was removed and two steps of rinsing with 200 µL of PBS were performed before renewing the RPMI medium.

In a first set of experiments, after 48h or 72h of biofilm incubation and two stages of rinsing with PBS, 200 µL of either phage PSE1 (10^9 PFU/mL), Tob (200 µg/mL), Van (100 µg/mL) or a combination of each antibiotic with phage PSE1 were applied on the pre-grown biofilms for 24h. After two rinsing steps with PBS, the biofilms were analyzed as explained in the section *Part IV – 5.2.7 Biofilm analysis*. In a second set of experiments, after 24h of biofilm incubation and two rinsing steps with PBS, 200 µL of different multiples of the MIC (1x, 2x, 5x and 10x) of either Van, Tob, Dox or Lin were applied on the pre-grown biofilms for 24h. After two rinsing steps with PBS, the biofilms were analyzed as explained in the section *Part IV – 5.2.7 Biofilm analysis*.

5.2.7 Biofilm analysis

5.2.7.1 Colony forming unit count

Biofilms were first washed to remove any residual planktonic cells and recuperated manually by scraping the bottom of the well plates with inoculation loops. The biofilm was then resuspended in 200 µL of PBS and sonicated in the wells (30s at 60% amplitude; Q700; QSonica, Newton, CT). Serial dilutions were plated out on TSA plates allowing for quantification of the viable bacterial cell count.

5.2.7.2 Biomass quantification

After drying overnight at 60°C, wells were stained during 10 min with 200 µL of 1% crystal violet (Sigma-Aldrich, Steinheim, Germany). After eliminating the excess of dye by rinsing the wells with deionized water, biofilm-bound crystal violet was solubilized in 200 µL of 66% acetic acid (Merck KGaA, Darmstadt, Germany). After 1h of solubilization, the optical density was read

at 570 nm using a Spectramax M3 spectrophotometer (Molecular Devices, San Jose, CA, USA).

5.2.7.3 Metabolic activity quantification

The metabolic activity of the biofilms was quantified using the resazurin assay, which is based on the reduction by living bacterial cells of the weakly fluorescent blue dye resazurin in highly fluorescent pink resorufin.[34] Biofilms washed twice with PBS were incubated with 200 µL of 10 mg L^{-1} resazurin solution (Sigma-Aldrich, Steinheim, Germany) for 4h at room temperature in the dark. Resorufin fluorescence was measured at a wavelength of 590 nm with an excitation wavelength of 550 nm using a Spectramax M3 spectrophotometer.

5.3 Results and discussion

Prior to conducting bacterial experiments, the appropriate culture medium must be selected. The solubilization of LL-37 was investigated in various culture media commonly used for antibacterial studies, *i.e.*, MHB, TSB, LB, and RPMI medium. Solubilization was assessed through turbidimetric analysis, and the results are depicted in Figure IV-5. 2 and in Figure IV-5. S1. The preparation of a 0.5 g L^{-1} solution of LL-37 in MHB, TSB, and LB media resulted in turbidity (Figure IV-5. 2a and Figure IV-5. S1). We can therefore conclude that LL-37 does not solubilize in these media and forms suspended precipitate particles. Steinberg *et al.* already highlighted that some peptides can precipitate when diluted into MHB medium.[35] To overcome this issue, they developed a slightly modified version of the CLSI method in which they prepared peptide solutions in 0.01% acetic acid.[33,35] In the case of LL-37 in MHB, Figure IV-5. 2b shows that no suspended precipitate particles are formed above a concentration of 1% acetic acid in MHB, but such a concentration seems too high for antibacterial studies. These results raise concerns regarding the use of MHB for assessing the antibacterial activity of LL-37, such as determining the MIC.[36–38]. As a result, all antibacterial analyses were conducted in RPMI, the sole medium in which LL-37 molecules remained soluble without forming a suspended precipitate particles.

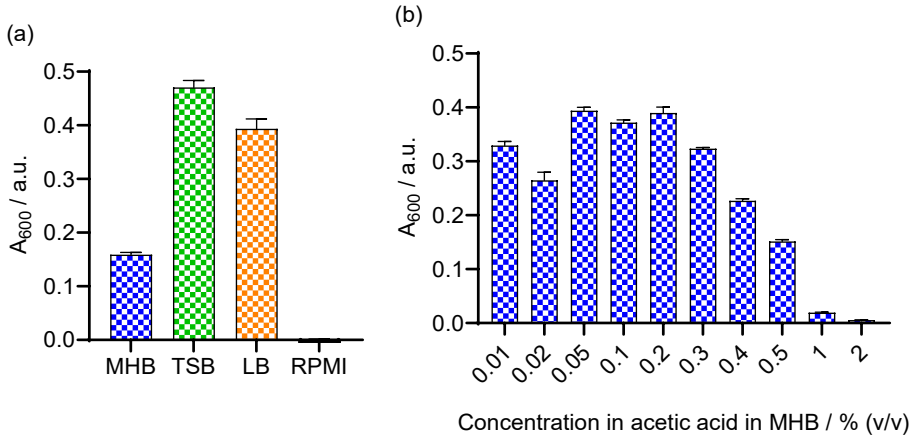

Figure IV-5. 2 – Turbidimetry measurements of 0.5 g L^{-1} LL-37 solutions in (a) MHB, TSB, LB, and RPMI media, and (b) in MHB medium with different concentrations of acetic acid. Error bars represent the standard deviation (n=3).

MICs for *S. epidermidis* ATCC 35984 strain were thus first determined in RPMI medium. This strain exhibited a MIC of >512 µg mL^{-1} for LL-37, 1 µg mL^{-1} for Van and 2 µg mL^{-1} for Tob. It was decided to treat the biofilms with a concentration of 100x the MIC of *S. epidermidis* ATCC 35984 strain, *i.e.*, 100 µg mL^{-1} for Van and 200 µg mL^{-1} for Tob, for both *S. epidermidis* reference and clinical strains. Concerning the PSE1 phages (ΦPSE1), they were inoculated at a concentration of 10^9 PFU mL^{-1}.

5.3.1 Reference biofilms formed by *S. epidermidis* ATCC 35984 *strain*

Preliminary data on the reference *S. epidermidis* and *S. aureus* strains and with a varying number of bilayers in the [LL-37-Hep] coating indicated optimal antibiofilm effect in terms of biomass for *S. epidermidis* ATCC 35984 and $[LL\text{-}37\text{-}Hep]_{15}$ (Figure IV-5. S2). Therefore, coatings incorporating 15 layers of bare LL-37 seems to provide a suitable balance between the amount of adsorbed LL-37, the antibiofilm effect and the time of preparation of the coating. First assays were then performed using these latter conditions, in uncoated and coated 96-well plates. Biofilms were obtained after 48h, after which ΦPSE1, Van and Tob were either applied individually or as a dual treatment modality for 24h on the pre-grown biofilms. Results are depicted in Figure IV-5. 3.

In terms of biomass (Figure IV-5. 3a), treatments applied in the absence of the LL-37-based coating exhibit negligible or no effect. On the contrary, the LL-37-based coating alone shows a significant effect resulting in decreased biofilm biomass. This effect is not significantly improved with ΦPSE1 or antibiotic treatment, and it is even reduced (more biomass detected) when LL-37-based coating is exposed to ΦPSE1, Tob, or a combination of both treatments (ΦPSE1 + Tob). These effects are not well understood, and further experiments are required to elucidate the underlying mechanisms. In contrast, when evaluating residual cultivable cells (Figure IV-5. 3b), no significant reductions are observed between colony forming unit (CFU) counts for biofilms grown in wells containing the LL-37-based coating and those grown in uncoated wells, excepted for those treated with Tob. Therefore, from a statistical standpoint, the mere presence of the ΦPSE1 + Tob, Van, or ΦPSE1 + Van treatment reduces the number of CFUs, and the LL-37-based coating does not show any significantly improved treatment outcome. Interestingly, the treatment by the Van results in a 1.75 $\log_{10}$ reduction, in comparison to the uncoated positive control (C^+), with an observed effect increased (reduction of 2.5 $\log_{10}$) for wells containing the LL-37-based coating. The addition of ΦPSE1 to Van, as a dual treatment, does not show any significantly improved treatment outcome.

Considering both effect on biomass and CFU counts for 48h *S. epidermidis* ATCC 35984 strain pre-grown biofilms, the results indicate that the most effective option is to limit biofilm formation with the LL-37-based coating and treat it with Van (reduction of 78% for the biomass and of 2.5 $\log_{10}$ for the CFUs).

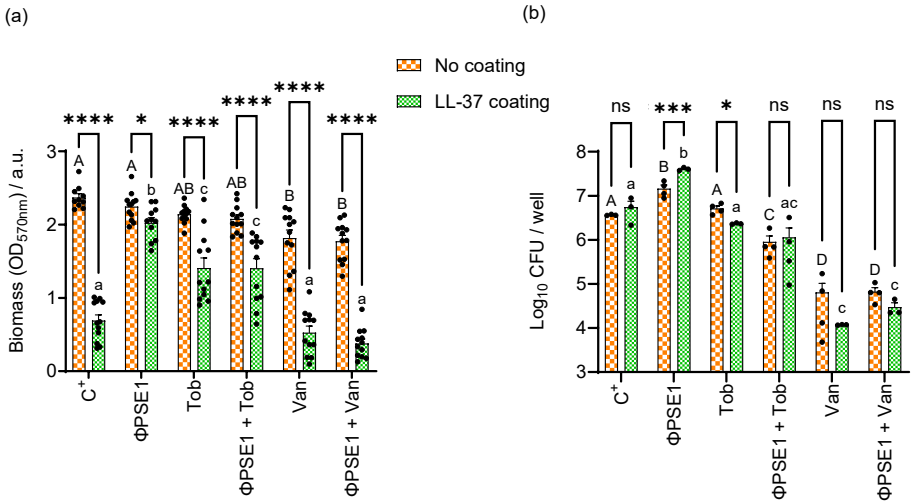

Figure IV-5. 3 – Effect of ΦPSE1 and/or antibiotic (Tob and Van) treatment on (a) the biomass and (b) the cultivable cells of 48h pre-formed *S. epidermidis* ATCC 35984 biofilms that have grown or not on a LL-37-based antimicrobial coating. C^+ = untreated biofilm (positive control). Values are mean ± SEM. Statistical analyses were performed by Student's *t*-tests (N=4 with n=3 per replicate for biomass analyses; and N=4 with n=1 per replicate for CFU analyses). Dixon's tests were performed to identify the outliers. Values with different letters are significantly different from each other ($p<0.05$). Capital letters compare the results for the treatment without coating; lowercase letters compare the results for the treatment with the LL-37-based coating. The significantly different values for a given treatment with or without LL-37 coating are shown by the p-values as follows: ns=non-significant, *=$p<0.05$, **=$p<0.01$, ***=$p<0.001$, ****=$p<0.0001$.

5.3.2 Biofilms formed by clinical *S. epidermidis* 10168 strain

After performing assays on a reference strain, the antibiofilm properties of the LL37-based coating have been investigated in a more orthopedically-relevant setting. To do so, the combined treatment approach has been evaluated on biofilms formed by the bacterial host strain of ΦPSE1, *i.e.*, *S. epidermidis* 10168. Both 48h and 72h pre-formed biofilms were treated with the same phage-antibiotic combinations as tested on reference strain (Figure IV-5. 4).

Interestingly, results varied drastically between both timeframes. First, for 48h pre-grown biofilms, as presented in Figure IV-5. 4a and b, the LL-37-based coating is shown to reduce both biomass and CFU counts, respectively

of 30% and 1.73 log_{10}, when used as a stand-alone agent. A ΦPSE1 or Tob monotherapy does not significantly reduce biomass and CFU counts, nor does it improve the effect of the antimicrobial coating. However, the effect of the LL-37-based coating on biomass is significantly improved upon ΦPSE1 and Tob combined treatment. The combination of ΦPSE1, Tob and LL-37-based coating results in the highest observed reduction in biomass, namely a reduction of 75% in comparison to the uncoated C^+ condition (Figure IV-5. 4a). This synergetic interaction is also resulting in higher reduction in cultivable cells compared to any of these agents when used as a monotherapy, with a reduction of 3.1 log_{10} in comparison to the uncoated C^+ condition (Figure IV-5. 4b). Unfortunately, no statistical difference from the coated C^+ samples can be confirmed because the experiment was reproduced only 2 times (N=2, with n=1). A Van monotherapy or a ΦPSE1 + Van combined treatment reduce biomass and CFU counts (in comparison to the uncoated C^+ condition). However, combining Van with the LL-37-based coating, in presence or absence of ΦPSE1, results in similar reduction patterns in biomass and CFU counts in comparison to the LL-37-coated C^+.

Therefore, for the *S. epidermidis* 10168 strain, the most effective therapy is the combination of LL-37-based coating with the ΦPSE1+Tob treatment. Indeed, a reduction of 75% in biomass and 3.1 log_{10} in CFUs are noticed in comparison to the uncoated C^+ condition (Figure IV-5. 4a and b). This highlights the necessity of combination therapies, as neither phage nor tobramycin administered individually, with or without LL-37-based coating, effectively reduces biofilm biomass or CFUs.

Additionally, while phage therapy showed no impact on the reference strain (Figure IV-5. 3), its efficacy on the orthopedic strain is noticed when combined with Tob. This underscores the importance of accurately defining treatment strategies based on the strain responsible for the infection.

In order to study the effect of biofilm formation time prior to application of the ΦPSE1 and/or antibiotics treatments, it has been decided to pre-grow the *S. epidermidis* 10168 clinical biofilms for 72h instead of 48h, as presented in Figure IV-5. 4c and d. We did not test 24h pre-grown biofilm, since after 1 day, the biofilms did not seem to be well formed and mature. So, in the case of 72h pre-formed biofilm, the LL-37-based coating, as a stand-alone agent, leads to a significant reduction of 18% in the biomass (vs. 30% with 48h pre-

grown biofilms). However, it is no longer seen to significantly reduce CFU counts. As for 48h pre-grown biofilms, the highest reduction in biomass was observed for the combined treatment of phage ΦPSE1 and Tob. However, the LL-37-based coating does not further improve the outcome, similar to observation with cultivable cells with the three beforementioned antimicrobial agents. For Van, significant reductions are observed only for cultivable cells, while neither the addition of ΦPSE1 nor the LL-37-based coating results in more reduction in CFU counts.

In comparison with 48h pre-grown biofilms, the combined treatment (LL-37-based coating with ΦPSE1+Tob) is less effective. Despite the slight biomass reduction attributed to the coating, delaying the application of the treatment for 24h (72h vs. 48h) reduces its efficacy. Hence, it appears that applying the treatment sooner enhances the effectiveness of combined treatment approaches. However, a study of the kinetics of biofilm formation should be carried out to confirm this conclusion.

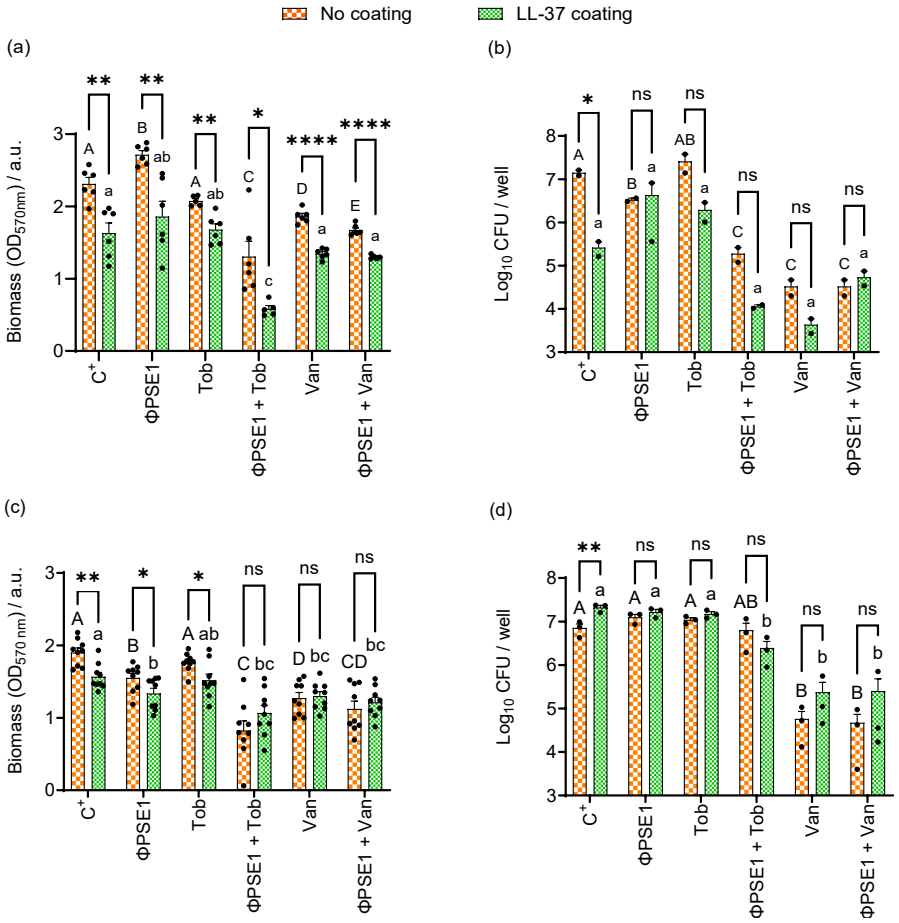

Figure IV-5. 4 – Effect of ΦPSE1 and/or antibiotic (Tob and Van) treatment on (a) the biomass and (b) the cultivable cells of 48h pre-formed *S. epidermidis* 10168 biofilms, and on (c) the biomass and (d) the cultivable cells of 72h pre-formed *S. epidermidis* 10168 biofilms, that have grown or not on LL-37-based antimicrobial coating. C^+ = untreated biofilm (positive control). Values are mean ± SEM. Statistical analyses were performed by Student's *t*-tests (N=2 with n=3 per replicate for biomass analyses at 48h; N=2 with n=1 per replicate for CFU analyses at 48h; N=3 with n=3 per replicate for biomass analyses at 72h; and N=3 with n=1 per replicate for CFU analyses at 72h). Dixon's tests were performed to identify the outliers. Values with different letters are significantly different from each other ($p<0.05$). Capital letters compare the results for the treatment without coating; lowercase letters compare the results for the treatment with the LL-37-based coating. The significantly different values for a given treatment with or without LL-37 coating are shown by the p-values as follows: ns=non-significant, *=$p<0.05$, **=$p<0.01$, ***=$p<0.001$, ****=$p<0.0001$.

In general, the assays performed in the present work clearly indicate varying outcomes based on the bacterial strain used and the duration of the biofilm formation before treatment application. This highlights the fact that many experimental parameters can influence the results.

Sorrentino *et al.* described the creation of a chimeric protein incorporating LL-37, that was immobilized on polystyrene surfaces, such as the 96-well plates used in the present work, resulting in the inhibition of *S. epidermidis* biofilm formation.[39] Although most of the performed experiments of the Sorrentino *et al.*'s study based their assumptions on biomass evaluation rather than also accounting for cultivable cells, it is clear from the data presented in the current manuscript that a reduction of biomass will not necessarily mean that less bacterial cells are recuperated and counted on agar plates in the lab.[39] This could result in serious overestimations of the impact or potential of a given treatment.

Notwithstanding some promising results for the antimicrobial LL-37-based coating, again certain limitations are seen as for all monotherapies and highlight the importance of combined treatment approach in the fight of biofilm-related infections. For both reference and clinical strains, the LL-37-based coating results in a significant reduction of the biofilm biomass, whether used as a stand-alone agent or in combination with another treatment. However, for the CFU counts, except for the coated positive control of *S. epidermidis* ATCC 35984, there is no statistically significant difference between the treatment alone and the treatment combined with the LL-37-based coating. Therefore, the approach of a combined therapy is particularly interesting, since the LL-37-based coating mainly acts on the biomass and the treatment on the cultivable cells. This reduction in the biofilm biomass could be the result of a disruption in the quorum sensing system and in the synthesis of EPS. Further investigations should be performed to confirm these hypotheses. Interestingly, the effects of the LL-37-based coating, as well as of the different treatments, on the biomass of 72h pre-grown biofilms is less significant than on the biomass of 48h pre-grown biofilms. After 72h, the biofilms are probably more robust and thus the cells embedded within it less susceptible to treatments. Despite the lack of experiments exploring biofilm formation kinetics, preliminary findings suggest that early treatment application yields greater effectiveness.

Regarding treatments, the addition of Van to the LL-37-based coating does not increase the reduction of biomass biofilm in comparison to LL-37-based coating as stand-alone treatment. However, it resulted in higher reductions of CFU counts, both for reference as for clinical strains, yet similar reductions were observed for a Van monotherapy. In conclusion Van seems to affect the cultivable cells without reducing the biofilm biomass. This lack of synergy between LL-37 and Van may be explained by their mode of action. Basically, LL-37 integrates into the membrane of the bacterial cell and forms a tetrameric channel structure, leading to the formation of a pore and thus finally to the lysis of the bacterial cell.[40] Van exerts its bactericidal effect by inhibiting the polymerization of peptidoglycans in the bacterial cell wall.[41] Since Van operates without needing to penetrate the bacterial cell, the pore formation by the LL-37 is not expected to improve its antimicrobial properties.

Some disparities also arise between the two strains. Phage application affects the biofilm of *S. epidermidis* 10168 strain, in terms of biomass and CFU counts especially on 48h pre-grown biofilms, and only in a triple treatment protocol, combining LL-37, ΦPSE1 and Tob. This effect is not observed on *S. epidermidis* ATCC 35984 strain. Phage therapy demonstrates high specificity as it relies on identifying and targeting specific receptors found on bacterial cells. The observed difference can thus be attributed to the presence of these receptors on the clinical strain while being absent on the reference one. Subsequently, for 48h pre-grown *S. epidermidis* 10168 biofilms, the combined treatment resulted in higher effective biomass and bacterial reductions than the sum of the individual treatments, highlighting the synergism between the LL-37-based coating, ΦPSE1 and Tob. The synergy of ΦPSE1 when combined with Tob, but not when combined with Van, can be explained by the mode of action of Tob. Contrary to Van, Tob binds to the 16s ribosomal RNA component of the bacterial 30s ribosomal unit, inhibiting the initiation step of translation.[42] It therefore inhibits protein synthesis upon entering the bacterial cell, which is favored by the pores formed in the bacterial membrane by LL-37. As bacterial cells embedded in mature biofilms are known to be in a less metabolically-active state, protein production will not be as active as in the planktonic free-floating state, resulting in higher tolerance towards Tob. However, Van is less affected by the metabolic state possibly explaining its higher efficacy on staphylococcus

biofilms. This more immediate killing could limit ΦPSE1 propagation while for Tob, synergies could be explained by the depolymerase activity of ΦPSE1, possibly reactivating bacterial metabolism and thus protein production. Taken together, these findings indicate that phage and antibiotic nature greatly affect the efficacy of combined treatments.

It is not the first time that synergetic interactions between LL-37 and other antimicrobial agents on biofilm structures have been identified. In 2023, Zhang *et al.* reported no clear antibiofilm effect of LL-37 when used as an individual agent. Yet, when combining it with a phage-derived endolysin, synergetic disruption of *E. faecalis* biofilms was observed.[43] However, as confirmed in the present work, full eradication of mature biofilms was not seen to be possible.

5.3.3 Studying the synergism between LL-37-based coating and vancomycin, tobramycin, doxycycline, or linezolid on *S. epidermidis* ATCC 35984 biofilms

Unfortunately, after all these experiments, it has come to our attention that an error was made in assessing the MIC of Tob. Contrary to the initial assessment of 2 µg mL^{-1} for the *S. epidermidis* ATCC 35984 strain in RPMI medium, the accurate MIC is now recognized to be 128-256 µg mL^{-1}. Therefore, we carried out a second set of experiments. The study was focused on *S. epidermidis* ATCC 35984 strain and was extended to two new antibiotics, namely Dox and Lin.

First, MIC assays for *S. epidermidis* ATCC 35984 strain were performed in RPMI medium. The MICs are 1 µg mL^{-1}, 128-256 µg m^{L-1}, 0.25 µg mL^{-1}, 1 µg mL^{-1} and >512 µg mL^{-1} for Van, Tob, Dox, Lin, and LL-37, respectively.

For this set of experiments, the treatments were applied on 24h *S. epidermidis* ATCC 35984 pre-grown biofilms. The effect of the LL-37-based coating as well as the different antibiotic treatments on the biofilm biomass and on the metabolism is depicted in Figure IV-5. 5 and Figure IV-5. 6, respectively. While the coating, in absence of antibiotics, significantly reduced the biomass of 48h pre-grown biofilms by 78% (Figure IV-5. 3), there is no difference for 24h pre-formed biofilms (Figure IV-5. 5). The effect of the LL-37-based coating appears to vary over time, as no destabilization is

noticed within 24h, but it becomes apparent after 48h. Concerning the antibiotic treatments, although no interaction of the coating and Van is observed, clear synergetic and concentration-dependent reductions of biofilm biomass were observed for all other antibiotic agents (Figure IV-5. 5). Indeed, the treatment of biofilms with antibiotics as stand-alone agents, even at concentrations as high as 10 times the MIC, does not diminish biofilm biomass. However, a reduction of up to 50% in biomass is observed from 2 times the MIC for Tob, Dox, and Lin when biofilms are cultivated on the LL-37-based coating. The observations made for the metabolism analysis are different to the ones made for the biomass. As shown in Figure IV-5. 6, antibiotics, excluding Van, can reduce biofilm metabolism by as much as 65%. Nevertheless, combining these treatments with the LL-37-based coating does not yield any statistically significant additional effects, except for Dox at 10 times the MIC. Further investigation is required to elucidate the synergistic effects of the LL-37-based coating and treatment on biomass, without affecting bacterial metabolism. One hypothesis should be that the coating and the treatment affect the ECM of the biofilm by reducing its EPS content, while exerting a limited impact on the bacteria themselves.

Therefore, data indicate promising additive effects when combining the antimicrobial coating with antibiotics targeting intracellular pathways (*i.e.*, Tob, Dox and Lin in this study). These results are coherent with the mode of action of LL-37. This latter is indeed a destabilizer of bacterial cell membranes thereby possibly potentiating the effects of such antibiotics. As Van is also affecting bacterial cell walls, this could explain the absence of additive effects when combined with the LL-37 coating.

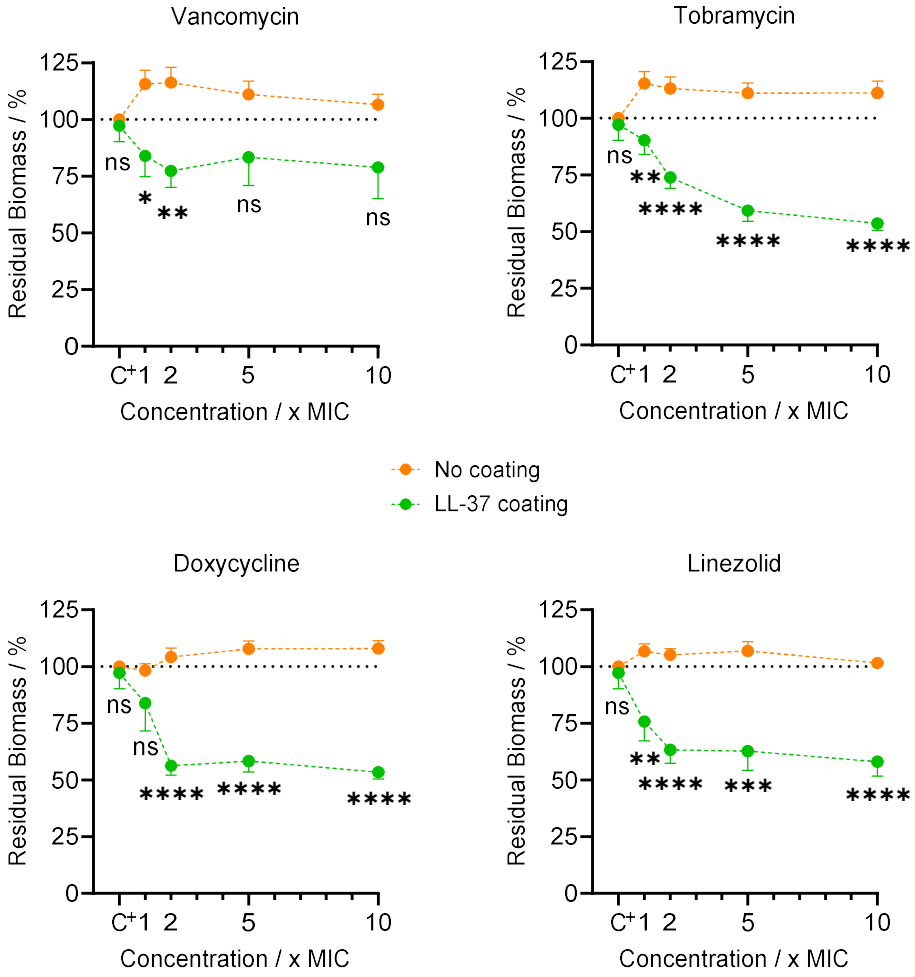

Figure IV-5. 1 – Residual biomass for 24h pre-formed *S. epidermidis* ATCC 35984 biofilms when combining a LL-37-based coating with different multiples of the MIC of either Van, Tob, Dox or Lin. C^+ = untreated biofilm (positive control). Values are mean ± SEM. Statistical analyses were performed by Student's *t*-tests (N=3 with n=3 per replicate). The significantly different values between LL-37 coated and non-coated surfaces, for a given MIC value of the antibiotic, are shown by the p-values as follows: ns=non-significant, *=p<0.05, **=p<0.01, ***=p<0.001, ****=p<0.0001.

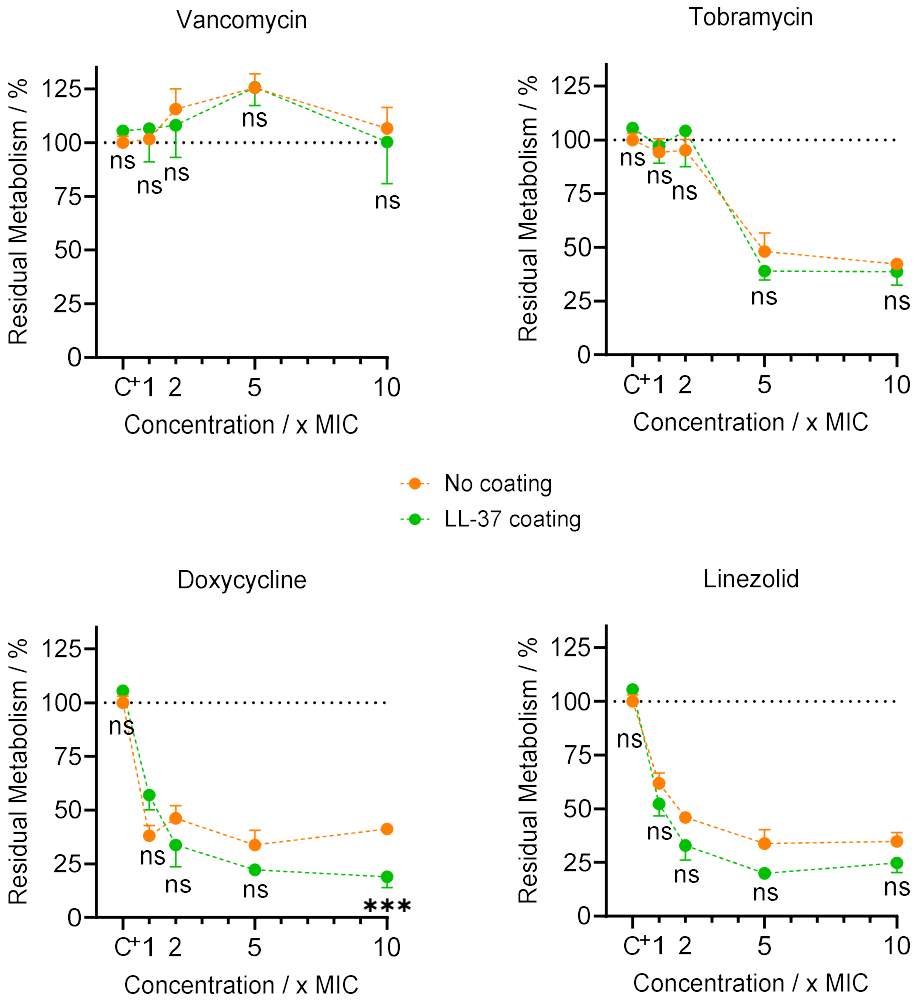

Figure IV-5. 2 – Residual metabolism for 24h pre-formed *S. epidermidis ATCC 35984* biofilms when combining a LL-37-based coating with different multiples of the MIC of either Van, Tob, Dox or Lin. C^+ = untreated biofilm (positive control). Values are mean ± SEM. Statistical analyses were performed by Student's *t*-tests (N=3 with n=3 per replicate). The significantly different values between LL-37 coated and non-coated surfaces, for a given MIC value of the antibiotic, are shown by the p-values as follows: ns=non-significant, *=p<0.05, **=p<0.01, ***=p<0.001, ****=p<0.0001.

5.4 Conclusion

In this study, we demonstrated that a coating, built using the LbL self-assembly technique and incorporating LL-37, an AMP, is able to reduce the biomass of biofilms formed by both a reference and a clinical *S. epidermidis* strain, depending on the timeframe of the biofilm pre-growth. However, CFU counts and cell metabolism are much less affected by this LL-37-based coating than the biomass. A multifaceted treatment approach using ΦPSE1 and routinely-used antibiotics showed interesting synergy results, also depending on the timeframe of the biofilm pre-growth and the bacterial strains. Generally, data suggest that the combination of LL-37 with antibiotics targeting intracellular pathways (Tob, Dox and Lin) is more efficient when compared to the combination with Van. This could be attributed to the mode of action of LL-37, which forms pores in the bacterial membranes. These pores facilitate the entry of antibiotics, enhancing their effectiveness. In our study, ΦPSE1 led to a decrease in biomass and CFUs, but this effect was observed only when combined with Tob and applied to the clinical *S. epidermidis* 10168 strain. It highlights that both preventive and treatment approach can lead to various outcomes depending on the pathogens and strains. Moreover, the biofilm pre-growth time, and thus the duration prior to treatment is essential. Even if kinetics analyses on biofilm formation were not performed, our preliminary data suggest that the sooner the biofilm is treated, the more its formation is disrupted. To the best of our knowledge, this study is the first to investigate the antibiofilm effect of a coating integrating LL-37 using the LbL technique, and we are convinced that these preliminary results demonstrate the requirement of a multifaceted approach that leverages all available antimicrobial weapons to overcome biofilm-associated infections. For instance, given the antibiofilm activity of ΦPSE1, which can be potentially attributed to depolymerases, as demonstrated by Gutiérrez *et al.*,[44] an innovative project would be to plan on using purified depolymerase as a phage-based protein and to integrate it in a multilayer film using the LbL technique.

5.5 Take-home messages

- To limit biofilm-associated infections, a strategy that integrates both preventive and therapeutic approaches should be implemented.
- Bacteria, especially in biofilm form, are formidable enemies. To effectively combat them, it is imperative to use all available weapons at our disposal, and thus implement multifaceted strategies.
- The results and thus the interpretations of the experiments may vary depending on the bacterial strain used and the *in vitro* experimental conditions, such as the growth medium, the pre-growth duration of the biofilm before treatment, etc. It is crucial to consider these factors.

5.6 Supplementary information

5.6.1 Turbidity of LL-37 solution in MHB, TSB, LB, and RPMI media

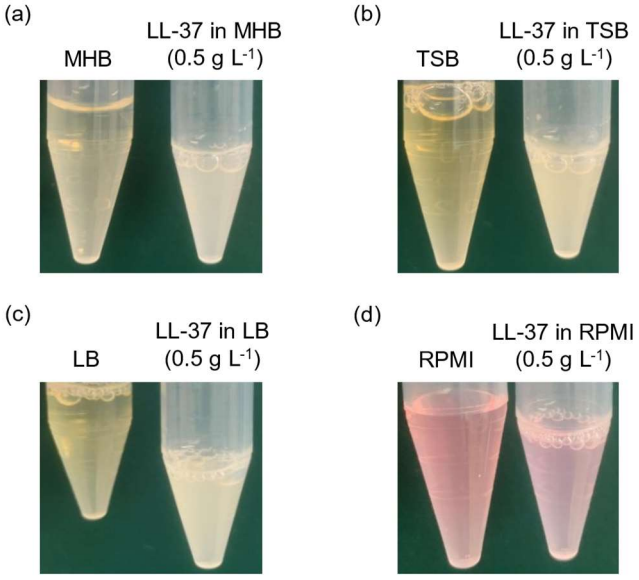

Figure IV-5. S1 – Visual observation of the turbidity of a 0.5 g L^{-1} solution of LL-37 in (a) MHB, (b) TSB, (c) LB, and (d) RPMI media.

5.6.2 Measurement of biomass for *S. aureus* ATCC 33591 and *S. epidermidis* ATCC 35984 biofilms as a function of the number of LL-37 layers in the coating

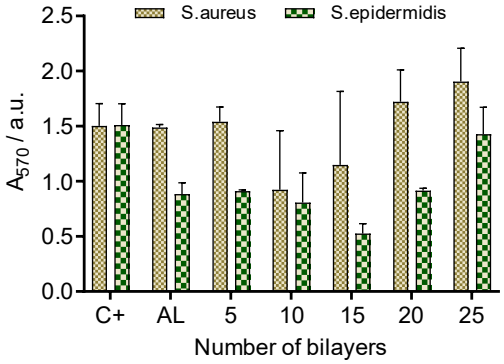

Figure IV-5. S2 – Effect of the number of bilayers forming the LL-37-based coating on the biomass of 48h pre-formed *S. aureus* ATCC 33591 and *S. epidermidis* ATCC 35984 biofilms. Values are mean ± SD (N=1 with n=3).

5.7 References

1. Karygianni, L., Ren, Z., Koo, H. & Thurnheer, T. Biofilm Matrixome: Extracellular Components in Structured Microbial Communities. *Trends Microbiol* **28**, 668–681 (2020).
2. Colilla, M., Izquierdo-Barba, I. & Vallet-Regí, M. The Role of Zwitterionic Materials in the Fight against Proteins and Bacteria. *Medicines* **5**, 125 (2018).
3. Khatoon, Z., McTiernan, C. D., Suuronen, E. J., Mah, T. F. & Alarcon, E. I. Bacterial biofilm formation on implantable devices and approaches to its treatment and prevention. *Heliyon* **4**, e01067 (2018).
4. Mengistu, D. A. *et al.* Global Incidence of Surgical Site Infection Among Patients: Systematic Review and Meta-Analysis. *Inquiry* **60**, (2023).
5. Li, M. *et al.* Chemical grafting of antibiotics into multilayer films through Schiff base reaction for self-defensive response to bacterial infections. *Chemical Engineering Journal* **382**, 122973 (2020).
6. Vuong, C. & Otto, M. *Staphylococcus epidermidis* infections. *Microbes Infect* **4**, 481–489 (2002).
7. Otto, M. Staphylococcal Biofilms. *Microbiol Spectr* **6**, (2018).
8. Oliveira, W. F. *et al. Staphylococcus aureus* and *Staphylococcus epidermidis* infections on implants. *Journal of Hospital Infection* **98**, 111–117 (2018).
9. Byrd, A. L., Belkaid, Y. & Segre, J. A. The human skin microbiome. *Nat Rev Microbiol* **16**, 143–155 (2018).
10. Koo, H., Allan, R. N., Howlin, R. P., Stoodley, P. & Hall-Stoodley, L. Targeting microbial biofilms: current and prospective therapeutic strategies. *Nat Rev Microbiol* **15**, 740–755 (2017).
11. Dragos, A. & Kovács, Á. T. The Peculiar Functions of the Bacterial Extracellular Matrix. *Trends Microbiol* **25**, 257–266 (2017).
12. Uruén, C., Chopo-Escuin, G., Tommassen, J., Mainar-Jaime, R. C. & Arenas, J. Biofilms as Promoters of Bacterial Antibiotic Resistance and Tolerance. *Antibiotics* **10**, 3 (2021).
13. VanEpps, J. S. & Younger, J. G. Implantable Device-Related Infection. *Shock* **46**, 597–608 (2016).

14. Bjarnsholt, T. The role of bacterial biofilms in chronic infections. *APMIS* **121**, 1–58 (2013).
15. Vishwakarma, A., Dang, F., Ferrell, A., Barton, H. A. & Joy, A. Peptidomimetic Polyurethanes Inhibit Bacterial Bio fi lm Formation and Disrupt Surface Established Biofilms. *J Am Chem Soc* **143**, 9440–9449 (2021).
16. Xu, C. *et al.* Is Treatment of Periprosthetic Joint Infection Improving Over Time? *J Arthroplasty* **35**, 1696-1702.e1 (2020).
17. Goh, G. S., Tornetta, P. & Parvizi, J. Facilitating the Approval Process of Anti-Infective Technologies and Advancing Them to the Market - Insights from an FDA Workshop on Orthopaedic Device-Related Infections. *J Bone Joint Surg* **103**, e57 (2021).
18. De Soir, S. *et al.* Exploiting phage-antibiotic synergies to disrupt *Pseudomonas aeruginosa* PAO1 biofilms in the context of orthopedic infections . *Microbiol Spectr* **12**, e03219 (2024).
19. Banerjee, I., Pangule, R. C. & Kane, R. S. Antifouling Coatings: Recent Developments in the Design of Surfaces That Prevent Fouling by Proteins, Bacteria, and Marine Organisms. *Advanced Materials* **23**, 690–718 (2011).
20. Mutschler, A. *et al.* Unexpected Bactericidal Activity of Poly(arginine)/Hyaluronan Nanolayered Coatings. *Chemistry of Materials* **28**, 8700–8709 (2016).
21. Kelleher, S. M. *et al.* Cicada Wing Surface Topography: An Investigation into the Bactericidal Properties of Nanostructural Features. *ACS Appl Mater Interfaces* **8**, 14966–14974 (2016).
22. Fernandes, J. S., Gentile, P., Pires, R. A., Reis, R. L. & Hatton, P. V. Multifunctional bioactive glass and glass-ceramic biomaterials with antibacterial properties for repair and regeneration of bone tissue. *Acta Biomater* **59**, 2–11 (2017).
23. Ferreres, G., Ivanova, K., Ivanov, I. & Tzanov, T. Nanomaterials and Coatings for Managing Antibiotic-Resistant Biofilms. *Antibiotics* **12**, 310 (2023).
24. Decher, G., Hong, J. D. & Schmitt, J. Buildup of ultrathin multilayer films by a self-assembly process: III. Consecutively alternating adsorption of anionic and cationic polyelectrolytes on charged surfaces. *Thin Solid Films* **210–211**, 831–835 (1992).

25. Vranckx, C. *et al.* Layer-by-Layer Nanoarchitectonics Using Protein-Polyelectrolyte Complexes toward a Generalizable Tool for Protein Surface Immobilization. *Langmuir* **38**, 5579–5589 (2022).
26. Vandamme, D., Landuyt, B., Luyten, W. & Schoofs, L. A comprehensive summary of LL-37, the factotum human cathelicidin peptide. *Cell Immunol* **280**, 22–35 (2012).
27. van Harten, R. M., van Woudenbergh, E., van Dijk, A. & Haagsman, H. P. Cathelicidins: Immunomodulatory Antimicrobials. *Vaccines* **6**, 63 (2018).
28. Lin, Q., Deslouches, B., Montelaro, R. C. & Di, Y. P. Prevention of ESKAPE pathogen biofilm formation by antimicrobial peptides WLBU2 and LL37. *Int J Antimicrob Agents* **52**, 667–672 (2018).
29. Memariani, M. & Memariani, H. Antifungal properties of cathelicidin LL-37: current knowledge and future research directions. *World J Microbiol Biotechnol* **40**, 34 (2023).
30. Ridyard, K. E. & Overhage, J. The potential of human peptide ll-37 as an antimicrobial and anti-biofilm agent. *Antibiotics* **10**, 650 (2021).
31. Dolinsky, T. J., Nielsen, J. E., McCammon, J. A. & Baker, N. A. PDB2PQR: An automated pipeline for the setup of Poisson-Boltzmann electrostatics calculations. *Nucleic Acids Res* **32**, 665–667 (2004).
32. Clinical and Laboratory Standards Institute (CLSI). Performance Standards for Antimicrobial Susceptibility Testing. (Wayne, Pennsylvania, USA, 2024).
33. Wiegand, I., Hilpert, K. & Hancock, R. E. W. Agar and broth dilution methods to determine the minimal inhibitory concentration (MIC) of antimicrobial substances. *Nat Protoc* **3**, 163–175 (2008).
34. Iglesias, Y. D., Wilms, T., Vanbever, R. & Van Bambeke, F. Activity of Antibiotics against *Staphylococcus aureus* in an In Vitro Model of Biofilms in the Context of Cystic Fibrosis: Influence of the Culture Medium. *Antimicrob Agents Chemother* **63**, e00602 (2019).
35. Steinberg, D. A. *et al.* Protegrin-1: a broad-spectrum, rapidly microbicidal peptide with in vivo activity. *Antimicrob Agents Chemother* **41**, 1738–1742 (1997).
36. Kang, J., Dietz, M. J. & Li, B. Antimicrobial peptide LL-37 is bactericidal against *Staphylococcus aureus* biofilms. *PLoS One* **14**, e0216676 (2019).

37. Geitani, R., Ayoub Moubareck, C., Touqui, L. & Karam Sarkis, D. Cationic antimicrobial peptides: Alternatives and/or adjuvants to antibiotics active against methicillin-resistant *Staphylococcus aureus* and multidrug-resistant *Pseudomonas aeruginosa*. *BMC Microbiol* **19**, 54 (2019).
38. Krishnamoorthy, R., Adhikari, P. & Anaikutti, P. Design, synthesis, and characterization of non-hemolytic antimicrobial peptides related to human cathelicidin LL-37. *RSC Adv* **13**, 15594–15605 (2023).
39. Sorrentino, I. *et al.* Development of anti-bacterial surfaces using a hydrophobin chimeric protein. *Int J Biol Macromol* **164**, 2293–2300 (2020).
40. Sancho-Vaello, E. *et al.* The structure of the antimicrobial human cathelicidin LL-37 shows oligomerization and channel formation in the presence of membrane mimics. *Sci Rep* **10**, 17356 (2020).
41. Nagarajan, R. Antibacterial activities and modes of action of vancomycin and related glycopeptides. *Antimicrob Agents Chemother* **35**, 605–609 (1991).
42. Kotra, L. P., Haddad, J. & Mobashery, S. Aminoglycosides: Perspectives on Mechanisms of Action and Resistance and Strategies to Counter Resistance. *Antimicrob Agents Chemother* **44**, 3249–3256 (2000).
43. Zhang, H. *et al.* Bactericidal synergism between phage endolysin Ply2660 and cathelicidin LL-37 against vancomycin-resistant Enterococcus faecalis biofilms. *NPJ Biofilms Microbiomes* **9**, 16 (2023).
44. Gutiérrez, D. *et al.* Role of the Pre-neck Appendage Protein (Dpo7) from Phage vB_SepiS-phiIPLA7 as an Anti-biofilm Agent in Staphylococcal Species. *Front Microbiol* **6**, 1315 (2015).

Part V – Conclusion and future prospects

1 Conclusion

1.1 General discussion and main achievements

This multidisciplinary thesis aimed at developing a coating displaying antibacterial properties. This was achieved through the assembly of multilayers integrating LL-37, an antimicrobial peptide (AMP). The multilayers were designed using the LbL self-assembly technique. It is well known in the literature that the charge heterogeneity of proteins and peptides can be a major setback for their LbL immobilization. Therefore, the surface charge of LL-37 was standardized via its complexation with Hep. The resulting $PPCs_{LL\text{-}37\text{-}Hep}$ were then used as new building blocks for LbL assembly. An in-depth analysis of the multilayers integrating $PPCs_{LL\text{-}37\text{-}Hep}$ was performed and the characteristics of these films were compared with the ones of films built with bare LL-37 molecules. The antibacterial properties of these latter were investigated through the study of *S. epidermidis* biofilm formation. In this section, the main results and achievements of the work will be summarized.

Our work builds upon the thesis of Aurélien vander Straeten, who developed a highly promising method for protein immobilization, featuring significant potential for applications in fields that require bioactive surfaces on inert materials.[1] The interest of using PPCs in LbL assemblies was demonstrated in his work. Indeed, lysozyme (Lyz) amount and its specific activity were significantly higher when PPCs were used instead of bare Lyz molecules.[2] This proof-of-concept study reported very interesting results, but was based on a single protein, *i.e.*, Lyz, and selected PEs, *i.e.*, PSS and PAH.[2,3]

1.1.1 PPCs as versatile building blocks for LbL assembly

The first step of the present work was to demonstrate the versatility of the use of PPCs as building blocks for protein surface immobilization. To do so, LL-37, Ins, Lyz, and Gox were complexed with Alg, PSS_I, Hep, and PAH. It was shown that PPCs formation can be controlled by adjusting their stoichiometry. This was expressed as a negative-to-positive (-)/(+net) or a positive-to-negative (+)/(-net) charge ratio depending on the protein charge at the investigated pH. In all cases, the addition of the PE to the protein

resulted in the formation of PPCs between (-)/(+net) or (+)/(-net) ≈ 0.5 and 2. Although the protein size did not influence this range of values, it was highly dependent on the PE charge density and the nature of the protein. For all tested PPCs, the resulting complex were then assembled with an oppositely-charged PE, *i.e.*, Chi, PAH, or Hep, using the LbL method. As a matter of comparison, LbL films integrating the bare protein with an oppositely-charged PE were assembled. Interestingly, we demonstrated that almost all multilayers grew to higher masses when using PPCs rather than bare protein molecules, and that a desorption is almost systematically observed upon PAH adsorption (not Chi) on a layer of PPCs. The larger masses are partially attributed to the higher hydration levels of multilayers containing PPCs compared to those incorporating bare proteins. However, since only QCM-D measurements were performed to compare growth profiles, we could, at this stage, not determine if the mass difference also arised from an increased amount of protein or PE in the multilayers, or only from changes in the multilayer architecture (higher water content in the film). This question was addressed in *Chapter 2*, *3*, and *4* through an in-depth analysis of the [LL-37-Hep] and [Chi-PPCs$_{\text{LL-37-Hep}}$] systems. The desorption from the multilayers upon PE adsorption is the result of a trade-off between PE-PE and protein-PE pairing strengths, and it is thus dependent on both PE and protein nature. Adsorption of a PE with high charge density onto a PPCs layer containing a protein with low charge density induces greater desorption. These findings are consistent with the ones of Aurélien vander Straeten.[1]

The results of *Chapter 1* confirm that PPCs can be used to immobilize a wide variety of protein and PEs in multilayers, but that these multilayers have different growth patterns depending on the protein and PE nature. Therefore, although LbL assembly is the most straightforward and intuitive approach for organizing molecules at interfaces, it is too naively depicted as a sequential arrangement of well-ordered layers, resembling a lasagna, which reflects the assembly method rather than the actual structure achieved through self-assembly. This may wrongly lead to assume that the multilayer is composed of the same constituents used for its fabrication, in the same ratio of amount, and that it maintains the structure represented by these simplified illustrations. Therefore, upon constructing a multilayer, it is essential to conduct a comprehensive investigation of its composition and

structure, as these cannot be accurately inferred solely from the assembly method or the constituent materials.

1.1.2 In-depth analysis of LL-37-based coatings

With the goal to design a coating that would prevent biofilm formation on medical implantable devices, I assumed that using PPCs could allow for greater immobilization of LL-37 on the surface, similar to the results obtained for Lyz by Aurélien vander Straeten.[1] However, understanding the interactions and competition between soluble and surface-immobilized species is essential, as well as accounting for the effects arising from the fine details of the assembly process. Thus, *Chapter 2*, *3* and *4* were dedicated to an in-depth analysis of the organization, architecture, composition, and dynamics of multilayers incorporating both bare LL-37 and $PPCs_{LL\text{-}37\text{-}Hep}$.

The $PPCs_{LL\text{-}37\text{-}Hep}$ were formed at a (-)/(+net) charge ratio of 1.5. This ratio can be related to the minimal amount of Hep needed to displace the equilibrium towards $PPCs_{LL\text{-}37\text{-}Hep}$ formation. Beyond this value, the LL-37 charges are compensated by Hep and the $PPCs_{LL\text{-}37\text{-}Hep}$ take a core-corona structure with a neutral internal domain and negatively-charged Hep chains dangling outside. The $PPCs_{LL\text{-}37\text{-}Hep}$ thus formed can be assembled with Chi using the LbL method. However, in a system with three constituent compounds, molecular rearrangements are possible. For example, free Hep molecules from the $PPCs_{LL\text{-}37\text{-}Hep}$ suspension or released from $PPCs_{LL\text{-}37\text{-}Hep}$ upon assembly could participate to [Chi-Hep] LbL assembly, which could result in the failure of immobilizing LL-37. XPS analyses in *Chapter 2*, and BCA assays in *Chapter 4*, highlighted the immobilization of LL-37 in these $PPCs_{LL\text{-}37\text{-}Hep}$-based multilayers. Even if a three-component system is compared to a two-component system, it has been demonstrated, in this work, that environmental conditions and assembly pathway have a major effect on the nano-architecture and organization of self-assembling multilayers.

First, it has been established that **the pH** of the solution significantly **influences the properties of the multilayers**. Multilayers have been built at pH 3.5 and 5. In the anchoring layer, we demonstrated through XPS analyses (*Chapter 2*) that since Chi is less charged at pH 5 compared to pH 3.5, a higher amount of Chi is incorporated into the film at pH 5 to overcompensate the Hep charge. The combined study using QCM-D analysis and ellipsometry

measurements, performed in *Chapter 3*, indicated that the films are more viscoelastic at pH 5 than at pH 3.5. The variations in rigidity/viscoelasticity of the Chi-$PPCs_{LL\text{-}37\text{-}Hep}$ films at pH 3.5 and pH 5 can be attributed to the conformation of Chi. At pH 3.5, Chi is highly ionized, resulting in strong electrostatic repulsion between charged segments along the chain, which increases chain stiffness and extends the PE chains. In contrast, at pH 5, with a lower charge density, Chi takes a 'loops and tails' configuration, leading to a more viscous behavior of the film. This 'loop and tail' configuration favors the water uptake. In terms of quantity of immobilized LL-37, more LL-37 is integrated in the multilayers at pH 3.5 than at pH 5.

Second, **the properties of the multilayers are** also **influenced by the** specific employed **assembly strategy**. It was demonstrated that layers built with $PPCs_{LL\text{-}37\text{-}Hep}$ are more viscoelastic and more hydrated than the bare LL-37-based multilayers. The differences in the viscoelastic properties of [LL-37-Hep] and [Chi-$PPCs_{LL\text{-}37\text{-}Hep}$] at pH 3.5 and pH 5 can be attributed to the differential hydration levels of the multilayers and the ionization degrees of the constituent compounds. In terms of mass of LL-37 immobilized on the surface, results from XPS analysis are not always consistent with those from BCA assays, suggesting that the composition of the extreme surface may be different from the bulk composition. For example, at pH 3.5 and after the adsorption of 25 bilayers, BCA assays highlighted that LL-37-based multilayer incorporates 19.7 ± 1.5 µg cm^{-2} of LL-37, *i.e.*, three times more than the $PPCs_{LL\text{-}37\text{-}Hep}$-based multilayer (6.3 ± 2.1 µg cm^{-2}). One possible explanation is that the adsorption of positively-charged Chi onto $PPCs_{LL\text{-}37\text{-}Hep}$ may displace LL-37 from the multilayer, thereby releasing some of the LL-37 molecules.

Finally, the cumulative mass of released LL-37 was examined at pH 3.5 and 5 as a function of time and bilayer number. A burst release was observed within the first 24 hours, followed by a more gradual release from day 1 to day 14. After 14 days of release, the coating is not depleted of its LL-37 content. This profile of release is particularly interesting, as the initial burst release is of moderate intensity (with less than 50% of immobilized LL-37 released), followed by a prolonged and gradual release over an extended duration. Therefore, this release profile is useful for targeting both bacteria in the early stages of infection and opportunistic pathogens beyond this period. Consequently, the benefit of the coated surface in terms of LL-37 release occurs within the initial hours to weeks.

1.1.3 Antibacterial activity of LL-37-based coatings

One of the major challenges with LL-37, in contrast to enzymes, lies in the inability to assess its antibacterial activity through standardized and rapid tests. The only feasible approach is to directly assess its effect on bacteria through tests such as MIC evaluation, biomass measurement, metabolic activity assays, CFU counts, etc. Once LL-37 is immobilized on the surface, its activity is assessed in bacterial media that are complex in terms of composition (sugars, proteins, etc.), and this can substantially impact LL-37's activity. As discussed in *Chapter 4*, the activity of LL-37 is contingent upon its conformation which is influenced by the environmental conditions in which LL-37 is present. Consequently, ineffectiveness of LL-37 against bacteria could be attributed to several factors, such as, ineffectiveness against the strain, insufficient immobilization of LL-37, denaturation during the immobilization process, loss of its α-helical conformation, complexation or precipitation with constituents of the analytical medium upon release from the coating, etc. Pinpointing the most likely cause remains challenging. To evaluate the antibiofilm activity of the LL-37-based coatings, experiments using LL-37 as a stand-alone preventive strategy and in combination with PSE1 phages and routinely-used antibiotics were performed on both *S. epidermidis* reference ATCC 35984 and clinical 10168 strains. Experiments were performed in RPMI, as it was the only medium that did not result in LL-37 precipitation. Results were presented in *Chapter 5* and highlighted that a $[LL\text{-}37\text{-}Hep]_{15}$-based coating is able to reduce the biomass of 48h and 72h pre-grown biofilms formed by both strains. However, CFU counts are much less affected by this LL-37-based coating than the biomass. Indeed, except for the 48h pre-formed *S. epidermidis* 10168 biofilms condition, LL-37-based coating as a stand-alone preventive agent did not reduce the cultivable bacterial cells. Therefore, a multifaceted approach has been studied. Interestingly, depending on the studied strain and the timeframe of the biofilm pre-growth, various outcomes can be obtained. The results generally suggested that the combination of LL-37-based coating with antibiotics targeting intracellular pathways (Tob, Dox, and Lin) is more effective compared to its combination with Van. This improved efficacy may be related to the LL-37's ability to create pores in bacterial membranes, which facilitates the penetration of antibiotics and enhances their effectiveness. Our investigation also revealed that PSE1 phage reduced both biomass and CFUs,

but this effect was observed exclusively when combined with Tob and applied to the clinical *S. epidermidis* 10168 strain. It is important to emphasize that these are preliminary findings, and further, more exhaustive research is necessary since the experimental conditions have a major impact on results. Future studies should include standardizing the biofilm pre-growth period, varying the concentration of different antibiotics, investigating the synergy between these antibiotics and specific phages, using clinical bacterial strains, and other relevant experimental conditions.

1.2 Key take-home messages

Interestingly, our study of LL-37-based LbL assemblies yielded results that differ from those obtained with Lyz, which was complexed with PSS and immobilized on the surface using PAH.[1,2] The formation of $PPCs_{LL\text{-}37\text{-}Hep}$ does not enhance the surface adsorption of LL-37. This difference between Lyz- and LL-37-based multilayers could be attributed to the structural nature of LL-37. While Lyz maintains a compact globular structure in ultrapure water, LL-37 adopts a long, disordered chain conformation, as seen in the *Chapter 4*. Consequently, the complexation and charge density homogenization of proteins/peptides by a counter-PE would be more effective for globular proteins.

Even if it is often assumed that the main driving force of the self-assembly strategy is the alternating adsorption of oppositely-charged species, and thus that any similar macromolecule would self-assemble the same way, this work highlights that assembly of proteins/peptides with PE depends on the protein/peptide nature, PE nature, pH conditions, adsorption sequence, and each of which can profoundly impact the resulting multilayers. Therefore, it seems crucial to choose the accurate conditions that fully match the specifications of a selected application, instead of using a proof-of-concept strategy.

This strategy has been applied in this thesis work. The focus has been set on a comprehensive study of LL-37 immobilization using the LbL technique. To the best of our knowledge, we are the first to have carried-out such an in-depth study, which is crucial to understand the composition, organization and architecture of antimicrobial peptide-based coatings aiming at preventing biofilm formation on medical implantable devices.

1.2.1 Fighting a biofilm with all available weapons: Better to prevent than to cure

In the event of infection and biofilm development on a medical implant, the first intervention involves mechanical removal of the biofilm through curettage. This process requires an additional surgical procedure, which poses considerable strain on the patient. In my opinion, our healthcare system often favors treatment over prevention.[4] Nevertheless, the adage 'prevention is better than cure' holds true. Therefore, the development of biocompatible materials that resist colonization by microbiological entities is considered a highly sought-after goal in the field of biomaterial-associated infections. Over the past decades, the significant increase in life expectancy has led to a sharp rise in the demand for medical implantable devices, along with a variety of associated medical and microbiological challenges. However, the occurrence of both airborne and surgical site infections remains inevitable, especially considering the ongoing antibiotic resistance crisis and the widespread prevalence of pan-drug resistant bacteria, including those present in hospital environments. With this in mind, this thesis aims to contribute to the field, recognizing that significant work is required to successfully address biomaterial-associated infections. If no action is taken, multidrug-resistant bacterial infections are predicted to cause more deaths than cancer in the coming years.[5] This emphasizes the urgency of the situation and the vital need for collaboration between scientists and clinicians to develop effective solutions. Considering the high resistance of biomaterial-associated infections, we thus recommend using a multifaceted approach with all the antibacterial weapons at our disposal.

2 Future prospects

2.1 Fundamental investigations of LL-37-based coatings

Throughout this research, we focused on LL-37; there are numerous antimicrobial peptides, antimicrobial polymers, and enzymes that influence biofilm formation, which could be incorporated into similar systems. There is a myriad of scientific studies dedicated to developing strategies to prevent biofilm formation on medical implantable devices.

We performed an in-depth analytical investigation to elucidate the structure and architecture of two specific LbL systems, *i.e.*, [LL-37-Hep] and [Chi-PPCs$_{LL-37-Hep}$]. At the end of this work, we obtained a robust comprehension of these systems, but much work remains to be done to thoroughly investigate their applicability. Indeed, the antibacterial effect was examined only towards the end of the work, which limited the opportunity to fully explore the coatings' potential. LL-37, recognized as the sole human cathelicidin AMP, and known for its antibacterial, antibiofilm, antiviral, antifungal, antitumor, and pro-angiogenic properties, appeared to be an ideal candidate for surface immobilization to develop a coating aimed at preventing biofilm formation. During our work, the identification of a very high MIC for the studied strain, along with the conformation-dependent activity of LL-37, tempered the initial enthusiasm. As observed in *Chapter 4*, the conformation of LL-37 is highly influenced by the surrounding environmental conditions. In their master thesis, Juliette Dewez and Bastien Croës sought to ascertain the conformation of LL-37 upon its release from the multilayer system.[6] Despite implementing various investigative approaches and optimizing the release protocol, they were unable to release a sufficient quantity of LL-37 to analyze its conformation using CD spectroscopy. In my view, this study would be essential and would fill a significant gap in the current analytical investigation. Assessing the conformation of LL-37 within multilayers using techniques such as polarization-modulated infrared reflection-absorption spectroscopy (PM-IRRAS) would also yield valuable insights.

Our findings, in the *Chapter 4*, revealed that the amount of immobilized LL-37 is greater when assembled in its bare form compared to its incorporation within PPCs. However, investigating the antibacterial properties of coatings integrating these PPCs would be of significant interest. Indeed, as demonstrated in *Chapter 3*, multilayers assembled with PPCs exhibit greater hydration compared to films composed of bare LL-37. It has been demonstrated that increased hydration of multilayers enhances their activity.[2] Consequently, even with a lower quantity of LL-37 immobilized on the surface, improved antibacterial activity could be demonstrated.

Based on preliminary results presented in *Chapter 5*, antibacterial studies were conducted on coatings incorporating 15 layers of bare LL-37. This setup was chosen as it provided a suitable balance between the amount of LL-37 adsorbed on the surface and the sample preparation time. However,

increasing the number of bilayers would extend the immobilized and subsequently released amount of LL-37. Investigating whether such an increase would enhance the antibacterial properties of the coating would be worthwhile.

Finally, we evaluated the impact of the LL-37 coating and various treatments (antibiotics and/or phages) on 24, 48, or 72h pre-formed biofilms. However, we did not investigate the kinetics of biofilm formation, specifically how the coating influences or delays the initial stages of biofilm development. This is essential, as I remain convinced–and the findings of this thesis corroborate this–that we must not only treat infections post-occurrence but also employ all available measures to prevent them.

2.2 Future work related to new findings

As detailed in the *Part I – Context of the research* and analyzed in the *Chapter 5*, phages are very interesting weapons to prevent and to treat biomaterial-associated infections. A side project of this thesis consisted of immobilizing whole bacteriophages on surfaces. Given that phages, and particularly tailed phages (constituting 95% of the phage population), exhibit a structural dipole moment between their tail and head, this could potentially be exploited to assemble them using the LbL technique. Theoretically, this LbL assembly integrating bacteriophages could, under ideal conditions, facilitate a self-perpetuating coating mechanism upon bacterial infection. Imagine a scenario where multiple active phages are incorporated into a LbL antimicrobial coating and can gradually diffuse over time. Hence, if multiple layers incorporating phages gradually release phages following the implantation of the device, this would maintain phage activity in the surrounding environment during the crucial first few days, providing protection against surgical site infections during this critical period. However, although most phages exhibit negatively-charged capsids and positively charged tail and tail fibers at physiological pH,[7] we were unable to immobilize them using the LbL method. One explanation involves the morphology of phage particles. Their large size, ranging from 30 to 200 nm, may weaken electrostatic interactions with the surface due to steric hindrance between the charges on the phages and the surface.[7,8] However, more experiments

should be performed to understand why the immobilization of phages through LbL failed.

An alternative approach to harnessing the antibiofilm potential of phages for antimicrobial coatings involves using their phage-derived enzymes, which target both bacterial cells and the biofilm structures and components. During its thesis project, Steven De Soir identified two novel depolymerase proteins in *de novo* isolated phages targeting *S. aureus* and *S. epidermidis*. One of these is derived from the PSE1 phage used in our experiments in *Chapter 5*. This protein is indicated to be a pre-neck appendage protein. Interestingly, Gutiérrez *et al.* reported a pre-neck appendage protein, labeled Dpo7, identified and derived from their staphylococcal phage vB_SepiS-philPLA7, to be an effective antibiofilm agent.[9] Pre-treatment of polystyrene surfaces with such depolymerase resulted in up to an 85% reduction in staphylococcal biofilms, with both *S. aureus* and *S. epidermidis* biofilms showing susceptibility to the depolymerase activity. Despite differences in nature and efficacy, studies on biofilms treated with depolymerases derived from phages targeting other bacteria like *E. coli*,[10] *P. aeruginosa*,[11] *A. baumannii*,[12] and *K. pneumoniae*[13] consistently demonstrated significant reductions in biofilm formation.[14] Therefore, the newly identified PSE1 depolymerase protein should be isolated from the phage to study its antibiofilm properties.

This depolymerase protein has been isolated, purified and produced by Steven De Soir, in collaboration with the Laboratory for Applied Biotechnology of the University of Ghent. Interestingly, once purified, this depolymerase can be used as a phage-based protein coating, using the LbL method, to prevent biofilm formation. To the best of our knowledge, scientific literature does not report the immobilization of a phage protein on medical implantable devices through LbL assembly. We believe that these phage-derived proteins could offer a highly promising alternative in the near future. Many challenges associated with whole phage-based coatings might be alleviated by using depolymerase proteins. Furthermore, incorporating only phage-derived proteins, rather than entire viral particles, may increase the likelihood of regulatory approval for clinical applications. This stimulating research is currently being pursued in a new project supported by Steven De Soir. We could also imagine constructing LbL multilayers incorporating a combination of antimicrobial agents, including depolymerases and antimicrobial peptides.

2.3 Application-oriented outlook: A gap between fundamental research and application?

One of the primary challenges in scientific research is to translate fundamental discoveries into practical applications. Frequently, the conditions and outcomes observed in controlled laboratory settings do not directly correspond to the ones of real-world environments.

2.3.1 The economic viewpoint

From a practical point of view, one significant challenge remains the high cost of LL-37, which raises concerns about the economic feasibility of LL-37-based coatings. Considering that a hip prosthesis currently costs around 400 euros, adding such a coating would significantly increase both production and final costs. However, as peptide synthesis costs continue to decrease, alongside the potential for enhanced efficacy of prostheses and the declining effectiveness of antibiotics, this additional expense may be justified, especially when considering the costs associated with revision surgeries in case of infection. To further reduce costs, the use of shorter AMPs, which are less expensive to synthesize, could be explored as an alternative to LL-37.

2.3.2 Sterility

In our context, this pertains to the operating room, where critical factors such as environmental sterility must be rigorously maintained. This practical consideration, essential from a clinical perspective, is frequently neglected in fundamental research. This was also the case in our study. Indeed, we focused on determining the antibiofilm properties of our coating without evaluating how the sterilization process might alter these properties. Industrial sterilization protocols are stringently regulated, and for medical implantable devices, it typically involves methods such as autoclaving, gamma irradiation or ethylene oxide.

Consider the practical example of a coated hip prosthesis that is intended for implantation in a patient. From a fundamental perspective, the coating would be applied sequentially, as performed in our study, within a controlled sterile environment, such as a laminar flow hood. However, from a practical

perspective, adapting this method to an industrial scale is challenging, as it would require maintaining a sterile environment throughout each stage of the process. Moreover, from the regulatory authorities' perspective, this process could also be problematic, since it is not possible to guarantee that an environment is 100% sterile, and thus there will be no approval if the final product is not adequately sterilized. Consequently, the LL-37-coated final product should be sterilized prior to use.

For proteins and peptides, whose activity is dependent on their conformation, post-manufacture sterilization could present significant challenges. Indeed, it is well-known that the combined effect of high temperature and pressure during autoclaving process, gamma radiations, ethylene oxide, or supercritical CO_2 can cause protein structure alterations.[15–18] Thus, comprehensive analyses should be conducted on the LL-37-based coatings with a view to future application.

2.3.3 Intraoperative handling and friction

Another challenge that arises when considering the reality of the operating theatre is the impact of intraoperative handling and friction on the integrity of the coating. Determining the coefficient of friction during hip replacement surgery is challenging. However, since rapid osseointegration is essential, the friction between the prosthesis and the bone is substantial. Thus, the critical questions are to what extent the surface coating remains intact under such friction and how this will affect the coating’s antibacterial properties. Fundamentally, experiments could be conducted to analyze the coating and its antibacterial efficacy as a function of applied friction. However, it seems evident that intraoperative handling and friction will considerably impact the coating. Protective measures could be devised to preserve the implant surface and thus the coating. One approach could involve applying a hydrogel to the surface. Indeed, hydrogels are essentially polymer chains forming a huge network trapping water within itself. LbL assemblies are inherently a form of hydrogel and are frequently described as nanogels. However, due to their thin structure, these nanogels are particularly susceptible to frictional forces. Thicker hydrogels behave like a solid while being mostly composed of liquid water, which gives them interesting properties such as smoothness, flexibility and high-water content. These characteristics make hydrogels

excellent materials for reducing frictional forces between the prosthesis and the bone. The use of such materials may raise questions about the strategic choices made throughout this thesis. Indeed, hydrogels are known for their applications in drug delivery systems. Consequently, they could be used to both reduce friction and allow for the sustained release of LL-37, or other antimicrobial compounds, into the surrounding environment. This strategy is particularly intriguing and could warrant investigation as a distinct research topic.

2.3.4 *In vitro* experiments

In the preliminary phase of assessing the antibacterial efficacy of a compound, material, coating, etc., *in vitro* assays are typically performed. However, *in vitro* conditions often fail to fully replicate the complexities and nuances of clinical and *in vivo* settings. Typically, our antibiofilm experiments were conducted with an initial inoculum of approximately $2.5*10^6$ bacteria. This inoculum was selected to achieve a homogeneous biofilm within 24h, thereby allowing to evaluate the antibiofilm efficacy of the various conditions tested. However, it has been established that the presence of an implantable medical device can prompt infection even with a low bacterial inoculum, such as 10^2 bacteria.[19] Consequently, the bacterial inoculum used in the *in vitro* studies is not completely representative of clinical conditions. It would thus be valuable to vary the initial inoculum and investigate the coating's effect on biofilm formation as a function of the bacterial load.

2.3.5 *In vivo* experiments

In vitro experiments were performed in RPMI medium with the *S. epidermidis* reference strain ATCC 35984 and the clinical strain 10168. As already broached in the context of this research, depending on the bacterial growth media, the biofilm formation of a same bacterial strain can be completely different, questioning the *in vitro* conditions in which the studies should be performed.[20] Indeed, can the results obtained in RPMI medium be translated to a physiological environment? Likewise, depending on the strain used to perform these *in vitro* experiments, results can also be completely different. The experimental laboratory conditions do not capture the complexity of

biofilms in clinical systems, where the chemical properties of the bulk fluid, the fluid dynamics, the surface topography, etc., highly impact the biofilm composition and structure, and thus its development.

When conducting *in vitro* experiments, it is essential to remember that biofilms from the researcher's perspective is not the one from the clinician's one. Consequently, for studies focused on treating, reducing, or preventing biofilms, the relevance of *in vitro* studies compared to *in vivo* studies may be questioned, considering the significant impact of experimental conditions on biofilm formation and behavior. Therefore, conducting an *in vivo* study of our coatings would be interesting.

In the same way, there are numerous concerns surrounding the limited translation from *in vivo* models to clinical studies.[21] This drawback highlights the limits of *in vivo* study, such as differences between humans and animals used for *in vivo* studies, the choice of animal for *in vivo* studies, or as already approached, the choice of bacterial strains.[22]

This highlights the significant unresolved issues and underscores the critical need for effective collaboration between researchers and clinicians to understand the complexities of these systems and address biofilm-related infections.

2.4 References

1. vander Straeten, A. Protein-polyelectrolyte complexes for the surface immobilization of bioactive proteins. (PhD Thesis, UCLouvain, 2019).
2. vander Straeten, A. *et al.* Protein–polyelectrolyte complexes to improve the biological activity of proteins in layer-by-layer assemblies. *Nanoscale* **9**, 17186–17192 (2017).
3. vander Straeten, A., Bratek-Skicki, A., Jonas, A. M., Fustin, C.-A. & Dupont-Gillain, C. Integrating Proteins in Layer-by-Layer Assemblies Independently of their Electrical Charge. *ACS Nano* **12**, 8372–8381 (2018).
4. Levine, S., Malone, E., Lekiachvili, A. & Briss, P. Health Care Industry Insights: Why the Use of Preventive Services Is Still Low. *Prev Chronic Dis* **16**, (2019).
5. O'Neill, J. Tackling drug-resistant infections infections globally: final report and recommendations. *The Review on Antimicrobial Resistance* London, (2016).
6. Dewez, J., Croës, B., Vranckx, C. & Dupont-Gillain, C. Preventing infections of hip joint prostheses: activity of an antimicrobial coating based on the LL-37 peptide. (UCLouvain, Louvain-la-Neuve, 2024).
7. O'Connell, L., Marcoux, P. R. & Roupioz, Y. Strategies for Surface Immobilization of Whole Bacteriophages: A Review. *ACS Biomater Sci Eng* **7**, 1987–2014 (2021).
8. Paczesny, J. & Bielec, K. Application of Bacteriophages in Nanotechnology. *Nanomaterials* **10**, 1944 (2020).
9. Gutiérrez, D. *et al.* Role of the Pre-neck Appendage Protein (Dpo7) from Phage vB_SepiS-phiIPLA7 as an Anti-biofilm Agent in Staphylococcal Species. *Front Microbiol* **6**, 1315 (2015).
10. Guo, Z. *et al.* Identification and Characterization of Dpo42, a Novel Depolymerase Derived from the *Escherichia coli* Phage vB_EcoM_ECOO78. *Front Microbiol* **8**, 1460 (2017).
11. Mi, L. *et al.* Identification of a lytic *Pseudomonas aeruginosa* phage depolymerase and its anti-biofilm effect and bactericidal contribution to serum. *Virus Genes* **55**, 394–405 (2019).
12. Hernandez-Morales, A. C. *et al.* Genomic and Biochemical Characterization of Acinetobacter Podophage Petty Reveals a Novel

Lysis Mechanism and Tail-Associated Depolymerase Activity. *J Virol* **92**, e01064 (2018).

13. Wu, Y. *et al.* A Novel Polysaccharide Depolymerase Encoded by the Phage SH-KP152226 Confers Specific Activity Against Multidrug-Resistant *Klebsiella pneumoniae* via Biofilm Degradation. *Front Microbiol* **10**, 2768 (2019).
14. Topka-Bielecka, G. *et al.* Bacteriophage-Derived Depolymerases against Bacterial Biofilm. *Antibiotics* **10**, 175 (2021).
15. Zhang, Y. *et al.* Effects of heating, autoclaving and ultra-high pressure on the solubility, immunoreactivity and structure of major allergens in egg. *Food Agric Immunol* **29**, 412–423 (2018).
16. Lalande, M. *et al.* Direct Radiation Effects on the Structure and Stability of Collagen and Other Proteins. *ChemBioChem* **20**, 2972–2980 (2019).
17. Chen, L. *et al.* Chemical Modifications of Therapeutic Proteins Induced by Residual Ethylene Oxide. *J Pharm Sci* **104**, 731–739 (2015).
18. Monhemi, H. & Housaindokht, M. R. The molecular mechanism of protein denaturation in supercritical CO2: The role of exposed lysine residues is explored. *J Supercrit Fluids* **147**, 222–230 (2019).
19. Zimmerli, W., Waldvogel, F. A., Vaudaux, P. & Nydegger, U. E. Pathogenesis of foreign body infection: description and characteristics of an animal model. *J Infect Dis* **146**, 487–497 (1982).
20. Hancock, V., Witsø, I. L. & Klemm, P. Biofilm formation as a function of adhesin, growth medium, substratum and strain type. *International Journal of Medical Microbiology* **301**, 570–576 (2011).
21. Romero, D. & Kolter, R. Will biofilm disassembly agents make it to market? *Trends Microbiol* **19**, 304–306 (2011).
22. Von Herrath, M. G. & Nepom, G. T. Lost in translation: Barriers to implementing clinical immunotherapeutics for autoimmunity. *Journal of Experimental Medicine* **202**, 1159–1162 (2005).

Les devises Shadok

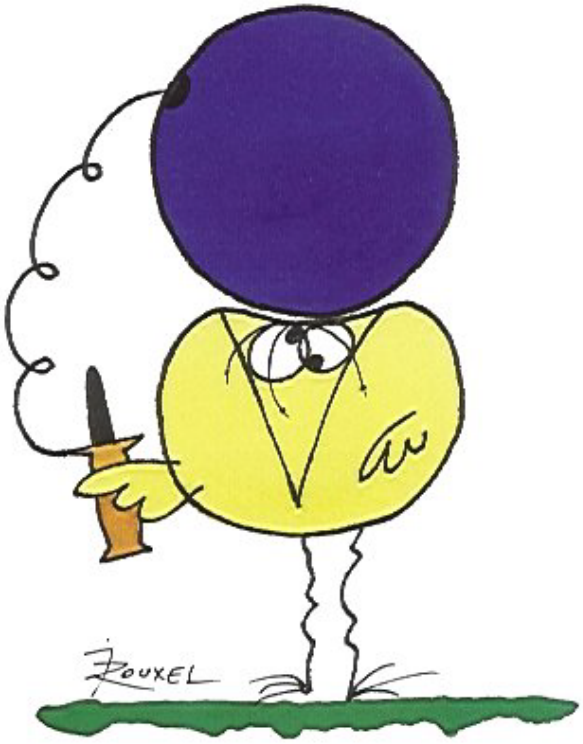

EN ESSAYANT CONTINUELLEMENT
ON FINIT PAR RÉUSSIR. DONC:
PLUS ÇA RATE, PLUS ON A
DE CHANCES QUE ÇA MARCHE.